

---

Electronic Thesis and Dissertation Repository

---

3-15-2021 2:00 PM

## Functional Role of DREAM and DYRK1A in High-Grade Serous Ovarian Cancer Cell Dormancy

Pirunthan Perampalam, *The University of Western Ontario*


Supervisor: Dick, Frederick A., *The University of Western Ontario*

: DiMattia, Gabriel E., *The University of Western Ontario*

A thesis submitted in partial fulfillment of the requirements for the Doctor of Philosophy degree in Biochemistry

© Pirunthan Perampalam 2021

Follow this and additional works at: <https://ir.lib.uwo.ca/etd>

 Part of the [Cancer Biology Commons](#), [Medical Cell Biology Commons](#), [Obstetrics and Gynecology Commons](#), [Oncology Commons](#), [Pathology Commons](#), and the [Translational Medical Research Commons](#)

---

### Recommended Citation

Perampalam, Pirunthan, "Functional Role of DREAM and DYRK1A in High-Grade Serous Ovarian Cancer Cell Dormancy" (2021). *Electronic Thesis and Dissertation Repository*. 7675.  
<https://ir.lib.uwo.ca/etd/7675>

This Dissertation/Thesis is brought to you for free and open access by Scholarship@Western. It has been accepted for inclusion in Electronic Thesis and Dissertation Repository by an authorized administrator of Scholarship@Western. For more information, please contact [wlsadmin@uwo.ca](mailto:wlsadmin@uwo.ca).

## Abstract

High-grade serous ovarian cancer (HGSOC) is the most common form of ovarian cancer. The majority of women are disproportionately diagnosed at an advanced stage (stage III-IV) of the disease when tumours have progressed beyond the ovaries or fallopian tubes and into the peritoneal cavity. Survival rates at late-stage are as low as 25% and chemoresistant disease recurrence is common, affecting up to 90% of patients. Multicellular clusters called spheroids contribute to dormancy, chemoresistance, and metastases and are a major challenge to treatment of HGSOC. Spheroid cells undergo reversible quiescence to evade chemotherapy in a process mediated by the mammalian DREAM complex and its initiating kinase, DYRK1A. Depletion of DYRK1A reduces spheroid cell survival and increases sensitivity to chemotherapy, highlighting it as an attractive therapeutic target. Herein we demonstrate the long-term consequences of DREAM loss in adult mice. DREAM deficient mice do not have proliferative control defects but develop systemic amyloidosis as a result of overexpression of apolipoproteins *Apoa1* and *Apoa4*. Overexpression of *Apoa1* and *Apoa4* were marked with increased B-MYB-MuvB (MMB) and decreased H2AZ deposition within gene bodies. The prolonged latency before developing amyloidosis suggests depriving cells of quiescence is tolerable for short periods of time. To broadly identify genetic vulnerabilities in spheroid cells, we employed an integrated strategy in which we investigated the transcriptional programming and also performed a loss-of-function genome-wide CRISPR screen in HGSOC spheroid cells. Towards this aim, we developed novel bioinformatic tools and methodology to facilitate high-throughput discovery of essential genes and pathways and anticipate these tools will have broad usability in transcriptional and loss-of-function studies. Using these tools, we identified the netrin signaling pathway as an essential mediator of HGSOC spheroid cell survival.

Specifically, components of netrin signaling are upregulated in spheroid cells and depletion of netrin ligands or receptors was sufficient to reduce spheroid cell viability. Our work highlights netrin signaling as a potential target for new metastatic ovarian cancer therapies. Taken together, the work presented herein provide more insight into the roles of DREAM and DYRK1A in HGSOc spheroid survival as well as implications of therapeutically targeting this pathway. HGSOc is a very deadly disease and there is an urgent need to develop new therapeutic strategies that can specifically target dormant chemoresistant spheroids in patients to treat or prevent relapse.

## Keywords

High-grade serous ovarian cancer, dormancy, quiescence, metastasis, spheroids, DREAM, DYRK1A, amyloidosis, netrin signaling, bioinformatic tools

## Summary for Lay Audience

The majority of ovarian cancer cases are diagnosed at an advanced stage when the disease has spread into the abdominal cavity. Survival rates in these women are extremely low. Treatment in these women is made difficult due to the presence of spheroids, which are clusters of cancer cells that have dislodged from tumours and float within the abdominal fluid. Spheroids are resistant to drugs and persist in a “sleeping” state called dormancy. These cells travel through the abdominal fluid and reawaken to spread the disease to new sites in the body. We previously identified the protein complex known as DREAM and the protein known as DYRK1A as essential factors that promote the survival of spheroids. DYRK1A is required to mobilize DREAM. Loss of DREAM or DYRK1A in spheroids reduces survival and enhances sensitivity to drugs, suggesting these are attractive targets for therapies. However, the mechanisms by which DREAM and DYRK1A promote spheroid survival and dormancy are not fully understood and the long-term consequences of DREAM loss in adults is not known. Herein we demonstrate the side-effects of prolonged DREAM loss in adult mice to investigate what would happen if DREAM is inhibited. We found that prolonged DREAM loss leads to the development of amyloidosis indicating this must be an important consideration for anti-DREAM drug therapies in ovarian cancer. Next, to identify new drug targets in dormant ovarian cancer, we screened spheroids and identified a family of genes that were previously uncharacterized in ovarian cancer and we show that they are regulated by DYRK1A. We show that disabling these genes reduces spheroid survival, indicating their potential as drug targets. We also describe new computational tools that facilitated this discovery and anticipate these tools will have broad usability in other studies. In summary, the work presented here adds to our understanding of the roles of DREAM and DYRK1A in ovarian cancer and informs of the

implications of targeting this pathway with drugs. Ovarian cancer is a very deadly disease and there is an urgent need to develop new treatment strategies to improve patient survival.

## Co-Authorship Statement

All chapters presented herein were written by Pirunthan Perampalam and edited by Dr. Frederick A. Dick. Pirunthan Perampalam performed all experiments and analyses except where noted below.

For Chapter 2, Pirunthan Perampalam participated in study design, carried out experiments in all figures, and wrote the manuscript. Haider M. Hassan participated in study design, experiments in Figures 2.1C and 2.15, and edited the manuscript. Grace E. Lilly carried out experiments in Figure 2.4D. Daniel T. Passos participated in experiments in Figures 2.1-2.2, and 2.4. Joseph Torchia participated in study design, Figures 2.1C and 2.15, and edited the manuscript. Patti K. Kiser participated in study design, provided pathology expertise, and data analysis in Figures 2.4, 2.6-2.10, and 2.14, and helped write the manuscript. Andrea Bozovic and Vathany Kulasingam carried out experiments in Figures 2.11C-D and helped write the manuscript. Frederick A. Dick participated in study design, data analysis, and helped write the manuscript.

For Chapter 3, Pirunthan Perampalam conceived and developed the software, tested it with sample data, and wrote the manuscript. Frederick A. Dick edited the manuscript.

For Chapter 4, Pirunthan Perampalam developed the software, analyzed and validated the data and wrote the manuscript. Pirunthan Perampalam and James I. MacDonald performed the experiments. James I. MacDonald and Frederick A. Dick edited the manuscript.

For Chapter 5, Pirunthan Perampalam participated in study design, carried out experiments in all figures, and wrote the manuscript. Gabriel E. DiMattia participated in study design. James I. MacDonald participated in study design, experiments in Figures 5.1, 5.5, and

5.6. Daniel T. Passos participated in experiments in Figure 5.6B. Frederick A. Dick participated in study design, data analysis, and edited the manuscript.



## Acknowledgments

I am greatly indebted to my supervisor, Dr. Frederick A. Dick. My work has benefited from his dedication and passion for rigorous scientific research. His unrelenting and selfless support of trainees created an environment that encouraged the pursuit of the most intractable problems. His willingness to teach is equaled by his willingness to learn from trainees and this fostered a prime environment that spurred the development of innovative and creative ideas and solutions. I wish to also express my sincerest appreciation of my co-supervisor, Dr. Gabriel E. DiMattia. From the start of my studies, his overwhelming insight and breadth of knowledge in the area of ovarian cancer challenged me to quickly develop my own knowledge in the field. Together, their motivation and confidence in my abilities have unequivocally elevated my work and have emboldened me to move ahead with the utmost confidence in myself as a translational scientist, and for that I offer my deepest gratitude.

I am grateful to Dr. Joseph S. Mymryk and Dr. Joseph Torchia for going beyond their commitments as my scientific advisory members and forming a genuine interest in my projects. They invested their time to provide mentorship, guidance, and advice even outside of committee meetings.

I would like to thank past and present members of our research lab for their feedback and assistance during the course of my studies. I am especially fortunate to have worked alongside two mentors and colleagues, Dr. James I. MacDonald and Dr. Daniel T. Passos, who have taught me an abundance of scientific knowledge and whose scientific scrutiny drove me to strive for excellence. I would also like to acknowledge past and present colleagues in the Victoria Research Laboratory and the Cancer Research Laboratory Program for making this an enjoyable experience full of lasting memories.

I am also grateful to Dr. Trevor G. Shepherd for his interest, discussions, and encouragement pertaining to my work. Additionally, I would like to thank the entire DREAM Team and the Translational Ovarian Cancer Research Group, especially Yudith Ramos-Valdes, for providing tools, resources, specimens, feedback, and assistance.

I would also like to pay special regards to my undergraduate thesis supervisor and continued mentor, Dr. Robert G. Tsushima, who recognized my passion for research and encouraged me to pursue this journey. One does not often appreciate early career mentors but the impact and significance of his guidance is not lost here.

The work presented herein would not be possible without the countless women who have donated tissue specimens. It is with their generous acts that we stand to one day conquer ovarian cancer.

Finally, I would like to thank my parents and brother, my extended family, and my friends, all of whom deserve recognition for their ceaseless encouragement and inspiration throughout my academic endeavours.

## Dedication

*To my parents and brother, for their sacrifices, inspiration, and support that made this journey possible.*

*And for ingraining in me at a young age the value of education and intellectual development.*

*“Don’t only practice your art, but force your way into its secrets, for it and knowledge can raise men to the divine.”*

– Ludwig van Beethoven

## List of Abbreviations

A2780	A2780 human ovarian cancer cell line
AApoAIV	apoA-IV amyloidosis
ADP	Adenosine diphosphate
AGPS	Alkylglycerone Phosphate Synthase
AKT	Protein kinase B; serine/threonine-specific protein kinase
<i>Alb</i>	Gene encoding serum Albumin
ALDEX	ANOVA-Like Differential Expression analysis
AMP	Adenosine monophosphate
AMPK	AMP-activated protein kinase
ANOVA	Analysis of variance
APCS	Serum Amyloid P-Component; encoded by <i>Apcs</i>
<i>Apoa1</i>	apolipoprotein A-I
<i>Apoa2</i>	apolipoprotein A-II
<i>Apoa4</i>	apolipoprotein A-IV
apoA-I	apolipoprotein A-I; encoded by <i>Apoa1</i>
apoA-II	apolipoprotein A-II; encoded by <i>Apoa2</i>
apoA-IV	apolipoprotein A-IV; encoded by <i>Apoa4</i>
apoE	Apolipoprotein E; encoded by <i>ApoE</i>
<i>ApoE</i>	apolipoprotein E
<i>ATM</i>	Ataxia Telangiectasia Mutated serine/threonine kinase
ATP	Adenosine Triphosphate
<i>ATR</i>	Ataxia Telangiectasia And Rad3-Related serine/threonine kinase
AUC	Area Under Curve
<i>AURKA</i>	Aurora Kinase A

BAGEL	Bayesian Analysis of Gene Essentiality
BAM	Binary Alignment Map (file format)
<i>BARD1</i>	BRCA1 Associated RING Domain 1
BEAVR	Browser-based tool for the Exploration And Visualization of RNA-seq data
BER	Base excision repair
BF	Bayes Factor
<i>BIRC5</i>	Baculoviral IAP Repeat Containing 5
B-MYB	B-Myb Proto-Oncogene, Transcription Factor
<i>BRCA</i>	Breast Cancer gene
<i>BRCA1</i>	Breast Cancer gene 1; Breast Cancer Type 1 Susceptibility Protein
<i>BRCA2</i>	Breast Cancer gene 2; Breast Cancer Type 2 Susceptibility Protein
<i>BRIP1</i>	BRCA1 Interacting Protein C-Terminal Helicase 1
BSA	Bovine Serum Albumin
C1	Cluster 1
C2	Cluster 2
C4	Cluster 4
C5	Cluster 5
CA125	Cancer antigen 125
<i>CCNA2</i>	Cyclin A2
<i>CCNB1</i>	Cyclin B1
<i>CCND1</i>	Cyclin D1
<i>CCNE1</i>	Cyclin E1
CCSRI	Canadian Cancer Society Research Institute
CD163	CD163 Molecule; CD163 antigen
CD44	CD44 Molecule; CD44 antigen

CD8	CD8 Molecule; CD8 antigen
<i>CDC20</i>	Cell Division Cycle 20
CDE	Cell cycle-Dependent Element
<i>CDH1</i>	Cadherin 1
<i>CDH2</i>	Cadherin 2
<i>CDH3</i>	Cadherin 3
CDK	Cyclin Dependent Kinase
<i>CDK1</i>	Cyclin Dependent Kinase 1
<i>CDK12</i>	Cyclin Dependent Kinase 12
CDK2	Cyclin Dependent Kinase 2
CDK4	Cyclin Dependent Kinase 4
<i>CDKN1A</i>	Cyclin Dependent Kinase Inhibitor 1A; encodes p21
<i>CDKN2A</i>	Cyclin Dependent Kinase Inhibitor 2A; encodes p16INK4A
<i>CHEK2</i>	Checkpoint Kinase 2
ChIP	Chromatin immunoprecipitation
CHR	Cell cycle genes Homology Region
CIC	Cortical Inclusion Cysts
CIHR	Canadian Institutes of Health Research
CK2	Casein Kinase 2
CKI	CDK inhibitors
CMV	Cytomegalovirus promoter
COV318	COV318 high-grade serous ovarian carcinoma cell line
CPU	Central Processing Unit
<i>CREBL2</i>	Cyclic adenosine monophosphate Responsive Element Binding Protein Like 2
CRISPR	Clustered Regularly Interspaced Short Palindromic Repeats

CSC	Cancer Stem Cell
<i>CSMD3</i>	CUB And Sushi Multiple Domains 3
CSV	comma-separated values (file format)
<i>CTNNB1</i>	Catenin Beta 1
CUB	Complement C1r/C1s, Uegf, Bmp1
CX-4945	Silmitasertib; inhibitor of casein kinase 2 (CK2)
DBD	DNA-Binding Domain
DCC	DCC Netrin 1 Receptor; Deleted In Colorectal Carcinoma
DGE	Differential Gene Expression
DIP13 $\alpha$	DCC-Interacting Protein 13-Alpha; alias for Adaptor Protein, Phosphotyrosine Interacting With Pleckstrin Homology Domain And Leucine Zipper 1 (APPL1)
DKK	Dickkopf WNT Signaling Pathway Inhibitor
<i>DLK1</i>	Delta Like Non-Canonical Notch Ligand 1
DMEM/F12	Dulbecco's Modified Eagle Medium/Nutrient Mixture F-12
DMSO	Dimethyl Sulfoxide
DNA	Deoxyribonucleic acid
DO	Disease Ontology
DP	Transcription Factor Dp; E2F Dimerization Partner
DP1	Transcription Factor Dp-1; E2F Dimerization Partner 1
DR	Dependence Receptor
DREAM	Dimerization partner, RB-like, E2F and Multi-vulval class B
<i>DSCAM</i>	Down Syndrome Cell Adhesion Molecule
DSCR	Down Syndrome Critical Region
DYRK1A	Dual Specificity Tyrosine Phosphorylation Regulated Kinase 1A
DYRK1B	Dual Specificity Tyrosine Phosphorylation Regulated Kinase 1B



E2F	E2F Transcription Factor
E2F4	E2F Transcription Factor 4
E2F5	E2F Transcription Factor 5
ECM	Extracellular Matrix
EDTA	Ethylenediaminetetraacetic Acid
<i>EGFP</i>	Enhanced Green Fluorescent Protein
EGFR	Epidermal Growth Factor Receptor
<i>EIF3D</i>	Eukaryotic Translation Initiation Factor 3 Subunit D
EMT	Epithelial-to-Mesenchymal Transition
EOC	Epithelial Ovarian Cancer/Carcinoma
<i>EPS15</i>	Epidermal Growth Factor Receptor Pathway Substrate 15
ER	Estrogen Receptor; also Enrichment Ratio
ERK	Extracellular signal-Regulated Kinase; Mitogen-Activated Protein Kinase
ERK1	Extracellular signal-Regulated Kinase 1; alias for Mitogen-Activated Protein Kinase 3 (MAPK3)
ERK2	Extracellular signal-Regulated Kinase 2; alias for Mitogen-Activated Protein Kinase 1 (MAPK1)
ES	Enrichment Score
F9	Mouse embryonal carcinoma cell line
FAK	Focal Adhesion Kinase 1; alias for Protein Tyrosine Kinase 2 (PTK2)
FASTQ	Text-based format for storing both a biological sequence (file format)
<i>FAT3</i>	FAT Atypical Cadherin 3
FBS	Fetal Bovine Serum
Fbxw7	F-Box And WD Repeat Domain Containing 7
FDR	False Discovery Rate
FFPE	formalin-fixed paraffin-embedded

FIGO	International Federation of Gynecology and Obstetrics
FOXM1	Forkhead Box M1
FOXO	Forkhead box class O
FTE	Fallopian Tube Epithelium
G0	G0 phase of cell cycle; quiescence
G1	G1 phase of cell cycle; Gap 1 phase; Growth 1 phase
G2	G2 phase of cell cycle; Gap 2 phase; Growth 2 phase
<i>GAPDH</i>	Glyceraldehyde-3-Phosphate Dehydrogenase
GB	Gigabyte
GCSF	Granulocyte Colony-Stimulating Factor
GeCKO	Genome-scale CRISPR Knock-Out
GEO	Gene Expression Omnibus
GIST	Gastrointestinal Stromal Tumors
GO-CRISPR	Guide-Only control CRISPR
GPCR	G Protein-Coupled Receptor
GSEA	Gene Set Enrichment Analysis
GTPase	Guanosine Triphosphatase
GUI	Graphical User Interface
H2AX	H2A.X Variant Histone
H2AZ	H2A.Z Variant Histone 1
HDAC	Histone Deacetylase
HDAC1	Histone Deacetylase 1
HDL	High-Density Lipoproteins
HEK293T	HEK293T Human Embryonic Kidney cell line
HEYA8	HEYA8 low-grade serous ovarian adenocarcinoma cell line

HGNC	Human Genome Organisation Gene Nomenclature Committee
HGSOC	High-Grade Serous Ovarian Cancer/Carcinoma
HIF	Hypoxia-Inducible Factor-1 alpha
HR	Homologous Recombination
HSC	Hematopoietic Stem Cell
HUGO	Human Genome Organisation
IAP	Inhibitor of apoptosis
ID	Identifier; or Internal Diameter
Ig	Immunoglobulin
<i>Ighm</i>	Immunoglobulin Heavy Constant Mu
IL	Interleukin
IL2	Interleukin 2
INDY	(1Z)-1-(3-ethyl-5-hydroxy-2(3H)-benzothiazoylidene)-2-propanone; DYRK1A/B inhibitor
iOvCa147	iOvCa147 high-grade serous ovarian carcinoma cell line
iOVCA185	Clear-cell ovarian carcinoma cell line
ITH	Intratumoural Heterogeneity
JAK	Janus Kinase
JPEG	Joint Photographic Experts Group (file format)
KDM	Histone Lysine Demethylases
KDM5B	Lysine Demethylase 5B
KEGG	Kyoto Encyclopedia of Genes and Genomes
<i>KIAA1731</i>	Centrosomal Protein 295; alias for CEP295
L <sub>0</sub>	Initial pooled sgRNA library
LC	Liquid Chromatography
LFC	Log <sub>2</sub> Fold Change

LGSOC	Low-Grade Serous Ovarian Cancer/Carcinoma
LIN37	Lin-37 DREAM MuvB Core Complex Component
LIN52	Lin-52 DREAM MuvB Core Complex Component
LIN54	Lin-54 DREAM MuvB Core Complex Component
LIN9	Lin-9 DREAM MuvB Core Complex Component
LKB1	Liver Kinase B1; alias for Serine/Threonine Kinase 11 (STK11)
LMD	Laser Capture Microdissection
LNCaP	Lymph-node-derived metastatic Prostate Cancer cell line
LSD1	small molecule Lysine-Specific Demethylase 1; alias SP2509
MAGeCK	Model-based Analysis of Genome-wide CRISPR-Cas9 Knockout
MALDI	Matrix-Assisted Laser Desorption/Ionization
<i>MAP3K6</i>	Mitogen-Activated Protein Kinase Kinase Kinase 6
MAPK	Mitogen-Activated Protein Kinase
MDM2	E3 Ubiquitin-Protein Ligase Mdm2
MEF	Mouse Embryonic Fibroblast
MET	Mesenchymal-to-Epithelial Transition
<i>MFN2</i>	Mitofusin 2
MLE	Maximum Likelihood Estimation
MMB	B-MYB-MuvB complex
MMP	Matrix Metalloprotease
<i>MRE11A</i>	Meiotic Recombination 11 Homolog A
MS	Mass Spectrometry
MSigDB	Molecular Signature Database
mTOR	mechanistic Target Of Rapamycin
MUP	Major Urinary Proteins

MYB	MYB Proto-Oncogene, Transcription Factor
<i>MYBL2</i>	B-Myb Proto-Oncogene; encodes B-MYB
<i>MYC</i>	Myc Proto-Oncogene Protein
NCT01199718	ClinicalTrials.gov Identifier: NCT01199718
NCT02977195	ClinicalTrials.gov Identifier: NCT02977195
NCT03897036	ClinicalTrials.gov Identifier: NCT03897036
NCT03904862	ClinicalTrials.gov Identifier: NCT03904862
<i>NEO1</i>	Neogenin 1 receptor
NEOC	Non-Epithelial Ovarian Cancer/Carcinoma
<i>NF1</i>	Neurofibromin 1
NGS	Next-Generation Sequencing
NHEJ	Non-Homologous End Joining
nLC-MS	nanoflow Liquid Chromatography-tandem Mass Spectrometry
NOD/SCID/ IL2 $\gamma^{\text{null}}$	Non-Obese Diabetic/Severe Combined Immunodeficient/IL2 receptor common gamma chain null mouse; NSG
<i>NOTCH3</i>	Notch Receptor 3
NP137	humanized monoclonal netrin-1 antibody
<i>NPM1</i>	Nucleophosmin 1
NSCLC	Non-Small-Cell Lung Cancer/Carcinoma
NSG	Non-Obese Diabetic/Severe Combined Immunodeficient/IL2 receptor common gamma chain null mouse
NTC	Non-Targeting Control
NTN1	Netrin-1
NTN3	Netrin-3
NTN4	Netrin-4
NTN5	Netrin-5

NTNG1	Netrin-G1
NTNG2	Netrin-G2
NuRD	Nucleosome Remodeling and Deacetylation complex
OS	Overall Survival; or Operating System
OSE	Ovarian Surface Epithelium
OVCAR3	OVCAR3 high-grade serous ovarian carcinoma cell line
OVCAR4	OVCAR4 high-grade serous ovarian carcinoma cell line
OVCAR8	OVCAR8 high-grade serous ovarian carcinoma cell line
p107	Retinoblastoma-Like Protein 1
p107 <sup>D</sup>	p107 protein incapable of assembling DREAM
p130	Retinoblastoma-Like Protein 2
<i>p130<sup>f</sup></i>	p130 allele floxed at exon 2
p16 <sup>INK4A</sup>	Cyclin Dependent Kinase Inhibitor 2A; encoded by <i>CDKN2A</i>
PAGE	Polyacrylamide Gel Electrophoresis
<i>PALB2</i>	Partner And Localizer Of BRCA2
PARP	Poly (ADP-Ribose) Polymerase
PBS	Phosphate-Buffered Saline
PCA	Principal Component Analysis
PCR	Polymerase Chain Reaction
<i>PDCD2L</i>	Programmed Cell Death 2 Like
PDF	Portable Document Format (file format)
<i>PDGFR</i>	Platelet Derived Growth Factor Receptor
PFI	Platinum-Free Interval
PFS	Progression-Free Survival
PI3K	Phosphatidylinositol-4,5-Bisphosphate 3-Kinase

<i>PIK3CA</i>	Phosphatidylinositol-4,5-Bisphosphate 3-Kinase Catalytic Subunit Alpha
PLD	Pegylated Liposomal Doxorubicin
PNG	Portable Network Graphics (file format)
<i>PSMD1</i>	Proteasome 26S Subunit, Non-ATPase 1
<i>PSMD2</i>	Proteasome 26S Subunit, Non-ATPase 2
<i>PTEN</i>	Phosphatase And Tensin Homolog
<i>RAD50</i>	RAD50 Double Strand Break Repair Protein
<i>RAD51</i>	RAD51 Recombinase
<i>RAD51B</i>	RAD51 Paralog B
<i>RAD51C</i>	RAD51 Paralog C
<i>RAD51D</i>	RAD51 Paralog D
RAM	Random-Access Memory
RB	Retinoblastoma
<i>RB1</i>	Retinoblastoma 1
RBBP4	RB Binding Protein 4, Chromatin Remodeling Factor
RBL1	Retinoblastoma-Like Protein 1; encodes p107
RBL2	Retinoblastoma-Like Protein 2; encodes p130
<i>RBM15</i>	RNA Binding Motif Protein 15
RING	Really Interesting New Gene
RIPA	Radioimmunoprecipitation Assay
RNA	Ribonucleic Acid
RNA-seq	RNA sequencing
ROC	Receiver Operating Characteristic Curve
<i>RPAP1</i>	RNA Polymerase II Associated Protein 1
RPM	Revolutions Per Minute

RRA	Robust Ranking Aggregation
RT-qPCR	Real-Time Quantitative Polymerase Chain Reaction
SCID	Severe Combined Immunodeficient
SDS	Sodium Dodecyl Sulfate
SDS-PAGE	Sodium Dodecyl Sulfate-Polyacrylamide Gel Electrophoresis
<i>SH3GL1</i>	SH3 Domain Containing Grb-2 Like 1, Endophilin A2
SIN3B	SIN3 Transcription Regulator Family Member B
SKOV3	SKOV3 ovarian adenocarcinoma cell line
<i>SLC2A11</i>	Solute Carrier Family 2 Member 11
SOX6	Sex Determining Region Y-Box 6
SP2509	small molecule Lysine-Specific Demethylase 1; alias LSD1
<i>SSH1</i>	Slingshot Protein Phosphatase 1
STAT	Signal Transducer And Activator Of Transcription
STAT3	Signal Transducer And Activator Of Transcription 3
STIC	Serous Tubal Intraepithelial Carcinomas
SVG	Scalable Vector Graphics (file format)
<i>SYAP1</i>	Synapse Associated Protein 1
T <sub>0</sub>	Initial culture condition
TAM	Tumour-Associated Macrophages
TCGA	The Cancer Genome Atlas
TEM	Transmission Electron Microscopy
T <sub>f</sub>	Final culture condition
TGF-β	Transforming Growth Factor Beta
TGF-βIII	Transforming Growth Factor Beta 3
TIFF	Tagged Image File Format



TIL	Tumour Infiltrating Lymphocytes
TME	Tumour Microenvironment
TOV1946	TOV1946 high-grade serous ovarian carcinoma cell line
<i>TP53</i>	Tumor Protein P53
TRACS	Toolset for the Ranked Analysis of GO-CRISPR Screens
<i>TRAF3IP1</i>	TRAF3 Interacting Protein 1
TSS	Transcription Start Site
TWIST1	Twist Family Basic Helix-Loop-Helix Transcription Factor 1
TXT	Text file format
ULA	Ultra-Low Attachment
UNC5	UNC5 netrin receptor
UNC5A	UNC5 netrin Receptor A
<i>UNC5B</i>	UNC5 netrin Receptor B
<i>UNC5C</i>	UNC5 netrin Receptor C
<i>UNC5D</i>	UNC5 netrin Receptor D
UNC5H	UNC5 homology; UNC5 netrin receptor homologs
UO126	UO126 selective inhibitor of MAPK/ERK
uPAR	urokinase-type Plasminogen Activator Receptor
VEGF	Vascular Endothelial Growth Factor
VEGFA	Vascular Endothelial Growth Factor A
VEGFR2	Vascular Endothelial Growth Factor Receptor 2
WD	Tryptophan-aspartic
WNT	Wnt/Wingless signaling pathway
<i>ZC3H7A</i>	Zinc Finger CCCH-Type Containing 7A
ZEB1	Zinc Finger E-Box Binding Homeobox 1

# Table of Contents

Abstract .....	ii
Keywords .....	iv
Summary for Lay Audience .....	v
Co-Authorship Statement.....	vii
Acknowledgments.....	ix
Dedication .....	xi
List of Abbreviations .....	xiii
List of Tables .....	xxxiii
List of Figures .....	xxxiv
List of Appendices .....	xxxvii
Chapter 1 .....	1
1 Introduction .....	1
1.1 Ovarian cancer .....	1
1.2 Subtype classification .....	2
1.3 High-grade serous ovarian carcinoma .....	4
1.3.1 Origin .....	4
1.3.2 Staging .....	9
1.3.3 Dissemination & metastases .....	11
1.3.4 Preclinical models of ovarian cancer .....	16
1.3.5 Summary of HGSOC .....	19
1.4 Genomic & transcriptomic characterization of HGSOC .....	20
1.4.1 Recurrent mutations & alterations .....	20
1.4.2 Genomic & transcriptomic subtyping.....	25
1.4.3 Copy number alterations & signatures.....	26

1.4.4	Summary of HGSOC genomics.....	28
1.5	Treatment of HGSOC and chemoresistance .....	29
1.5.1	Surgery & chemotherapy .....	29
1.5.2	Relapse.....	30
1.5.3	Targeted therapies.....	32
1.5.4	Chemoresistance .....	34
1.5.5	Summary of HGSOC treatment.....	36
1.6	Tumour dormancy.....	38
1.6.1	Types of dormancy in cancer .....	38
1.6.2	Quiescence .....	40
1.6.3	Loss of cell cycle control .....	43
1.6.4	Targeting dormancy in cancer .....	47
1.6.5	Summary of HGSOC dormancy .....	50
1.7	The mammalian DREAM complex .....	51
1.7.1	DREAM and MuvB .....	51
1.7.2	Cell cycle control by DREAM and MuvB.....	54
1.7.3	DREAM and MuvB in cancer.....	57
1.7.4	DREAM in HGSOC .....	58
1.7.5	Pharmacological inhibition of DYRK1A.....	59
1.7.6	Summary of the DREAM complex.....	61
1.8	Summary of HGSOC .....	61
1.9	Scope of thesis .....	63
1.10	References .....	67
Chapter 2	.....	93
2	Disrupting the DREAM transcriptional repressor complex induces apolipoprotein overexpression and systemic amyloidosis in mice.....	93

2.1	Abstract .....	93
2.2	Introduction .....	94
2.3	Results .....	96
2.3.1	Generation of adult DREAM assembly deficient mice .....	96
2.3.2	<i>p107<sup>D/D</sup>;p130<sup>-/-</sup></i> mice exhibit compromised renal function and disrupted tissue structure in multiple organs .....	101
2.3.3	Systemic amyloidosis is evident in <i>p107<sup>D/D</sup>;p130<sup>-/-</sup></i> mice .....	108
2.3.4	Apolipoproteins predominate in amyloid fibrils and are overexpressed in <i>p107<sup>D/D</sup>;p130<sup>-/-</sup></i> mice.....	114
2.3.5	DREAM disruption leads to H2AZ loss at apolipoprotein genes.....	125
2.4	Discussion .....	128
2.5	Materials and Methods.....	132
2.5.1	Mouse genetics.....	132
2.5.2	Genotyping p130 exon 2 deletion in mice .....	132
2.5.3	Western blotting.....	135
2.5.4	Chromatin immunoprecipitation (ChIP).....	135
2.5.5	Ccna2 promoter pulldown.....	136
2.5.6	Tissue preparation and staining .....	137
2.5.7	Scoring amyloid damage to tissues.....	137
2.5.8	Proteinuria assay .....	137
2.5.9	Creatinine assay .....	138
2.5.10	Protein identification.....	138
2.5.11	Transmission Electron Microscopy (TEM) .....	138
2.5.12	Amyloid subtyping by laser microdissection mass spectrometry (LMD/MS) .....	139
2.5.13	RT-qPCR.....	141
2.5.14	Statistics .....	141

2.5.15 Study Approval .....	141
2.6 Acknowledgements .....	142
2.7 References .....	143
Chapter 3 .....	148
3 BEAVR: A Browser-based tool for the Exploration and Visualization of RNA-seq data .....	148
3.1 Abstract .....	148
3.2 Background .....	149
3.3 Implementation .....	150
3.3.1 Interface & typical workflow .....	150
3.3.2 Representation of results & data exploration .....	155
3.3.3 Installation .....	157
3.3.4 Run time consideration .....	158
3.4 Results & Discussion .....	159
3.4.1 A typical use case .....	159
3.4.2 Future work .....	168
3.5 Conclusions .....	169
3.6 Availability and Requirements .....	170
3.7 Availability of data and materials .....	171
3.8 Funding .....	171
3.9 Acknowledgements .....	171
3.10 References .....	172
Chapter 4 .....	174
4 GO-CRISPR: a highly controlled workflow to improve discovery of gene essentiality in loss-of-function screens .....	174
4.1 Abstract .....	174
4.2 Introduction .....	174

4.3 Results.....	177
4.3.1 The GO-CRISPR Workflow .....	177
4.3.2 Discovering Ovarian Cancer Spheroid Vulnerabilities.....	181
4.3.3 Validation of TRACS Gene Essentiality Predictions .....	185
4.3.4 GO-CRISPR and TRACS Identify Novel Pathways in HGSOC .....	189
4.3.5 Comparison of GO-CRISPR with conventional CRISPR screen workflows .....	189
4.4 Discussion.....	196
4.5 Materials and methods .....	197
4.5.1 Generation of Cas9-positive cells .....	197
4.5.2 GeCKO v2 library preparation.....	197
4.5.3 GO-CRISPR screen in iOvCa147 cells.....	198
4.5.4 High-throughput next generation sequencing (NGS) .....	199
4.5.5 Analysis with MAGeCK.....	199
4.5.6 Analysis with BAGEL .....	200
4.5.7 Analysis with TRACS.....	200
4.5.8 Data exploration using VisualizeTRACS .....	200
4.5.9 The TRACS algorithm.....	201
4.5.10 Pathway analysis.....	202
4.5.11 Generation of single-gene knockouts.....	203
4.5.12 Statistics .....	203
4.6 Data and Code Availability.....	204
4.7 References.....	205
Chapter 5.....	207
5 Netrin and its dependence receptors are mediators of high-grade serous ovarian cancer cell survival .....	207
5.1 Abstract.....	207

5.2	Introduction.....	207
5.3	Results.....	211
5.3.1	Components of netrin signaling are essential factors for HGSOC spheroid cell survival.....	211
5.3.2	Netrin signaling components are enriched in HGSOC spheroid cells ....	214
5.3.3	Netrin signaling components are commonly essential in HGSOC spheroid cells .....	222
5.4	Discussion.....	227
5.5	Materials and methods .....	231
5.5.1	Engineering Cas9+ cells .....	231
5.5.2	GeCKO v2 library preparation.....	231
5.5.3	GO-CRISPR screen in iOvCa147, OVCAR8, and TOV1946 cells.....	232
5.5.4	GO-CRISPR screen analysis with TRACS.....	233
5.5.5	Generating DYRK1A knockout cells .....	233
5.5.6	DYRK1A immunoprecipitation kinase assay.....	234
5.5.7	Real-time qPCR (RT-qPCR).....	234
5.5.8	RNA preparation and RNA-sequencing .....	236
5.5.9	RNA-sequencing analyses .....	237
5.5.10	Pathway enrichment analyses .....	237
5.5.11	Western blots .....	238
5.5.12	Generation of single-gene knockouts.....	238
5.5.13	Spheroid viability assays.....	239
5.5.14	Statistical analyses .....	239
5.6	References.....	240
Chapter 6	.....	244
6	Discussion .....	244
6.1	Summary of findings.....	244

6.2 Prolonged loss of DREAM causes systemic amyloidosis in mice .....	245
6.3 Components of netrin signaling are essential factors for spheroid cell viability	247
6.4 Transcriptional control by DREAM and DYRK1A .....	250
6.5 Significance of bioinformatic tools.....	251
6.6 Conclusion .....	252
6.7 References.....	254
Appendices.....	259
Curriculum Vitae .....	262



## List of Tables

Table 2.1 LMD/MS analysis of an endpoint $p107^{D/D};p130^{-/-}$ liver.....	119
Table 2.2 Primers used for PCR experiments in Chapter 2 .....	133
Table 4.1 Top 10 genes with the most negative Enrichment Ratio (ER) in TRACS .....	186
Table 5.1 Primers used for experiments in Chapter 5.....	235

## List of Figures

Figure 1.1 Classification of ovarian cancers.....	3
Figure 1.2 Origin of HGSOC.....	6
Figure 1.3 Dissemination and metastases of HGSOC .....	13
Figure 1.4 <i>In vitro</i> model of HGSOC spheroid dissemination .....	18
Figure 1.5 Most common gene & pathway alterations in HGSOC .....	21
Figure 1.6 Types of tumour dormancy .....	39
Figure 1.7 Cell cycle control by the CDK/cyclin-RB-E2F axis .....	45
Figure 1.8 Treating dormancy in cancer.....	48
Figure 1.9 Cell cycle control by DREAM and MuvB .....	53
Figure 2.1 DREAM assembly is disrupted in $p107^{D/D};p130^{-/-}$ mice.....	98
Figure 2.2 Strategy to create DREAM assembly deficient mice.....	100
Figure 2.3 <i>In vitro</i> DREAM assembly defect in $p107^{D/D};p130^{-/-}$ mice.....	102
Figure 2.4 $p107^{D/D};p130^{-/-}$ mice have shortened lifespan and compromised organ function	104
Figure 2.5 Normal liver, spleen, and kidney mass in $p107^{D/D};p130^{-/-}$ mice .....	106
Figure 2.6 Similar Ki67 staining in control and $p107^{D/D};p130^{-/-}$ tissues .....	107
Figure 2.7 Systemic amyloidosis in $p107^{D/D};p130^{-/-}$ mice.....	110
Figure 2.8 Aggregate pathology scores for phenotypes observed in tissue sections .....	112
Figure 2.9 Tissue distribution and disease severity of amyloidosis in $p107^{D/D};p130^{-/-}$ mice	113
Figure 2.10 H&E histology of control and $p107^{D/D};p130^{-/-}$ brains .....	115

Figure 2.11 ApoA-IV is the most abundant amyloidogenic protein in <i>p107<sup>D/D</sup>;p130<sup>-/-</sup></i> amyloid deposits .....	117
Figure 2.12 Normal expression of amyloid associated protein coding genes in <i>p107<sup>D/D</sup>;p130<sup>-/-</sup></i> mice.....	121
Figure 2.13 <i>Ighm</i> is overexpressed in <i>p107<sup>D/D</sup>;p130<sup>-/-</sup></i> bone and spleen .....	123
Figure 2.14 Absence of myeloma like amyloid deposits in <i>p107<sup>D/D</sup>;p130<sup>-/-</sup></i> mice.....	124
Figure 2.15 B-MYB is recruited to <i>Apoa1</i> and <i>Apoa4</i> promoters in DREAM assembly-deficient <i>p107<sup>D/D</sup>;p130<sup>-/-</sup></i> mice.....	126
Figure 2.16 Loss of DREAM assembly in <i>p107<sup>D/D</sup>;p130<sup>-/-</sup></i> mice promotes MYB-MuvB assembly that drives systemic AApoAIV amyloidosis due to constitutive overexpression of <i>Apoa4</i> .....	129
Figure 3.1 Overview of BEAVR's graphical user interface and typical workflow .....	151
Figure 3.2 BEAVR requires two inputs: a read count table file and a sample treatment matrix file .....	153
Figure 3.3 DGE table output from a typical use case for BEAVR.....	160
Figure 3.4 Illustrating variance across samples using principal component analysis (PCA) and sample clustering.....	162
Figure 3.5 Visualizing normalized read counts and differential gene expression between experimental groups.....	163
Figure 3.6 Identification of enriched pathways among differentially expressed genes.....	166
Figure 4.1 Typical experimental workflow for GO-CRISPR screening and analysis using TRACS.....	178
Figure 4.2 Typical analysis workflow using TRACS to identify essential genes .....	180
Figure 4.3 Genes with low Library ES tend to have extreme Initial ES and/or Final ES.....	183

Figure 4.4 Validation of TRACS gene essentiality predictions.....	187
Figure 4.5 MAGeCK and BAGEL are unable to identify essential genes in our screen using Cas9 positive read data .....	191
Figure 4.6 Top-ranked genes by MAGeCK have low representation in the T0 pool of cells .....	193
Figure 4.7 TRACS accurately classifies non-targeting controls and robustly classifies known essential and non-essential gene sets .....	194
Figure 4.8 TRACS selects for essential genes based on the most sgRNAs.....	195
Figure 5.1 Components of netrin signaling are essential factors for HGSOc spheroid viability .....	212
Figure 5.2 Generation of <i>DYRK1A</i> <sup>-/-</sup> iOvCa147 cells and validation of abrogated DYRK1A activity.....	215
Figure 5.3 <i>DYRK1A</i> <sup>-/-</sup> spheroid cells have reduced viability and increased chemosensitivity. ....	217
Figure 5.4 Netrin signaling pathway components are upregulated in iOvCa147 spheroid cells but downregulated in <i>DYRK1A</i> <sup>-/-</sup> spheroid cells. ....	220
Figure 5.5. Netrin signaling components are commonly essential in HGSOc spheroid cells .....	223
Figure 5.6. Netrin signaling components are upregulated in HGSOc spheroid cells and mediate viability.....	225

## List of Appendices

Appendix A Permission for reproduction from the Journal of Clinical Investigation.....	259
Appendix B Permission for reproduction from BMC Bioinformatics.....	260
Appendix C Pre-print availability of manuscript presented in Chapter 4.....	261

# Chapter 1

## 1 Introduction

### 1.1 Ovarian cancer

Ovarian cancer represents a heterogenous group of carcinomas that involve the ovary and fallopian tube. The incidence rate of ovarian cancer is disproportionate to its mortality rate. It is estimated that there are 240,000 new cases globally each year representing approximately 3.6% of annual cancer cases<sup>1</sup>. It was estimated that 152,000 women succumbed to the disease worldwide in the same year<sup>1</sup>. In 2020, the Canadian Cancer Society estimated 3,100 new cases and 1,950 deaths annually<sup>2</sup>. The American Cancer Society estimated there would be 22,240 new cases and 14,070 deaths in 2018<sup>3</sup>. These incidence rates and alarming mortality figures have established ovarian cancer as the most devastating of all female reproductive cancers<sup>4</sup>. Despite increased awareness and advancements in ovarian cancer research, patient survival trends have failed to improve significantly over the last decade<sup>5,6</sup>. The startling mortality figures are largely due to late-diagnosis in the majority of women (70%)<sup>6</sup>. The five-year survival rate of women diagnosed with stage I disease is 90% but beyond stage II, this falls sharply to less than 25%<sup>6</sup>. The poor prognosis of women diagnosed with late-stage disease indicates a critical requirement for both improved screening and therapeutics.

## 1.2 Subtype classification

Although it was originally considered to be a unitary disease, it is now understood that ovarian cancer encompasses several different malignancies of various origins which can be further divided into subtypes based on their molecular and histological composition, cells of origin, and clinical features<sup>6-8</sup>. The vast majority of ovarian cancers, about 90%, arise through the transformation of epithelial cells and are therefore classified as epithelial ovarian cancer (EOC)<sup>5,6</sup>. In contrast, only about 10% of ovarian cancers are designated as non-epithelial ovarian cancer (NEOC) and originate from germ-cell, sex-cord stromal tissues or mixed-cell types<sup>5</sup>. EOC is itself a broad classification which can be further divided into four subtypes based on morphology and clinical features, including clear-cell (10%), endometrioid (10%), mucinous (10%), and serous (70%) carcinomas<sup>5,9</sup>. Serous carcinomas can be further classified as high-grade serous ovarian carcinoma (HGSOC) (90%) or low-grade serous ovarian carcinoma (LGSOC) (10%)<sup>5,6</sup> (**Figure 1.1**).

Molecular and genetic analyses of EOC have led to two distinct tumour grade categories: type I and type II tumours<sup>10,11</sup>. Type I tumours are indolent and less aggressive than their type II counterparts<sup>6</sup>. These slow-growing tumours are generally found localized to the ovary at the time of diagnosis, which usually occurs at an early-stage of disease development<sup>6,12</sup>. Type I tumours include LGSOC as well as low-grade endometrioid, clear-cell, and mucinous carcinomas<sup>13</sup>. In contrast, type II tumours are very aggressive, progress rapidly, present at an advanced stage, and are widely disseminated beyond the site of origin<sup>12,13</sup>. Compared to type I tumours, type II tumours are also genetically unstable and harbor more mutations<sup>12-14</sup>. Type II tumours include high-grade endometrioid and undifferentiated carcinomas, but HGSOC is by far the most prevalent and considered to

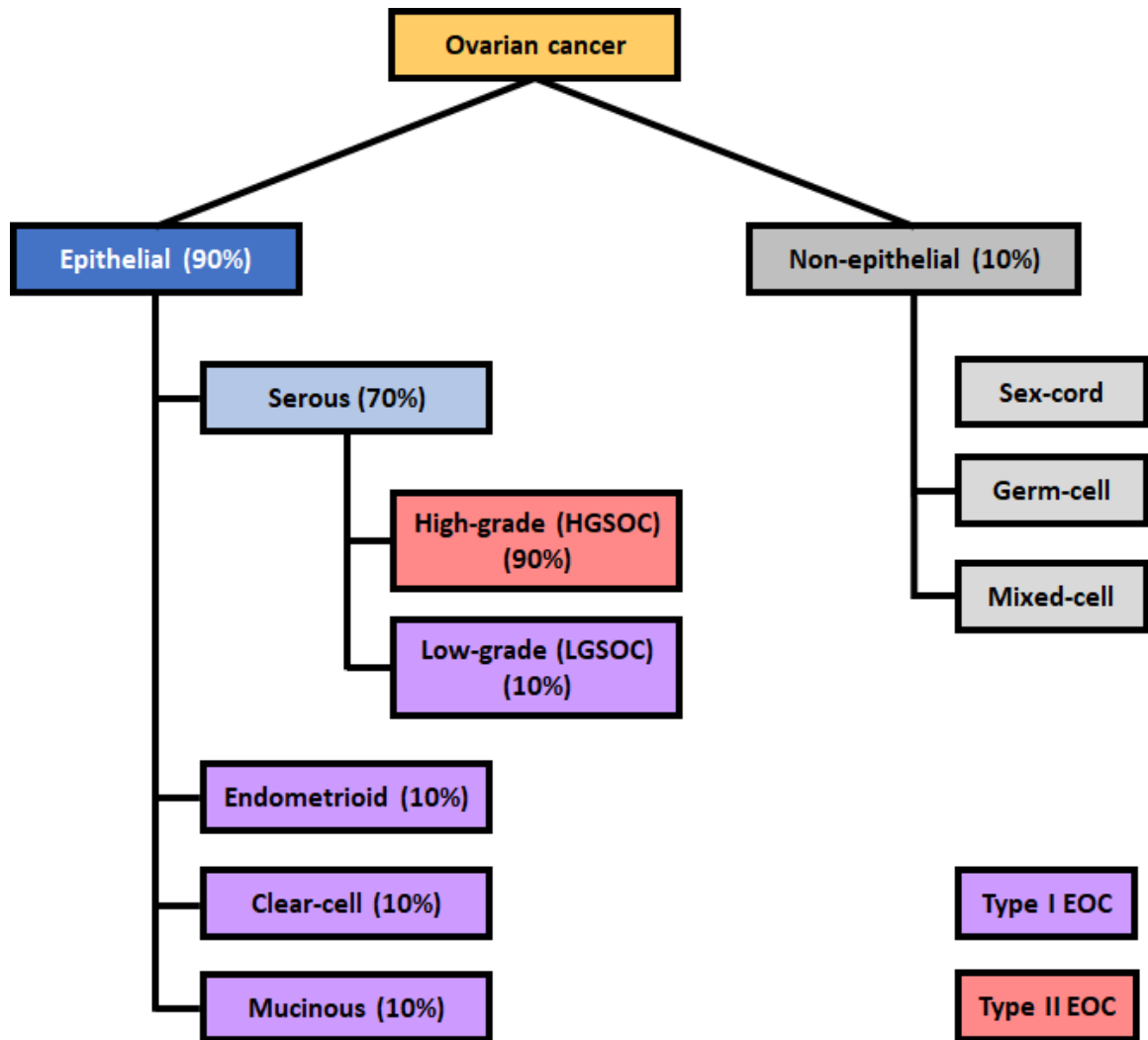


**Figure 1.1. Classification of ovarian cancers.** The majority of ovarian cancers (90%) occur through the transformation of epithelial cells and are called epithelial ovarian cancer (EOC). EOC can be further classified into subtypes based on morphology and clinical features: serous carcinoma (70%), endometrioid carcinoma (10%), clear-cell carcinoma (10%), and mucinous carcinoma (10%). Serous cancer can be further subdivided into low-grade serous ovarian carcinoma (LGSOC) and high-grade serous ovarian carcinoma (HGSOC). HGSOC cases account for 90% of all serous carcinomas and represent the majority of all ovarian cancer cases worldwide. EOC can also be subdivided by molecular and genetic characteristics into Type I (LGSOC, endometrioid, clear-cell, mucinous; highlighted in purple) or type II (HGSOC; highlighted in red). Non-EOC subtypes account for 10% of all ovarian carcinomas and include sex-cord, germ-cell, and mixed-cell types.



the prototypical type II neoplasm<sup>13,14</sup>. HGSOC accounts for over 81% of all type II tumours, over 60% of all ovarian carcinoma cases, and over 70% of all EOC deaths<sup>5,6,12</sup>. Therefore, despite some shared similarities, HGSOC and LGSOC are two distinct neoplasms with contrasting disease progression and patient outcomes.

## 1.3 High-grade serous ovarian carcinoma

### 1.3.1 Origin

The site of origin for HGSOC has been long debated since the histology of tumours do not always resemble ovarian tissues. It was originally thought to arise from the ovarian surface epithelium (OSE), a layer of cells related to the lining of the peritoneal cavity<sup>15-17</sup>. The OSE was favoured because patients with LGSOC had tumours localized to the ovary at the time of diagnosis which was similar to some early-stage HGSOC patients presenting with only ovarian involvement<sup>6</sup>. Additionally, omitting distant metastases, late-stage HGSOC patients showed both ovarian and fallopian involvement. HGSOC was therefore regarded as a more advanced phase of LGSOC that also originated from the ovary, specifically the OSE. That the OSE is derived from the coelomic epithelium which is closely related to the mesothelial lining of the peritoneal cavity supported this viewpoint since advanced stage HGSOC most often presented with widespread peritoneal dissemination<sup>18</sup>. This gave rise to the “incessant ovulation” hypothesis, which suggested the local rupturing and regeneration of the OSE during ovulation may contribute to carcinogenesis as a result of a failure to repair DNA damage caused by increased inflammation<sup>17,19,20</sup>. Further supporting this hypothesis was the observation that ruptured OSE may invaginate toward the ovarian stroma to form cortical inclusion cysts (CICs)<sup>16</sup>.

Exposure of CICs to the pro-growth and pro-differentiation hormones typically found within the ovarian stroma was thought to be sufficient to transform the pre-cancerous lesions into neoplasms if they already harbored mutations<sup>6,16,17,21</sup>.

Still, this hypothesis was strongly contested since the histology of HGSOC tumours do not resemble ovarian tissues. Several transgenic mouse models have provided evidence for tumorigenesis of the OSE due to inactivation or mutation of a small subset of genes including *Brcal*, *Kras*, *Lkb1*, *Pten*, *Rb1*, and *Trp53*<sup>6</sup>. However not all of these mice developed advanced stage (stage III-IV) tumours or aggressive metastases as observed in human HGSOC cases, suggesting the OSE may not be the primary source for human HGSOC. A new hypothesis suggesting HGSOC arises from the Müllerian epithelium – an epithelial lining found throughout the female urogenital system including the fallopian tubes – was proposed in 1999<sup>22</sup>. The Müllerian epithelium closely resembles the histology of HGSOC tumours, unlike the OSE<sup>15</sup>. This theory gained increased acceptance as advances in genetic and histological analyses revealed that women carrying germline *BRCA1/2* mutations had an increased lifetime risk of developing ovarian cancer, particularly HGSOC<sup>12</sup>. *BRCA* mutant carriers were susceptible to developing tumours on ovarian, fallopian, and peritoneal surfaces which led to the prophylactic bilateral salpingo-oophorectomy (surgical removal of the ovaries and fallopian tubes)<sup>19,23</sup>. Histological analyses of these ovaries and fallopian tubes found more preneoplastic changes in the fallopian tubes compared to the ovaries, providing further evidence to support the fallopian tubes as the site of origin<sup>16,24</sup>. Analyses of the fimbria of fallopian tubes revealed the presence of precancerous lesions which are now known as serous tubal intraepithelial carcinomas (STICs)<sup>16</sup> (**Figure 1.2**).

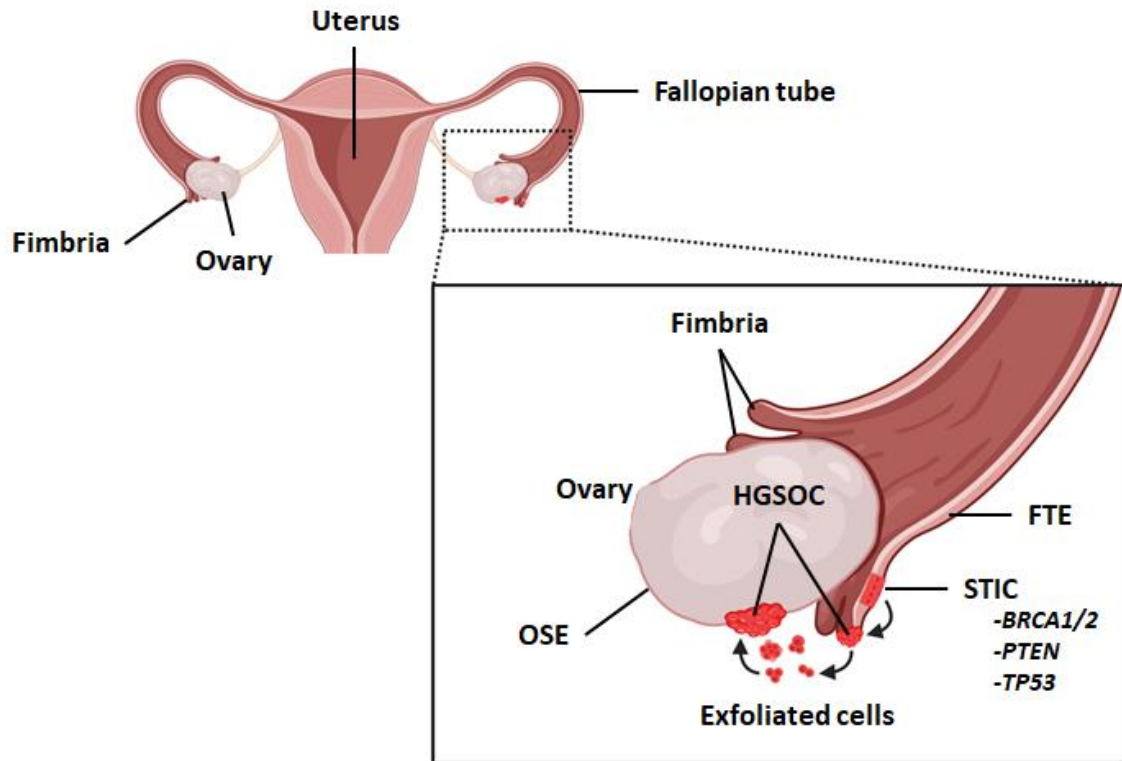


**Figure 1.2. Origin of HGSOC.** The STIC lesion model is the prevailing theory of HGSOC carcinogenesis. Serous tubal intraepithelial carcinomas (STICs) arise from the fallopian tube epithelium (FTE) on the fimbriae of the fallopian tube. STICs are premalignant and noninvasive but have features that resemble HGSOC including chromosome abnormalities and perturbations of *BRCA1/2*, *PTEN*, and *TP53*. STICs could develop in the FTE and progress into malignant HGSOC. Malignant cells could also exfoliate from the site of origin and transplant into the ovarian surface epithelium (OSE) on the ovary.

STICs are premalignant and noninvasive lesions with histological features that closely resemble HGSOC, such as enlarged nuclei, hyperchromasia, and coarse chromatin aggregates<sup>7,25-27</sup>. STICs also have increased genomic instability and tend to possess gene alterations in *BRCA1/2*, *PTEN*, and *TP53* – features that are characteristic of HGSOC<sup>6,7,28,29</sup>. Paired analyses of HGSOC tumours and STICs from the same patients have exposed shared genetic alterations including a case in which *CCNE1* – the gene encoding G1/S-specific cyclin E1 – was amplified in both STICs and primary tumours<sup>30</sup>. Paired genetic analyses of ovarian and fallopian tube tumours, as well as metastatic peritoneal tumours from the same patients, have shown that these tumours are evolutionarily related to STICs<sup>31,32</sup>. Transcriptional profiling of HGSOC tumours have also shown similar gene expression patterns between HGSOC and the fallopian tube epithelium (FTE)<sup>33</sup>.

Together, these studies provide strong evidence that the most likely origin of HGSOC may be the FTE. Yet a subset of HGSOC patients present with ovarian but not fallopian tube involvement<sup>34</sup>. A new theory suggests STICs could develop in the FTE and then exfoliate and transplant into the OSE where they can be incorporated into CICs and be subject to the microenvironment of the ovarian stroma which is more favourable for neoplastic development as previously described<sup>16,34-36</sup> (**Figure 1.2**). Indeed, the fimbriae are located on the distal fallopian tube, directly adjacent to the ovary. Novel mouse models have provided support for this notion that transformed lesions could originate on the fallopian tubes and transplant into the ovaries<sup>35</sup>. Mice engineered with targeted mutations in the FTE give rise to STICs which can later progress to advanced stage HGSOC<sup>37</sup>. In one study, 35% of mice with inactivated *Brcal*, *Nf1*, *Rb1*, and *Trp53* in the FTE developed

STICs and more than 65% developed fallopian tube tumours while only 40% developed ovarian tumours<sup>38</sup>. Since mutations were only targeted to the FTE, it can be inferred that the resulting ovarian tumours in these mice were of fallopian tube origin.

Engineered mouse models as described above with targeted mutations in the FTE have provided valuable insight into HGSOC progression<sup>37</sup>. In the above study, over 12% of mice also developed peritoneal tumours and ascites – the accumulation of fluid in the peritoneal cavity that accompanies late-stage HGSOC and likely caused by impaired lymph node drainage<sup>38</sup>. In another mouse model, inactivation of just three genes (*Brcal*, *Pten*, *Trp53*) in the FTE was sufficient to produce STICs (40%) and subsequent HGSOC (80%)<sup>38</sup>. A similar study utilizing a larger cohort of mice with inactivation of *Brcal/2* and *Pten* combined with overexpression of mutant p53 found over 80% of mice developed STICs and over 70% had ovarian tumours and peritoneal tumours<sup>39</sup>. In contrast, several mouse models engineered to induce STIC formation do not progress to HGSOC or do not progress to advanced stage HGSOC with peritoneal involvement<sup>37</sup>. Such models have revealed further investigation is necessary and question whether STICs are absolutely critical for HGSOC development.

Although earlier studies sampling women undergoing prophylactic bilateral salpingo-oophorectomy identified STICs in up to 50% of cases, the most recent clinical data suggests STICs only occur in less than 12% of high-risk women<sup>23,37,40</sup>. *BRCA1/2* mutations may potentially accelerate the transformation of premalignant STICs into HGSOC, likely explaining why STICs are found in larger portions among *BRCA1/2* mutant carriers<sup>6</sup>. However, a study in 2011 of *BRCA1/2* carriers diagnosed with early-stage HGSOC revealed approximately 78% had ovarian tumours while only 21% had fallopian

tube tumours. In sporadic, non-hereditary HGSOCS (90% of all HGSOCS), the presence of STICs ranges widely from less than one quarter to almost two-thirds of all cases<sup>37</sup>. While the evidence thus far indicates STICs are a risk factor for HGSOCS, the absence of STICs from a majority of HGSOCS cases, in conjunction with mouse models that develop STICs but not advanced stage HGSOCS, suggests there is perhaps an as-yet undiscovered mechanism. The cell of origin for a majority of HGSOCS cases remains unclear, and HGSOCS progression – from initiation to peritoneal metastases – is still poorly understood<sup>13,41</sup>.

### 1.3.2 Staging

The majority of women present with late-stage (stage III-IV) HGSOCS and have a poor five-year survival rate of only 25%<sup>5,6</sup>. In contrast, patients diagnosed at stage I have a five-year survival rate of 90% as the disease is highly curable at early-stage. The cause of this significant difference in survival is due to the rapid progression of HGSOCS beyond stage II, involving peritoneal tissue, lymph nodes, and distant organs<sup>6</sup>. Pathological evaluation of patients and tumour staging is dependent on tissue biopsies, surveying of lymph nodes, and assessment of abdominal fluid<sup>5</sup>. The widely accepted International Federation of Gynecology and Obstetrics (FIGO) staging system has recently been revised to reflect the acceptance of Müllerian epithelium-derived tumours with ovarian or fallopian tube origins<sup>42</sup>.

In stage I, tumours are confined to one (stage IA) or both (stage IB) ovaries or fallopian tubes without any tumours on the surfaces of the ovaries or fallopian tubes<sup>42,43</sup>. Stage IC indicates the presence of tumours on either surface, ruptured tumour capsules, or

the presence of malignant ascites<sup>42,43</sup>. At stage II, tumours develop beyond the ovaries or fallopian tubes and into the pelvic region, often invading into the uterus or pelvic intraperitoneal tissues<sup>42,43</sup>. Stage III indicates tumour invasion into the peritoneal lining outside the pelvis and may also be accompanied by metastases to the retroperitoneal lymph nodes (stage IIIA) or involvement beyond the pelvic region (stage IIIB)<sup>42,43</sup>. Stage IIIC indicates the presence of metastatic nodules greater than 2 mm and may include liver or spleen involvement<sup>42-44</sup>. By stage IV, distant metastases can be observed in organs outside of the abdominal cavity, including the liver, spleen and lungs<sup>42,43</sup>. Pleural effusion may also be present in the lungs and distant lymph nodes outside the abdominal cavity may have metastases<sup>42,43</sup>.

The confinement of tumours to the pelvic region in stage I-II HGSOE means patients are mostly asymptomatic or experience pain or discomforts that are incorrectly attributed to other ailments<sup>5,10,42,45</sup>. Although increased awareness and screening has increased diagnosis at early-stage, the relatively mild early symptoms have contributed to the problem of the majority of HGSOE cases being diagnosed at late-stage (70%)<sup>45</sup>. By the time these women present to the clinic, distant metastases are widespread, often with numerous tumour nodules in the peritoneal lining and extra-abdominal organs<sup>10</sup>. The accumulation of malignant ascites fluid also causes bloating of the abdomen and increases the pressure exerted on visceral organs which can cause immense pain<sup>5,10,28</sup>. Moreover, ascites fluid contains multicellular aggregates of tumour cells – termed spheroids – which have exfoliated from primary tumours and/or secondary tumours<sup>46</sup>. The presence of numerous secondary microscopic lesions and spheroids in ascites fluid complicates treatment procedures for late-stage patients. Whereas early-stage patients may undergo

surgical debulking and/or salpingo-oophorectomy, it is difficult to confidently and precisely remove every secondary lesion in late-stage patients. Additionally, spheroids may act as a source of recurrence and reseed disease in patients following surgical procedures<sup>47</sup>. The heterogeneity of HGSOC, and indeed the diversity between all ovarian cancer subtypes as a whole, have made development of successful and reliable screening strategies difficult. Therefore, there is an urgent need to improve outcomes for late-stage patients.

### 1.3.3 Dissemination & metastases

The majority of cancer-related deaths are due to the metastatic spread of the primary tumours and this is especially true for HGSOC<sup>48-50</sup>. When women present with late-stage HGSOC, widespread metastatic disease within the peritoneal cavity has already taken shape whereby rapidly growing tumour nodules obstruct organs and lead to ascites formation<sup>15</sup>. Organ obstruction and cachexia is the leading cause of patient mortality<sup>51</sup>. HGSOC metastases are unique to the disease and does not follow the paradigms observed in other metastatic cancers. The rapid progression towards metastatic disease in HGSOC patients and the challenges in treating such patients necessitates an understanding of HGSOC dissemination and metastases.

Compared to metastasis of other cancers, HGSOC metastasis is poorly understood<sup>15</sup>. Unlike other cancers, HGSOC predominantly disseminates within the peritoneal cavity instead of hematogenously. This occurs through a passive process, termed transcoelomic metastasis, by which tumour cells exfoliate from primary tumour sites and are carried to distant sites by the physiological flow of peritoneal fluid without a requirement to invade and extravasate from vasculature<sup>52</sup> (**Figure 1.3A**). Without any



anatomical barriers between the female reproductive system and visceral organs, there is nothing to occlude transcoelomic metastasis events<sup>52</sup>. Once they are detached, the cells circulate within the peritoneal fluid and reattach to new sites and tend to favour, but are not limited to, the peritoneal lining and omentum<sup>52</sup> (**Figure 1.3B**). Almost all HGSOC patients with metastases have tumours implanted on the omentum, a fatty pad covering the abdominal cavity and bowel<sup>15,52</sup>. HGSOC tumour cells only reattach and invade the mesothelium which is a layer of epithelial cells covering the surface of visceral organs, the omentum, and the diaphragm<sup>15,53</sup>. Once colonized, secondary HGSOC tumours do not invade beyond the surface of affected tissues<sup>6,15</sup>.

Before HGSOC tumour cells exfoliate from the primary tumour, they undergo epithelial-to-mesenchymal transition (EMT) to aid in disruption of cell-cell attachments that bind the tumours to the basement membrane<sup>47,54</sup>. During this event, a “cadherin switch” occurs whereby the cells downregulate expression of *CDH1* (E-cadherin) and upregulate *CDH2* (N-cadherin) and *CDH3* (P-cadherin)<sup>47,55</sup>. Loss of the cell adhesion factor E-cadherin with a concomitant increase of matrix metalloproteases (MMPs) disrupts anchoring of the cells to the solid tumour mass and allows the cells to shed<sup>47</sup>. Recent live-imaging revealed that HGSOC tumour cells shed from primary tumours either as single cells or in clusters. However, the majority of single cells died due to detachment from the basement membrane whereas multicellular clusters – called spheroids – survived<sup>56</sup>. Indeed, *in vitro* studies have shown that spheroid formation allows disseminated HGSOC tumour cells to survive anoikis (anchorage deprivation) and remain in suspension for long periods of time<sup>6,15,57</sup>. Multicellular spheroids float in suspension as they are passively circulated within the peritoneal cavity by the physiological peritoneal fluid and they maintain a

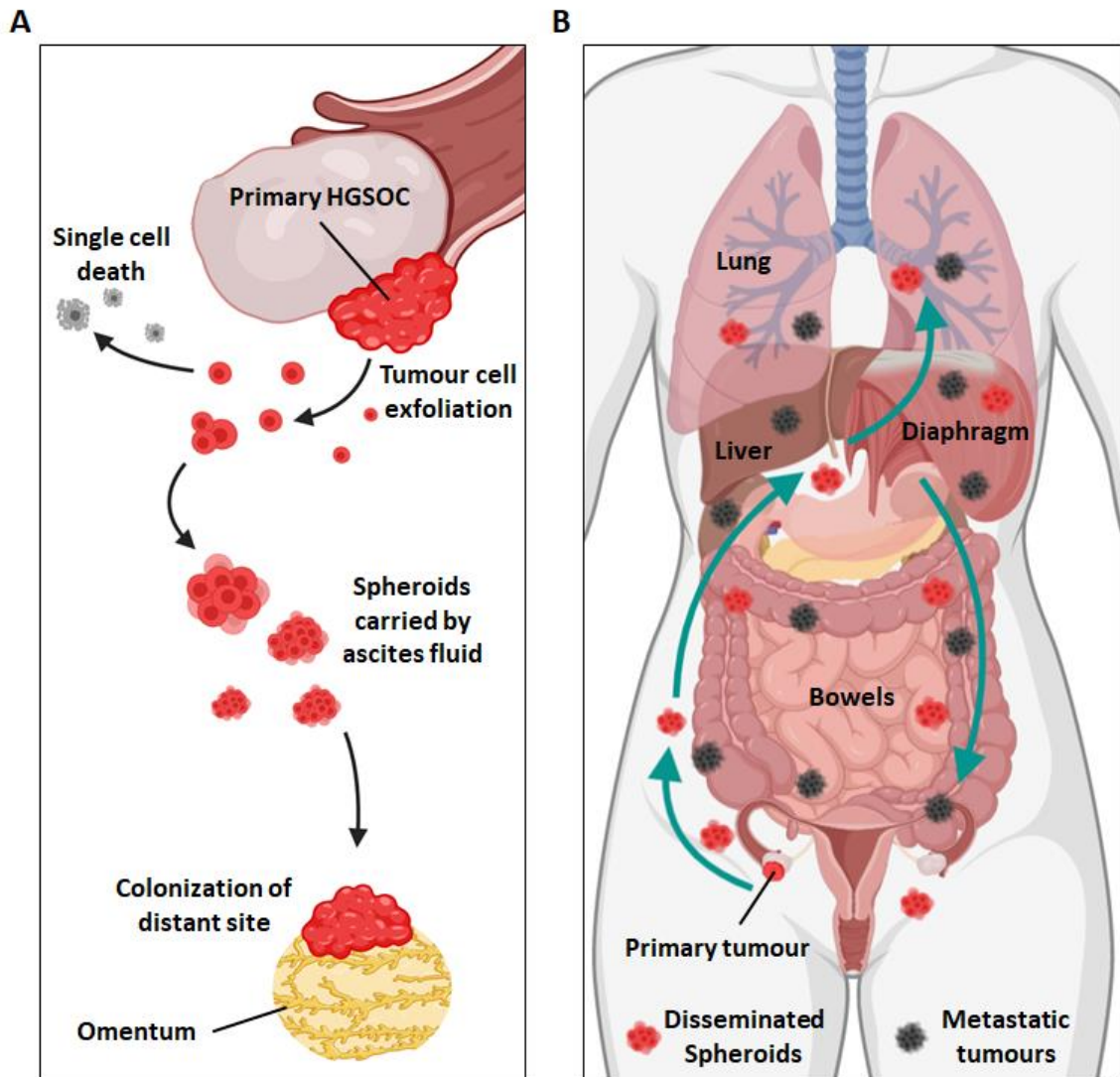


**Figure 1.3. Dissemination and metastases of HGSOc.** (A) Cells from the primary tumour can exfoliate from the solid tumour and shed into the peritoneal fluid. Cells may detach as single cells or in multicellular clusters called spheroids. Single cells cannot survive anchorage-independent conditions and undergo cell death due to anoikis. Spheroid cells can survive anchorage deprivation and are carried by the peritoneal fluid (ascites fluid) to distant sites. Invasive spheroids can then embed into the mesothelium of new sites and colonize the new tissue surface. The omentum (subsection shown) is a common site for HGSOc metastases. (B) Spheroid cells (red) are carried throughout the peritoneal cavity by the natural flow of ascites fluid (green arrows). Spheroid cells may circulate within ascites for prolonged periods before encountering a new surface to colonize. Spheroid cells can reattach to new mesothelial surfaces to form metastatic tumours (black). Some common metastatic sites include the bowels, liver, diaphragm, lungs, and omentum (not shown).

mesenchymal phenotype with low E-cadherin and high N/P-cadherins<sup>52,54,58</sup>. Reduced E-cadherin expression in disseminated tumour cells compared to the primary HGSOc tumour correlates with increased invasiveness and poor survival among patients<sup>47</sup>.

The vast majority of HGSOc patients present with an accumulation of fluid in the peritoneal cavity, known as ascites, which often accompanies the presence of spheroids<sup>47</sup>. The accumulation of ascites can be attributed to several factors such as poor drainage of lymphatics due to obstructions by spheroids, or increased vascular permeability due to an increase of vascular endothelial growth factors (VEGFs) secreted by normal and tumour cells<sup>59</sup>. Reduced reabsorption of fluid through mesothelium and increased peritoneal oncotic pressure can also lead to accumulation of ascites<sup>47</sup>. It is not known at which stage of disease ascites develops – whether it is an early event required for HGSOc metastasis or if it is a hallmark of late-stage disease – but clinical observations from patients suggests the latter, and its presence signifies poor prognosis<sup>52</sup>. This is primarily because ascites facilitates the spread of metastatic disease by disseminating malignant spheroids as previously mentioned (section 1.3.2). Ascites also contains several acellular factors that promote survival of spheroid cells and enhances growth of secondary tumours, including mitogens, immune cells, cytokines, and soluble extracellular matrix (ECM) proteins<sup>60</sup>. These factors have been found to vary with HGSOc stage with more advanced HGSOc disease correlating with higher concentrations of factors in ascites. Factors such as mitogens and cytokines are not only secreted by normal cells but also by tumour cells, which greatly exacerbates the pro-survival, pro-proliferative, and pro-angiogenic peritoneal environment while suppressing immune response<sup>60</sup>. Adipocytes in the omentum also secrete cytokines, namely interleukins including IL-6 and IL-8, which can contribute

to spheroid invasion of the omentum. IL-6 activates the JAK/STAT pathway and AKT phosphorylation leading to pro-growth and anti-apoptotic signaling cues in spheroid cells<sup>61</sup>. Increased IL-6 expression is indicative of chemoresistance and poor prognosis. Similarly, increased concentration of VEGF ligands in ascites improves spheroid cell survival and correlates with poor patient outcomes<sup>28</sup>. VEGFA binding to VEGFR2 receptors found on spheroid cells protects the cells from anoikis<sup>15</sup>. Ascites fluid also upregulates the expression of CD44, a cell surface glycoprotein, increasing the migratory and invasive properties of spheroid cells that facilitates implantation into new peritoneal surfaces<sup>15</sup>. Ascites fluid is therefore part of the active tumour microenvironment (TME) for tumour cells and spheroid cells alike and is a challenging component of HGSOc dissemination and metastases.

Following dissemination, spheroid cells undergo a coordinated process consisting of intricate steps involving ECM proteins, transcriptional changes, and mesenchymal-to-epithelial transition (MET) to colonize the mesothelium of distant sites<sup>47</sup>. Integrins facilitate reattachment of suspended spheroid cells to new mesothelial surfaces through interactions with collagen type I/IV, laminin, and fibronectin, as well as CD44-binding hyaluronan<sup>54</sup>. Upregulation of E-cadherin, even while N/P-cadherin expression is high, can also promote adhesion in a subset of “hybrid” epithelial/mesenchymal spheroid cells<sup>15</sup>. The hybrid epithelial/mesenchymal phenotype provides added survival benefits in suspension and promotes chemoresistance<sup>54,58</sup>. Once attached to the mesothelium, spheroid cells initiate mesothelial clearance through several MMPs, integrins, and myosin-mediated force to remove adjacent mesothelial cells<sup>62</sup>. Mesothelial clearance is improved in spheroid cells expressing mesenchymal markers or EMT transcriptional profiles and inhibition of these

markers, such as TWIST1 or ZEB1, decreases clearance activity<sup>63</sup>. Spheroid cells then undergo MET to revert to an epithelial phenotype that promotes proliferation and growth of the new tumour<sup>54,58</sup>. Additionally, primary cells isolated from patient ascites and cultured *in vitro* are able to maintain their spheroid-forming capacity and with no discernible differences to spheroids found *in vivo*<sup>64</sup>.

The present understanding of HGSOc tumour exfoliation, aggregation into spheroids, and implantation at distant sites is limited, but clinical observations, cell culture models, and pre-clinical mouse models have provided substantial evidence that spheroids play a crucial role in the dissemination and metastases of HGSOc. Spheroids present many challenges to therapy and is an important area of study if HGSOc patient outcomes are to be improved.

#### 1.3.4 Preclinical models of ovarian cancer

A study in 2013 that characterized the ovarian cancer cell lines used at the time revealed that the two most commonly used cell lines (SKOV3 and A2780) accounted for approximately 60% of publications<sup>65</sup>. Unfortunately, comparative genomic characterization of these cell lines with the TCGA data published in 2011 revealed that these two lines, along with others, were not representative of HGSOc<sup>65-67</sup>. This study led to a shift in experimental design to favour cell lines that more accurately represented the disease<sup>6</sup>. Moreover, it encouraged the development of patient-derived primary cell lines<sup>6</sup>. Several institutions across the world now use patient-derived HGSOc cells for both *in vitro* cell culture and *in vivo* xenograft studies<sup>68</sup>. Not only do ascites-derived cells represent the genomic landscape that characterizes HGSOc, such as TP53 mutation and chromosome

rearrangements, they also more closely represent clinically observed chemoresistance to platinum treatment<sup>68-70</sup>.

Several *in vitro* models have been employed to investigate HGSOC spheroid formation and metastases. These models use either cell lines or patient-derived primary cells to investigate spheroid cells in a three-dimensional *ex-vivo* environment<sup>71</sup>. In a fallopian tube model that recapitulates the FTE, fallopian tube secretory and ciliated epithelial cells isolated from fallopian tube fimbriae were co-cultured with on a collagen type IV-coated substrate to study stress response and carcinogenesis<sup>72</sup>. Another method cultured fallopian tube secretory epithelial cells on specially-coated plates to resemble the FTE ECM and induce spheroid formation<sup>71</sup>. The hanging drop method has also been used to induce spheroid formation<sup>73</sup>. In contrast, the *in vitro* data presented herein employs a three-dimensional model that recapitulates HGSOC spheroid dissemination found *in vivo*<sup>64</sup>. HGSOC cell lines or ascites-derived HGSOC cells are cultured in ultra-low attachment (ULA) plates which are coated in a neutrally charged, non-ionic, covalently-bound hydrophilic hydrogel (**Figure 1.4**). When transferred from adherent or monolayer conditions to ULA plates, HGSOC cells remain in suspension and spontaneously form spheroids<sup>57,64</sup>. These spheroids can then be incubated in suspension conditions for extended periods before being transferred to regular plasticware to facilitate reattachment. Hence this process recapitulates spheroid formation and reattachment to a new surface and allows for the investigation of metastases in a controlled *in vitro* environment<sup>64</sup>. Ascites-derived spheroid aggregates formed using this method have been shown to histologically and morphologically resemble those found *in vivo*<sup>64</sup>. HGSOC cell lines and ascites-derived spheroids can also be transplanted intraperitoneally into xenograft mice to recapitulate

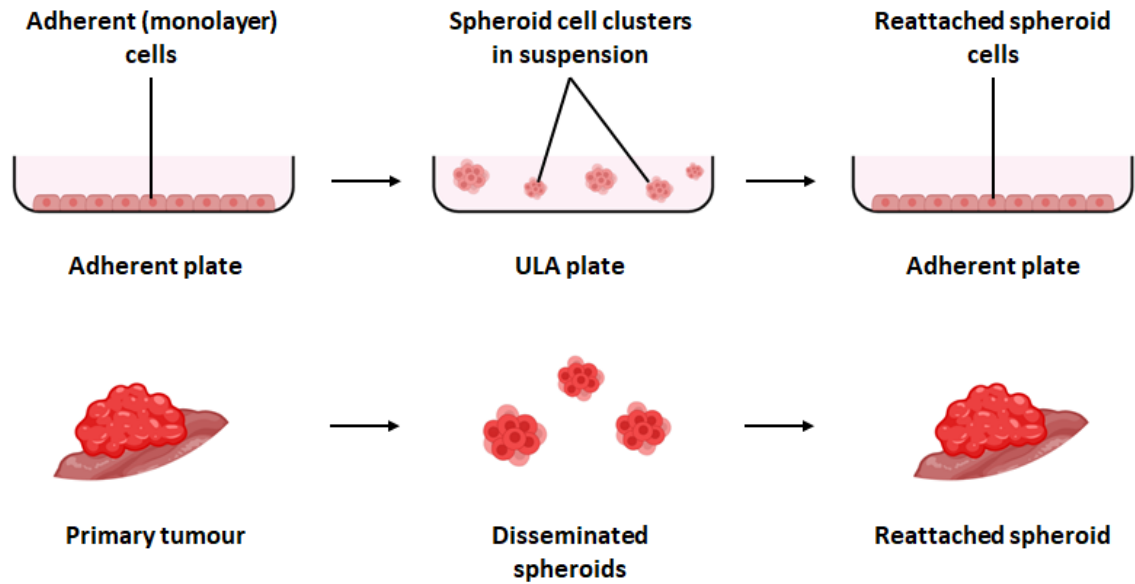


**Figure 1.4. *In vitro* model of HGSOC spheroid dissemination.** HGSOC cell lines or ascites-derived HGSOC cells can be cultured *in vitro* in regular plasticware under monolayer or adherent conditions. This recapitulates pro-growth conditions as in the primary solid tumour. When these cells are collected and transferred to suspension conditions established using ultra-low attachment (ULA) plates, the cells spontaneously form spheroids without any further stimulation and resemble spheroids formed *in vivo* in patients. Spheroid cells can be cultured in ULA plates for prolonged periods to investigate spheroid biology. These spheroids can then be collected and transferred to regular plasticware to enable reattachment under adherent conditions. In this way, spheroid formation and reattachment can be investigated *in vitro*.

dissemination and metastases *in vivo*<sup>74</sup>. These spheroids invade much of the same tissues and organs observed clinically in patients<sup>74</sup>. Xenograft mice will even develop ascites which can be collected to extract disseminated tumour cells and TME factors<sup>75</sup>. Unfortunately, many of the HGSOc cell lines deemed to represent clinical HGSOc with high genomic fidelity do not grow well following intraperitoneal transplantation in nude mice. These cell lines require severe combined immunodeficient (SCID) or NOD/SCID/IL2 $\gamma$ <sup>null</sup> (NSG) mice which do not allow for the investigation of immune cell contributions to HGSOc<sup>76</sup>.

### 1.3.5 Summary of HGSOc

HGSOc is the most common type of ovarian cancer<sup>5,6</sup>. In the large majority of cases, women present to the clinic at an advanced stage in which the disease has spread beyond the primary tumour and into the peritoneal cavity, affecting multiple tissues and organs. Metastases of HGSOc tumour cells are unique in that they rarely metastasize hematogenously. Instead, tumour cells can exfoliate from solid tumours and shed directly into the peritoneal fluid. These tumour cells then aggregate together to form multicellular clusters called spheroids. The formation of spheroids allows the cells to survive in suspension conditions. Spheroids are carried by the physiological peritoneal fluid to distant sites where they invade the mesothelium to form secondary lesions. The accumulation of peritoneal fluid, called ascites, accompanies the presence of spheroids. It is not clear at which stage of the disease ascites develops, but it signifies poor prognosis. Ascites fluid contains several factors that promote survival, chemoresistance, and invasiveness of



spheroid cells. Several *in vitro* and *in vivo* models of ovarian cancer have been developed to recapitulate the phenomenon of spheroid dissemination.

## 1.4 Genomic & transcriptomic characterization of HGSOC

### 1.4.1 Recurrent mutations & alterations

A landmark study by The Cancer Genome Atlas (TCGA) in 2011 uncovered the invariable heterogeneity present across all HGSOC cases and provided the first broad insights on the relatively few gene alterations shared across patients compared to other cancers<sup>67,77</sup>. Many genes and pathways are disrupted in HGSOC and the most common are shown in **Figure 1.5**. A predominant gene found to be mutated almost universally across all HGSOC cases is the *TP53* tumour suppressor gene<sup>77,78</sup>. *TP53* mutations have also been discovered in STICs, suggesting that *TP53* mutations may potentially be early driver events for HGSOC development<sup>31</sup>. *TP53* mutations found in HGSOC patients can be characterized as missense (70.4%), nonsense (8.67%), frameshift (12%), or splice mutations (5.1%)<sup>79</sup>. The vast majority of these mutations, approximately 80%, are found on the DNA-binding domain (DBD) of p53<sup>79,80</sup>. These mutations can be translated into altered p53 protein structure, either through truncations or misfolding, causing loss of function, gain of function (oncogenic), or dominant negative phenotypes<sup>81</sup>. Mutant p53 is also more stable than wild type p53 because it can no longer bind to MDM2/4 and evades protein degradation<sup>82</sup>. Stabilizing p53 mutations in fallopian tube secretory epithelial cells improves survival in suspension conditions<sup>83</sup>. Missense mutations such as R273H, R175H, and R248Q can also lead to more aggressive and invasive phenotypes<sup>84</sup>. Studies have therefore shown that the type and location of *TP53* mutations can have an effect on patient

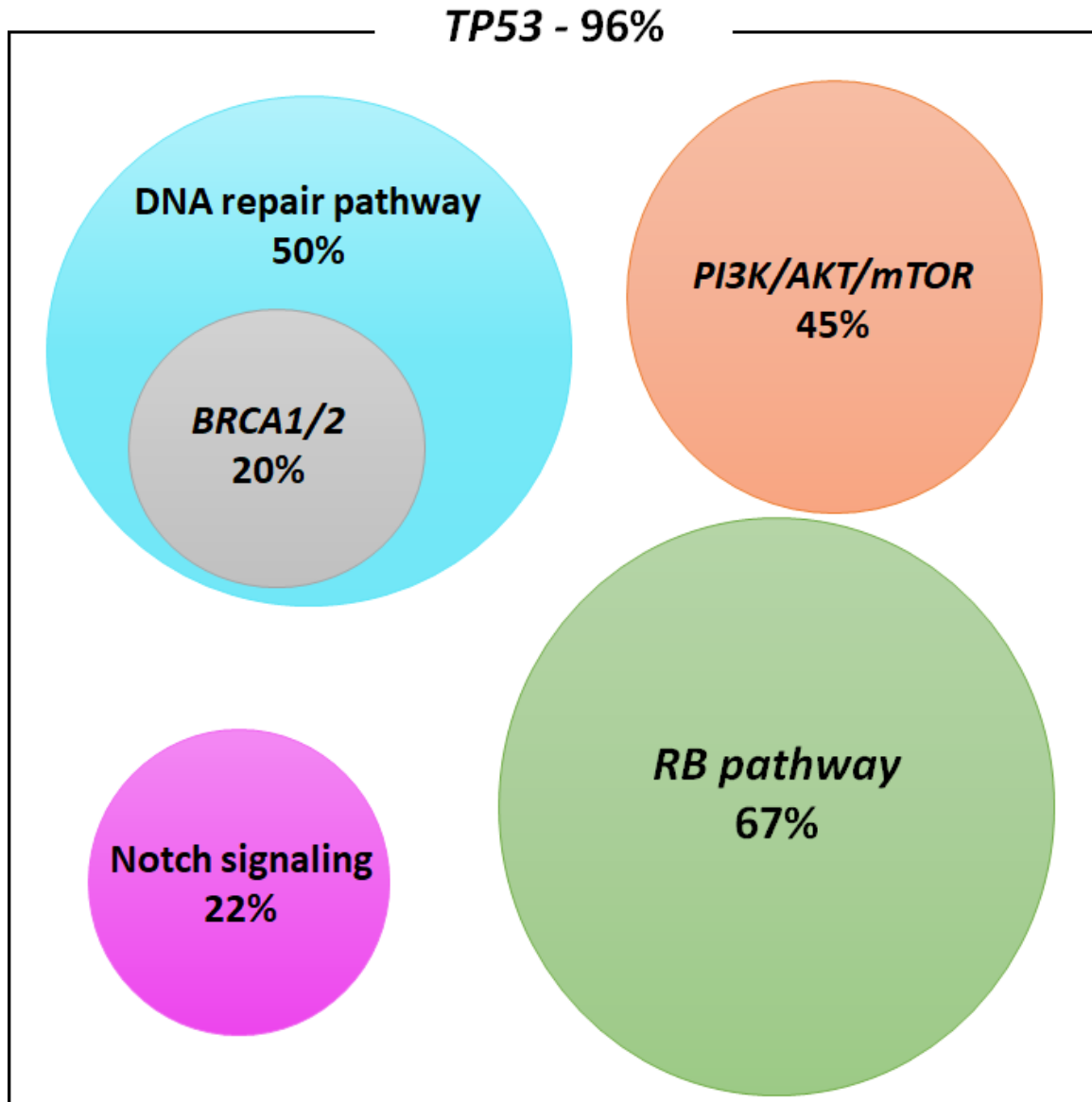


**Figure 1.5. Most common gene & pathway alterations in HGSOc.** *TP53* mutations are almost universal in HGSOc with 96% of tumours carrying mutant p53. While other genetic mutations in individual genes are not as prevalent, cellular pathways are widely disrupted across HGSOc. Disrupted pathways include: RB pathway (67%), PI3K/AKT/mTOR pathway (45%), Homologous recombination (HR)-mediated DNA repair pathway (50%), and the Notch signaling pathway (22%). Of particular note are the prevalence of *BRCA1/2* (15-0%) mutations in HGSOc. *BRCA1/2* mutations (20%) are the most common form of DNA repair pathway disruption in HGSOc.

outcomes<sup>85,86</sup>. Patients with mutations in the DNA major groove interacting residues of p53 have improved overall survival (OS) compared to those with mutations in the DNA minor groove interacting residues<sup>85</sup>. Specific oncogenic *TP53* mutations can also be used to stratify HGSOc patients with chemoresistant or recurrent tumours<sup>87,88</sup>. Aberrant p53 function may also occur through amplification of *MDM2/4* caused by copy number alterations since *MDM2/4* are required for normal p53 equilibrium<sup>80</sup>. The broad spectrum of mutations found in *TP53* alone reflect the heterogeneity present in HGSOc.

Beyond *TP53*, the next most commonly mutated genes in HGSOc are *BRCA1* and *BRCA2*, although their occurrence is not universal as *TP53* mutations<sup>66,89</sup>. The contributions of germline *BRCA1/2* mutations to EOC are clear and this led to the development of prophylactic bilateral salpingo-oophorectomy<sup>19,89-92</sup>. *BRCA1* and *BRCA2* function in the DNA repair pathway and homologous recombination (HR)<sup>93,94</sup>. When double-stranded DNA breaks occur during DNA replication, HR provides cells with a reliable error-free mechanism to repair breaks<sup>95</sup>. When this pathway is impaired, cells revert to non-homologous end joining (NHEJ) which is error-prone and can lead to genomic instability and carcinogenesis, most notably ovarian cancer or breast cancer<sup>93-95</sup>. *BRCA1* also plays a role in cell cycle control, mitosis, chromatin remodeling, and transcriptional regulation<sup>96-98</sup>. While inheriting mutant *BRCA1* or *BRCA2* alleles increases the risk of developing ovarian cancer (44% for *BRCA1*; 11-27% *BRCA2*), only 15-20% of HGSOc cases have germline or somatic *BRCA1/2* mutations<sup>66,99-103</sup>. A broader search inclusive of all HR-mediated DNA repair pathway members reveals even more recurrent mutations. These genes include *ATM*, *ATR*, *BARD1*, *BRIP1*, *CDK12*, *CHEK2*, *MRE11A*, *PALB2*, *PTEN*, *RAD50*, *RAD51* paralogs (*RAD51B*, *RAD51C*, and *RAD51D*), and the

Fanconi anemia genes<sup>5,6,99,104-108</sup>. Collectively, mutations in genes required for HR-mediated DNA repair can be found in at least 50% of all HGSOC cases<sup>66</sup>. The involvement of these genes suggests that while *BRCA1/2* may not account for a majority of HGSOC cases, alterations in the HR-mediated DNA repair are frequently found in HGSOC and contributes to the genomic instability and heterogeneity of the disease<sup>6,66</sup>.

Less frequent recurrent mutations involve *CSMD3* (6%), *CDKN2A* (2%), *FAT3* (6%), *NF1* (11%), and *RBI* (10%)<sup>6,66,99,109</sup>. The roles of *CSMD3*, *FAT3*, and *NF1* in HGSOC are not clear but their mutations have also been detected in other cancers<sup>110-116</sup>. *FAT3* and *NF1* may potentially act as tumour suppressors or mediate chemoresistance<sup>113,116,117</sup>. Despite the low prevalence of direct *RBI* or *CDKN2A* mutations, retinoblastoma (RB) pathway disruption is common in HGSOC, occurring in approximately 67% of cases<sup>66</sup>. Cyclin-dependent kinases (CDK), namely CDK4/6, phosphorylate and inactivate RB protein which releases it from E2Fs and enables transcriptional activity of E2F target genes, including *BRCA1*<sup>118-120</sup>. The CDK/cyclin-RB-E2F axis functions in cell cycle control and alterations can amount to dysfunctional proliferation. *CDKN2A* encodes p16<sup>INK4A</sup> which is a negative regulator of CDK4/6 and acts to suppress the G1/S transition<sup>118,119,121</sup>. In contrast, alterations in genes that promote the G1/S transition are more common, including *CCNE1*, *CCND1*, and *MYC*, and are each found in over 20% of HGSOC tumours<sup>66</sup>. *CCND1* encodes cyclin D1 which activates the aforementioned CDK4/6. *CCNE1* encodes cyclin E1 which similarly promotes G1/S transition by activating CDK2<sup>122,123</sup>. *CCNE1* is found on the 19q12 locus which is susceptible to copy number alterations in EOC<sup>13,124,125</sup>. An *in vitro* study showed that *CCNE1* knockdown in HGSOC cells resulted in G1 arrest and reduced viability but only

in cells with 19q12 amplification<sup>124</sup>. Another study showed that high *CCNE1* expression, with or without 19q12 amplification, can be used to stratify patients by genomic instability, response to chemotherapies and OS<sup>126-128</sup>. Overexpression of *CCNE1* combined with a missense mutation in *TP53* in fallopian tube secretory epithelial cells increases proliferation and resistance to anoikis<sup>30,129</sup>. Interestingly, HGSOC patients with amplified *CCNE1* typically have intact HR-mediated DNA repair pathway genes, including *BRCA1* and *BRCA2*, indicating that gain of *CCNE1* may be a unique early driver event in HGSOC tumorigenesis<sup>13</sup>. Indeed, concomitant increase of *CCNE1* transcription and cyclin E1 protein levels have been found in precursor STICs<sup>129-131</sup>. Additionally, a synthetic lethality screen identified HR-mediated DNA repair components are essential in HGSOC cell lines with 19q12 amplification<sup>132</sup>. This suggests genomic instability caused by 19q12 amplification and HR-mediated DNA repair are mutually exclusive and at least one of these pathways must be retained for tumour cell survival<sup>13</sup>. These data demonstrate that although recurrent alterations in CDK/cyclin-RB-E2F axis members occur at low frequency compared to *TP53* or *BRCA1/2*, their alterations are collectively found in a large majority of HGSOC cases<sup>13,66</sup>. Analogous to the diversity of alterations found in HR-mediated DNA repair genes, the variety of alterations in CDK/cyclin-RB-E2F axis members demonstrate the heterogeneity that is widely apparent in HGSOC.

Recurrent mutations and copy number alterations found in other pathways include FOXM1 (87%), PI3K/Ras (45%), and Notch (22%)<sup>66</sup>. Normally, p53 is a negative regulator of FOXM1, a transcription factor that regulates G2/M-specific genes<sup>133</sup>. Consequently, overactivation of the FOXM1 pathway may be a result of mutant p53 in these cases. Amplification of PI3K/Ras components, including *PIK3CA* and *AKT*, correlate

with reduced OS<sup>66,134,135</sup>. *PTEN* loss or decreased *PTEN* expression has been observed in 50-75% of cases<sup>136</sup>. Overall, PI3K/Ras alterations increase proliferation of tumours and decrease response to chemotherapies<sup>135,137,138</sup>. The majority (50%) of Notch alterations were found in *NOTCH3*, encoding the Notch3 receptor, and a recent study has implicated a ligand encoding gene, *DLK1* to have an important role in EMT and metastases<sup>66,139,140</sup>.

#### 1.4.2 Genomic & transcriptomic subtyping

The variety of these mutations characterizes the genetic diversity present in HGSOC. Advances in genomic and transcriptomic sequencing technologies have greatly added to the current understanding of HGSOC and several groups have attempted to stratify HGSOC as subtypes based on genomic or transcriptomic signatures<sup>141,142</sup>. The first of these studies defined four distinct subtypes of HGSOC: C1-mesenchymal, C2-immunoreactive, C4-differentiated, and C5-proliferative<sup>142</sup>. C1 had gene expression relating to ECM proteins, cell adhesion, and angiogenesis and is associated with poor patient outcomes<sup>31,142</sup>. Both C2 and C4 had some overlapping expression of genes involved in immune cell activation with the latter also having reduced stromal response; both have better patient outcomes<sup>31,142</sup>. C5 had the worst patient outcomes and expressed mesenchymal genes with increased cadherin signaling and low immune expression<sup>31,142</sup>. The reduced survival exhibited by patients with C1 or C5 tumours displaying mesenchymal activity can potentially be attributed to increased aggressiveness and chemoresistance sustained by spheroids.

This subtyping method is now widely accepted and other groups have confirmed its findings, however, recently a new “anti-mesenchymal” subtype has been proposed to

address the heterogeneity in the C4-differentiated cluster, demonstrating the continued evolution of our current understanding of HGSOC<sup>141,143</sup>. The nature of peritoneal dissemination onto multiple sites further adds to the genomic and transcriptional complexities as stroma signatures and immune signatures of the TME confound such analyses<sup>144</sup>. This was exemplified by a recent study in which PTEN loss was found to be a common driver event in 36% of the TCGA HGSOC cohort whereas the original 2011 study only found PTEN loss in 6% of cases<sup>66,136</sup>. This study used a novel computational approach to correct PTEN expression bias caused by tumour stroma<sup>136</sup>. Novel computational approaches are therefore necessary to obtain prognostically valuable data from complex studies confounded by heterogeneity<sup>144</sup>.

### 1.4.3 Copy number alterations & signatures

Copy number alterations are universally pervasive in HGSOC. An in-depth computational study in 2018 analyzing 117 HGSOC cases demonstrated that patients can also be stratified by copy number signatures, ranging from 1 to 7<sup>145</sup>. In this study, Macintyre et al. linked unique copy number signatures to the underlying mechanisms, such as breakage-fusion-bridge events due to telomere shortening and oncogenic Ras/MAPK (mitogen-activated protein kinase) signaling in copy number signature 1; or impaired cell cycle control amounting to focal amplification in copy number signature 6<sup>145</sup>. Copy number signature 6 also displayed the largest copy number changes among all patients (8-30 copies) and included amplifications in *CCNE1*, *CCND1*, *CDK2*, *CDK4*, or *MYC* as well as deletion or inactivation of *RBI* or *CDK12*<sup>145</sup>. Patients in this cohort were also more likely

to have mutations in Toll-like receptor signaling and PI3K/AKT signaling<sup>145</sup>. This study highlighted the heterogeneity across HGSOC patients.

High-throughput genomic studies have revealed that heterogeneity not only exists across patients, but also within individual patients in the form of intratumoural heterogeneity (ITH)<sup>146-148</sup>. Chromosomal instability and tumorigenesis directed by early oncogenic driver events stimulates additional gene alterations that confer selective advantages<sup>149-151</sup>. This leads to subclones within the same tumour that are genetically distinct but have overlapping alterations<sup>152</sup>. The burden of multiple mutations, especially in HR-mediated DNA repair genes, can lead to loss of essential functions in some cases and increase sensitivity to chemotherapy as observed in patients with germline *BRCA2* mutations<sup>153-156</sup>. However, genomic instability and ITH can also give rise to chemoresistant tumour cell populations<sup>150,151</sup>. Several studies have shown that both spatial and temporal ITH play a role in HGSOC progression and metastases. One study found that alterations in oncogenic driver genes (*CTNNB1*, *NF1*, *PDGFR*, *PIK3CA*, *RBM15*, and *SH3GL1*) existed only in spatially separated subclones<sup>157</sup>. Another study highlighted that spatial and temporal ITH can exist at the time of late-stage diagnosis and before initiation of chemotherapy<sup>158</sup>. A retrospective computational study demonstrated that the degree of clonal expansion can vary following chemotherapy, and patients with increased clonal expansion have shorter survival and are at increased risk of developing chemoresistant HGSOC recurrence<sup>146</sup>. The barrier-free dissemination of HGSOC spheroids into the peritoneal cavity may potentially accelerate ITH clonal expansion at secondary sites. Therefore, genomic and transcriptomic characterizations of primary HGSOC tumours



alone may not be sufficient to stratify tumours since late-stage diagnosis can present in concert with ITH and varying degrees of clonal expansion<sup>152</sup>.

#### 1.4.4 Summary of HGSOC genomics

The aneuploidy and heterogeneity are indisputable hallmarks of HGSOC<sup>66</sup>. Unlike other cancers, frequent recurrent genetic alterations are low, but several pathways are known to be commonly altered in HGSOC patients allowing for genomic or transcriptomic clustering and subtyping<sup>66</sup>. The genomic characterization presented herein reveals that multiple combinations of signaling pathways may be driving HGSOC progression with few unifying features across patients. This heterogeneity has made the development of effective therapies challenging. Several pathways may be simultaneously impaired and inhibition of one means the tumour cells are able to bypass inhibition through another pathway. It may also be likely that specific mutations are not widespread across the majority of HGSOC patients – as implied by the low frequency of recurrent mutations – limiting the broad application of potential targeted inhibitors limited. However, despite the inherent and invariable genomic instability that persists in all HGSOC cases, tumour cells must still retain function of essential genes, particularly those that facilitate EMT/MET, mesothelial clearance, angiogenesis, immune evasion, chemoresistance – and in the case of spheroid cells – genes that allow for multicellular aggregation and protection from anoikis in suspension conditions. The mechanisms entailing widespread peritoneal dissemination – which afflicts the vast majority of HGSOC patients – shares a common route: spheroid dissemination through physiological peritoneal fluid (ascites). Therefore, understanding the biology of spheroids is critical to HGSOC etiology. There may

potentially be specific essential genes or processes during spheroid formation and dissemination that can be targeted to improve the current standard of care despite genetic diversity. Treatment of HGSOc and the role of spheroids in tumour recurrence will be explored in subsequent sections.

## 1.5 Treatment of HGSOc and chemoresistance

### 1.5.1 Surgery & chemotherapy

Upon diagnosis of HGSOc, a patient is referred for cytoreductive surgery<sup>5</sup>. Depending on the aggressiveness of the cancer at the time of diagnosis, this procedure seeks to debulk the tumour burden by removing all macroscopic tumours and may include peritonectomy, omentectomy, and en bloc resection of the viscera<sup>5</sup>. It is challenging to achieve complete removal of all macroscopic residual disease in advanced stage patients<sup>159</sup>. The presence of 1 cm residual disease following surgery is considered “optimal”; >1 cm residual disease is “suboptimal”<sup>5</sup>. Late-stage patients that receive complete tumour debulking without any residual disease have significantly better outcomes following chemotherapy compared to “optimal” late-stage patients<sup>160,161</sup>. Late-stage “optimal” patients have increased progression-free survival (PFS) than “suboptimal” late-stage patients<sup>160-162</sup>.

The standard HGSOc adjuvant chemotherapy for the last 20 years has been a platinum-taxane polytherapy consisting of either cisplatin or carboplatin in combination with paclitaxel or docetaxel<sup>163-167</sup>. There have been attempts to improve this treatment regimen by varying the delivered dose-density or mode of delivery, such as intraperitoneal

delivery but clinical trials have shown reduced patient tolerability and limited improvements in OS or PFS<sup>159,168,169</sup>. For example, while intraperitoneal delivery of cisplatin increases the peritoneal concentration of cisplatin leading to improved OS and PFS, toxicity was also found to increase which has restrained adoption of the technique<sup>168,169</sup>. Patients unable to endure cytoreductive surgery will instead receive neoadjuvant chemotherapy where they undergo the first half of chemotherapy, followed by cytoreductive surgery, and finally the remainder of the chemotherapy<sup>170,171</sup>. Clinical trials have shown that neoadjuvant chemotherapy followed by cytoreductive surgery has similar OS and PFS to primary cytoreductive surgery followed by adjuvant chemotherapy<sup>170,171</sup>. Importantly, neoadjuvant chemotherapy reduced the number of postoperative deaths, suggesting its usefulness for critically ill patients<sup>171</sup>. Regardless of the method employed – adjuvant or neoadjuvant chemotherapy – the goal of HGSOc treatment is to mitigate the symptoms with palliative care to prolong survival of patients.

### 1.5.2 Relapse

Relapse is a challenging and – especially for advanced-stage patients – a defining feature of HGSOc. Over 70% of patients with HGSOc respond positively to cytoreductive surgery in combination with adjuvant or neoadjuvant chemotherapy<sup>51</sup>. Unfortunately, over 80% of these patients will experience relapse<sup>5</sup>. Recurrent HGSOc is generally considered to be incurable<sup>5</sup>. It occurs asymptotically in most patients and imaging-based detection methods routinely fail to identify residual disease in the months following first-line chemotherapy<sup>5</sup>. Relapse is usually detected by increased serum levels of cancer antigen 125 (CA125), a peptide secreted by HGSOc cells<sup>172,173</sup>. However, relapse can occur

without increased levels of CA125 and CA125 alone is not sufficient to initiate second-line therapy. A study comparing delayed second-line treatment (initiated at the onset of observable symptoms) to early second-line treatment (initiated upon high CA125 detection) showed no significant improvements in OS<sup>174</sup>. Approximately half of recurrent patients present with chemoresistance<sup>5</sup>. Patients with recurrent disease who respond well to second-line chemotherapy also face challenges as the burden of additional chemotherapy regimens reduces quality of life and affects the overall efficacy of treatment<sup>5,175</sup>. With each recurrence, the sensitivity to chemotherapy decreases significantly; a study found that second-line chemotherapy had clinical response in 52% of patients compared to only 12% in third-line chemotherapy<sup>5</sup>. Ultimately, 90% of advanced-stage patients develop platinum-resistance during the course of the disease<sup>34</sup>.

Treatment of recurrent HGSOc is guided by sensitivity to chemotherapy which is determined by a patient's platinum-free interval (PFI) – the time between the end of first-line chemotherapy and the onset of relapse<sup>5</sup>. The PFI has been shown to have prognostic value<sup>5,176-179</sup>. A short PFI (<6 months) indicates platinum-resistant recurrent disease and poor outcomes<sup>177</sup>. A PFI greater than 12 months is considered to be very platinum-sensitive with potentially improved PFS<sup>180</sup>. Second-line chemotherapy for platinum-sensitive recurrent disease is generally the same as first-line therapy, but may include additional options such as pegylated liposomal doxorubicin (PLD)<sup>181,182</sup>. Platinum-resistant disease is more challenging as chemotherapy options are limited, but various combinations are now available with the advent of targeted therapies.

### 1.5.3 Targeted therapies

The use of targeted therapies seeks to exploit vulnerabilities of HGSOC cells to create synthetic lethality. DNA damage response pathways have become an attractive target since they are impaired in 50% of all HGSOC cases, with 15-20% of patients harboring mutations specifically in *BRCA1/2* which are involved in HR-mediated DNA repair<sup>66,183</sup>. Cells with impaired HR-mediated DNA repair must rely on base excision repair (BER) or error-prone NHEJ to repair damaged DNA<sup>184</sup>. A major component of BER is poly (ADP-ribose) polymerase (PARP), which binds directly to DNA to initiate repair<sup>185,186</sup>. Inhibition of PARP with PARP inhibitors (PARPi), especially in cells deficient for HR-mediated DNA repair, promotes error-prone NHEJ which increases genomic instability and ultimately leads to apoptosis<sup>185,187</sup>. Clinical trials have investigated the use of PARPi (niraparib, olaparib, rucaparib, and veliparib) in combination with chemotherapy to treat HGSOC<sup>188-190</sup>. Olaparib is the most studied and early clinical trials showed increased PFS in recurrent HGSOC with *BRCA1/2* mutations<sup>159,189,191-194</sup>. It has also been shown to be more effective in these patients compared to PLD. A phase II trial found olaparib was also effective at improving PFS in 50% of patients with *BRCA* wild type recurrent HGSOC, however the response was significantly lower (4%) in platinum-resistant recurrent disease<sup>195,196</sup>. Rucaparib and niraparib have been approved for use as maintenance therapy for both platinum-sensitive and platinum-resistant patients regardless of *BRCA1/2* status due to beneficial improvements in PFS<sup>197-199</sup>. Veliparib was recently evaluated for its efficacy as a first-line therapy in conjunction with platinum-based chemotherapy<sup>200</sup>. The combination, followed by veliparib maintenance therapy, improved PFS compared to chemotherapy alone<sup>200</sup>. Overall PARPi have now been approved as first-

line or maintenance therapy for patients with recurrent disease as clinical data reveals improvements in PFS but not in OS<sup>201</sup>.

IL-6, which activates the JAK/STAT pathway and AKT phosphorylation as previously discussed (section 1.3.3), contributes to spheroid dissemination in the peritoneal cavity and chemoresistance<sup>202,203</sup>. Phase I and II clinical trials evaluated siltuximab (a monoclonal antibody targeting IL-6) for its potential as a therapy for recurrent HGSOc but it had limited benefit and did not improve overall survival (OS)<sup>204,205</sup>. Similarly, increased concentration of VEGF ligands in ascites improves spheroid cell survival and correlates with poor patient outcomes<sup>206</sup>. VEGFA binding to VEGFR2 receptors found on spheroid cells protects the spheroids from anoikis and facilitates angiogenesis during invasion<sup>15</sup>. Bevacizumab (a monoclonal antibody targeting VEGFA) has been approved for use in late-stage and recurrent HGSOc in combination with first-line chemotherapy to improve PFS although it had no effect on OS<sup>206,207</sup>. Other anti-angiogenic therapies that target the VEGF pathway and related receptor tyrosine kinases have also been evaluated and they have shown analogous improvements in PFS but not OS<sup>208</sup>.

Targeted therapies have undoubtedly provided benefits to HGSOc patients<sup>6</sup>. Numerous clinical trials have demonstrated that pairing second-line and third-line treatments with targeted therapies can improve PFS in patients. However, even these novel combinations have failed to achieve meaningful improvements in OS. In 2010 it was unanimously agreed that PFS is the preferred measurable endpoint and the aim of treatment should be to palliate symptoms and delay the inevitable relapse in advanced-stage HGSOc patients<sup>207,209</sup>. The combination of tumour heterogeneity, aneuploidy, and peritoneal dissemination contribute to chemoresistance which makes treating HGSOc a challenge.

#### 1.5.4 Chemoresistance

Retrospective studies have shown that chemoresistance in HGSOC can manifest as intrinsic resistance or acquired resistance<sup>210</sup>. In both cases, the invariable ITH and genomic instability play a significant role in the failure to manage the disease. As previously discussed (section 1.4.3), patients may present with spatial and temporal heterogeneity at the time of late-stage diagnosis and may already have platinum-resistant tumours (intrinsic resistance)<sup>210</sup>. Alternatively, during first-line or subsequent (second-line or third-line) therapies, clonal expansion may also give rise to advantageous populations of HGSOC cells which can evade chemotherapy and become platinum-resistant (acquired resistance)<sup>152,210</sup>. Therefore, the ITH and genomic instability present several opportunities for chemoresistant niches to form, either on already established primary tumour sites or on distant metastases propagated by disseminated HGSOC spheroids<sup>152</sup>. The mechanisms whereby HGSOC cells achieve acquired resistance in HGSOC are aided by DNA repair pathways, the TME, or disseminating spheroid cells<sup>210</sup>.

Compared to patients with wild type *BRCA* genes, patients with *BRCA1/2* mutations respond better to platinum-based chemotherapy and this also translates to better prognosis<sup>152</sup>. Out of the 15-20% of HGSOC cases that have germline or somatic *BRCA1/2* mutations, 73% occur in platinum-sensitive patients<sup>66</sup>. This data correlates well with clinical trials for PARPi in which olaparib combined with chemotherapy improved platinum sensitivity, suggesting that HR-mediated DNA repair plays a role in chemoresistance<sup>190,191,193,195,196</sup>. In the presence of platinum-based chemotherapy drugs that crosslink DNA, cells that maintain the ability to efficiently repair damaged DNA will avoid apoptosis and progress through the cell cycle while cells deficient for adequate DNA repair

will undergo programmed cell death<sup>211</sup>. The role of DNA repair pathways in chemoresistance is emphasized in *BRCA1*-deficient patients with recurrent tumours that had undergone reversions to restore *BRCA1* function following first-line chemotherapy<sup>212</sup>.

The TME for HGSOC is unique in that it is composed of the peritoneal cavity and all of its constituents, including immune cells, ECM proteins, secreted ligands and growth factors, vasculature, the omentum, and – in advanced-stage HGSOC patients – the ascites fluid which acts as a medium for peritoneal spheroid dissemination. Immune cells such as tumour-associated macrophages (TAMs) and tumour infiltrating lymphocytes (TILs) can affect chemoresistance as well as HGSOC recurrence<sup>213-216</sup>. One study performed transcriptomic profiling of paired primary and recurrent tumours from platinum-sensitive recurrent HGSOC patients and showed that tumours clustered as “immune active” or “immune silent” based on expression of immune-related genes<sup>217</sup>. Other studies have revealed the balance of CD8+ TILs and regulatory T cells (Tregs) is related to patient survival<sup>218-220</sup>. The concentration of TAMs and interleukins (IL-6 and IL-10) have been shown to be inversely proportional to patient survival; higher levels of these interleukins and CD163+ TAMs are correlated with chemoresistance and relapse<sup>221</sup>. Additionally, the previously discussed transcriptomic-based subtyping of HGSOC patients (section 1.4.2) demonstrated that patients with low immune expression (C1 and C5 subtypes) have poor survival outcomes<sup>142</sup>. These studies demonstrate the TME may have a role in chemoresistance and relapse.

The ascites fluid contains another major source of chemoresistance and relapse in patients: multicellular spheroid cell aggregates<sup>47</sup>. These free-floating three-dimensional aggregates are complexes of exfoliated HGSOC cells. Spheroids present several



advantages relative to exfoliated HGSOC cells: aggregated spheroid cells survive longer in anchorage-independent conditions compared to single cells, the three-dimensional nature of spheroids inhibits drug penetration, and spheroids cells escape DNA-damaging chemotherapy agents by exiting the cell cycle and entering a quiescent (G0) state where replication and metabolic activity are decreased<sup>57,222-226</sup>. Several studies have shown that spheroid cells are resistant to platinum- and taxane-based chemotherapy agents<sup>227</sup>. Additionally, spheroid cells have been shown to express markers of stemness, such as Oct-4, c-Kit, Nanog, and Myc, leading to postulations that spheroids function as ovarian cancer stem cells (CSCs)<sup>228,229</sup>. Indeed, spheroid cells have been shown to display characteristics of CSCs, including regulating tumorigenesis, progression, and invasiveness. Spheroid cells can remarkably control cell cycle progression to enter quiescence and remain dormant or perform self-renewal functions<sup>57,229,230</sup>. Clinical evidence and *in vitro* studies provide evidence that populations of spheroids can survive chemotherapy and give rise to a chemoresistant niche that can remain undetected and eventually lead to relapse<sup>231,232</sup>. Hence understanding the mechanisms of spheroid cell biology can significantly improve treatment and survival of advanced-stage HGSOC patients.

### 1.5.5 Summary of HGSOC treatment

The standard care for HGSOC patients consists of cytoreductive debulking surgery and platinum-taxane chemotherapy (carboplatin, cisplatin, and paclitaxel). This has remained largely unchanged in the last 20 years, although variations of adjuvant or neoadjuvant chemotherapy are available. Cytoreductive debulking surgery is difficult in late-stage patients who present with wide-spread dissemination of tumours within the

peritoneal cavity. Furthermore, while patients may initially respond to chemotherapy, relapse is frequent and nearly inevitable in late-stage patients. The high degree of heterogeneity and genomic instability of HGSOC complicates treatment and reduces PFS survival as relapse can present with platinum-resistant tumours. Novel targeted therapies such as PARPi (niraparib, olaparib, rucaparib, and veliparib) and anti-angiogenic inhibitors (bevacizumab) used either alone or in combination with standard chemotherapy have prolonged PFS but have not provided meaningful improvements to OS. Unfortunately, the current arsenal of therapies available for HGSOC – especially for late-stage patients – aim to palliate symptoms and prolong the inevitable relapse that occurs in over 80% of cases. Spheroids play a large role in chemoresistance and relapse by forming a chemoresistant niche that can reseed disease. These spheroids express markers of stemness and are highly invasive and metastatic and are naturally disseminated by peritoneal fluid (ascites). Studies have shown that exfoliated HGSOC cells gain several advantages by aggregating into spheroids: survival in anchorage-independent conditions, and proliferative control whereby spheroid cells enter a state of quiescence. Quiescent or dormant cells evade chemotherapy, can survive in suspension for extended periods of time, and can eventually lead to relapse upon invasion of distant mesothelial tissues. Disseminated chemoresistant spheroid populations are the primary culprits of this as yet insurmountable hurdle<sup>28</sup>. Elucidating the mechanisms of spheroid dormancy and viability are critical to developing novel therapeutic strategies to specifically target the chemoresistant niche to prevent relapse in patients.

## 1.6 Tumour dormancy

### 1.6.1 Types of dormancy in cancer

Metastasis in HGSOC is uniquely and predominantly transcoelomic whereby HGSOC cells exfoliate from tumours and shed into the peritoneal fluid<sup>52</sup>. There, they aggregate together to form multicellular clusters of cells called spheroids<sup>47</sup>. Peritoneal fluid carries spheroids to distant sites where they can invade the mesothelial lining of visceral organs<sup>233</sup>. Spheroids can also exist in a clinically undetectable and a reversible dormant state<sup>234</sup>. Dormant spheroid cells are especially dangerous because they can survive first-line chemotherapy for prolonged periods and cause relapse<sup>56</sup>.

Tumour dormancy is divided into three categories: cellular dormancy, angiogenic dormancy, and immune-mediated dormancy<sup>235</sup> (**Figure 1.6**). In cellular dormancy, tumour cells enter a reversible state of dormancy and exit the cell cycle. In angiogenic dormancy, the tumour mass is maintained by a balance between proliferation and apoptosis due to poor vascularization. In immune-mediated dormancy, the tumour mass is maintained in equilibrium by constant cytotoxic activity. These categories are not mutually exclusive and tumour dormancy can be caused by different events including transcriptional control from the primary tumour, TME-induced stress, or chemotherapy<sup>236</sup>. HGSOC spheroids remain dormant during anchorage-independent conditions until they reattach to new mesothelial surfaces and this has been observed both clinically and in *ex vivo* environments<sup>234</sup>.

Much of the present understanding of cellular dormancy comes from CSC studies in other highly metastatic cancer types, such as breast, colon, glioblastoma, head and neck, melanoma, and prostate cancer, and also from hematopoietic stem cells (HSCs)<sup>237</sup>. The

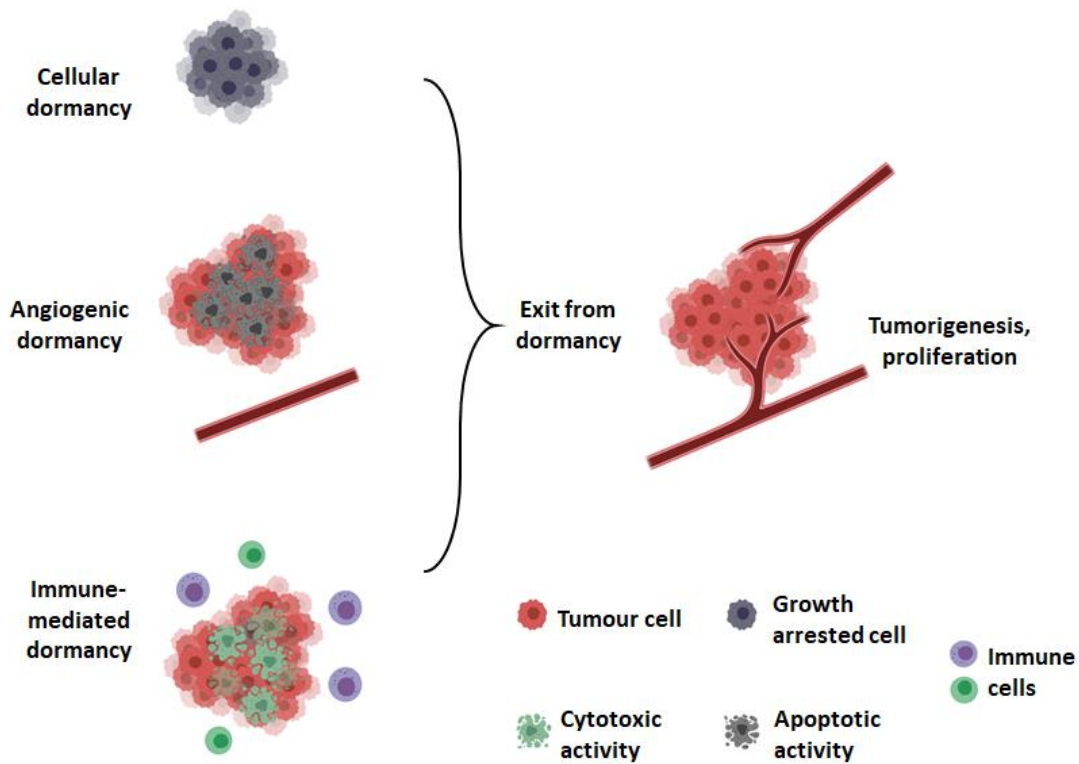


**Figure 1.6. Types of tumour dormancy.** There are three methods for tumour cells to achieve dormancy. In cellular dormancy, tumour cells can enter a reversible growth arrested state whereby they exit the cell cycle. Growth arrested cells are not susceptible to anti-proliferative chemotherapy agents. In angiogenic dormancy, poor vascularization prevents further growth of the tumour mass. Cells may undergo apoptosis due to lack of nutrients or growth factors, which can then allow some cells to grow. The tumour mass is maintained by a balance of proliferation and cell death. In immune-mediated dormancy, the tumour mass is maintained by immune-mediated cytotoxic activity. Infiltrating immune cells are able to kill tumour cells, but not sufficiently to cause the entire tumour mass to regress. Instead, the tumour mass is maintained by a balance of immune cell activity and proliferation. These three categories are not distinct and tumours may use one or more methods to achieve dormancy. When dormant cells re-enter the cell cycle, achieve angiogenesis to direct new vasculature, or evade immune-mediated cytotoxic activity, they can exit dormancy and undergo tumorigenesis and proliferation.

current understanding of dormancy in HGSOC is comparatively lacking. Although these cancer types primarily metastasize hematogenously unlike HGSOC, parallels can still be drawn from their respective disseminated dormant cells. The mechanisms of dormancy identified in these cancer types also have a strong resemblance to HSCs which undergo reversible dormancy and self-renewal<sup>236</sup>. It is widely accepted that dormancy contributes to residual disease in highly metastatic cancers and that dissemination to distant tissues can potentially promote adaptations to new microenvironments and conditions<sup>238-240</sup>. Dormant cancer cells are inherently able to respond to stimuli (or lack thereof) in growth-constraining conditions to survive nutrient deprivation, hypoxia, or chemotherapy<sup>241</sup>. Subsequently, stimuli from growth-promoting conditions can induce proliferation<sup>236</sup>. It has been suggested that dormancy is an intrinsic characteristic of cancer cells that allows them to perform maintenance and self-renewal functions, gain new mutations that allow for colonization of new tissues, or to evade the immune system or chemotherapy<sup>237</sup>. These stimuli act on various signaling pathways to modulate dormant cancer cell activity.

### 1.6.2 Quiescence

The mammalian cell cycle consists of four distinct phases: mitosis (M), DNA synthesis (S), and the two gap phases G1 and G2<sup>242</sup>. In cellular dormancy, tumour cells exit the cell cycle and become arrested in a phase termed G0 that is often referred to as quiescence<sup>243</sup>. Quiescence is reversible and is maintained until adequate growth-promoting conditions are met in the TME<sup>244</sup>. Studies from multiple cancer types and HSCs have revealed a myriad of signaling pathways that can influence quiescence in CSCs<sup>237</sup>. These stimuli can be intrinsic, such as intracellular signaling or transcriptional reprogramming,

or extrinsic, such as extracellular signaling or changes in the TME<sup>237</sup>. These stimuli can be grouped into three broad categories: mitogen deprivation, contact inhibition, or loss of cell adhesion. Mitogen deprivation, contact inhibition, and loss of adhesion are highly relevant to HGSOc spheroids persisting in suspension in ascites and each process may play a role in the prolonged survival of dormant spheroids in patients.

Studies from CSCs have shown that quiescence can be induced through stem cell signaling pathways. Increased Notch activity has been shown to maintain quiescence in breast cancer cells<sup>245</sup>. Notch signaling is important for embryogenesis and self-renewal of stem cells and is also a hallmark of CSCs<sup>237</sup>. One study demonstrated that Notch signaling induces quiescence in HSCs through cyclin D repression and this pathway may also be active in quiescent tumour cells<sup>246,247</sup>. Hedgehog signaling is another important embryogenesis pathway that has been implicated in CSC quiescence<sup>248,249</sup>. Deletion of the Patched receptor activates the Hedgehog signaling pathway and induces quiescence in neural stem cells and lung epithelial cells, potentially as a result of Hedgehog-mediated activation of CDK inhibitors (CKIs)<sup>246,250</sup>. Similarly, Wnt signaling has also been found to be involved in the maintenance of quiescence in HSCs<sup>251</sup>. Transforming growth factor beta (TGF- $\beta$ ) present in the external milieu of disseminated head and neck cancer and prostate cancer cells induce quiescence through TGF- $\beta$ -mediated repression of *CDK4* expression<sup>252,253</sup>. In contrast, TGF- $\beta$  ligands have also been shown to promote growth, migration, and invasion in cancer. This incongruous behaviour is consistent with TGF- $\beta$ 's ability to act as both a tumour suppressor, but also promote tumorigenesis through EMT and angiogenesis<sup>254</sup>.

The p38 MAPK pathway has been shown to play a role in dormancy and many growth factors and cytokines converge on this pathway. For example, one study showed that the TGF- $\beta$ III receptor and the cell adhesion molecule, endoglin, is required for the maintenance of p38 MAPK-mediated quiescence<sup>252,255</sup>. Additionally, activation of p38 MAPK in the absence of proliferative signals results in low extracellular signal-regulated kinase 1/2 (ERK1/2) activity and induces quiescence<sup>255</sup>. This is particularly important for disseminated tumour cells that lack integrin-mediated cell adhesion signaling<sup>256,257</sup>. Importantly, high p38 MAPK activity and low ERK1/2 activity – first identified in dormant head and neck cancer – is now considered a signature of dormant cancer cells<sup>258</sup>. This signature was later identified in the vast majority (90%) of dormant cancer cell lines including ovarian cancer<sup>240,253</sup>. Both p38 MAPK and ERK1/2 activity were found to be regulated by the urokinase-type plasminogen activator receptor (uPAR)<sup>259</sup>. Decreased uPAR activity in turn resulted in reduced focal adhesion kinase (FAK) and Src activity which suppressed ERK1/2 and activated p38 MAPK, promoting quiescence<sup>260</sup>. Studies have also shown that p38 MAPK can induce quiescence through the activation of p53, p21, and cyclin D<sup>237,260</sup>.

The PI3K/AKT/mTOR pathway also plays a role in tumour dormancy and quiescence. Reduced AKT signaling was observed in quiescent patient-derived HGSOc spheroids<sup>64,261</sup>. AKT activation can also stimulate Notch signaling to promote stemness and quiescence in CSCs<sup>237</sup>. In contrast, mTOR is a key regulator of proliferation and its suppression is necessary to maintain quiescence in HSCs and cancer cell lines<sup>262-265</sup>. The Forkhead box class O (FOXO) transcription factors, which are downstream effectors of PI3K/AKT/mTOR, modulate adaptive metabolic mechanisms during oxidative stress

responses in dormant cancer cells<sup>266</sup>. Studies suggest that external stress, such as nutrient deprivation, reduce PI3K/AKT/mTOR activity and induce autophagy and quiescence in dormant breast cancer, head and neck cancer, and ovarian cancer<sup>267</sup>. Under hypoxic conditions, mTOR activation can induce hypoxia-inducible factor-1 $\alpha$  (HIF-1 $\alpha$ ) which can subsequently lead to quiescence and autophagy<sup>237,268</sup>. Inhibition of PI3K/AKT/mTOR signaling in patient-derived HGSOc spheroids promotes autophagy as a survival mechanism<sup>64,261</sup>. Liver kinase B1 (LKB1) has a critical role in metabolic activity during hypoxia and has been shown to modulate mTOR, FOXO, and AMP-activated protein kinase (AMPK)<sup>269</sup>. Loss of LKB1 not only reduces quiescent HSC populations, but also ablates HGSOc spheroids and reduces peritoneal metastases in xenograft mice<sup>226,269,270</sup>. PI3K/AKT/mTOR signaling is therefore a mediator of proliferation and quiescence that can dynamically respond to environmental cues to preserve survival in dormant cells.

### 1.6.3 Loss of cell cycle control

Regardless of the upstream signaling pathways driving quiescence, dormant cells must successfully block cell cycle progression in order to remain arrested in G<sub>0</sub>. However, in order to permit reentry into the cell cycle, this block must be reversible. Dormant cancer cells can achieve this by modulating the CDK/cyclin-RB-E2F axis which includes cyclins, cyclin dependent kinases and their inhibitors, the RB family members, and E2F transcription factors<sup>118,212</sup>. The RB family (RB, RBL1/p107, and RBL2/p130) and E2F transcription factors cooperate to form complexes that transcriptionally regulate a multitude of genes that control progression through the cell cycle<sup>271</sup>. RB proteins bind directly to E2F family members to sequester them and repress their transcriptional



activity<sup>271</sup> (**Figure 1.7**). Transcriptional inhibition is relieved by CDK-mediated hyperphosphorylation of RB proteins resulting in the dissociation of RB proteins from the E2F-DP1 heterodimer and allowing the de-repression of E2F target genes<sup>118,272</sup>. The E2F family is composed of eight members including activators and repressors, but only E2Fs 1-5 are known to interact with the RB family<sup>118,271,273,274</sup>. E2Fs 1-3 primarily associate with RB and are known as activators<sup>118,271,273,274</sup>. E2Fs 4-5 are known as repressors and mostly associate with the two RB-like proteins, p107 and p130<sup>118,271,273,274</sup>. E2F4 has also been shown to bind to RB<sup>118,271,273,274</sup>. Cell cycle control in this manner through the CDK/cyclin-RB-E2F axis is frequently abrogated in cancer as previously discussed (section 1.4.1). Although the most common form of CDK/cyclin-RB-E2F axis deregulation in HGSOc manifests as functional loss of the CKI p16<sup>INK4A</sup> (*CDKN2A*), which occurs in 30% of cases, experiments show that the CKI p21 (*CDKN1A*) is required for the maintenance of quiescence in stem cells and cancer cell lines<sup>66,260,275</sup>. Amplification of cyclins D1 (*CCND1*) and E1 (*CCNE1*) occur in 20% and 4% of HGSOc cases, respectively<sup>66</sup>. Direct functional loss of RB1 occurs in 10% of patients as a result of mutations or deletions in *RB1*<sup>66</sup>. Aberrations in the CDK/cyclin-RB-E2F axis can therefore promote proliferation or quiescence by directly modulating the activity of pathway members or by deregulating the expression of downstream transcriptional targets or crosstalk with other effectors such as p53 and PI3K/AKT<sup>237,276</sup>.

Loss of cell cycle control may also occur through dysregulation of Survivin, p53, Myc, cul-1, or cdc20<sup>277</sup>. Survivin displays biphasic activity depending on metastasis or invasion and participates in cell cycle control and autophagy<sup>278-281</sup>. It is regulated by many upstream pathways including CDK/cyclin-RB-E2F, JAK/STAT, PI3K/AKT/mTOR, p53,

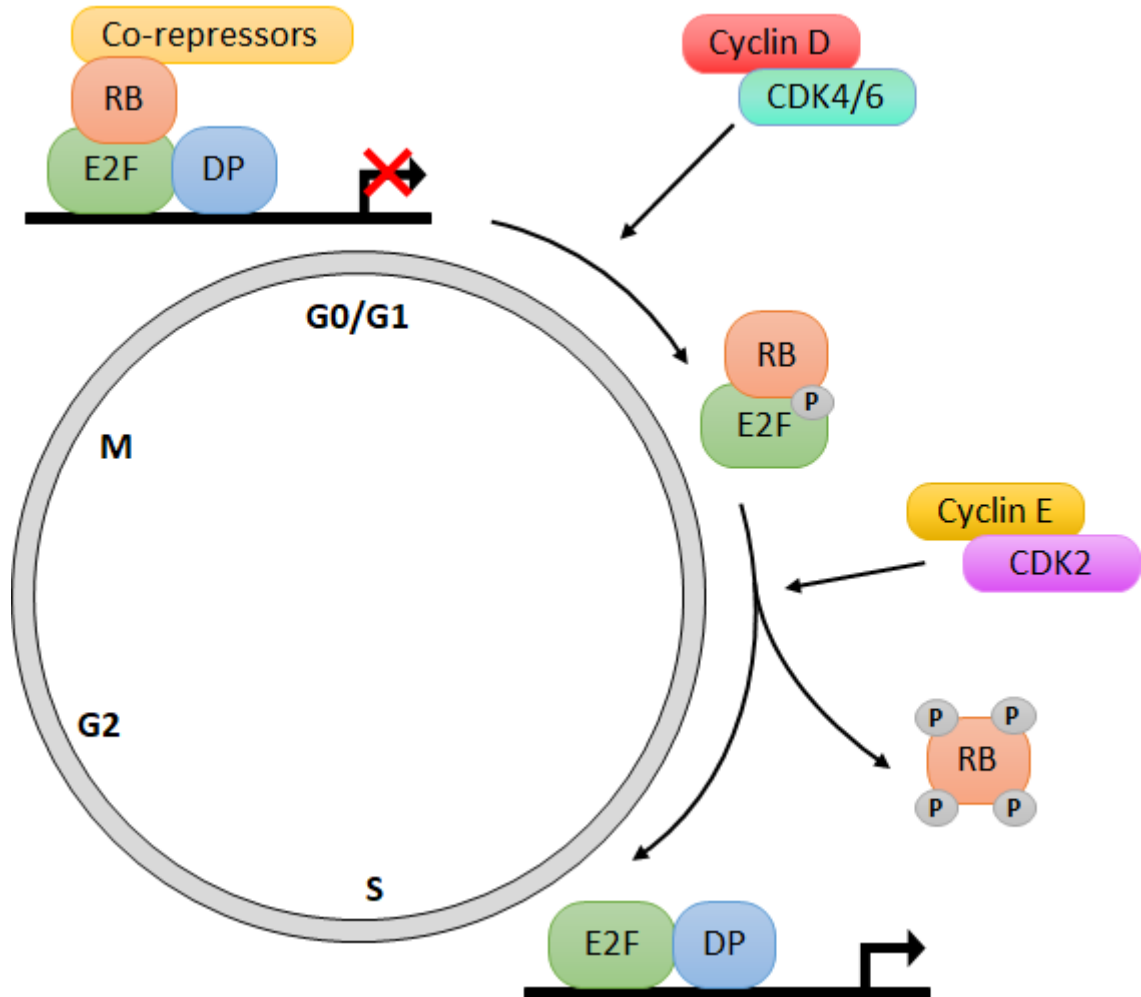


**Figure 1.7. Cell cycle control by the CDK/cyclin-RB-E2F axis.** The established model of cell cycle control by the retinoblastoma protein (RB). RB binds to heterodimeric E2F-DP transcription factors to repress their transcriptional activity during G0/G1 by recruiting co-repressors that can remodel chromatin such as histone deacetylases (HDACs) or histone lysine demethylases (KDMs). Upon mitogenic stimulation, cyclin-dependent kinase (CDK) complexes phosphorylate and inactivate RB during S phase. This releases E2F-DP heterodimers, allowing for the progression of transcriptional programs required for DNA replication.

TGF- $\beta$ , and Wnt. One study showed the introduction of mutant p53 abolished quiescence in wild type HSCs<sup>282</sup>. Myc expression has been shown to be inversely correlated to proliferative activity in CSCs<sup>237,283-285</sup>. Both cul-1 and cdc20 control cell cycle progression by mediating the G1/G0 transition and by controlling proteasome-mediated degradation of cell cycle regulators, respectively<sup>282,286-288</sup>. Impaired chromatin remodeling can also lead to loss of cell cycle control. For example, dysregulated histone lysine demethylase, KDM5B, slowed cell cycle progression in a population of chemoresistant melanoma cells<sup>289</sup>. Additionally, various KDMs were found to be upregulated in cancer cells that survived anti-proliferative therapy<sup>260</sup>. Histone deacetylases (HDACs) can cause G2 arrest when depleted or repress p53 functions when overexpressed as well as contributing to RB-E2F-mediated gene expression<sup>260</sup>.

RB family members also play a role in a recently discovered cell cycle regulatory complex called the mammalian DREAM complex<sup>290,291</sup>. DREAM is a highly conserved multi-subunit complex that was originally identified in *Drosophila* and consists of **DP**, an **RB**-like protein (either p107 or p130, but never RB), an **E2F**, and the **MuvB** (multi-vulval class B) core<sup>292</sup>. DREAM assembly is initiated by dual-specificity tyrosine phosphorylation-regulated kinase (DYRK1A)<sup>290,291</sup>. Osteosarcoma cells deficient for DYRK1A were unable to enter quiescence<sup>290</sup>. DYRK1A has also been shown to maintain quiescence by degrading cyclin D and stabilizing the CKI p27<sup>293,294</sup>. Both DYRK1A and its paralog DYRK1B play a role in initiating and maintaining G0 arrest in breast, colon, melanoma, ovarian, and pancreatic cancer cells<sup>57,295-297</sup>.

#### 1.6.4 Targeting dormancy in cancer

Although the current understanding of dormancy in cancer has increased significantly in the last decade, there is still no consensus on the best approach to target dormancy. Three distinct approaches have been suggested: i) maintain the dormant state of cells to prevent relapse; ii) awaken dormant cells to increase sensitivity to chemotherapy; or iii) target quiescence-promoting pathways to directly eliminate dormant cells<sup>260</sup> (**Figure 1.8**). Each method has advantages and disadvantages. For example, while maintaining the dormant state of cells could prevent metastases and relapse, some dormant cells may continue to slowly progress through the cell cycle so minimal residual disease may require lifelong treatment. Forcing dormant cells to re-enter the cell cycle can increase susceptibility to existing anti-proliferative chemotherapy, but treatment could fail if the cells gain resistance or do not completely respond to chemotherapy. Directly killing dormant cells, especially in combination with first-line therapy, could potentially eliminate all dormant populations, but it may also provide selection for more aggressive phenotypes. Therefore, the most optimal approach is still debated and remains controversial.

Breast cancer studies have provided evidence that maintaining a dormant state by suppressing proliferative signals is sufficient to maintain quiescence and prevent recurrence<sup>298</sup>. Hormone-deprivation therapy in estrogen receptor (ER) positive breast cancer is sufficient to maintain dormancy and improve OS<sup>299,300</sup>. Moreover, treatment with a selective inhibitor of ERK (UO126) successfully blocked proliferative signals and maintained dormancy of disseminated tumour cells<sup>257</sup>. Itraconazole inhibits growth and maintains dormant phenotypes by acting on Hedgehog signaling, the PI3K/AKT/mTOR axis, and Wnt signaling in colorectal cancer and melanoma<sup>301,302</sup>. Three-dimensional cell

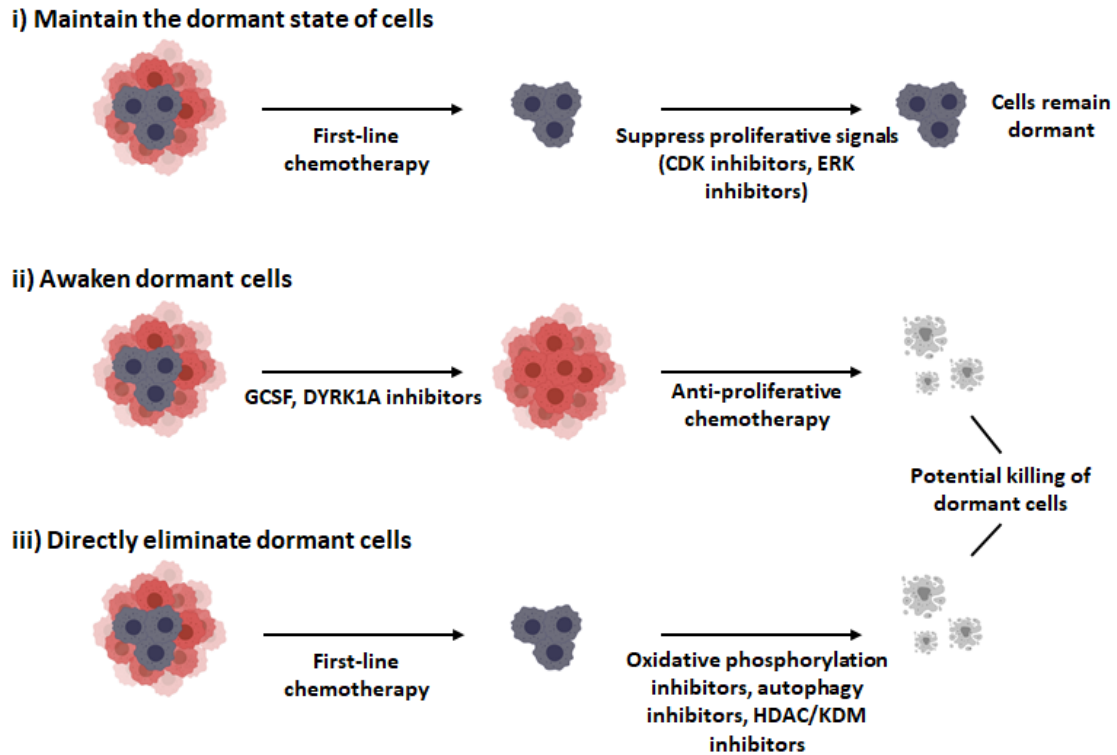


**Figure 1.8. Treating dormancy in cancer.** Dormancy in cancer can be targeted using three methods. **(i)** Maintain the dormant state of cells: Following first-line chemotherapy, dormant cells can be treated with inhibitors that suppress proliferative signals in order to sustain dormancy. These inhibitors may include CDK inhibitors or ERK inhibitors to block growth signals. The goal of this method is to indefinitely maintain dormancy to prevent relapse. However, minimal residual disease may be unavoidable and would require lifelong treatment. Additionally, slow cycling cells could acquire mutations and escape dormancy to cause relapse. **(ii)** Awaken dormant cells: Dormant cells can be treated with specific growth factors, such as granulocyte colony-stimulating factor (GCSF) or DYRK1A inhibitors to force re-entry into the cell cycle. This would allow anti-proliferative chemotherapy agents to target dividing cells and induce cell death. The disadvantage is that cells may acquire mutations and escape chemotherapy and cause relapse. **(iii)** Directly eliminate dormant cells: In this method, first-line chemotherapy is followed by specific treatments that inhibit processes required for quiescence, such as oxidative phosphorylation, autophagy, and chromatin remodeling. This allows for the direct killing of dormant cells without forcing re-entry into the cell cycle.

culture models of breast cancer have also suggested that targeting integrin, MMPs, and epidermal growth factor receptor (EGFR) could keep cells in a dormant state<sup>303-306</sup>. Suppression of mitogen signaling is therefore a potentially beneficial route to treat dormancy.

Alternatively, targeting specific TME factors or enzymes could reverse quiescence and coax cells to re-enter the cell cycle<sup>307,308</sup>. Stimulation of quiescent leukemia cells with granulocyte colony-stimulating factor (GCSF) causes re-entry into the cell cycle and increases sensitivity to chemotherapy<sup>309,310</sup>. Depletion of the E3 ubiquitin ligase Fbxw7 stabilizes Myc, Notch, and cyclin E which forces quiescent leukemia cells to re-enter the cell cycle and become susceptible to imatinib<sup>237</sup>. Similarly, inhibition of DYRK1A can induce cell cycle progression and increase sensitivity to chemotherapy. DYRK1A inhibition with harmine also increases sensitivity to imatinib in gastrointestinal stromal tumours (GIST)<sup>311</sup>. A small molecule inhibitor of DYRK1B was also shown to enhance sensitivity to gemcitabine in quiescent pancreatic cancer cells<sup>296</sup>.

The fear of awakening dormant cells is that it could potentially lead to rapid cell division cycles and unmanageable metastases if it is not immediately followed by effective anti-proliferative chemotherapy<sup>260</sup>. It has therefore been suggested that identifying specific therapeutic vulnerabilities of dormant cells and developing appropriate novel drugs may be more effective and avoid worsening a patient's condition<sup>260</sup>. For example, mitochondrial respiration was required for dormant pancreatic cell survival and they were eliminated with an oxidative phosphorylation inhibitor<sup>312</sup>. Targeting KDMs or HDACs using selective inhibitors has also shown promise in eliminating dormant cancer cells in various cancers<sup>313-315</sup>. Inhibition of autophagy reduced survival of dormant breast cancer cells<sup>316</sup>. A similar

study was also recently conducted in HGSOc spheroids<sup>317</sup>. The heterogeneity of HGSOc affords tumour cells with many mutations that could potentially provide spheroid cells with selective advantages that mediate entry into quiescence and escape from anoikis and chemotherapy. Therefore, identifying such mechanisms that are essential for HGSOc spheroid survival can potentially lead to new drug therapies that can specifically target and eliminate spheroid cells before relapse.

### 1.6.5 Summary of HGSOc dormancy

HGSOc spheroid cells constitute a chemoresistant and dormant niche in patients that can cause relapse and multi-organ metastases in patients. The present understanding of ovarian cancer dormancy is very limited and much of the knowledge comes from CSCs found in other cancer types as well as HSCs. CSCs have striking resemblance to HSCs in that they express stem cell markers, can undergo self-renewal, and enter a reversible state of dormancy – called quiescence – upon loss of mitogen signaling in the TME. Dormancy is an inherent feature of cancer cells that allows them to evade the immune system and chemotherapy and gain new mutations for survival. Quiescence occurs through G0 cell cycle arrest and can be achieved by dysregulation of many pathways, including PI3K/AKT/mTOR, p38 MAPK, CDK/cyclin-RB-E2F and others. Methods to treat dormancy remain controversial and each have advantages and disadvantages that must be evaluated in order to effectively suppress or eliminate dormant cells and prevent relapse, which is a major cause of mortality in HGSOc. HGSOc heterogeneity across patients and ITH may present challenges since a multitude of aberrant pathways could facilitate dormancy in spheroid cells. However, encouraging evidence from other cancer types

suggests that targeting dormancy by awakening them to enhance anti-proliferative drug sensitivity, or directly eliminating quiescent cells by exploiting vulnerabilities can be successful and could potentially improve OS.

## 1.7 The mammalian DREAM complex

### 1.7.1 DREAM and MuvB

The RB family consists of three closely related pocket proteins: RB, p107, and p130<sup>118,271,273,274</sup>. The regulation of E2F transcription factors by RB family members occurs in a cell cycle-dependent manner<sup>118,271,273,274</sup>. At the start of G1, the promoters of E2F responsive genes are largely populated with p130-E2F4 complexes that silences these genes<sup>318</sup>. In mid- to late G1, p107 replaces p130 at the promoters of E2F responsive genes and by late G1, RB-E2F complexes are the most abundant and prevent gene activation by masking the E2F activation domain of E2Fs<sup>118,271,273,274,318</sup>. In G0, p130 is bound to E2F4-containing complexes and it maintains the highest level of expression out of the three pocket proteins, suggesting an important role for p130 during quiescence<sup>318</sup>. Studies have shown that p130-E2F4 are part of the mammalian DREAM complex which is assembled in quiescence<sup>292,318-321</sup>. Many unknowns remain about DREAM but its roles in normal growth and development as well its implications in cancer are becoming apparent.

DREAM assembly is mediated by DYRK1A which phosphorylates LIN52 and provides an interaction surface for p130<sup>290,292,322</sup> (**Figure 1.9A**). This allows p130-E2F4-DP to bind to LIN52 which itself is part of the MuvB core complex consisting of LIN9, LIN37, LIN52, LIN54, and RBBP4<sup>323,324</sup>. DREAM disassembly occurs when CDK2/4



phosphorylate p130 and MuvB proteins<sup>291,323,325,326</sup>. MuvB then dissociates from DREAM and binds to either B-MYB or FOXM1 to form MYB-MuvB (MMB) or FOXM1-MuvB, respectively<sup>318,323,324,327</sup> (**Figure 1.9B**). In the absence of DREAM, MuvB promotes gene expression and cell cycle progression<sup>57,318,328</sup>. Thus, DREAM and MuvB have opposing roles in the cell cycle. Recent studies have revealed that DREAM plays an essential role in differentiation, proliferation, and tumour suppression by acting as a transcriptional repressor<sup>57,323</sup>. Additionally, the transcription factors B-MYB and FOXM1 are overexpressed in many cancers including ovarian cancer<sup>66,329,330</sup>. Hence understanding the function of DREAM and MuvB in cancer progression and dormancy is an important area of research.

DREAM and MuvB are evolutionarily conserved protein complexes that were first identified in *Drosophila* and *C. elegans*<sup>292</sup>. Over the last decade, studies have uncovered the roles of each subunit in DREAM and MuvB. The Ser28 residue of LIN52 is phosphorylated by DYRK1A which allows its LxSxExL motif to interact with the LxCxE binding cleft of either p130 or p107<sup>290,331</sup>. LIN52 is also required for binding B-MYB to form MMB<sup>332</sup>. LIN54 provides the ability to interact with the cell cycle genes homology region (CHR) motif in promoters while E2F4-DP recognize the cell cycle-dependent element (CDE) motifs<sup>328,333,334</sup>. RBBP4 potentially helps to recruit chromatin remodeling factors since it is known to interact with SIN3B and the nucleosome remodeling and deacetylation (NuRD) complex which are HDAC-containing complexes<sup>292</sup>. *In vitro* and *in vivo* studies suggest that LIN9 is structurally important for DREAM and MuvB and interacts directly with LIN52 and RBBP4<sup>331,335-337</sup>. LIN9 also appears to be important for FOXM1-MuvB assembly and has recently been shown to interact with SIN3B<sup>338,339</sup>. LIN37

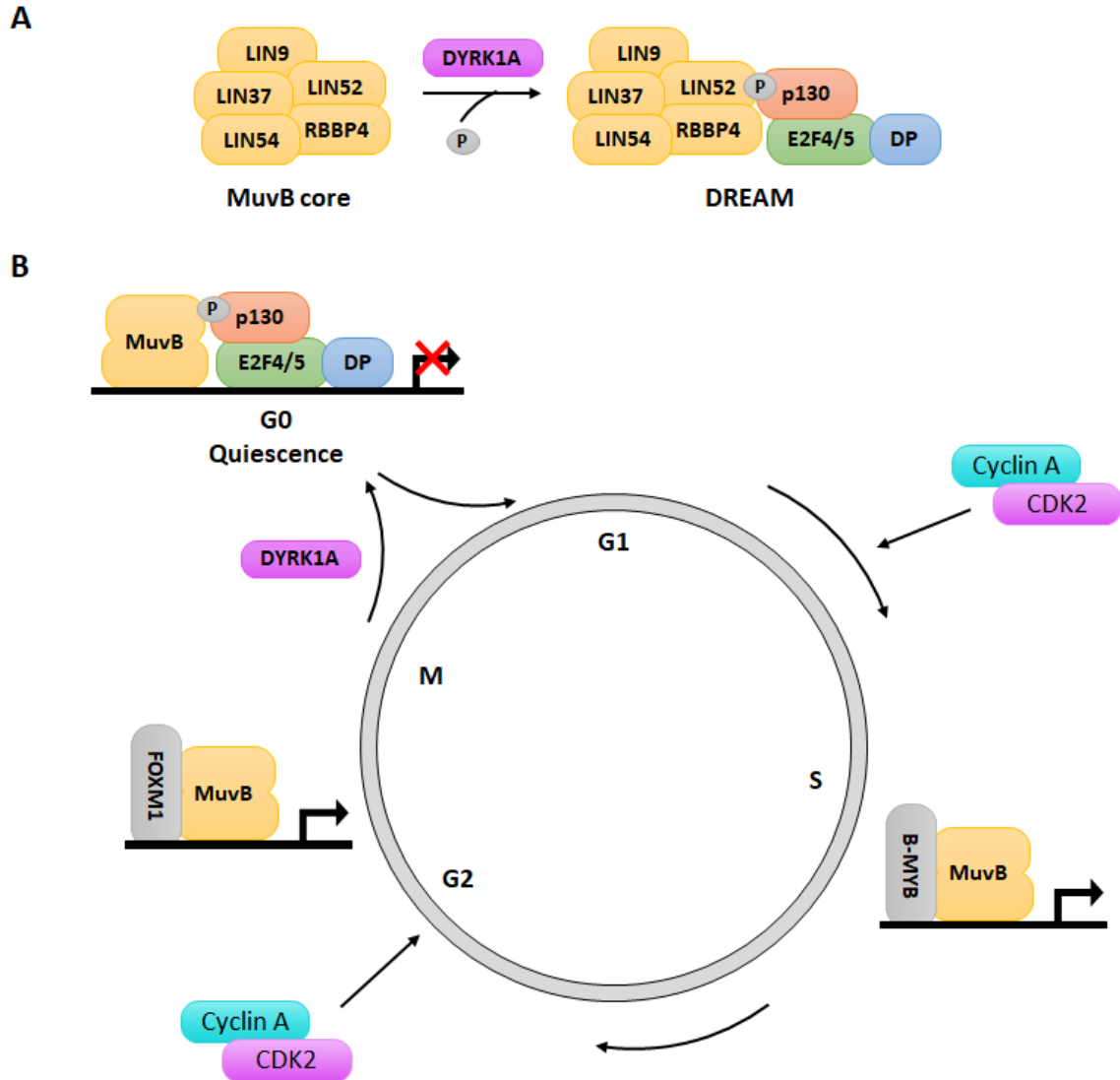


**Figure 1.9. Cell cycle control by DREAM and MuvB.** (A) DREAM consists of: DP; an RB-like (either p107 or p130); E2F4/5; And the MuvB core (which itself is a complex containing LIN9, LIN37, LIN52, LIN54, and RBBP4). DREAM assembly is mediated by dual-specificity-tyrosine-phosphorylation regulated kinase (DYRK1A). The kinase phosphorylates LIN52 at its Ser28 residue which permits binding of the MuvB core to the p107/p130-E2F4/5-DP complex and allows the cell to enter quiescence. (B) DREAM is assembled at G0 to enter and maintain quiescence. When cells re-enter the cell cycle, p130-E2F4/5-DP dissociates from the MuvB core complex. MuvB then binds to the transcription factor B-MYB to form B-MYB-MuvB (MMB). MMB binds to target promoters in S-phase to induce transcriptional activation of cell cycle genes. In G2, MuvB dissociates from B-MYB and instead binds to the transcription factor FOXM1 to form FOXM1-MuvB. Cyclin A/CDK2-mediated phosphorylation of B-MYB and FOXM1 is required for assembly. In this way, FOXM1-MuvB transcriptionally activates late cell cycle gene expression. DREAM and MuvB therefore cooperate to control quiescence and cell cycle progression as a transcriptional repressor and activator, respectively.

appears to be important for transcriptional repression by DREAM but not for MMB-mediated activation<sup>340</sup>. Together, these components assemble to form DREAM in G<sub>0</sub>, MMB in S phase, and FOXM1-MuvB in G<sub>2</sub> to control gene expression in a cell cycle-dependent manner.

### 1.7.2 Cell cycle control by DREAM and MuvB

Many studies have shown that DREAM is required for entering and maintaining quiescence. DREAM binds to several hundred cell cycle genes that are known to achieve their peak expression during G<sub>1</sub>/S or G<sub>2</sub>/M phases of the cell cycle<sup>291,325</sup>. Depletion of components required for DREAM assembly leads to de-repression of these genes. Knockdown of LIN9 increased cell cycle gene expression in quiescent cells and decreased mitotic gene expression in cycling cells suggesting it is important for both DREAM and MuvB function<sup>291,324,341,342</sup>. Similarly, depletion of LIN52 or LIN54 leads to increased expression of cell cycle genes<sup>291,333,342,343</sup>. In contrast, knockout of LIN37 suggests that it is not essential for MuvB activity but required for DREAM-mediated repression and quiescence<sup>292</sup>. Although p130 is the most abundant RB-like protein during quiescence, its depletion increases p107 which can then compensate for p130 deficiency and assemble DREAM<sup>57,318,322</sup>. However, when both p107 and p130 are concurrently depleted, DREAM assembly is impaired and there is a shift towards MMB, gene activation, and cell cycle progression<sup>322</sup>. Experiments from *p107*<sup>-/-</sup>;*p130*<sup>-/-</sup> mice show that mouse embryonic fibroblasts (MEFs) deficient for both RB-like proteins have increased expression of DREAM target genes and exit quiescence earlier than wild type MEFs<sup>344</sup>. Simultaneous mutation of the LxCxE binding cleft of *p107* combined with knockout of *p130* impaired

DREAM assembly in mice<sup>322</sup>. These mice displayed abnormal endochondral bone development and demonstrated that DREAM is required to induce growth arrest in chondrocytes<sup>322</sup>. Mice homozygous for these mutations were found to be neonatal lethal<sup>322</sup>. Similarly, knockout of LIN9, which is important for DREAM and MuvB, also causes lethality in mice<sup>337</sup>. It has been suggested that E2F4 and E2F5 may also compensate for each other in DREAM<sup>318</sup>. Together, these studies demonstrate that disruption of DREAM or MuvB leads to loss of cell cycle control.

DREAM binds to its target genes by recognizing CHR and CDE motifs near the transcription start site (TSS) of promoters<sup>345,346</sup>. These motifs are shared by many cell cycle genes and are often found in close proximity to each other<sup>345</sup>. Binding to CHR and CDE is mediated by LIN54 and E2F-DP, respectively<sup>318</sup>. None of the subunits in DREAM have any enzymatic activity and therefore must rely on other factors to silence gene expression. Initial hypotheses for how DREAM may induce gene repression followed from the well-established interactions of RB-E2F and chromatin modifiers. RB-E2F interacts with HDAC1/2 and the SIN3B/HDAC complex<sup>347,348</sup>. It has been suggested that RBBP4 may also interact with these chromatin modifiers. However, RB interacts with the aforementioned chromatin modifiers through the LxCxE motif which is occupied in DREAM by the p130-LIN52 interaction<sup>292</sup>. The mechanism of gene repression by DREAM is therefore likely to be distinct from RB-E2F mediated repression<sup>292</sup>.

A study in *C. elegans* showed that DREAM represses genes by altering nucleosome positioning<sup>349</sup>. Enrichment of the histone variant H2AZ is routinely observed at promoters and is associated with gene expression<sup>350</sup>. On the other hand, gene body deposition is associated with repression<sup>350</sup>. Loss of DREAM in *C. elegans* did not alter deposition of

H2AZ at promoters but led to reduced H2AZ within gene bodies, suggesting a mechanism for repression. DREAM assembly was correlated with a significant increase of gene body H2AZ at known DREAM target genes<sup>351</sup>. Evidence of this has also come from studies in *Drosophila* where the DREAM ortholog acts as a repressor and activator<sup>292</sup>. Loss of DREAM leads to decreased H2AZ resulting in de-repression of cell cycle genes<sup>351</sup>.

When DREAM assembly is impaired by depletion of required subunits or inhibition of DYRK1A, quiescence cannot be maintained and the cells instead assemble MMB<sup>57</sup>. MMB localizes to promoters of target genes, such as *MYBL2* which encodes B-MYB, using CHR motifs or MYB binding sites<sup>352</sup>. For example, mutation of the MYB binding site on *BIRC5*, which encodes Survivin, reduced LIN9 and B-MYB binding<sup>352</sup>. Transcriptional activation by MMB is dependent on phosphorylation of B-MYB by cyclin A/CDK2<sup>353,354</sup>. Depletion of B-MYB or MuvB core proteins leads to decreased late cell cycle (G2/M) gene expression and mitotic arrest indicating that MMB is required for normal cell cycle progression<sup>318</sup>. Mitotic arrest was observed in mice deficient for LIN9 as well as F9 embryonal carcinoma cells deficient for either LIN9 or B-MYB<sup>341</sup>. Recent studies have demonstrated that B-MYB and MuvB also cooperate with FOXM1 to regulate late cell cycle gene expression<sup>323</sup>. Similar to B-MYB, cyclin A/CDK2 phosphorylation of FOXM1 is required for assembly of FOXM1-MuvB<sup>318</sup>. Loss of FOXM1 also leads to deficiencies in mitosis and reduced levels of cell cycle gene expression. Mutation of the aforementioned MYB binding site on *BIRC5* also ablated FOXM1 recruitment to the promoter<sup>355</sup>. This is consistent with other studies that show MuvB is required for FOXM1 binding at promoters<sup>356,357</sup>. Together, these studies show that DREAM, MuvB, B-MYB, and FOXM1

are interrelated through shared or opposing functions to control quiescence and cell cycle progression.

### 1.7.3 DREAM and MuvB in cancer

B-MYB is frequently mutated or overexpressed in cancer and is used as part of a proliferative signature to predict prognosis as well as a biomarker test for breast cancer<sup>358</sup>. Increased *MYBL2* gene expression is generally associated with poor OS in many different cancer types<sup>359</sup>. Similarly, FOXM1 is overexpressed in many cancer types, including ovarian cancer, and indicates poor OS<sup>360-362</sup>. In these cancers, overexpression of MuvB, B-MYB, or FOXM1 could promote MMB/FOXM1-MuvB activity which can drive proliferation and increase tumorigenesis. Inhibition of these factors in breast cancer cells reduced proliferation<sup>363</sup>. One study showed that loss of B-MYB or LIN9 reduced tumorigenesis in a mouse model of lung cancer<sup>364</sup>. Alternatively, alterations that promote DREAM assembly could potentially promote quiescence and chemoresistance. Depletion of LIN52 or combined depletion of both LIN54 and E2F4 were sufficient to increase sensitivity to chemotherapy in GIST, indicating DREAM contributes to chemoresistance in GIST<sup>365,366</sup>.

The presence of MuvB in DREAM and MMB/FOXM1-MuvB complexes presents a challenge for targeting DREAM in cancer. Inhibiting individual MuvB core subunits would impair DREAM assembly but also affect transcriptional activation as previously discussed<sup>318</sup>. An attractive target to disrupt DREAM assembly, and specifically quiescence, is DYRK1A. Studies across many cancer cells have shown that DREAM-mediated quiescence can be inhibited by inactivation of DYRK1A or its paralog DYRK1B.

Treatment of non-small-cell lung cancer (NSCLC) cells with harmine, a potent DYRK1A inhibitor<sup>367</sup>, increased sensitivity to osimertinib<sup>368</sup>. Harmine inhibition also increased sensitivity to Bcl-2 inhibitors in primary NSCLC cells<sup>369</sup>. Treatment with harmine reversed quiescence and enhanced imatinib sensitivity in GIST, consistent with combined LIN54/E2F4 depletion studies<sup>370</sup>. Inhibition of DYRK1A in pancreatic ductal adenocarcinoma suppressed tumour progression by inhibiting proliferation<sup>371</sup>. Together, these cell culture and mouse model studies provide overwhelming evidence that inhibiting DREAM assembly can force cell cycle re-entry and increase susceptibility to chemotherapy.

#### 1.7.4 DREAM in HGSOC

We previously identified components of DREAM as essential for the survival of HGSOC spheroids cultured from a panel of EOC cell lines<sup>57</sup>. Specifically, depletion of MuvB core subunits, RB-like proteins, or DYRK1A decreased survival of spheroid cells but not asynchronously growing cells<sup>57</sup>. Additionally, HGSOC spheroids cultured from a patient-derived cell line (iOvCa147) upregulate the G0 markers p130 and p27<sup>57,372-374</sup>. Upon shRNA-mediated depletion of DYRK1A in iOvCa147 cells, DREAM fails to assemble in spheroids<sup>57</sup>. Instead, the MuvB complex co-immunoprecipitates with B-MYB, indicating that DREAM assembly is impaired. Consistent with reduced DREAM assembly, DREAM target genes such as *CDK1*, *CCNA2*, and *MYBL2* were de-repressed<sup>57</sup>. This de-repression was detected at 6 hours after spheroid formation in DYRK1A or p130 depleted spheroid cells<sup>57</sup>. Tritiated-thymidine assays revealed that DYRK1A depleted spheroid cells failed to achieve quiescence and continued to synthesize new DNA at 6- and 12 hours

following spheroid formation<sup>57</sup>. Neither de-repression of DREAM target genes or increased DNA synthesis were detectable after 24 hours, likely as a result of increased apoptosis and loss of spheroid cell viability due to anoikis<sup>57</sup>. DYRK1A depleted spheroid cells exhibited increased S-phase from 6 hours through to 12 hours, indicating that without DREAM, these spheroid cells fail to arrest and continue to replicate DNA<sup>57</sup>. Compared to control spheroid cells, there was a dramatic increase in cell death in DYRK1A depleted spheroid cells at 24 hours<sup>57</sup>.

Pharmacological inhibition of DYRK1A across a panel of ovarian cancer cell lines (iOvCa147, HEYA8, OVCAR8, iOVCA185) recapitulated these findings<sup>57</sup>. Inhibition of DYRK1A with harmine or INDY (a potent DYRK1A/B inhibitor<sup>375</sup>) decreased spheroid cell viability in suspension<sup>57</sup>. Harmine or INDY treatment disrupted p130 binding to MuvB. INDY also significantly enhanced sensitivity of spheroid cells to carboplatin<sup>57</sup>. Together, this data demonstrated that DREAM is an important factor for mediating quiescence in HGSOc spheroid cells. Without DREAM, spheroid cells fail to enter quiescence and continue to cycle and ultimately become susceptible to anoikis.

### 1.7.5 Pharmacological inhibition of DYRK1A

DREAM inhibition using pharmacological inhibitors of DYRK1A provide a translational approach to targeting DREAM and quiescence in cancer. Indeed, several studies have shown inhibitors such as harmine and INDY can disrupt DREAM assembly and enhance sensitivity to chemotherapy in various cancer types<sup>367,369-371</sup>. Unfortunately, the inhibitors used in these studies either have not been evaluated for clinical use or have toxic side effects<sup>376</sup>. For example, INDY has not undergone preclinical testing and harmine



is also a monoamine oxidase A inhibitor which can lead to adverse effects<sup>376,377</sup>. Recently, CX-4945 was described to have efficacy to inhibit DYRK1A<sup>375</sup>. CX-4945 is a previously described casein kinase 2 (CK2) inhibitor<sup>378</sup>. CX-4945 has higher potency than both INDY and harmine<sup>375</sup>. Clinical trials are currently underway to determine the safety and efficacy of CX-4945 in treating recurrent medulloblastoma (NCT03904862), advanced or metastatic basal cell carcinoma (NCT03897036), and relapsed multiple myeloma (NCT01199718).

Inhibition of DYRK1A as a therapy may be challenging due to DYRK1A's involvement in multiple pathways. DYRK1A has been characterized in neurogenesis and its genetic locus is within the Down Syndrome critical region (DSCR)<sup>379,380</sup>. As such, DYRK1A overexpression has been associated with Down Syndrome, Alzheimer's disease, and Parkinson's disease<sup>379</sup>. In some tumors, inhibition of DYRK1A alone may not be sufficient to inhibit DREAM. DYRK1B is overexpressed in some tumors and may be the predominant kinase that assembles DREAM<sup>290,381</sup>. We previously demonstrated this in HGSOC spheroids as a subset of cell lines had reduced viability in suspension following DYRK1B depletion<sup>57</sup>. *DYRK1B* amplification is also present in 10% of ovarian cancer cases<sup>66,323</sup>. Therefore, it may be beneficial to simultaneously inhibit both DYRK1A and DYRK1B. Pharmacological inhibition of DYRK1A/B has been demonstrated to reverse quiescence and increase sensitivity to chemotherapy and the identification of a clinically safe inhibitor may prove to be a valuable tool in targeting quiescence and dormancy in HGSOC and other cancers<sup>57,382</sup>.

### 1.7.6 Summary of the DREAM complex

DREAM and MuvB are evolutionarily conserved multisubunit complexes that cooperate to regulate the cell cycle and permit entry into quiescence<sup>291,292,318,356</sup>. Studies have shown that DREAM is required for normal growth arrest in cells and MuvB, together with binding partners B-MYB and FOXM1, are required for late cell cycle gene expression and mitosis<sup>318,323</sup>. DREAM's repressive activity is mediated by H2AZ deposition within the gene bodies of target genes<sup>351</sup>. In the absence of DREAM, B-MYB and FOXM1 cooperate with MuvB to form MMB and FOXM1-MuvB, respectively, which act as transcriptional activators<sup>318</sup>. Importantly, DREAM is assembled in quiescent HGSOC spheroid cells and is essential for their survival<sup>57</sup>. Impairment of DREAM activity, either through depletion of required components or pharmacological inhibition of the assembly factor DYRK1A, is sufficient to block assembly and force spheroid cells to re-enter the cell cycle. These spheroid cells are then susceptible to anoikis due to cycling in anchorage-independent conditions and also have increased sensitivity to chemotherapy such as carboplatin<sup>57</sup>. Inhibition of DREAM through DYRK1A therefore has potential therapeutic value to directly target and eliminate the chemoresistant niche of HGSOC spheroid cells.

## 1.8 Summary of HGSOC

HGSOC is very deadly disease if not identified early in patients<sup>5</sup>. Unfortunately, in many women it is not diagnosed until late-stage, primarily because it is asymptomatic during early stages and shares the symptoms of less severe ailments. Presently, there is no reliable screening test available for HGSOC which means many patients will continue to be diagnosed at late-stage<sup>6</sup>. Therefore, there is an urgent need to develop new therapies to

treat this disease. Current treatment options include cytoreductive surgery followed by adjuvant or neoadjuvant chemotherapy. However, a characteristic of late-stage HGSOC is the presence of multicellular aggregates, called spheroids, which complicates treatment and surgical resection. Spheroids contribute to widespread dissemination of tumour cells, amounting to many secondary lesions throughout the peritoneal cavity, making surgical resection very difficult. Additionally, spheroid cells are dormant, enabling them to survive anti-proliferative chemotherapy and act as a chemoresistant niche that can reseed disease<sup>57</sup>. Indeed, relapse is a major cause for concern in HGSOC; while over 70% of patients respond well to chemotherapy, over 80% will unfortunately experience relapse<sup>5</sup>. Recurrent HGSOC is generally considered to be incurable<sup>5</sup>.

HGSOC is characterized by a high degree of heterogeneity and genomic instability with multiple perturbed genes and pathways, some of which include *TP53*, *BRCA1/2*, CDK/cyclin-RB-E2F, PI3K/AKT/mTOR, and Notch signaling<sup>66</sup>. Additionally, intratumoural spatial and temporal heterogeneity has been observed in treatment-naïve HGSOC patients, highlighting how quickly tumour cells can gain selectively advantageous mutations<sup>152</sup>. Hence HGSOC spheroid cells may potentially acquire many abrogated pathways that allow proliferation, differentiation, metastases, and dormancy. The multitude of mutated pathways and genomic instability may potentially mean that a “one-size fits all” therapeutic approach may not broadly apply to all patients. However, some studies have shown that the mutational burden of HGSOC tumour cells can be exploited to create synthetic vulnerabilities<sup>13</sup>. For example, functional DNA repair pathways are important for a subset of HGSOC tumours<sup>13</sup>. Spheroid cells that subvert the cell cycle by assembling DREAM can be targeted using DYRK1A inhibitors to force cell cycle re-entry

and cell death due to anoikis or enhanced chemosensitivity<sup>57</sup>. As demonstrated by previous studies, identifying novel vulnerabilities in spheroid cells that exploit these and other essential processes in HGSOc cells can be aided by novel computational and experimental approaches<sup>144</sup>. There is an urgent need for novel therapies that can effectively prevent or reduce relapse in advanced-stage HGSOc patients. The discovery and characterization of spheroid-specific vulnerabilities is therefore a critical area of research.

## 1.9 Scope of thesis

Dormancy and quiescence mediate resistance to anti-proliferative chemotherapy in HGSOc patients<sup>5,56</sup>. Spheroid populations are responsible for peritoneal dissemination of tumours and relapse following first-line therapy<sup>15</sup>. We have previously shown that DREAM is upregulated in spheroid cells and contributes to quiescence and chemoresistance<sup>57</sup>. Depletion of DYRK1A or its pharmacological inhibition impaired DREAM assembly and enhanced spheroid cell sensitivity to carboplatin<sup>57</sup>. This presents an appealing therapeutic option for HGSOc. However, DREAM assembly is required for normal growth arrest and we have previously shown that it is essential for early development in mice<sup>322</sup>. Loss of DREAM assembly factors leads to abnormal bone development and eventual lethality<sup>322</sup>. The role of mammalian DREAM in adults remains unexplored and requires investigation as it is a likely target for cancer therapy.

To elucidate the role of DREAM in adults, we developed a mouse model to conditionally disrupt DREAM assembly in adult mice (Chapter 2). We did not observe proliferative defects or neoplasms as a result of DREAM loss. However, after a prolonged latency, DREAM deficient mice develop systemic amyloidosis. Amyloid fibrils were

found in the liver, kidney, spleen, and heart tissues of these mice. Kidney tissues were the most affected and this was accompanied by proteinuria and increased creatinine, signifying kidney failure. Compared to mice with intact DREAM, DREAM deficient mice had reduced survival. Amyloid subtyping of affected mouse tissues revealed that the major amyloid-causing constituent of the amyloid deposits was apolipoprotein A-IV (apoA-IV). Interestingly, both apoA-IV protein and *Apoa4* gene expression levels were increased in DREAM deficient mice. Finally, we show that in mice with intact DREAM, DREAM localizes to CDE/CHR motifs found in the *Apoa4* promoter leading to increased gene body deposition of H2AZ. In DREAM deficient mice, this is abrogated and instead MMB binds to the promoter to induce gene expression. Together, this shows that DREAM loss in adults can lead to amyloidosis as a result of increase apolipoprotein expression.

DREAM and DYRK1A cooperate to enable quiescence in spheroid cells, but the present understanding of dormancy and quiescence in the context of ovarian cancer is lacking compared to other cancer types. Our goal was to therefore broadly identify genes and pathways that may provide spheroid cells with selective advantages to enable survival in suspension. Identification of such genes and their involved pathways could potentially allow for the development of novel therapeutic strategies to specifically target chemoresistant spheroids in HGSOV. To enable high-throughput discovery of genes and pathways, we developed a bioinformatics tool called BEAVR (A **B**rowser-based tool for the **E**xploration **A**nd **V**isualization of **R**Naseq data) (Chapter 3)<sup>383</sup>. BEAVR provides an easy-to-use interface for the analysis and visualization of RNA-sequencing (RNA-seq) datasets and generates publication-quality figures.

We also employed a loss-of-function genome-wide CRISPR screen to enable high-throughput discovery of genes and pathways that are specifically essential for spheroid cell survival. Standard genome-wide CRISPR screening methodology – both experimental and computational – failed to identify essential genes in our model system. This was attributed to the complexity of a three-dimensional *in vitro* spheroid model and the spontaneous cell death that can occur in spheroid cells under the stress of suspension culture conditions. This can lead to loss of single guide RNAs (sgRNAs) which can be incorrectly attributed to bona fide loss-of-function due to gene editing. To overcome this, we developed GO-CRISPR (**G**uide-**O**nly control **C**RISPR), a scalable loss-of-function screening method that can be used to discover essential genes in standard monolayer (two-dimensional) or complex three-dimensional culture conditions such as dormant HGSOc spheroids. We also developed TRACS (**T**oolset for the **R**anked **A**nalysis of **G**O-**C**RISPR **S**creens) to automate the analysis of GO-CRISPR screens in an easy-to-use graphical software package (Chapter 4)<sup>384</sup>.

Together with the use of BEAVR, GO-CRISPR, and TRACS, we identified a novel, previously uncharacterized pathway in the context of HGSOc that mediates survival of spheroid cells (Chapter 5). Specifically, using BEAVR, we identified genes and their respective pathways that are differentially expressed in spheroid cells and also dysregulated in *DYRK1A*<sup>-/-</sup> spheroid cells. We performed GO-CRISPR in a panel of three HGSOc cell lines (iOvCa147, TOV1946, OVCAR8). Analysis with TRACS showed that the netrin signaling pathway was mutually essential across all three cell lines. Importantly, this pathway was also identified in our transcriptional analyses by BEAVR. Netrin is well-characterized in axon development but has recently been implicated in cancer. Strikingly,

knockout of netrin receptors across a wider panel of HGSOC cell lines reduced survival in spheroid cells. Together, this work highlights the netrin signaling pathway as a new therapeutic target to specifically eliminate spheroid cells in HGSOC.

## 1.10 References

- 1 Wambecke, A. *et al.* The influence of long non-coding RNAs on the response to chemotherapy in ovarian cancer. *Gynecol Oncol* **156**, 726-733, doi:10.1016/j.ygyno.2019.12.020 (2020).
- 2 Brenner, D. R. *et al.* Projected estimates of cancer in Canada in 2020. *CMAJ* **192**, E199-E205, doi:10.1503/cmaj.191292 (2020).
- 3 Torre, L. A. *et al.* Ovarian cancer statistics, 2018. *CA: a cancer journal for clinicians* **68**, 284-296, doi:10.3322/caac.21456 (2018).
- 4 Brucks, J. A. Ovarian cancer. The most lethal gynecologic malignancy. *Nurs Clin North Am* **27**, 835-845 (1992).
- 5 Matulonis, U. A. *et al.* Ovarian cancer. *Nature Reviews Disease Primers* **2**, 16061, doi:10.1038/nrdp.2016.61 (2016).
- 6 Lisio, M. A., Fu, L., Goyeneche, A., Gao, Z. H. & Telleria, C. High-Grade Serous Ovarian Cancer: Basic Sciences, Clinical and Therapeutic Standpoints. *Int J Mol Sci* **20**, doi:10.3390/ijms20040952 (2019).
- 7 Kindelberger, D. W. *et al.* Intraepithelial carcinoma of the fimbria and pelvic serous carcinoma: Evidence for a causal relationship. *Am J Surg Pathol* **31**, 161-169, doi:10.1097/01.pas.0000213335.40358.47 (2007).
- 8 Pentheroudakis, G. & Pavlidis, N. Serous papillary peritoneal carcinoma: unknown primary tumour, ovarian cancer counterpart or a distinct entity? A systematic review. *Crit Rev Oncol Hematol* **75**, 27-42, doi:10.1016/j.critrevonc.2009.10.003 (2010).
- 9 Berns, E. M. & Bowtell, D. D. The changing view of high-grade serous ovarian cancer. *Cancer Res* **72**, 2701-2704, doi:10.1158/0008-5472.Can-11-3911 (2012).
- 10 Kurman R.J., C. M. L., Herrington C.S., Young R.H. *WHO Classification of Tumours of Female Reproductive Organs*. 4th ed. edn, (WHO, 2014).
- 11 Shih Ie, M. & Kurman, R. J. Ovarian tumorigenesis: a proposed model based on morphological and molecular genetic analysis. *Am J Pathol* **164**, 1511-1518, doi:10.1016/s0002-9440(10)63708-x (2004).
- 12 Kurman, R. J. & Shih Ie, M. The Dualistic Model of Ovarian Carcinogenesis: Revisited, Revised, and Expanded. *Am J Pathol* **186**, 733-747, doi:10.1016/j.ajpath.2015.11.011 (2016).
- 13 Kroeger, P. T., Jr. & Drapkin, R. Pathogenesis and heterogeneity of ovarian cancer. *Curr Opin Obstet Gynecol* **29**, 26-34, doi:10.1097/GCO.0000000000000340 (2017).
- 14 Ramalingam, P. Morphologic, Immunophenotypic, and Molecular Features of Epithelial Ovarian Cancer. *Oncology (Williston Park)* **30**, 166-176 (2016).
- 15 Lengyel, E. Ovarian cancer development and metastasis. *Am J Pathol* **177**, 1053-1064, doi:10.2353/ajpath.2010.100105 (2010).
- 16 Ahmed, N., Abubaker, K., Findlay, J. & Quinn, M. Cancerous ovarian stem cells: obscure targets for therapy but relevant to chemoresistance. *J Cell Biochem* **114**, 21-34, doi:10.1002/jcb.24317 (2013).
- 17 Zhang, S. *et al.* Both fallopian tube and ovarian surface epithelium are cells-of-origin for high-grade serous ovarian carcinoma. *Nature Communications* **10**, 5367, doi:10.1038/s41467-019-13116-2 (2019).



- 18 Auersperg, N., Wong, A. S. T., Choi, K.-C., Kang, S. K. & Leung, P. C. K. Ovarian Surface Epithelium: Biology, Endocrinology, and Pathology. *Endocrine Reviews* **22**, 255-288, doi:10.1210/edrv.22.2.0422 (2001).
- 19 Klotz, D. M. & Wimberger, P. Cells of origin of ovarian cancer: ovarian surface epithelium or fallopian tube? *Arch Gynecol Obstet* **296**, 1055-1062, doi:10.1007/s00404-017-4529-z (2017).
- 20 Fathalla, M. F. Incessant ovulation--a factor in ovarian neoplasia? *Lancet* **2**, 163, doi:10.1016/s0140-6736(71)92335-x (1971).
- 21 Kuhn, E., Kurman, R. J. & Shih, I. M. Ovarian Cancer Is an Imported Disease: Fact or Fiction? *Curr Obstet Gynecol Rep* **1**, 1-9, doi:10.1007/s13669-011-0004-1 (2012).
- 22 Dubeau, L. The cell of origin of ovarian epithelial tumors and the ovarian surface epithelium dogma: does the emperor have no clothes? *Gynecol Oncol* **72**, 437-442, doi:10.1006/gyno.1998.5275 (1999).
- 23 Piek, J. M. *et al.* Dysplastic changes in prophylactically removed Fallopian tubes of women predisposed to developing ovarian cancer. *J Pathol* **195**, 451-456, doi:10.1002/path.1000 (2001).
- 24 Medeiros, F. *et al.* The tubal fimbria is a preferred site for early adenocarcinoma in women with familial ovarian cancer syndrome. *Am J Surg Pathol* **30**, 230-236, doi:10.1097/01.pas.0000180854.28831.77 (2006).
- 25 Bachert, S. E., McDowell, A., Jr., Piecoro, D. & Baldwin Branch, L. Serous Tubal Intraepithelial Carcinoma: A Concise Review for the Practicing Pathologist and Clinician. *Diagnostics (Basel)* **10**, 102, doi:10.3390/diagnostics10020102 (2020).
- 26 Weinberger, V., Bednarikova, M., Cibula, D. & Zikan, M. Serous tubal intraepithelial carcinoma (STIC) - clinical impact and management. *Expert Rev Anticancer Ther* **16**, 1311-1321, doi:10.1080/14737140.2016.1247699 (2016).
- 27 Vaughan, M. H., Modesitt, S. C., Mo, Y. & Trowbridge, E. R. Serous tubal intraepithelial carcinoma: an incidental finding at the time of prophylactic bilateral salpingo-oophorectomy. *Case Rep Obstet Gynecol* **2015**, 760429, doi:10.1155/2015/760429 (2015).
- 28 Ahmed, N. & Stenvers, K. L. Getting to know ovarian cancer ascites: opportunities for targeted therapy-based translational research. *Front Oncol* **3**, 256, doi:10.3389/fonc.2013.00256 (2013).
- 29 Kuhn, E. *et al.* TP53 mutations in serous tubal intraepithelial carcinoma and concurrent pelvic high-grade serous carcinoma--evidence supporting the clonal relationship of the two lesions. *J Pathol* **226**, 421-426, doi:10.1002/path.3023 (2012).
- 30 Kuhn, E. *et al.* CCNE1 amplification and centrosome number abnormality in serous tubal intraepithelial carcinoma: further evidence supporting its role as a precursor of ovarian high-grade serous carcinoma. *Modern Pathology* **29**, 1254-1261, doi:10.1038/modpathol.2016.101 (2016).
- 31 Testa, U., Petrucci, E., Pasquini, L., Castelli, G. & Pelosi, E. Ovarian Cancers: Genetic Abnormalities, Tumor Heterogeneity and Progression, Clonal Evolution and Cancer Stem Cells. *Medicines (Basel)* **5**, 16, doi:10.3390/medicines5010016 (2018).

- 32 Lee, Y. *et al.* A candidate precursor to serous carcinoma that originates in the distal fallopian tube. *J Pathol* **211**, 26-35, doi:10.1002/path.2091 (2007).
- 33 Marquez, R. T. *et al.* Patterns of Gene Expression in Different Histotypes of Epithelial Ovarian Cancer Correlate with Those in Normal Fallopian Tube, Endometrium, and Colon. *Clinical Cancer Research* **11**, 6116, doi:10.1158/1078-0432.CCR-04-2509 (2005).
- 34 Bowtell, D. D. *et al.* Rethinking ovarian cancer II: reducing mortality from high-grade serous ovarian cancer. *Nat Rev Cancer* **15**, 668-679, doi:10.1038/nrc4019 (2015).
- 35 Karnezis, A. N., Cho, K. R., Gilks, C. B., Pearce, C. L. & Huntsman, D. G. The disparate origins of ovarian cancers: pathogenesis and prevention strategies. *Nat Rev Cancer* **17**, 65-74, doi:10.1038/nrc.2016.113 (2017).
- 36 Kurman, R. J. & Shih Ie, M. The origin and pathogenesis of epithelial ovarian cancer: a proposed unifying theory. *Am J Surg Pathol* **34**, 433-443, doi:10.1097/PAS.0b013e3181cf3d79 (2010).
- 37 Kim, J. *et al.* Cell Origins of High-Grade Serous Ovarian Cancer. *Cancers* **10**, 433, doi:10.3390/cancers10110433 (2018).
- 38 Zhai, Y. *et al.* High-grade serous carcinomas arise in the mouse oviduct via defects linked to the human disease. *J Pathol* **243**, 16-25, doi:10.1002/path.4927 (2017).
- 39 Perets, R. *et al.* Transformation of the fallopian tube secretory epithelium leads to high-grade serous ovarian cancer in Brca;Tp53;Pten models. *Cancer Cell* **24**, 751-765, doi:10.1016/j.ccr.2013.10.013 (2013).
- 40 Piek, J. M. *et al.* BRCA1/2-related ovarian cancers are of tubal origin: a hypothesis. *Gynecol Oncol* **90**, 491, doi:10.1016/s0090-8258(03)00365-2 (2003).
- 41 Sherman, M. E. *et al.* Rationale for Developing a Specimen Bank to Study the Pathogenesis of High-Grade Serous Carcinoma: A Review of the Evidence. *Cancer Prev Res (Phila)* **9**, 713-720, doi:10.1158/1940-6207.Capr-15-0384 (2016).
- 42 Prat, J. Staging classification for cancer of the ovary, fallopian tube, and peritoneum. *Int J Gynaecol Obstet* **124**, 1-5, doi:10.1016/j.ijgo.2013.10.001 (2014).
- 43 Javadi, S., Ganeshan, D. M., Qayyum, A., Iyer, R. B. & Bhosale, P. Ovarian Cancer, the Revised FIGO Staging System, and the Role of Imaging. *AJR Am J Roentgenol* **206**, 1351-1360, doi:10.2214/ajr.15.15199 (2016).
- 44 Baek, S. J. *et al.* Stage IIIC epithelial ovarian cancer classified solely by lymph node metastasis has a more favorable prognosis than other types of stage IIIC epithelial ovarian cancer. *J Gynecol Oncol* **19**, 223-228, doi:10.3802/jgo.2008.19.4.223 (2008).
- 45 Gilbert, L. *et al.* Assessment of symptomatic women for early diagnosis of ovarian cancer: results from the prospective DOvE pilot project. *Lancet Oncol* **13**, 285-291, doi:10.1016/s1470-2045(11)70333-3 (2012).
- 46 Worzfeld, T. *et al.* The Unique Molecular and Cellular Microenvironment of Ovarian Cancer. *Frontiers in oncology* **7**, 24-24, doi:10.3389/fonc.2017.00024 (2017).
- 47 Lengyel, E. Ovarian cancer development and metastasis. *The American journal of pathology* **177**, 1053-1064, doi:10.2353/ajpath.2010.100105 (2010).

- 48 Abramson, D. H., Ellsworth, R. M. & Zimmerman, L. E. Nonocular cancer in retinoblastoma survivors. *Trans Sect Ophthalmol Am Acad Ophthalmol Otolaryngol* **81**, 454-457 (1976).
- 49 Dillekås, H., Rogers, M. S. & Straume, O. Are 90% of deaths from cancer caused by metastases? *Cancer medicine* **8**, 5574-5576, doi:10.1002/cam4.2474 (2019).
- 50 Kim, O. *et al.* In vivo modeling of metastatic human high-grade serous ovarian cancer in mice. *PLOS Genetics* **16**, e1008808, doi:10.1371/journal.pgen.1008808 (2020).
- 51 Bast, R. C., Jr., Hennessy, B. & Mills, G. B. The biology of ovarian cancer: new opportunities for translation. *Nat Rev Cancer* **9**, 415-428, doi:10.1038/nrc2644 (2009).
- 52 Tan, D. S., Agarwal, R. & Kaye, S. B. Mechanisms of transcoelomic metastasis in ovarian cancer. *Lancet Oncol* **7**, 925-934, doi:10.1016/s1470-2045(06)70939-1 (2006).
- 53 Kenny, H. A. *et al.* Mesothelial cells promote early ovarian cancer metastasis through fibronectin secretion. *The Journal of clinical investigation* **124**, 4614-4628, doi:10.1172/JCI74778 (2014).
- 54 Loret, N., Denys, H., Tummers, P. & Berx, G. The Role of Epithelial-to-Mesenchymal Plasticity in Ovarian Cancer Progression and Therapy Resistance. *Cancers* **11**, 838, doi:10.3390/cancers11060838 (2019).
- 55 Patel, I. S., Madan, P., Getsios, S., Bertrand, M. A. & MacCalman, C. D. Cadherin switching in ovarian cancer progression. *Int J Cancer* **106**, 172-177, doi:10.1002/ijc.11086 (2003).
- 56 Yang, Y. n. *et al.* Reversing platinum resistance in ovarian cancer multicellular spheroids by targeting Bcl-2. *Onco Targets Ther* **12**, 897-906, doi:10.2147/OTT.S187015 (2019).
- 57 MacDonald, J. *et al.* A Systematic Analysis of Negative Growth Control Implicates the DREAM Complex in Cancer Cell Dormancy. *Mol Cancer Res* **15**, 371-381, doi:10.1158/1541-7786.MCR-16-0323-T (2017).
- 58 Klymenko, Y., Kim, O. & Stack, M. S. Complex Determinants of Epithelial: Mesenchymal Phenotypic Plasticity in Ovarian Cancer. *Cancers* **9**, 104, doi:10.3390/cancers9080104 (2017).
- 59 Byrne, A. T. *et al.* Vascular endothelial growth factor-trap decreases tumor burden, inhibits ascites, and causes dramatic vascular remodeling in an ovarian cancer model. *Clin Cancer Res* **9**, 5721-5728 (2003).
- 60 Ahmed, N. & Stenvers, K. L. Getting to know ovarian cancer ascites: opportunities for targeted therapy-based translational research. *Frontiers in oncology* **3**, 256-256, doi:10.3389/fonc.2013.00256 (2013).
- 61 Zegeye, M. M. *et al.* Activation of the JAK/STAT3 and PI3K/AKT pathways are crucial for IL-6 trans-signaling-mediated pro-inflammatory response in human vascular endothelial cells. *Cell Communication and Signaling* **16**, 55, doi:10.1186/s12964-018-0268-4 (2018).
- 62 Iwanicki, M. P. *et al.* Ovarian cancer spheroids use myosin-generated force to clear the mesothelium. *Cancer Discov* **1**, 144-157, doi:10.1158/2159-8274.CD-11-0010 (2011).

- 63 Davidowitz, R. A. *et al.* Mesenchymal gene program-expressing ovarian cancer spheroids exhibit enhanced mesothelial clearance. *J Clin Invest* **124**, 2611-2625, doi:10.1172/jci69815 (2014).
- 64 Correa, R. J., Peart, T., Valdes, Y. R., DiMattia, G. E. & Shepherd, T. G. Modulation of AKT activity is associated with reversible dormancy in ascites-derived epithelial ovarian cancer spheroids. *Carcinogenesis* **33**, 49-58, doi:10.1093/carcin/bgr241 (2012).
- 65 Domcke, S., Sinha, R., Levine, D. A., Sander, C. & Schultz, N. Evaluating cell lines as tumour models by comparison of genomic profiles. *Nat Commun* **4**, 2126, doi:10.1038/ncomms3126 (2013).
- 66 Cancer Genome Atlas Research, N. Integrated genomic analyses of ovarian carcinoma. *Nature* **474**, 609-615, doi:10.1038/nature10166 (2011).
- 67 Network, T. C. G. A. R. Erratum: Integrated genomic analyses of ovarian carcinoma. *Nature* **490**, 292-292, doi:10.1038/nature11453 (2012).
- 68 Létourneau, I. J. *et al.* Derivation and characterization of matched cell lines from primary and recurrent serous ovarian cancer. *BMC Cancer* **12**, 379, doi:10.1186/1471-2407-12-379 (2012).
- 69 Beaufort, C. M. *et al.* Ovarian cancer cell line panel (OCCP): clinical importance of in vitro morphological subtypes. *PLoS One* **9**, e103988, doi:10.1371/journal.pone.0103988 (2014).
- 70 Kreuzinger, C. *et al.* Molecular characterization of 7 new established cell lines from high grade serous ovarian cancer. *Cancer Lett* **362**, 218-228, doi:<https://doi.org/10.1016/j.canlet.2015.03.040> (2015).
- 71 Lawrenson, K. *et al.* In vitro three-dimensional modeling of fallopian tube secretory epithelial cells. *BMC Cell Biol* **14**, 43-43, doi:10.1186/1471-2121-14-43 (2013).
- 72 Levanon, K. *et al.* Primary ex vivo cultures of human fallopian tube epithelium as a model for serous ovarian carcinogenesis. *Oncogene* **29**, 1103-1113, doi:10.1038/onc.2009.402 (2010).
- 73 Kelm, J. M., Timmins, N. E., Brown, C. J., Fussenegger, M. & Nielsen, L. K. Method for generation of homogeneous multicellular tumor spheroids applicable to a wide variety of cell types. *Biotechnol Bioeng* **83**, 173-180, doi:10.1002/bit.10655 (2003).
- 74 Buensuceso, A., Ramos-Valdes, Y., DiMattia, G. E. & Shepherd, T. G. AMPK-Independent LKB1 Activity Is Required for Efficient Epithelial Ovarian Cancer Metastasis. *Molecular Cancer Research* **18**, 488, doi:10.1158/1541-7786.MCR-19-0530 (2020).
- 75 Bankert, R. B. *et al.* Humanized Mouse Model of Ovarian Cancer Recapitulates Patient Solid Tumor Progression, Ascites Formation, and Metastasis. *PLOS ONE* **6**, e24420, doi:10.1371/journal.pone.0024420 (2011).
- 76 Odunsi, A. *et al.* Fidelity of human ovarian cancer patient-derived xenografts in a partially humanized mouse model for preclinical testing of immunotherapies. *Journal for ImmunoTherapy of Cancer* **8**, e001237, doi:10.1136/jitc-2020-001237 (2020).
- 77 Network, C. G. A. Integrated genomic analyses of ovarian carcinoma. *Nature* **474**, 609-615, doi:10.1038/nature10166 (2011).

- 78 López-Reig, R. & López-Guerrero, J. A. The hallmarks of ovarian cancer: proliferation and cell growth. *European Journal of Cancer Supplements* **15**, 27-37, doi:<https://doi.org/10.1016/j.ejcsup.2019.12.001> (2020).
- 79 Zhang, Y., Cao, L., Nguyen, D. & Lu, H. TP53 mutations in epithelial ovarian cancer. *Transl Cancer Res* **5**, 650-663, doi:10.21037/tcr.2016.08.40 (2016).
- 80 Ahmed, A. A. *et al.* Driver mutations in TP53 are ubiquitous in high grade serous carcinoma of the ovary. *J Pathol* **221**, 49-56, doi:10.1002/path.2696 (2010).
- 81 Donehower, L. A. *et al.* Integrated Analysis of TP53 Gene and Pathway Alterations in The Cancer Genome Atlas. *Cell reports* **28**, 1370-1384.e1375, doi:10.1016/j.celrep.2019.07.001 (2019).
- 82 Mantovani, F., Collavin, L. & Del Sal, G. Mutant p53 as a guardian of the cancer cell. *Cell Death & Differentiation* **26**, 199-212, doi:10.1038/s41418-018-0246-9 (2019).
- 83 Iwanicki, M. P. *et al.* Mutant p53 regulates ovarian cancer transformed phenotypes through autocrine matrix deposition. *JCI Insight* **1**, doi:10.1172/jci.insight.86829 (2016).
- 84 Candeias, M. M., Hagiwara, M. & Matsuda, M. Cancer-specific mutations in p53 induce the translation of  $\Delta 160$ p53 promoting tumorigenesis. *EMBO Rep* **17**, 1542-1551, doi:10.15252/embr.201541956 (2016).
- 85 Seagle, B.-L. L. *et al.* Survival of patients with structurally-grouped TP53 mutations in ovarian and breast cancers. *Oncotarget* **6**, 18641-18652, doi:10.18632/oncotarget.4080 (2015).
- 86 Brachova, P. *et al.* TP53 oncomorphic mutations predict resistance to platinum- and taxane-based standard chemotherapy in patients diagnosed with advanced serous ovarian carcinoma. *Int J Oncol* **46**, 607-618, doi:10.3892/ijo.2014.2747 (2015).
- 87 Seagle, B. L. *et al.* TP53 hot spot mutations in ovarian cancer: selective resistance to microtubule stabilizers in vitro and differential survival outcomes from The Cancer Genome Atlas. *Gynecol Oncol* **138**, 159-164, doi:10.1016/j.ygyno.2015.04.039 (2015).
- 88 Zhang, G. N. *et al.* TP53 K351N mutation-associated platinum resistance after neoadjuvant chemotherapy in patients with advanced ovarian cancer. *Gynecol Oncol* **132**, 752-757, doi:10.1016/j.ygyno.2014.01.028 (2014).
- 89 Kuchenbaecker, K. B. *et al.* Risks of Breast, Ovarian, and Contralateral Breast Cancer for BRCA1 and BRCA2 Mutation Carriers. *Jama* **317**, 2402-2416, doi:10.1001/jama.2017.7112 (2017).
- 90 Castilla, L. H. *et al.* Mutations in the BRCA1 gene in families with early-onset breast and ovarian cancer. *Nat Genet* **8**, 387-391, doi:10.1038/ng1294-387 (1994).
- 91 Finch, A. P. *et al.* Impact of oophorectomy on cancer incidence and mortality in women with a BRCA1 or BRCA2 mutation. *J Clin Oncol* **32**, 1547-1553, doi:10.1200/jco.2013.53.2820 (2014).
- 92 Antoniou, A. *et al.* Average Risks of Breast and Ovarian Cancer Associated with *BRCA1* or *BRCA2* Mutations Detected in Case Series Unselected for Family History: A Combined Analysis of 22 Studies. *The American Journal of Human Genetics* **72**, 1117-1130, doi:10.1086/375033 (2003).

- 93 Walsh, C. S. Two decades beyond BRCA1/2: Homologous recombination, hereditary cancer risk and a target for ovarian cancer therapy. *Gynecol Oncol* **137**, 343-350, doi:<https://doi.org/10.1016/j.ygyno.2015.02.017> (2015).
- 94 Wu, J., Lu, L.-Y. & Yu, X. The role of BRCA1 in DNA damage response. *Protein & Cell* **1**, 117-123, doi:10.1007/s13238-010-0010-5 (2010).
- 95 Roy, R., Chun, J. & Powell, S. N. BRCA1 and BRCA2: different roles in a common pathway of genome protection. *Nature reviews. Cancer* **12**, 68-78, doi:10.1038/nrc3181 (2011).
- 96 Deng, C.-X. BRCA1: cell cycle checkpoint, genetic instability, DNA damage response and cancer evolution. *Nucleic acids research* **34**, 1416-1426, doi:10.1093/nar/gkl010 (2006).
- 97 Yoshida, K. & Miki, Y. Role of BRCA1 and BRCA2 as regulators of DNA repair, transcription, and cell cycle in response to DNA damage. *Cancer Sci* **95**, 866-871, doi:10.1111/j.1349-7006.2004.tb02195.x (2004).
- 98 Deng, C. X. BRCA1: cell cycle checkpoint, genetic instability, DNA damage response and cancer evolution. *Nucleic Acids Res* **34**, 1416-1426, doi:10.1093/nar/gkl010 (2006).
- 99 Lheureux, S., Gourley, C., Vergote, I. & Oza, A. M. Epithelial ovarian cancer. *The Lancet* **393**, 1240-1253, doi:10.1016/S0140-6736(18)32552-2 (2019).
- 100 Ford, D. *et al.* Genetic heterogeneity and penetrance analysis of the BRCA1 and BRCA2 genes in breast cancer families. The Breast Cancer Linkage Consortium. *Am J Hum Genet* **62**, 676-689, doi:10.1086/301749 (1998).
- 101 Patch, A. M. *et al.* Whole-genome characterization of chemoresistant ovarian cancer. *Nature* **521**, 489-494, doi:10.1038/nature14410 (2015).
- 102 Zhang, S. *et al.* Frequencies of BRCA1 and BRCA2 mutations among 1,342 unselected patients with invasive ovarian cancer. *Gynecol Oncol* **121**, 353-357, doi:10.1016/j.ygyno.2011.01.020 (2011).
- 103 Alsop, K. *et al.* BRCA mutation frequency and patterns of treatment response in BRCA mutation-positive women with ovarian cancer: a report from the Australian Ovarian Cancer Study Group. *J Clin Oncol* **30**, 2654-2663, doi:10.1200/jco.2011.39.8545 (2012).
- 104 Song, H. *et al.* Contribution of Germline Mutations in the RAD51B, RAD51C, and RAD51D Genes to Ovarian Cancer in the Population. *J Clin Oncol* **33**, 2901-2907, doi:10.1200/jco.2015.61.2408 (2015).
- 105 Ramus, S. J. *et al.* Germline Mutations in the BRIP1, BARD1, PALB2, and NBN Genes in Women With Ovarian Cancer. *J Natl Cancer Inst* **107**, doi:10.1093/jnci/djv214 (2015).
- 106 Norquist, B. M. *et al.* Inherited Mutations in Women With Ovarian Carcinoma. *JAMA Oncol* **2**, 482-490, doi:10.1001/jamaoncol.2015.5495 (2016).
- 107 Walsh, T. *et al.* Mutations in 12 genes for inherited ovarian, fallopian tube, and peritoneal carcinoma identified by massively parallel sequencing. *Proceedings of the National Academy of Sciences* **108**, 18032, doi:10.1073/pnas.1115052108 (2011).
- 108 Norquist, B. M. *et al.* Inherited Mutations in Women With Ovarian Carcinoma. *JAMA oncology* **2**, 482-490, doi:10.1001/jamaoncol.2015.5495 (2016).

- 109 Yamulla, R. J., Nalubola, S., Flesken-Nikitin, A., Nikitin, A. Y. & Schimenti, J. C. Most Commonly Mutated Genes in High-Grade Serous Ovarian Carcinoma Are Nonessential for Ovarian Surface Epithelial Stem Cell Transformation. *Cell Reports* **32**, 108086, doi:<https://doi.org/10.1016/j.celrep.2020.108086> (2020).
- 110 Zhao, X. *et al.* Integrative analysis of cancer driver genes in prostate adenocarcinoma. *Mol Med Rep* **19**, 2707-2715, doi:10.3892/mmr.2019.9902 (2019).
- 111 Qiu, Z. *et al.* A novel mutation panel for predicting etoposide resistance in small-cell lung cancer. *Drug Des Devel Ther* **13**, 2021-2041, doi:10.2147/dddt.S205633 (2019).
- 112 Wang, H., Shen, L., Li, Y. & Lv, J. Integrated characterisation of cancer genes identifies key molecular biomarkers in stomach adenocarcinoma. *J Clin Pathol* **73**, 579-586, doi:10.1136/jclinpath-2019-206400 (2020).
- 113 Katoh, M. Function and cancer genomics of FAT family genes (review). *Int J Oncol* **41**, 1913-1918, doi:10.3892/ijo.2012.1669 (2012).
- 114 Longacre, M. *et al.* A Comparative Analysis of Genetic and Epigenetic Events of Breast and Ovarian Cancer Related to Tumorigenesis. *Int J Mol Sci* **17**, doi:10.3390/ijms17050759 (2016).
- 115 Katoh, Y. & Katoh, M. Comparative integromics on FAT1, FAT2, FAT3 and FAT4. *Int J Mol Med* **18**, 523-528 (2006).
- 116 Pearson, A. *et al.* Inactivating NF1 Mutations Are Enriched in Advanced Breast Cancer and Contribute to Endocrine Therapy Resistance. *Clin Cancer Res* **26**, 608-622, doi:10.1158/1078-0432.Ccr-18-4044 (2020).
- 117 Kurimchak, A. M. *et al.* Intrinsic Resistance to MEK Inhibition through BET Protein-Mediated Kinome Reprogramming in NF1-Deficient Ovarian Cancer. *Mol Cancer Res* **17**, 1721-1734, doi:10.1158/1541-7786.Mcr-18-1332 (2019).
- 118 Dick, F. A. & Rubin, S. M. Molecular mechanisms underlying RB protein function. *Nature reviews. Molecular cell biology* **14**, 297-306, doi:10.1038/nrm3567 (2013).
- 119 Giacinti, C. & Giordano, A. RB and cell cycle progression. *Oncogene* **25**, 5220-5227, doi:10.1038/sj.onc.1209615 (2006).
- 120 Wang, A., Schneider-Broussard, R., Kumar, A. P., MacLeod, M. C. & Johnson, D. G. Regulation of BRCA1 expression by the Rb-E2F pathway. *J Biol Chem* **275**, 4532-4536, doi:10.1074/jbc.275.6.4532 (2000).
- 121 Ezhevsky, S. A., Ho, A., Becker-Hapak, M., Davis, P. K. & Dowdy, S. F. Differential regulation of retinoblastoma tumor suppressor protein by G(1) cyclin-dependent kinase complexes in vivo. *Molecular and cellular biology* **21**, 4773-4784, doi:10.1128/MCB.21.14.4773-4784.2001 (2001).
- 122 Fu, M., Wang, C., Li, Z., Sakamaki, T. & Pestell, R. G. Minireview: Cyclin D1: Normal and Abnormal Functions. *Endocrinology* **145**, 5439-5447, doi:10.1210/en.2004-0959 (2004).
- 123 Stacey, D. W. Cyclin D1 serves as a cell cycle regulatory switch in actively proliferating cells. *Curr Opin Cell Biol* **15**, 158-163, doi:10.1016/s0955-0674(03)00008-5 (2003).
- 124 Etemadmoghadam, D. *et al.* Amplicon-Dependent CCNE1 Expression Is Critical for Clonogenic Survival after Cisplatin Treatment and Is Correlated with 20q11

- Gain in Ovarian Cancer. *PLOS ONE* **5**, e15498, doi:10.1371/journal.pone.0015498 (2010).
- 125 Patch, A. M. *et al.* Whole-genome characterization of chemoresistant ovarian cancer. *Nature* **521**, 489-494, doi:10.1038/nature14410 (2015).
- 126 Etemadmoghadam, D. *et al.* Integrated genome-wide DNA copy number and expression analysis identifies distinct mechanisms of primary chemoresistance in ovarian carcinomas. *Clinical cancer research : an official journal of the American Association for Cancer Research* **15**, 1417-1427, doi:10.1158/1078-0432.CCR-08-1564 (2009).
- 127 Farley, J. *et al.* Cyclin E expression is a significant predictor of survival in advanced, suboptimally debulked ovarian epithelial cancers: a Gynecologic Oncology Group study. *Cancer Res* **63**, 1235-1241 (2003).
- 128 Nakayama, N. *et al.* Gene amplification CCNE1 is related to poor survival and potential therapeutic target in ovarian cancer. *Cancer* **116**, 2621-2634, doi:10.1002/cncr.24987 (2010).
- 129 Karst, A. M. *et al.* Cyclin E1 deregulation occurs early in secretory cell transformation to promote formation of fallopian tube-derived high-grade serous ovarian cancers. *Cancer Res* **74**, 1141-1152, doi:10.1158/0008-5472.Can-13-2247 (2014).
- 130 Kuhn, E. *et al.* CCNE1 amplification and centrosome number abnormality in serous tubal intraepithelial carcinoma: further evidence supporting its role as a precursor of ovarian high-grade serous carcinoma. *Mod Pathol* **29**, 1254-1261, doi:10.1038/modpathol.2016.101 (2016).
- 131 Sehdev, A. S., Kurman, R. J., Kuhn, E. & Shih Ie, M. Serous tubal intraepithelial carcinoma upregulates markers associated with high-grade serous carcinomas including Rsf-1 (HBXAP), cyclin E and fatty acid synthase. *Mod Pathol* **23**, 844-855, doi:10.1038/modpathol.2010.60 (2010).
- 132 Etemadmoghadam, D. *et al.* Synthetic lethality between CCNE1 amplification and loss of BRCA1. *Proceedings of the National Academy of Sciences of the United States of America* **110**, 19489-19494, doi:10.1073/pnas.1314302110 (2013).
- 133 Barsotti, A. M. & Prives, C. Pro-proliferative FoxM1 is a target of p53-mediated repression. *Oncogene* **28**, 4295-4305, doi:10.1038/onc.2009.282 (2009).
- 134 Hanrahan, A. J. *et al.* Genomic complexity and AKT dependence in serous ovarian cancer. *Cancer Discov* **2**, 56-67, doi:10.1158/2159-8290.CD-11-0170 (2012).
- 135 Gasparri, M. L. *et al.* PI3K/AKT/mTOR Pathway in Ovarian Cancer Treatment: Are We on the Right Track? *Geburtshilfe Frauenheilkd* **77**, 1095-1103, doi:10.1055/s-0043-118907 (2017).
- 136 Martins, F. C. *et al.* Combined image and genomic analysis of high-grade serous ovarian cancer reveals PTEN loss as a common driver event and prognostic classifier. *Genome Biol* **15**, 526, doi:10.1186/s13059-014-0526-8 (2014).
- 137 Deng, J. *et al.* Inhibition of PI3K/Akt/mTOR signaling pathway alleviates ovarian cancer chemoresistance through reversing epithelial-mesenchymal transition and decreasing cancer stem cell marker expression. *BMC Cancer* **19**, 618, doi:10.1186/s12885-019-5824-9 (2019).



- 138 Cheaib, B., Auguste, A. & Leary, A. The PI3K/Akt/mTOR pathway in ovarian cancer: therapeutic opportunities and challenges. *Chin J Cancer* **34**, 4-16, doi:10.5732/cjc.014.10289 (2015).
- 139 Huang, C.-C. *et al.* Delta-like 1 homologue promotes tumorigenesis and epithelial-mesenchymal transition of ovarian high-grade serous carcinoma through activation of Notch signaling. *Oncogene* **38**, 3201-3215, doi:10.1038/s41388-018-0658-5 (2019).
- 140 Park, J. T. *et al.* Notch3 overexpression is related to the recurrence of ovarian cancer and confers resistance to carboplatin. *The American journal of pathology* **177**, 1087-1094, doi:10.2353/ajpath.2010.100316 (2010).
- 141 Konecny, G. E. *et al.* Prognostic and therapeutic relevance of molecular subtypes in high-grade serous ovarian cancer. *Journal of the National Cancer Institute* **106**, dju249, doi:10.1093/jnci/dju249 (2014).
- 142 Tothill, R. W. *et al.* Novel molecular subtypes of serous and endometrioid ovarian cancer linked to clinical outcome. *Clin Cancer Res* **14**, 5198-5208, doi:10.1158/1078-0432.Ccr-08-0196 (2008).
- 143 Wang, C. *et al.* Pooled Clustering of High-Grade Serous Ovarian Cancer Gene Expression Leads to Novel Consensus Subtypes Associated with Survival and Surgical Outcomes. *Clinical Cancer Research* **23**, 4077, doi:10.1158/1078-0432.CCR-17-0246 (2017).
- 144 Clifford, C. *et al.* Multi-omics in high-grade serous ovarian cancer: Biomarkers from genome to the immunome. *Am J Reprod Immunol* **80**, e12975, doi:10.1111/aji.12975 (2018).
- 145 Macintyre, G. *et al.* Copy number signatures and mutational processes in ovarian carcinoma. *Nat Genet* **50**, 1262-1270, doi:10.1038/s41588-018-0179-8 (2018).
- 146 Schwarz, R. F. *et al.* Spatial and Temporal Heterogeneity in High-Grade Serous Ovarian Cancer: A Phylogenetic Analysis. *PLOS Medicine* **12**, e1001789, doi:10.1371/journal.pmed.1001789 (2015).
- 147 Wang, Y. K. *et al.* Genomic consequences of aberrant DNA repair mechanisms stratify ovarian cancer histotypes. *Nat Genet* **49**, 856-865, doi:10.1038/ng.3849 (2017).
- 148 Bashashati, A. *et al.* Distinct evolutionary trajectories of primary high-grade serous ovarian cancers revealed through spatial mutational profiling. *J Pathol* **231**, 21-34, doi:10.1002/path.4230 (2013).
- 149 Hanahan, D. & Weinberg, Robert A. Hallmarks of Cancer: The Next Generation. *Cell* **144**, 646-674, doi:10.1016/j.cell.2011.02.013 (2011).
- 150 Lee, A. J. *et al.* Chromosomal instability confers intrinsic multidrug resistance. *Cancer Res* **71**, 1858-1870, doi:10.1158/0008-5472.Can-10-3604 (2011).
- 151 Bakhoun, S. F., Danilova, O. V., Kaur, P., Levy, N. B. & Compton, D. A. Chromosomal instability substantiates poor prognosis in patients with diffuse large B-cell lymphoma. *Clin Cancer Res* **17**, 7704-7711, doi:10.1158/1078-0432.Ccr-11-2049 (2011).
- 152 Salomon-Perzyński, A., Salomon-Perzyńska, M., Michalski, B. & Skrzypulec-Plinta, V. High-grade serous ovarian cancer: the clone wars. *Arch Gynecol Obstet* **295**, 569-576, doi:10.1007/s00404-017-4292-1 (2017).

- 153 Turner, N. C. & Reis-Filho, J. S. Genetic heterogeneity and cancer drug resistance. *Lancet Oncol* **13**, e178-185, doi:10.1016/s1470-2045(11)70335-7 (2012).
- 154 Birkbak, N. J. *et al.* Paradoxical relationship between chromosomal instability and survival outcome in cancer. *Cancer Res* **71**, 3447-3452, doi:10.1158/0008-5472.Can-10-3667 (2011).
- 155 Baumbusch, L. O. *et al.* High Levels of Genomic Aberrations in Serous Ovarian Cancers Are Associated with Better Survival. *PLOS ONE* **8**, e54356, doi:10.1371/journal.pone.0054356 (2013).
- 156 Norquist, B. *et al.* Secondary Somatic Mutations Restoring BRCA1/2 Predict Chemotherapy Resistance in Hereditary Ovarian Carcinomas. *Journal of Clinical Oncology* **29**, 3008-3015, doi:10.1200/JCO.2010.34.2980 (2011).
- 157 Bashashati, A. *et al.* Distinct evolutionary trajectories of primary high-grade serous ovarian cancers revealed through spatial mutational profiling. *The Journal of Pathology* **231**, 21-34, doi:<https://doi.org/10.1002/path.4230> (2013).
- 158 Lee, J.-Y. *et al.* Tumor evolution and intratumor heterogeneity of an epithelial ovarian cancer investigated using next-generation sequencing. *BMC Cancer* **15**, 85, doi:10.1186/s12885-015-1077-4 (2015).
- 159 Jayson, G. C., Kohn, E. C., Kitchener, H. C. & Ledermann, J. A. Ovarian cancer. *Lancet* **384**, 1376-1388, doi:10.1016/S0140-6736(13)62146-7 (2014).
- 160 Horowitz, N. S. *et al.* Does aggressive surgery improve outcomes? Interaction between preoperative disease burden and complex surgery in patients with advanced-stage ovarian cancer: an analysis of GOG 182. *J Clin Oncol* **33**, 937-943, doi:10.1200/jco.2014.56.3106 (2015).
- 161 Chang, S. J., Hodeib, M., Chang, J. & Bristow, R. E. Survival impact of complete cytoreduction to no gross residual disease for advanced-stage ovarian cancer: a meta-analysis. *Gynecol Oncol* **130**, 493-498, doi:10.1016/j.ygyno.2013.05.040 (2013).
- 162 Chang, S. J., Bristow, R. E. & Ryu, H. S. Impact of complete cytoreduction leaving no gross residual disease associated with radical cytoreductive surgical procedures on survival in advanced ovarian cancer. *Ann Surg Oncol* **19**, 4059-4067, doi:10.1245/s10434-012-2446-8 (2012).
- 163 Vasey, P. A. *et al.* Phase III randomized trial of docetaxel-carboplatin versus paclitaxel-carboplatin as first-line chemotherapy for ovarian carcinoma. *J Natl Cancer Inst* **96**, 1682-1691, doi:10.1093/jnci/djh323 (2004).
- 164 Ozols, R. F. *et al.* Phase III trial of carboplatin and paclitaxel compared with cisplatin and paclitaxel in patients with optimally resected stage III ovarian cancer: a Gynecologic Oncology Group study. *J Clin Oncol* **21**, 3194-3200, doi:10.1200/jco.2003.02.153 (2003).
- 165 du Bois, A. *et al.* A randomized clinical trial of cisplatin/paclitaxel versus carboplatin/paclitaxel as first-line treatment of ovarian cancer. *J Natl Cancer Inst* **95**, 1320-1329, doi:10.1093/jnci/djg036 (2003).
- 166 Bookman, M. A. *et al.* Evaluation of new platinum-based treatment regimens in advanced-stage ovarian cancer: a Phase III Trial of the Gynecologic Cancer Intergrgroup. *J Clin Oncol* **27**, 1419-1425, doi:10.1200/jco.2008.19.1684 (2009).

- 167 McGuire, W. P. *et al.* Cyclophosphamide and cisplatin compared with paclitaxel and cisplatin in patients with stage III and stage IV ovarian cancer. *N Engl J Med* **334**, 1-6, doi:10.1056/nejm199601043340101 (1996).
- 168 Lopez, J. A. *et al.* Clinical pharmacology of intraperitoneal cisplatin. *Gynecol Oncol* **20**, 1-9, doi:10.1016/0090-8258(85)90118-0 (1985).
- 169 Francis, P. *et al.* Phase I feasibility and pharmacologic study of weekly intraperitoneal paclitaxel: a Gynecologic Oncology Group pilot Study. *J Clin Oncol* **13**, 2961-2967, doi:10.1200/jco.1995.13.12.2961 (1995).
- 170 Vergote, I. *et al.* Neoadjuvant chemotherapy or primary surgery in stage IIIC or IV ovarian cancer. *N Engl J Med* **363**, 943-953, doi:10.1056/NEJMoa0908806 (2010).
- 171 Kehoe, S. *et al.* Primary chemotherapy versus primary surgery for newly diagnosed advanced ovarian cancer (CHORUS): an open-label, randomised, controlled, non-inferiority trial. *Lancet* **386**, 249-257, doi:10.1016/s0140-6736(14)62223-6 (2015).
- 172 Rustin, G. J., Marples, M., Nelstrop, A. E., Mahmoudi, M. & Meyer, T. Use of CA-125 to define progression of ovarian cancer in patients with persistently elevated levels. *J Clin Oncol* **19**, 4054-4057, doi:10.1200/jco.2001.19.20.4054 (2001).
- 173 Salani, R. *et al.* Posttreatment surveillance and diagnosis of recurrence in women with gynecologic malignancies: Society of Gynecologic Oncologists recommendations. *Am J Obstet Gynecol* **204**, 466-478, doi:10.1016/j.ajog.2011.03.008 (2011).
- 174 Rustin, G. J. *et al.* Early versus delayed treatment of relapsed ovarian cancer (MRC OV05/EORTC 55955): a randomised trial. *Lancet* **376**, 1155-1163, doi:10.1016/s0140-6736(10)61268-8 (2010).
- 175 Castells, M. C. *et al.* Hypersensitivity reactions to chemotherapy: outcomes and safety of rapid desensitization in 413 cases. *J Allergy Clin Immunol* **122**, 574-580, doi:10.1016/j.jaci.2008.02.044 (2008).
- 176 Tomao, F., D'Incalci, M., Biagioli, E., Peccatori, F. A. & Colombo, N. Restoring platinum sensitivity in recurrent ovarian cancer by extending the platinum-free interval: Myth or reality? *Cancer* **123**, 3450-3459, doi:10.1002/cncr.30830 (2017).
- 177 da Costa, A. A. B. A. *et al.* Prognostic impact of platinum sensitivity in ovarian carcinoma patients with brain metastasis. *BMC Cancer* **19**, 1194, doi:10.1186/s12885-019-6382-x (2019).
- 178 Pujade-Lauraine, E. & Combe, P. Recurrent ovarian cancer. *Annals of Oncology* **27**, i63-i65, doi:<https://doi.org/10.1093/annonc/mdw079> (2016).
- 179 Roncolato, F. T. *et al.* Predictors of progression free survival, overall survival and early cessation of chemotherapy in women with potentially platinum sensitive (PPS) recurrent ovarian cancer (ROC) starting third or subsequent line ( $\geq 3$ ) chemotherapy - The GCIG symptom benefit study (SBS). *Gynecol Oncol* **156**, 45-53, doi:10.1016/j.ygyno.2019.10.001 (2020).
- 180 Chuang, Y.-T. & Chang, C.-L. Extending platinum-free interval in partially platinum-sensitive recurrent ovarian cancer by a non-platinum regimen: Its possible clinical significance. *Taiwanese Journal of Obstetrics and Gynecology* **51**, 336-341, doi:<https://doi.org/10.1016/j.tjog.2012.07.003> (2012).
- 181 Gibson, J.-M., Alzghari, S., Ahn, C., Trantham, H. & La-Beck, N. M. The role of pegylated liposomal doxorubicin in ovarian cancer: a meta-analysis of randomized

- clinical trials. *Oncologist* **18**, 1022-1031, doi:10.1634/theoncologist.2013-0126 (2013).
- 182 Green, A. E. & Rose, P. G. Pegylated liposomal doxorubicin in ovarian cancer. *Int J Nanomedicine* **1**, 229-239 (2006).
- 183 Gee, M. E., Faraahi, Z., McCormick, A. & Edmondson, R. J. DNA damage repair in ovarian cancer: unlocking the heterogeneity. *Journal of ovarian research* **11**, 50-50, doi:10.1186/s13048-018-0424-x (2018).
- 184 Chatterjee, N. & Walker, G. C. Mechanisms of DNA damage, repair, and mutagenesis. *Environ Mol Mutagen* **58**, 235-263, doi:10.1002/em.22087 (2017).
- 185 Eisemann, T. & Pascal, J. M. Poly(ADP-ribose) polymerase enzymes and the maintenance of genome integrity. *Cell Mol Life Sci* **77**, 19-33, doi:10.1007/s00018-019-03366-0 (2020).
- 186 Morales, J. *et al.* Review of poly (ADP-ribose) polymerase (PARP) mechanisms of action and rationale for targeting in cancer and other diseases. *Crit Rev Eukaryot Gene Expr* **24**, 15-28, doi:10.1615/critreveukaryotgeneexpr.2013006875 (2014).
- 187 Dulaney, C., Marcrom, S., Stanley, J. & Yang, E. S. Poly(ADP-ribose) polymerase activity and inhibition in cancer. *Semin Cell Dev Biol* **63**, 144-153, doi:10.1016/j.semcd.2017.01.007 (2017).
- 188 LaFargue, C. J., Dal Molin, G. Z., Sood, A. K. & Coleman, R. L. Exploring and comparing adverse events between PARP inhibitors. *The Lancet. Oncology* **20**, e15-e28, doi:10.1016/S1470-2045(18)30786-1 (2019).
- 189 Montemorano, L., Lightfoot, M. D. & Bixel, K. Role of Olaparib as Maintenance Treatment for Ovarian Cancer: The Evidence to Date. *Onco Targets Ther* **12**, 11497-11506, doi:10.2147/OTT.S195552 (2019).
- 190 Ledermann, J. *et al.* Olaparib maintenance therapy in platinum-sensitive relapsed ovarian cancer. *N Engl J Med* **366**, 1382-1392, doi:10.1056/NEJMoa1105535 (2012).
- 191 Bixel, K. & Hays, J. L. Olaparib in the management of ovarian cancer. *Pharmgenomics Pers Med* **8**, 127-135, doi:10.2147/PGPM.S62809 (2015).
- 192 Huang, X.-z. *et al.* Efficacy and Prognostic Factors for PARP Inhibitors in Patients With Ovarian Cancer. *Frontiers in Oncology* **10**, 958 (2020).
- 193 Papa, A., Caruso, D., Strudel, M., Tomao, S. & Tomao, F. Update on Poly-ADP-ribose polymerase inhibition for ovarian cancer treatment. *J Transl Med* **14**, 267, doi:10.1186/s12967-016-1027-1 (2016).
- 194 Fong, P. C. *et al.* Poly(ADP)-ribose polymerase inhibition: frequent durable responses in BRCA carrier ovarian cancer correlating with platinum-free interval. *J Clin Oncol* **28**, 2512-2519, doi:10.1200/jco.2009.26.9589 (2010).
- 195 Gelmon, K. A. *et al.* Olaparib in patients with recurrent high-grade serous or poorly differentiated ovarian carcinoma or triple-negative breast cancer: a phase 2, multicentre, open-label, non-randomised study. *Lancet Oncol* **12**, 852-861, doi:10.1016/s1470-2045(11)70214-5 (2011).
- 196 Ledermann, J. *et al.* Olaparib maintenance therapy in patients with platinum-sensitive relapsed serous ovarian cancer: a preplanned retrospective analysis of outcomes by BRCA status in a randomised phase 2 trial. *Lancet Oncol* **15**, 852-861, doi:10.1016/s1470-2045(14)70228-1 (2014).

- 197 Pignata, S., S, C. C., Du Bois, A., Harter, P. & Heitz, F. Treatment of recurrent ovarian cancer. *Ann Oncol* **28**, viii51-viii56, doi:10.1093/annonc/mdx441 (2017).
- 198 Mirza, M. R. *et al.* Niraparib Maintenance Therapy in Platinum-Sensitive, Recurrent Ovarian Cancer. *N Engl J Med* **375**, 2154-2164, doi:10.1056/NEJMoa1611310 (2016).
- 199 Coleman, R. L. *et al.* Rucaparib maintenance treatment for recurrent ovarian carcinoma after response to platinum therapy (ARIEL3): a randomised, double-blind, placebo-controlled, phase 3 trial. *Lancet* **390**, 1949-1961, doi:10.1016/s0140-6736(17)32440-6 (2017).
- 200 Coleman, R. L. *et al.* Veliparib with First-Line Chemotherapy and as Maintenance Therapy in Ovarian Cancer. *New England Journal of Medicine* **381**, 2403-2415, doi:10.1056/NEJMoa1909707 (2019).
- 201 Mirza, M. R. *et al.* The forefront of ovarian cancer therapy: update on PARP inhibitors. *Annals of Oncology* **31**, 1148-1159, doi:10.1016/j.annonc.2020.06.004 (2020).
- 202 Wang, Y. *et al.* IL-6 mediates platinum-induced enrichment of ovarian cancer stem cells. *JCI Insight* **3**, doi:10.1172/jci.insight.122360 (2018).
- 203 Browning, L., Patel, M. R., Horvath, E. B., Tawara, K. & Jorcyk, C. L. IL-6 and ovarian cancer: inflammatory cytokines in promotion of metastasis. *Cancer Manag Res* **10**, 6685-6693, doi:10.2147/CMAR.S179189 (2018).
- 204 Coward, J. *et al.* Interleukin-6 as a therapeutic target in human ovarian cancer. *Clin Cancer Res* **17**, 6083-6096, doi:10.1158/1078-0432.Ccr-11-0945 (2011).
- 205 Angevin, E. *et al.* A phase I/II, multiple-dose, dose-escalation study of siltuximab, an anti-interleukin-6 monoclonal antibody, in patients with advanced solid tumors. *Clin Cancer Res* **20**, 2192-2204, doi:10.1158/1078-0432.Ccr-13-2200 (2014).
- 206 Garcia, A. & Singh, H. Bevacizumab and ovarian cancer. *Ther Adv Med Oncol* **5**, 133-141, doi:10.1177/1758834012467661 (2013).
- 207 Colombo, N., Conte, P. F., Pignata, S., Raspagliesi, F. & Scambia, G. Bevacizumab in ovarian cancer: Focus on clinical data and future perspectives. *Critical Reviews in Oncology/Hematology* **97**, 335-348, doi:<https://doi.org/10.1016/j.critrevonc.2015.08.017> (2016).
- 208 Reinhaller, A. Antiangiogenic therapies in ovarian cancer. *Memo* **9**, 139-143, doi:10.1007/s12254-016-0282-4 (2016).
- 209 Thigpen, T. *et al.* First-Line Therapy in Ovarian Cancer Trials. *International Journal of Gynecologic Cancer* **21**, 756, doi:10.1097/IGC.0b013e31821ce75d (2011).
- 210 Binju, M. *et al.* Mechanisms underlying acquired platinum resistance in high grade serous ovarian cancer - a mini review. *Biochim Biophys Acta Gen Subj* **1863**, 371-378, doi:10.1016/j.bbagen.2018.11.005 (2019).
- 211 Basourakos, S. P. *et al.* Combination Platinum-based and DNA Damage Response-targeting Cancer Therapy: Evolution and Future Directions. *Current medicinal chemistry* **24**, 1586-1606, doi:10.2174/0929867323666161214114948 (2017).
- 212 Wiedemeyer, W. R., Beach, J. & Karlan, B. Reversing Platinum Resistance in High-Grade Serous Ovarian Carcinoma: Targeting BRCA and the Homologous Recombination System. *Frontiers in Oncology* **4**, 34 (2014).

- 213 Yin, M. *et al.* Tumor-Associated Macrophages (TAMs): A Critical Activator In Ovarian Cancer Metastasis. *Oncotargets Ther* **12**, 8687-8699, doi:10.2147/OTT.S216355 (2019).
- 214 Yang, Y., Yang, Y., Yang, J., Zhao, X. & Wei, X. Tumor Microenvironment in Ovarian Cancer: Function and Therapeutic Strategy. *Frontiers in Cell and Developmental Biology* **8**, 758 (2020).
- 215 Ghoneum, A., Afify, H., Salih, Z., Kelly, M. & Said, N. Role of tumor microenvironment in ovarian cancer pathobiology. *Oncotarget* **9**, 22832-22849, doi:10.18632/oncotarget.25126 (2018).
- 216 Penet, M.-F. *et al.* Ascites Volumes and the Ovarian Cancer Microenvironment. *Frontiers in oncology* **8**, 595-595, doi:10.3389/fonc.2018.00595 (2018).
- 217 Kreuzinger, C. *et al.* A Complex Network of Tumor Microenvironment in Human High-Grade Serous Ovarian Cancer. *Clinical Cancer Research* **23**, 7621, doi:10.1158/1078-0432.CCR-17-1159 (2017).
- 218 Ojalvo, L. S. *et al.* Tumor-associated macrophages and the tumor immune microenvironment of primary and recurrent epithelial ovarian cancer. *Human Pathology* **74**, 135-147, doi:<https://doi.org/10.1016/j.humpath.2017.12.010> (2018).
- 219 Wolf, D. *et al.* The Expression of the Regulatory T Cell-Specific Forkhead Box Transcription Factor FoxP3 Is Associated with Poor Prognosis in Ovarian Cancer. *Clinical Cancer Research* **11**, 8326, doi:10.1158/1078-0432.CCR-05-1244 (2005).
- 220 Sato, E. *et al.* Intraepithelial CD8<sup>+</sup> tumor-infiltrating lymphocytes and a high CD8<sup>+</sup>/regulatory T cell ratio are associated with favorable prognosis in ovarian cancer. *Proceedings of the National Academy of Sciences of the United States of America* **102**, 18538, doi:10.1073/pnas.0509182102 (2005).
- 221 Reinartz, S. *et al.* Mixed-polarization phenotype of ascites-associated macrophages in human ovarian carcinoma: Correlation of CD163 expression, cytokine levels and early relapse. *International Journal of Cancer* **134**, 32-42, doi:<https://doi.org/10.1002/ijc.28335> (2014).
- 222 Correa, R. J. *et al.* Combination of AKT inhibition with autophagy blockade effectively reduces ascites-derived ovarian cancer cell viability. *Carcinogenesis* **35**, 1951-1961, doi:10.1093/carcin/bgu049 (2014).
- 223 Shield, K. *et al.* Alpha2beta1 integrin affects metastatic potential of ovarian carcinoma spheroids by supporting disaggregation and proteolysis. *J Carcinog* **6**, 11, doi:10.1186/1477-3163-6-11 (2007).
- 224 Shield, K., Ackland, M. L., Ahmed, N. & Rice, G. E. Multicellular spheroids in ovarian cancer metastases: Biology and pathology. *Gynecol Oncol* **113**, 143-148, doi:10.1016/j.ygyno.2008.11.032 (2009).
- 225 Dong, Y. *et al.* Paclitaxel Resistance and Multicellular Spheroid Formation Are Induced by Kallikrein-Related Peptidase 4 in Serous Ovarian Cancer Cells in an Ascites Mimicking Microenvironment. *PLOS ONE* **8**, e57056, doi:10.1371/journal.pone.0057056 (2013).
- 226 Peart, T. *et al.* Intact LKB1 activity is required for survival of dormant ovarian cancer spheroids. *Oncotarget* **6**, 22424-22438, doi:10.18632/oncotarget.4211 (2015).

- 227 Motohara, T. & Katabuchi, H. Ovarian Cancer Stemness: Biological and Clinical Implications for Metastasis and Chemotherapy Resistance. *Cancers (Basel)* **11**, doi:10.3390/cancers11070907 (2019).
- 228 Liao, J. *et al.* Ovarian cancer spheroid cells with stem cell-like properties contribute to tumor generation, metastasis and chemotherapy resistance through hypoxia-resistant metabolism. *PLoS One* **9**, e84941, doi:10.1371/journal.pone.0084941 (2014).
- 229 Ip, C. K. M. *et al.* Stemness and chemoresistance in epithelial ovarian carcinoma cells under shear stress. *Scientific Reports* **6**, 26788, doi:10.1038/srep26788 (2016).
- 230 Wang, Q. *et al.* Autophagy Is Indispensable for the Self-Renewal and Quiescence of Ovarian Cancer Spheroid Cells with Stem Cell-Like Properties. *Oxid Med Cell Longev* **2018**, 7010472, doi:10.1155/2018/7010472 (2018).
- 231 Varas-Godoy, M., Rice, G. & Illanes, S. E. The Crosstalk between Ovarian Cancer Stem Cell Niche and the Tumor Microenvironment. *Stem Cells Int* **2017**, 5263974, doi:10.1155/2017/5263974 (2017).
- 232 Pease, J. C., Brewer, M. & Tirnauer, J. S. Spontaneous spheroid budding from monolayers: a potential contribution to ovarian cancer dissemination. *Biology Open* **1**, 622, doi:10.1242/bio.2012653 (2012).
- 233 Sehoul, J. *et al.* Intra-abdominal tumor dissemination pattern and surgical outcome in 214 patients with primary ovarian cancer. *J Surg Oncol* **99**, 424-427, doi:10.1002/jso.21288 (2009).
- 234 Osisami, M. & Keller, E. T. Mechanisms of Metastatic Tumor Dormancy. *Journal of clinical medicine* **2**, 136-150, doi:10.3390/jcm2030136 (2013).
- 235 Sosa, M. S., Bragado, P. & Aguirre-Ghiso, J. A. Mechanisms of disseminated cancer cell dormancy: an awakening field. *Nature reviews. Cancer* **14**, 611-622, doi:10.1038/nrc3793 (2014).
- 236 Gao, X.-L., Zhang, M., Tang, Y.-L. & Liang, X.-H. Cancer cell dormancy: mechanisms and implications of cancer recurrence and metastasis. *Onco Targets Ther* **10**, 5219-5228, doi:10.2147/OTT.S140854 (2017).
- 237 Lee, S. H., Reed-Newman, T., Anant, S. & Ramasamy, T. S. Regulatory Role of Quiescence in the Biological Function of Cancer Stem Cells. *Stem Cell Reviews and Reports* **16**, 1185-1207, doi:10.1007/s12015-020-10031-8 (2020).
- 238 Lin, W. C. *et al.* Dormant cancer cells contribute to residual disease in a model of reversible pancreatic cancer. *Cancer Res* **73**, 1821-1830, doi:10.1158/0008-5472.Can-12-2067 (2013).
- 239 Lin, W.-c. *et al.* Dormant cancer cells contribute to residual disease in a model of reversible pancreatic cancer. *Cancer research* **73**, 1821-1830, doi:10.1158/0008-5472.CAN-12-2067 (2013).
- 240 Park, S.-Y. & Nam, J.-S. The force awakens: metastatic dormant cancer cells. *Experimental & Molecular Medicine* **52**, 569-581, doi:10.1038/s12276-020-0423-z (2020).
- 241 Rankin, E. B. & Giaccia, A. J. Hypoxic control of metastasis. *Science* **352**, 175-180, doi:10.1126/science.aaf4405 (2016).
- 242 Harper, J. V. & Brooks, G. The mammalian cell cycle: an overview. *Methods Mol Biol* **296**, 113-153, doi:10.1385/1-59259-857-9:113 (2005).

- 243 Aguirre-Ghiso, J. A. Models, mechanisms and clinical evidence for cancer dormancy. *Nature reviews. Cancer* **7**, 834-846, doi:10.1038/nrc2256 (2007).
- 244 Pelayo, R. *et al.* Cell cycle quiescence of early lymphoid progenitors in adult bone marrow. *Stem Cells* **24**, 2703-2713, doi:10.1634/stemcells.2006-0217 (2006).
- 245 Abravanel, D. L. *et al.* Notch promotes recurrence of dormant tumor cells following HER2/neu-targeted therapy. *J Clin Invest* **125**, 2484-2496, doi:10.1172/jci74883 (2015).
- 246 Moore, N. & Lyle, S. Quiescent, Slow-Cycling Stem Cell Populations in Cancer: A Review of the Evidence and Discussion of Significance. *J Oncol* **2011**, 396076, doi:10.1155/2011/396076 (2011).
- 247 Catelain, C. *et al.* The Notch Delta-4 ligand helps to maintain the quiescence and the short-term reconstitutive potential of haematopoietic progenitor cells through activation of a key gene network. *Stem Cell Research* **13**, 431-441, doi:<https://doi.org/10.1016/j.scr.2014.10.002> (2014).
- 248 Peng, T. *et al.* Hedgehog actively maintains adult lung quiescence and regulates repair and regeneration. *Nature* **526**, 578-582, doi:10.1038/nature14984 (2015).
- 249 Daynac, M. *et al.* Hedgehog Controls Quiescence and Activation of Neural Stem Cells in the Adult Ventricular-Subventricular Zone. *Stem Cell Reports* **7**, 735-748, doi:10.1016/j.stemcr.2016.08.016 (2016).
- 250 Wu, J., Qu, Z., Fei, Z. W., Wu, J. H. & Jiang, C. P. Role of stem cell-derived exosomes in cancer (Review). *Oncol Lett* **13**, 2855-2866, doi:10.3892/ol.2017.5824 (2017).
- 251 Chavali, M. *et al.* Non-canonical Wnt signaling regulates neural stem cell quiescence during homeostasis and after demyelination. *Nature Communications* **9**, 36, doi:10.1038/s41467-017-02440-0 (2018).
- 252 Bragado, P. *et al.* TGF- $\beta$ 2 dictates disseminated tumour cell fate in target organs through TGF- $\beta$ -RIII and p38 $\alpha$ / $\beta$  signalling. *Nature Cell Biology* **15**, 1351-1361, doi:10.1038/ncb2861 (2013).
- 253 Yu-Lee, L. Y. *et al.* Osteoblast-Secreted Factors Mediate Dormancy of Metastatic Prostate Cancer in the Bone via Activation of the TGF $\beta$ RIII-p38MAPK-pS249/T252RB Pathway. *Cancer Res* **78**, 2911-2924, doi:10.1158/0008-5472.Can-17-1051 (2018).
- 254 Huang, J. J. & Blobel, G. C. Dichotomous roles of TGF- $\beta$  in human cancer. *Biochemical Society transactions* **44**, 1441-1454, doi:10.1042/BST20160065 (2016).
- 255 Borges, L., Oliveira, V. K. P., Baik, J., Bendall, S. C. & Perlingeiro, R. C. R. Serial transplantation reveals a critical role for endoglin in hematopoietic stem cell quiescence. *Blood* **133**, 688-696, doi:10.1182/blood-2018-09-874677 (2019).
- 256 Barkan, D. *et al.* Inhibition of Metastatic Outgrowth from Single Dormant Tumor Cells by Targeting the Cytoskeleton. *Cancer Research* **68**, 6241, doi:10.1158/0008-5472.CAN-07-6849 (2008).
- 257 Barkan, D. *et al.* Metastatic Growth from Dormant Cells Induced by a Col-I-Enriched Fibrotic Environment. *Cancer Research* **70**, 5706, doi:10.1158/0008-5472.CAN-09-2356 (2010).



- 258 Aguirre-Ghiso, J. A., Estrada, Y., Liu, D. & Ossowski, L. ERK(MAPK) activity as a determinant of tumor growth and dormancy; regulation by p38(SAPK). *Cancer Res* **63**, 1684-1695 (2003).
- 259 Aguirre Ghiso, J. A., Kovalski, K. & Ossowski, L. Tumor dormancy induced by downregulation of urokinase receptor in human carcinoma involves integrin and MAPK signaling. *J Cell Biol* **147**, 89-104, doi:10.1083/jcb.147.1.89 (1999).
- 260 Recasens, A. & Munoz, L. Targeting Cancer Cell Dormancy. *Trends Pharmacol Sci* **40**, 128-141, doi:10.1016/j.tips.2018.12.004 (2019).
- 261 Correa, R. J. M. *et al.* Combination of AKT inhibition with autophagy blockade effectively reduces ascites-derived ovarian cancer cell viability. *Carcinogenesis* **35**, 1951-1961, doi:10.1093/carcin/bgu049 (2014).
- 262 Ito, K. *et al.* PML targeting eradicates quiescent leukaemia-initiating cells. *Nature* **453**, 1072-1078, doi:10.1038/nature07016 (2008).
- 263 Matsubara, S. *et al.* mTOR plays critical roles in pancreatic cancer stem cells through specific and stemness-related functions. *Scientific Reports* **3**, 3230, doi:10.1038/srep03230 (2013).
- 264 Francipane, M. G. & Lagasse, E. Selective targeting of human colon cancer stem-like cells by the mTOR inhibitor Torin-1. *Oncotarget; Vol 4, No 11: November 2013* (2013).
- 265 Dubrovskaya, A. *et al.* The role of PTEN/Akt/PI3K signaling in the maintenance and viability of prostate cancer stem-like cell populations. *Proceedings of the National Academy of Sciences* **106**, 268, doi:10.1073/pnas.0810956106 (2009).
- 266 Laissue, P. The forkhead-box family of transcription factors: key molecular players in colorectal cancer pathogenesis. *Mol Cancer* **18**, 5, doi:10.1186/s12943-019-0938-x (2019).
- 267 Dobbin, Z. C. & Landen, C. N. The Importance of the PI3K/AKT/MTOR Pathway in the Progression of Ovarian Cancer. *Int J Mol Sci* **14**, doi:10.3390/ijms14048213 (2013).
- 268 Dodd, K. M., Yang, J., Shen, M. H., Sampson, J. R. & Tee, A. R. mTORC1 drives HIF-1 $\alpha$  and VEGF-A signalling via multiple mechanisms involving 4E-BP1, S6K1 and STAT3. *Oncogene* **34**, 2239-2250, doi:10.1038/onc.2014.164 (2015).
- 269 Gan, B. *et al.* Lkb1 regulates quiescence and metabolic homeostasis of haematopoietic stem cells. *Nature* **468**, 701-704, doi:10.1038/nature09595 (2010).
- 270 Buensuceso, A., Ramos-Valdes, Y., DiMattia, G. E. & Shepherd, T. G. AMPK-Independent LKB1 Activity Is Required for Efficient Epithelial Ovarian Cancer Metastasis. *Molecular cancer research : MCR* **18**, 488-500, doi:10.1158/1541-7786.mcr-19-0530 (2020).
- 271 Henley, S. A. & Dick, F. A. The retinoblastoma family of proteins and their regulatory functions in the mammalian cell division cycle. *Cell division* **7**, 10, doi:10.1186/1747-1028-7-10 (2012).
- 272 Kim, K. Y. *et al.* PRMT4-mediated arginine methylation negatively regulates retinoblastoma tumor suppressor protein and promotes E2F-1 dissociation. *Molecular and cellular biology* **35**, 238-248, doi:10.1128/mcb.00945-14 (2015).
- 273 Korenjak, M. *et al.* Native E2F/RBF complexes contain Myb-interacting proteins and repress transcription of developmentally controlled E2F target genes. *Cell* **119**, 181-193, doi:10.1016/j.cell.2004.09.034 (2004).

- 274 Chicas, A. *et al.* Dissecting the unique role of the retinoblastoma tumor suppressor during cellular senescence. *Cancer Cell* **17**, 376-387, doi:10.1016/j.ccr.2010.01.023 (2010).
- 275 Kippin, T. E., Martens, D. J. & van der Kooy, D. p21 loss compromises the relative quiescence of forebrain stem cell proliferation leading to exhaustion of their proliferation capacity. *Genes Dev* **19**, 756-767, doi:10.1101/gad.1272305 (2005).
- 276 Kohno, S., Kitajima, S., Sasaki, N. & Takahashi, C. Retinoblastoma tumor suppressor functions shared by stem cell and cancer cell strategies. *World J Stem Cells* **8**, 170-184, doi:10.4252/wjsc.v8.i4.170 (2016).
- 277 Casimiro, M. C., Crosariol, M., Loro, E., Li, Z. & Pestell, R. G. Cyclins and Cell Cycle Control in Cancer and Disease. *Genes Cancer* **3**, 649-657, doi:10.1177/1947601913479022 (2012).
- 278 Suzuki, A. *et al.* Survivin initiates cell cycle entry by the competitive interaction with Cdk4/p16INK4a and Cdk2/Cyclin E complex activation. *Oncogene* **19**, 3225-3234, doi:10.1038/sj.onc.1203665 (2000).
- 279 Wheatley, S. P. & Altieri, D. C. Survivin at a glance. *Journal of Cell Science* **132**, jcs223826, doi:10.1242/jcs.223826 (2019).
- 280 Garg, H., Suri, P., Gupta, J. C., Talwar, G. P. & Dubey, S. Survivin: a unique target for tumor therapy. *Cancer Cell International* **16**, 49, doi:10.1186/s12935-016-0326-1 (2016).
- 281 Lin, T. Y. *et al.* BIRC5/Survivin is a novel ATG12-ATG5 conjugate interactor and an autophagy-induced DNA damage suppressor in human cancer and mouse embryonic fibroblast cells. *Autophagy* **16**, 1296-1313, doi:10.1080/15548627.2019.1671643 (2020).
- 282 Chen, S. *et al.* Gain-of-Function Mutant p53 Enhances Hematopoietic Stem Cell Self-Renewal. *Blood* **124**, 260-260, doi:10.1182/blood.V124.21.260.260 (2014).
- 283 Dong, P. *et al.* Division of labour between Myc and G1 cyclins in cell cycle commitment and pace control. *Nature Communications* **5**, 4750, doi:10.1038/ncomms5750 (2014).
- 284 Shichiri, M., Hanson, K. D. & Sedivy, J. M. Effects of c-myc expression on proliferation, quiescence, and the G0 to G1 transition in nontransformed cells. *Cell Growth Differ* **4**, 93-104 (1993).
- 285 Yoshida, G. J. Emerging roles of Myc in stem cell biology and novel tumor therapies. *Journal of Experimental & Clinical Cancer Research* **37**, 173, doi:10.1186/s13046-018-0835-y (2018).
- 286 Kipreos, E. T., Lander, L. E., Wing, J. P., He, W. W. & Hedgecock, E. M. *cul-1* Is Required for Cell Cycle Exit in *C. elegans* and Identifies a Novel Gene Family. *Cell* **85**, 829-839, doi:10.1016/S0092-8674(00)81267-2 (1996).
- 287 Qiao, R. *et al.* Mechanism of APC/C<sup>sup</sup>&CDC20<sup>sup</sup>: activation by mitotic phosphorylation. *Proceedings of the National Academy of Sciences* **113**, E2570, doi:10.1073/pnas.1604929113 (2016).
- 288 Kramer, E. R., Scheuringer, N., Podtelejnikov, A. V., Mann, M. & Peters, J.-M. Mitotic Regulation of the APC Activator Proteins CDC20 and CDH1. *Molecular Biology of the Cell* **11**, 1555-1569, doi:10.1091/mbc.11.5.1555 (2000).

- 289 Roesch, A. *et al.* A Temporarily Distinct Subpopulation of Slow-Cycling Melanoma Cells Is Required for Continuous Tumor Growth. *Cell* **141**, 583-594, doi:<https://doi.org/10.1016/j.cell.2010.04.020> (2010).
- 290 Litovchick, L., Florens, L. A., Swanson, S. K., Washburn, M. P. & DeCaprio, J. A. DYRK1A Protein Kinase Promotes Quiescence and Senescence Through DREAM Complex Assembly. *Genes Dev* **25**, 801-813 (2011).
- 291 Litovchick, L. *et al.* Evolutionarily conserved multisubunit RBL2/p130 and E2F4 protein complex represses human cell cycle-dependent genes in quiescence. *Mol Cell* **26**, 539-551, doi:10.1016/j.molcel.2007.04.015 (2007).
- 292 Fischer, M. & Muller, G. A. Cell cycle transcription control: DREAM/MuvB and RB-E2F complexes. *Crit Rev Biochem Mol Biol* **52**, 638-662, doi:10.1080/10409238.2017.1360836 (2017).
- 293 Soppa, U. *et al.* The Down syndrome-related protein kinase DYRK1A phosphorylates p27Kip1 and Cyclin D1 and induces cell cycle exit and neuronal differentiation. *Cell Cycle* **13**, 2084-2100, doi:10.4161/cc.29104 (2014).
- 294 Chen, J.-Y., Lin, J.-R., Tsai, F.-C. & Meyer, T. Dosage of Dyrk1a Shifts Cells within a p21-Cyclin D1 Signaling Map to Control the Decision to Enter the Cell Cycle. *Molecular Cell* **52**, 87-100, doi:<https://doi.org/10.1016/j.molcel.2013.09.009> (2013).
- 295 Deng, X., Ewton, D. Z. & Friedman, E. Mirk/Dyrk1B Maintains the Viability of Quiescent Pancreatic Cancer Cells by Reducing Levels of Reactive Oxygen Species. *Cancer Research* **69**, 3317, doi:10.1158/0008-5472.CAN-08-2903 (2009).
- 296 Ewton, D. Z. *et al.* Inactivation of Mirk/Dyrk1b Kinase Targets Quiescent Pancreatic Cancer Cells. *Molecular Cancer Therapeutics* **10**, 2104, doi:10.1158/1535-7163.MCT-11-0498 (2011).
- 297 Hu, J., Nakhla, H. & Friedman, E. Transient arrest in a quiescent state allows ovarian cancer cells to survive suboptimal growth conditions and is mediated by both Mirk/dyrk1b and p130/RB2. *Int J Cancer* **129**, 307-318, doi:10.1002/ijc.25692 (2011).
- 298 Ormerod, M. G., Titley, J. C., Smith, T. A. D., Tombs, A. L. & Eccles, S. Proliferative behaviour of an oestrogen sensitive rat mammary tumour: evidence for a paracrine interaction between tumour and stroma. *British Journal of Cancer* **67**, 107-111, doi:10.1038/bjc.1993.18 (1993).
- 299 Abderrahman, B. & Jordan, V. C. Rethinking Extended Adjuvant Antiestrogen Therapy to Increase Survivorship in Breast Cancer. *JAMA Oncology* **4**, 15-16, doi:10.1001/jamaoncol.2017.3510 (2018).
- 300 Davies, C. *et al.* Long-term effects of continuing adjuvant tamoxifen to 10 years versus stopping at 5 years after diagnosis of oestrogen receptor-positive breast cancer: ATLAS, a randomised trial. *The Lancet* **381**, 805-816, doi:[https://doi.org/10.1016/S0140-6736\(12\)61963-1](https://doi.org/10.1016/S0140-6736(12)61963-1) (2013).
- 301 Buczaccki, S. J. A. *et al.* Itraconazole targets cell cycle heterogeneity in colorectal cancer. *Journal of Experimental Medicine* **215**, 1891-1912, doi:10.1084/jem.20171385 (2018).
- 302 Liang, G. *et al.* Itraconazole exerts its anti-melanoma effect by suppressing Hedgehog, Wnt, and PI3K/mTOR signaling pathways. *Oncotarget* **8**, 28510-28525, doi:10.18632/oncotarget.15324 (2017).

- 303 Ghajar, C. M. Metastasis prevention by targeting the dormant niche. *Nature reviews. Cancer* **15**, 238-247, doi:10.1038/nrc3910 (2015).
- 304 Weaver, V. M. *et al.* Reversion of the malignant phenotype of human breast cells in three-dimensional culture and in vivo by integrin blocking antibodies. *J Cell Biol* **137**, 231-245, doi:10.1083/jcb.137.1.231 (1997).
- 305 Beliveau, A. *et al.* Raf-induced MMP9 disrupts tissue architecture of human breast cells in three-dimensional culture and is necessary for tumor growth in vivo. *Genes Dev* **24**, 2800-2811, doi:10.1101/gad.1990410 (2010).
- 306 Wang, F. *et al.* Reciprocal interactions between beta1-integrin and epidermal growth factor receptor in three-dimensional basement membrane breast cultures: a different perspective in epithelial biology. *Proc Natl Acad Sci U S A* **95**, 14821-14826, doi:10.1073/pnas.95.25.14821 (1998).
- 307 Ghajar, C. M. Metastasis prevention by targeting the dormant niche. *Nature Reviews Cancer* **15**, 238-247, doi:10.1038/nrc3910 (2015).
- 308 Linde, N., Fluegen, G. & Aguirre-Ghiso, J. A. in *Advances in Cancer Research* Vol. 132 (eds Danny R. Welch & Paul B. Fisher) 45-71 (Academic Press, 2016).
- 309 Saito, Y. *et al.* Induction of cell cycle entry eliminates human leukemia stem cells in a mouse model of AML. *Nature Biotechnology* **28**, 275-280, doi:10.1038/nbt.1607 (2010).
- 310 Di Tullio, A. *et al.* The combination of CHK1 inhibitor with G-CSF overrides cytarabine resistance in human acute myeloid leukemia. *Nature Communications* **8**, 1679, doi:10.1038/s41467-017-01834-4 (2017).
- 311 Boichuk, S. *et al.* The DREAM Complex Mediates GIST Cell Quiescence and Is a Novel Therapeutic Target to Enhance Imatinib-Induced Apoptosis. *Cancer Research* **73**, 5120, doi:10.1158/0008-5472.CAN-13-0579 (2013).
- 312 Viale, A. *et al.* Oncogene ablation-resistant pancreatic cancer cells depend on mitochondrial function. *Nature* **514**, 628-632, doi:10.1038/nature13611 (2014).
- 313 Liao, B. B. *et al.* Adaptive Chromatin Remodeling Drives Glioblastoma Stem Cell Plasticity and Drug Tolerance. *Cell Stem Cell* **20**, 233-246.e237, doi:10.1016/j.stem.2016.11.003 (2017).
- 314 Dalvi, M. P. *et al.* Taxane-Platin-Resistant Lung Cancers Co-develop Hypersensitivity to JumonjiC Demethylase Inhibitors. *Cell Reports* **19**, 1669-1684, doi:<https://doi.org/10.1016/j.celrep.2017.04.077> (2017).
- 315 Vinogradova, M. *et al.* An inhibitor of KDM5 demethylases reduces survival of drug-tolerant cancer cells. *Nature Chemical Biology* **12**, 531-538, doi:10.1038/nchembio.2085 (2016).
- 316 Vera-Ramirez, L., Vodnala, S. K., Nini, R., Hunter, K. W. & Green, J. E. Autophagy promotes the survival of dormant breast cancer cells and metastatic tumour recurrence. *Nature Communications* **9**, 1944, doi:10.1038/s41467-018-04070-6 (2018).
- 317 Singha, B. *et al.* Inhibiting ULK1 kinase decreases autophagy and cell viability in high-grade serous ovarian cancer spheroids. *Am J Cancer Res* **10**, 1384-1399 (2020).
- 318 Sadasivam, S. & DeCaprio, J. A. The DREAM complex: master coordinator of cell cycle-dependent gene expression. *Nature reviews. Cancer* **13**, 585-595, doi:10.1038/nrc3556 (2013).

- 319 Dick, F. A. & Mymryk, J. S. Sweet DREAMs for Hippo. *Genes & development* **25**, 889-894, doi:10.1101/gad.2050411 (2011).
- 320 Fischer, M., Grossmann, P., Padi, M. & DeCaprio, J. A. Integration of TP53, DREAM, MMB-FOXM1 and RB-E2F target gene analyses identifies cell cycle gene regulatory networks. *Nucleic Acids Res* **44**, 6070-6086, doi:10.1093/nar/gkw523 (2016).
- 321 Fischer, M., Quaas, M., Steiner, L. & Engeland, K. The p53-p21-DREAM-CDE/CHR pathway regulates G2/M cell cycle genes. *Nucleic Acids Res* **44**, 164-174, doi:10.1093/nar/gkv927 (2016).
- 322 Forristal, C. *et al.* Loss of the mammalian DREAM complex deregulates chondrocyte proliferation. *Mol Cell Biol* **34**, 2221-2234 (2014).
- 323 Iness, A. N. & Litovchick, L. MuvB: A Key to Cell Cycle Control in Ovarian Cancer. *Front Oncol* **8**, 223, doi:10.3389/fonc.2018.00223 (2018).
- 324 Pilkinton, M., Sandoval, R. & Colamonici, O. R. Mammalian Mip/LIN-9 interacts with either the p107, p130/E2F4 repressor complex or B-Myb in a cell cycle-phase-dependent context distinct from the Drosophila dREAM complex. *Oncogene* **26**, 7535-7543, doi:10.1038/sj.onc.1210562 (2007).
- 325 Litovchick, L., Florens, L. A., Swanson, S. K., Washburn, M. P. & DeCaprio, J. A. DYRK1A protein kinase promotes quiescence and senescence through DREAM complex assembly. *Genes & development* **25**, 801-813, doi:10.1101/gad.2034211 (2011).
- 326 Odajima, J. *et al.* Proteomic Landscape of Tissue-Specific Cyclin E Functions in Vivo. *PLoS genetics* **12**, e1006429-e1006429, doi:10.1371/journal.pgen.1006429 (2016).
- 327 Sadasivam, S., Duan, S. & DeCaprio, J. A. The MuvB complex sequentially recruits B-Myb and FoxM1 to promote mitotic gene expression. *Genes & development* **26**, 474-489, doi:10.1101/gad.181933.111 (2012).
- 328 Müller, G. A. *et al.* The CHR site: definition and genome-wide identification of a cell cycle transcriptional element. *Nucleic acids research* **42**, 10331-10350, doi:10.1093/nar/gku696 (2014).
- 329 Jin, Y. *et al.* B-Myb Is Up-Regulated and Promotes Cell Growth and Motility in Non-Small Cell Lung Cancer. *Int J Mol Sci* **18**, 860, doi:10.3390/ijms18060860 (2017).
- 330 Gartel, A. L. FOXM1 in Cancer: Interactions and Vulnerabilities. *Cancer Research* **77**, 3135, doi:10.1158/0008-5472.CAN-16-3566 (2017).
- 331 Guiley, K. Z. *et al.* Structural mechanisms of DREAM complex assembly and regulation. *Genes Dev* **29**, 961-974, doi:10.1101/gad.257568.114 (2015).
- 332 Iness, A. N. *et al.* The cell cycle regulatory DREAM complex is disrupted by high expression of oncogenic B-Myb. *Oncogene* **38**, 1080-1092, doi:10.1038/s41388-018-0490-y (2019).
- 333 Schmit, F., Cremer, S. & Gaubatz, S. LIN54 is an essential core subunit of the DREAM/LINC complex that binds to the cdc2 promoter in a sequence-specific manner. *Febs j* **276**, 5703-5716, doi:10.1111/j.1742-4658.2009.07261.x (2009).
- 334 Marceau, A. H. *et al.* Structural basis for LIN54 recognition of CHR elements in cell cycle-regulated promoters. *Nature communications* **7**, 12301-12301, doi:10.1038/ncomms12301 (2016).

- 335 Pilkinton, M., Sandoval, R., Barrett, K., Tian, X. & Colamonici, O. R. Mip/LIN-9 can inhibit cell proliferation independent of the pocket proteins. *Blood Cells Mol Dis* **39**, 272-277, doi:10.1016/j.bcmd.2007.05.006 (2007).
- 336 Pilkinton, M., Sandoval, R., Song, J., Ness, S. A. & Colamonici, O. R. Mip/LIN-9 regulates the expression of B-Myb and the induction of cyclin A, cyclin B, and CDK1. *J Biol Chem* **282**, 168-175, doi:10.1074/jbc.M609924200 (2007).
- 337 Reichert, N. *et al.* Lin9, a subunit of the mammalian DREAM complex, is essential for embryonic development, for survival of adult mice, and for tumor suppression. *Molecular and cellular biology* **30**, 2896-2908, doi:10.1128/MCB.00028-10 (2010).
- 338 Bainor, A. J. *et al.* The HDAC-Associated Sin3B Protein Represses DREAM Complex Targets and Cooperates with APC/C to Promote Quiescence. *Cell reports* **25**, 2797-2807.e2798, doi:10.1016/j.celrep.2018.11.024 (2018).
- 339 Wiseman, E. F. *et al.* Dereglulation of the FOXM1 target gene network and its coregulatory partners in oesophageal adenocarcinoma. *Mol Cancer* **14**, 69-69, doi:10.1186/s12943-015-0339-8 (2015).
- 340 Mages, C. F., Wintsche, A., Bernhart, S. H. & Müller, G. A. The DREAM complex through its subunit Lin37 cooperates with Rb to initiate quiescence. *eLife* **6**, e26876, doi:10.7554/eLife.26876 (2017).
- 341 Reichert, N. *et al.* Lin9, a subunit of the mammalian DREAM complex, is essential for embryonic development, for survival of adult mice, and for tumor suppression. *Mol Cell Biol* **30**, 2896-2908, doi:10.1128/mcb.00028-10 (2010).
- 342 Fischer, M. & Müller, G. A. Cell cycle transcription control: DREAM/MuvB and RB-E2F complexes. *Critical Reviews in Biochemistry and Molecular Biology* **52**, 638-662, doi:10.1080/10409238.2017.1360836 (2017).
- 343 Kittler, R. *et al.* Genome-scale RNAi profiling of cell division in human tissue culture cells. *Nat Cell Biol* **9**, 1401-1412, doi:10.1038/ncb1659 (2007).
- 344 Hurford, R. K., Jr., Cobrinik, D., Lee, M. H. & Dyson, N. pRB and p107/p130 are required for the regulated expression of different sets of E2F responsive genes. *Genes Dev* **11**, 1447-1463 (1997).
- 345 Müller, G. A. *et al.* The CHR promoter element controls cell cycle-dependent gene transcription and binds the DREAM and MMB complexes. *Nucleic Acids Res* **40**, 1561-1578, doi:10.1093/nar/gkr793 (2012).
- 346 Fischer, M., Quaas, M., Steiner, L. & Engeland, K. The p53-p21-DREAM-CDE/CHR pathway regulates G2/M cell cycle genes. *Nucleic acids research* **44**, 164-174, doi:10.1093/nar/gkv927 (2016).
- 347 Talluri, S. & Dick, F. A. Regulation of transcription and chromatin structure by pRB: Here, there and everywhere. *Cell Cycle* **11**, 3189-3198, doi:10.4161/cc.21263 (2012).
- 348 Uchida, C. Roles of pRB in the Regulation of Nucleosome and Chromatin Structures. *BioMed Research International* **2016**, 5959721, doi:10.1155/2016/5959721 (2016).
- 349 Latorre, I. *et al.* The DREAM complex promotes gene body H2A.Z for target repression. *Genes & development* **29**, 495-500, doi:10.1101/gad.255810.114 (2015).

- 350 Giaimo, B. D., Ferrante, F., Herchenröther, A., Hake, S. B. & Borggreffe, T. The histone variant H2A.Z in gene regulation. *Epigenetics Chromatin* **12**, 37-37, doi:10.1186/s13072-019-0274-9 (2019).
- 351 Latorre, I. *et al.* The DREAM complex promotes gene body H2A.Z for target repression. *Genes Dev* **29**, 495-500, doi:10.1101/gad.255810.114 (2015).
- 352 Knight, A. S., Notaridou, M. & Watson, R. J. A Lin-9 complex is recruited by B-Myb to activate transcription of G2/M genes in undifferentiated embryonal carcinoma cells. *Oncogene* **28**, 1737-1747, doi:10.1038/onc.2009.22 (2009).
- 353 Saville, M. K. & Watson, R. J. The cell-cycle regulated transcription factor B-Myb is phosphorylated by cyclin A/Cdk2 at sites that enhance its transactivation properties. *Oncogene* **17**, 2679-2689, doi:10.1038/sj.onc.1202503 (1998).
- 354 Johnson, T. K., Schweppe, R. E., Septer, J. & Lewis, R. E. Phosphorylation of B-Myb regulates its transactivation potential and DNA binding. *J Biol Chem* **274**, 36741-36749, doi:10.1074/jbc.274.51.36741 (1999).
- 355 Down, C. F., Millour, J., Lam, E. W. & Watson, R. J. Binding of FoxM1 to G2/M gene promoters is dependent upon B-Myb. *Biochim Biophys Acta* **1819**, 855-862, doi:10.1016/j.bbagr.2012.03.008 (2012).
- 356 Sadasivam, S., Duan, S. & DeCaprio, J. A. The MuvB complex sequentially recruits B-Myb and FoxM1 to promote mitotic gene expression. *Genes Dev* **26**, 474-489, doi:10.1101/gad.181933.111 (2012).
- 357 Chen, X. *et al.* The forkhead transcription factor FOXM1 controls cell cycle-dependent gene expression through an atypical chromatin binding mechanism. *Mol Cell Biol* **33**, 227-236, doi:10.1128/mcb.00881-12 (2013).
- 358 Paik, S. *et al.* A multigene assay to predict recurrence of tamoxifen-treated, node-negative breast cancer. *N Engl J Med* **351**, 2817-2826, doi:10.1056/NEJMoa041588 (2004).
- 359 Thorner, A. R. *et al.* In vitro and in vivo analysis of B-Myb in basal-like breast cancer. *Oncogene* **28**, 742-751, doi:10.1038/onc.2008.430 (2009).
- 360 Liu, M. *et al.* FoxM1B is overexpressed in human glioblastomas and critically regulates the tumorigenicity of glioma cells. *Cancer Res* **66**, 3593-3602, doi:10.1158/0008-5472.Can-05-2912 (2006).
- 361 Kalin, T. V. *et al.* Increased levels of the FoxM1 transcription factor accelerate development and progression of prostate carcinomas in both TRAMP and LADY transgenic mice. *Cancer Res* **66**, 1712-1720, doi:10.1158/0008-5472.Can-05-3138 (2006).
- 362 Lok, G. T. *et al.* Aberrant activation of ERK/FOXM1 signaling cascade triggers the cell migration/invasion in ovarian cancer cells. *PLoS One* **6**, e23790, doi:10.1371/journal.pone.0023790 (2011).
- 363 Wolter, P., Hanselmann, S., Patschull, G., Schruf, E. & Gaubatz, S. Central spindle proteins and mitotic kinesins are direct transcriptional targets of MuvB, B-MYB and FOXM1 in breast cancer cell lines and are potential targets for therapy. *Oncotarget* **8**, 11160-11172, doi:10.18632/oncotarget.14466 (2017).
- 364 Iltzsche, F. *et al.* An important role for Myb-MuvB and its target gene KIF23 in a mouse model of lung adenocarcinoma. *Oncogene* **36**, 110-121, doi:10.1038/onc.2016.181 (2017).

- 365 Boichuk, S. *et al.* The DREAM complex mediates GIST cell quiescence and is a novel therapeutic target to enhance imatinib-induced apoptosis. *Cancer Res* **73**, 5120-5129, doi:10.1158/0008-5472.Can-13-0579 (2013).
- 366 DeCaprio, J. A. & Duensing, A. The DREAM complex in antitumor activity of imatinib mesylate in gastrointestinal stromal tumors. *Curr Opin Oncol* **26**, 415-421, doi:10.1097/cco.000000000000090 (2014).
- 367 Uhl, K. L., Schultz, C. R., Geerts, D. & Bachmann, A. S. Harmine, a dual-specificity tyrosine phosphorylation-regulated kinase (DYRK) inhibitor induces caspase-mediated apoptosis in neuroblastoma. *Cancer Cell International* **18**, 82, doi:10.1186/s12935-018-0574-3 (2018).
- 368 Li, Y.-L. *et al.* DYRK1A inhibition suppresses STAT3/EGFR/Met signalling and sensitizes EGFR wild-type NSCLC cells to AZD9291. *Journal of cellular and molecular medicine* **23**, 7427-7437, doi:10.1111/jcmm.14609 (2019).
- 369 Li, Y. *et al.* DYRK1A suppression restrains Mcl-1 expression and sensitizes NSCLC cells to Bcl-2 inhibitors. *Cancer Biol Med* **17**, 387-400, doi:10.20892/j.issn.2095-3941.2019.0380 (2020).
- 370 DeCaprio, J. A. & Duensing, A. The DREAM complex in antitumor activity of imatinib mesylate in gastrointestinal stromal tumors. *Current opinion in oncology* **26**, 415-421, doi:10.1097/CCO.000000000000090 (2014).
- 371 Luna, J. *et al.* DYRK1A modulates c-MET in pancreatic ductal adenocarcinoma to drive tumour growth. *Gut* **68**, 1465-1476, doi:10.1136/gutjnl-2018-316128 (2019).
- 372 Rivard, N., L'Allemain, G., Bartek, J. & Pouyssegur, J. Abrogation of p27Kip1 by cDNA Antisense Suppresses Quiescence (G0 State) in Fibroblasts. *Journal of Biological Chemistry* **271**, 18337-18341 (1996).
- 373 Carroll, J. S. *et al.* p27<sup>and</sup>Kip1<sup>and</sup>; Induces Quiescence and Growth Factor Insensitivity in Tamoxifen-treated Breast Cancer Cells. *Cancer Research* **63**, 4322 (2003).
- 374 Smith, E. J., Leone, G., DeGregori, J., Jakoi, L. & Nevins, J. R. The accumulation of an E2F-p130 transcriptional repressor distinguishes a G0 cell state from a G1 cell state. *Molecular and Cellular Biology* **16**, 6965, doi:10.1128/MCB.16.12.6965 (1996).
- 375 Kim, H. *et al.* A chemical with proven clinical safety rescues Down-syndrome-related phenotypes in through DYRK1A inhibition. *Disease models & mechanisms* **9**, 839-848, doi:10.1242/dmm.025668 (2016).
- 376 Ionescu, A. *et al.* DYRK1A kinase inhibitors with emphasis on cancer. *Mini Rev Med Chem* **12**, 1315-1329, doi:10.2174/13895575112091315 (2012).
- 377 Wright, E. E., Bird, J. L. & Feldman, J. M. The effect of harmine and other monoamine oxidase inhibitors on N-acetyltransferase activity. *Res Commun Chem Pathol Pharmacol* **24**, 259-272 (1979).
- 378 Mandato, E. *et al.* CX-4945, a Selective Inhibitor of Casein Kinase 2, Synergizes with B Cell Receptor Signaling Inhibitors in Inducing Diffuse Large B Cell Lymphoma Cell Death. *Curr Cancer Drug Targets* **18**, 608-616, doi:10.2174/1568009617666170427110450 (2018).
- 379 Laham, A. J., Saber-Ayad, M. & El-Awady, R. DYRK1A: a down syndrome-related dual protein kinase with a versatile role in tumorigenesis. *Cellular and Molecular Life Sciences*, doi:10.1007/s00018-020-03626-4 (2020).



- 380 Stringer, M., Goodlett, C. R. & Roper, R. J. Targeting trisomic treatments: optimizing Dyrk1a inhibition to improve Down syndrome deficits. *Mol Genet Genomic Med* **5**, 451-465, doi:10.1002/mgg3.334 (2017).
- 381 Becker, W. A wake-up call to quiescent cancer cells - potential use of DYRK1B inhibitors in cancer therapy. *Febs j* **285**, 1203-1211, doi:10.1111/febs.14347 (2018).
- 382 Hu, J., Deng, H. & Friedman, E. A. Ovarian cancer cells, not normal cells, are damaged by Mirk/Dyrk1B kinase inhibition. *Int J Cancer* **132**, 2258-2269, doi:10.1002/ijc.27917 (2013).
- 383 Perampalam, P. & Dick, F. A. BEAVR: a browser-based tool for the exploration and visualization of RNA-seq data. *BMC Bioinformatics* **21**, 221, doi:10.1186/s12859-020-03549-8 (2020).
- 384 Perampalam, P., McDonald, J. I. & Dick, F. A. GO-CRISPR: a highly controlled workflow to discover gene essentiality in loss-of-function screens. *bioRxiv*, 2020.2006.2004.134841, doi:10.1101/2020.06.04.134841 (2020).

## Chapter 2

### 2 Disrupting the DREAM transcriptional repressor complex induces apolipoprotein overexpression and systemic amyloidosis in mice

#### 2.1 Abstract

DREAM is a transcriptional repressor complex that regulates cell proliferation and its loss causes neonatal lethality in mice. To investigate DREAM function in adult mice, we utilized an assembly defective p107 protein and conditional deletion of its redundant family member p130. In the absence of DREAM assembly, mice displayed shortened survival characterized by systemic amyloidosis, but no evidence of excessive cellular proliferation. Amyloid deposits were found in the heart, liver, spleen, and kidneys, but not the brain or bone marrow. Using laser capture microdissection followed by mass spectrometry, we identified apolipoproteins as the most abundant components of amyloids. Intriguingly, apoA-IV was the most detected amyloidogenic protein in amyloid deposits, suggesting AApoAIV amyloidosis. AApoAIV is a recently described form whereby wildtype apoA-IV has been shown to predominate in amyloid plaques. We determined that DREAM directly regulates *Apoa4* by chromatin immunoprecipitation and that the histone variant H2AZ is reduced from the *Apoa4* gene body in DREAM's absence, leading to overexpression. Collectively, we describe a mechanism by which epigenetic misregulation causes apolipoprotein overexpression and amyloidosis, potentially explaining the origins of non-genetic amyloid subtypes.

## 2.2 Introduction

Amyloidosis is a disease characterized by the misfolding and aggregation of proteins into ordered  $\beta$ -sheet fibrils that are deposited extracellularly within organs or tissues<sup>1</sup>. Presently, there are over thirty-five different proteins known to be amyloidogenic in humans which has led to the classification of amyloidosis into different subtypes based on the causative protein and the organs or tissues affected<sup>2,3</sup>. Systemic amyloidosis involves multiple organs and/or tissues as a result of protein deposition at distal sites due to circulation<sup>4</sup>. Several members of the apolipoprotein family have been associated with systemic amyloidosis, these include apolipoprotein A-I (apoA-I), apolipoprotein A-II (apoA-II), and apolipoprotein A-IV (apoA-IV)<sup>5</sup>. These proteins are predominantly made in the liver, although their expression has also been reported in the heart and spleen<sup>6-8</sup>. ApoA-I and apoA-II are constituents of high-density lipoproteins (HDL) and are commonly implicated in hereditary amyloidosis<sup>9,10</sup>. ApoA-IV can exist as part of HDL or circulate in a lipid-free state<sup>11-13</sup>. Like apolipoprotein E (apoE) and serum amyloid P-component (APCS), apoA-IV was originally considered to be an amyloid signature protein present in many different amyloid pathologies<sup>14,15</sup>. However, new mass spectrometry based methods of characterizing protein identities has suggested apoA-IV has amyloidogenic properties leading to the clinical designation of apoA-IV amyloidosis (AApoAIV)<sup>16</sup>. Importantly, the expansion of protein identities in amyloidosis revealed by mass spectrometry creates a more complex landscape of disease etiology and raises new questions of the origins of non-hereditary forms of the disease.

Epigenetic mechanisms often govern gene expression levels in eukaryotic cells. In particular, deposition of nucleosomes containing the histone variant H2AZ represses gene

expression in a number of different biological scenarios through its accumulation in target genes<sup>17-19</sup>. A key regulator of H2AZ is the DREAM complex that possesses nucleosome binding activity and is thought to function as a chaperone to deposit H2AZ at its target genes<sup>17,20</sup>. DREAM was initially described as a cell cycle regulatory complex that targets proliferation-related genes through a bipartite promoter element composed of a cell cycle homology region (CHR) and a cell cycle-dependent element (CDE)<sup>17,20,21</sup>. These elements are well conserved in metazoan promoters and much of our understanding of DREAM regulation is derived from cell proliferation studies in culture<sup>22,23</sup>, or development in fruit flies and worms<sup>24-26</sup>. In fruit flies, DREAM not only represses transcription, but also associates with MYB like proteins to serve as a transcriptional activator<sup>27</sup>. In mammals DREAM disassembles upon the initiation of proliferation and is replaced at promoters by MYB containing complexes that activate transcription<sup>23</sup>. For this reason, it is unclear if DREAM deficiency in lower organisms can be related to its physiological role in mammals, particularly because many phenotypes relate to fruit fly and worm specific aspects of gonadal development<sup>21,26</sup>.

In mammals, under quiescent conditions, DREAM is comprised of a **DP** protein, an **RB** family protein (either p107 or p130), an **E2F**, and the **MuvB** core of proteins (made up of LIN9, LIN37, LIN52, LIN54, and RBBP4)<sup>21,28</sup>. Upon cell cycle entry, DREAM is disassembled and the MuvB core partners with B-MYB to form MYB-MuvB complexes that activate gene expression required for progression through mitosis<sup>28-30</sup>. Consequently, mammalian DREAM function has been difficult to study as all of its components have non-DREAM functions, and deletions of their encoding genes in mice has resulted in embryonic or neonatal lethality<sup>31-34</sup>. Consequently, much of our knowledge of DREAM function in

mammals is largely derived from cell culture experiments investigating proliferative control, leaving its role in mammalian physiology largely unexplored.

To circumvent the early developmental consequences of DREAM loss, we devised a conditional model for inactivation of DREAM in adult mice. We utilized tamoxifen-inducible deletion of the p130 encoding gene<sup>35</sup>, in combination with a constitutive p107 mutant that is unable to interact with the MuvB core<sup>36</sup>. Therefore, these mice express the components of DREAM, but are unable to assemble the complex. We show that these mice have diminished survival, exhibit symptoms of renal failure, and develop systemic amyloidosis affecting the heart, kidney, liver, and spleen. Transcriptional and proteomic analyses demonstrate that *Apoa4* is overexpressed in the liver and apoA-IV is the most abundant protein found in amyloids of these mice. Chromatin immunoprecipitation (ChIP) analyses demonstrate that DREAM is replaced by B-MYB at the promoter of *Apoa4* with a concurrent decreased localization of H2AZ within the gene body. These data reveal a connection between DREAM, altered epigenetic regulation of hepatic apolipoprotein expression, and development of systemic AApoA-IV amyloidosis.

## 2.3 Results

### 2.3.1 Generation of adult DREAM assembly deficient mice

Early lethality of mice deficient for DREAM components has limited insight into its function in mammals. Consequently, we generated a conditional mouse model to disrupt DREAM complex assembly in young adult animals by eliminating the physical contact between the MuvB subunit LIN52 and p107/p130 (**Figure 2.1A**). We utilized a previously

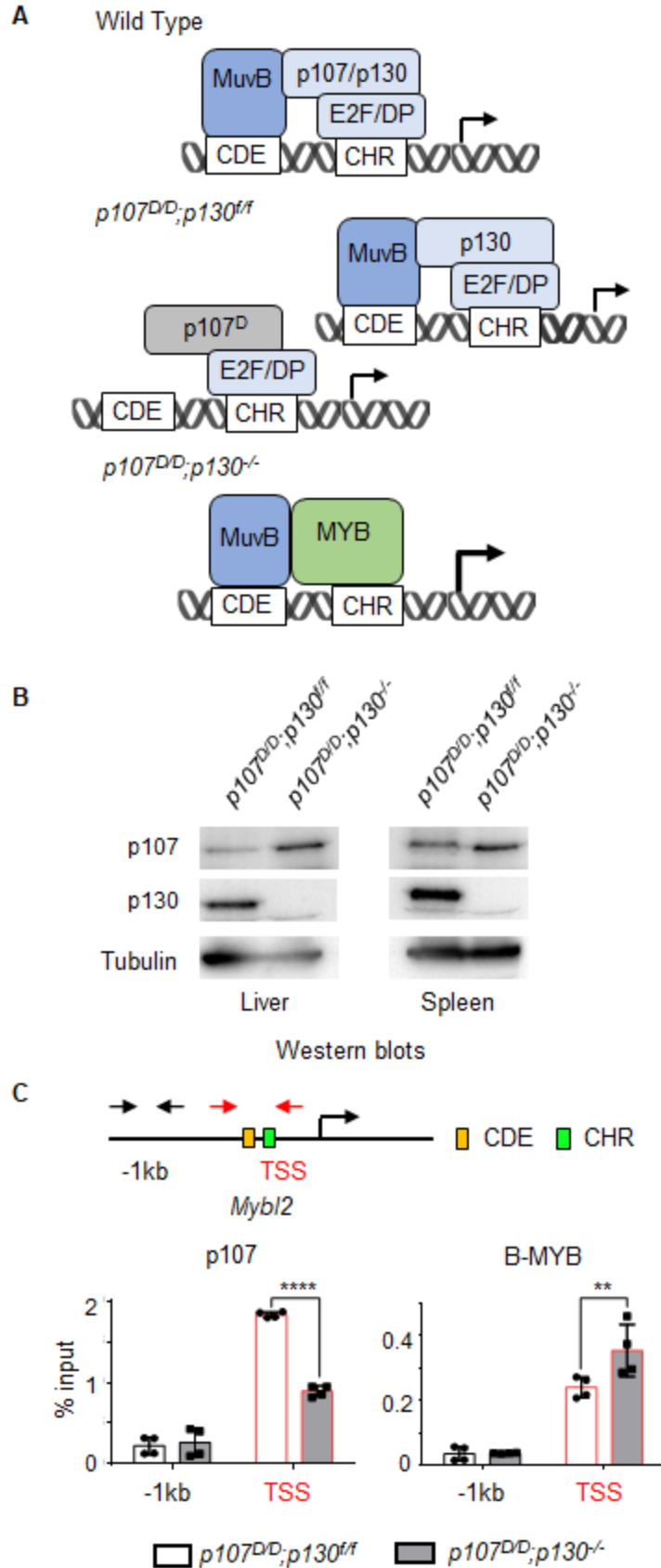


**Figure 2.1. DREAM assembly is disrupted in  $p107^{D/D};p130^{-/-}$  mice.** (A) Either one of the RB-like proteins, p107 or p130, can participate in DREAM assembly by binding to MuvB in wild type mice and repressing transcription. In  $p107^{D/D};p130^{+/+}$  mice, the  $p107^D$  mutation prevents it from binding MuvB, rendering p107<sup>D</sup> unable to participate in DREAM assembly but is still able to form p107-E2F complexes at CHR elements. p130 is now the only RB-like family member able to mediate DREAM assembly in  $p107^{D/D};p130^{+/+}$  mice. In  $p107^{D/D};p130^{-/-}$  mice, ablation of p130 ( $p130^{-/-}$ ) combined with p107<sup>D</sup> prevents DREAM assembly. The MuvB core now binds to B-MYB to form MYB-MuvB and activates transcription. (B) Protein extracts were prepared from the livers and spleens of 3-month old  $p107^{D/D};p130^{-/-}$  and  $p107^{D/D};p130^{+/+}$  control mice. The expression of p107<sup>D</sup> and p130 protein levels was detected by western blotting and Tubulin serves as a loading control. (C) ChIP-qPCR assay to detect p107<sup>D</sup> and B-MYB binding at the TSS of *Mybl2*, a known DREAM target. Illustration depicts primers used for qPCR and the regions of interest: black arrows = negative control 1 kb upstream of TSS; red arrows = approximately 100 bp region surrounding TSS and containing CDE (blue box) and CHR (green) motifs. Chromatin was prepared from livers and p107 and B-MYB antibodies were used to precipitate associated DNA (n=4 for each). Graphs show mean quantities of the indicated genome locations precipitated and error bars indicate one standard deviation. Two-way ANOVA was performed for each and significance levels are indicated (\* denotes  $P < 0.05$ ; and \*\*\*\* denotes  $P < 0.0001$ ).

described missense allele of *Rbl1* in which the encoded p107 protein is unable to interact with LIN52<sup>36,37</sup> (**Figure 2.1A**). Since this mutation leaves p130 available to participate in DREAM assembly, we employed a ubiquitously expressed UBC-Cre-ERT2 system to conditionally delete *Rbl2* (that encodes p130) in adult mice and prevent DREAM assembly<sup>38</sup> (**Figure 2.1A**). The inability to assemble DREAM has previously been shown to result in ectopic MYB-MuvB assembly at DREAM regulated genes, even in growth arrested conditions<sup>23,36</sup> (**Figure 2.1A**), therefore we first sought to determine if tamoxifen treatment of these mice resulted in DREAM loss and a gain of MYB-MuvB assembly.

For simplicity we will refer to the mutant allele of p107 as *p107<sup>D</sup>*, the conditional allele of p130 as *p130<sup>f</sup>*, and its Cre inactivated form as *p130<sup>-</sup>*. At eight weeks of age, *UBC-CreERT2;p107<sup>D/D</sup>;p130<sup>f/f</sup>* mice were injected with tamoxifen (**Figure 2.2A**). We confirmed successful deletion of *p130* exon 2 in the brain, heart, liver, kidney, spleen, bone, and tail by PCR at one week post injection, and also demonstrate that it persists 2 years after tamoxifen treatment in *p107<sup>D/D</sup>;p130<sup>-</sup>* mice (**Figure 2.2B-D**). We next determined the protein levels of both p107 and p130 in *p107<sup>D/D</sup>;p130<sup>f/f</sup>* control and *p107<sup>D/D</sup>;p130<sup>-</sup>* mice. We prepared cell lysates from the liver and spleen four weeks after tamoxifen administration. Western blotting demonstrated that the p130 protein was undetectable in both the liver and spleen of *p107<sup>D/D</sup>;p130<sup>-</sup>* mice, further validating successful deletion of *p130* (**Figure 2.1B**). Additionally, p107<sup>D</sup> protein was detectable in the livers and spleens of both *p107<sup>D/D</sup>;p130<sup>f/f</sup>* and *p107<sup>D/D</sup>;p130<sup>-</sup>* mice.

To validate loss of DREAM assembly in *p107<sup>D/D</sup>;p130<sup>-</sup>* mice, we performed ChIP-qPCR assays to interrogate p107 and B-MYB occupancy at the promoter for *Mybl2*, the



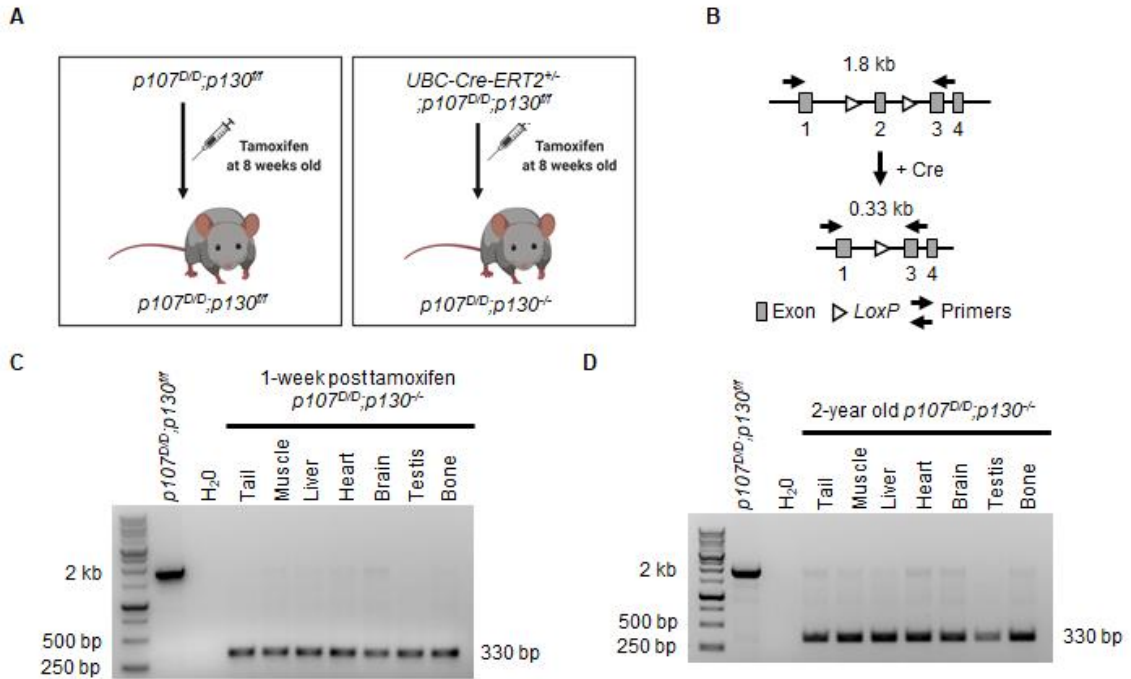


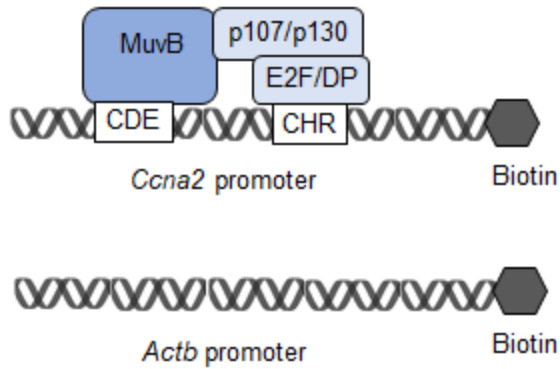
**Figure 2.2. Strategy to create DREAM assembly deficient mice.** (A) Tamoxifen treatment of control ( $p107^{D/D};p130^{ff}$ ) and  $UBC-Cre-ERT2^{+/-};p107^{D/D};p130^{ff}$  at 8 weeks of age was used to produce adult control mice that are  $p107^{D/D};p130^{ff}$  and the comparative cohort that are  $p107^{D/D};p130^{-/-}$ . (B) PCR genotyping strategy to detect knockout of p130 by conditional deletion of exon 2. Horizontal black arrows indicate annealing sites for genotyping primers to confirm deletion of exon 2. LoxP sites flank exon 2 and upon Cre activation, exon 2 is excised removing approximately 1.47 kb of genomic sequence. (C)-(D): Validation of p130 exon 2 deletion by genotype PCR. Tissues obtained from mice 1-week (C) or 2 years (D) following tamoxifen treatment. The primer pair shown in (B) was used to detect successful excision of exon 2. PCR was performed on the indicated samples and products were resolved on agarose gels. Wildtype amplicon: 1.8 kb. Deleted allele amplicon: 330 bp.

gene for B-MYB itself and a known DREAM target<sup>23,28,30,39,40</sup>. We designed primer pairs to encompass the CDE and CHR elements at the transcriptional start site (TSS), as well as a -1 kb upstream control (**Figure 2.1C**). Since p130 is absent in  $p107^{D/D};p130^{-/-}$  mice, we surveyed p107<sup>D</sup> occupancy and found it present at the *Mybl2* promoter in  $p107^{D/D};p130^{ff}$  mice, indicative of some p107-E2F4 binding at the CHR site independent of DREAM (**Figure 2.1C**). Occupancy of p107<sup>D</sup> at this site was diminished in  $p107^{D/D};p130^{-/-}$  mice and this was coupled with a marked increase in B-MYB occupancy, consistent with MYB-MuvB binding and displacing p107<sup>D</sup>-E2F complexes when p130 is no longer able to assemble into DREAM (**Figure 2.1C**). We also confirmed DREAM disruption in  $p107^{D/D};p130^{-/-}$  mice using an *in vitro* promoter pulldown assay that relies on tandem CDE and CHR elements for stable DREAM binding (**Figure 2.3A**). In these experiments p130 is detectable on this probe in  $p107^{D/D};p130^{ff}$  derived extracts, but not  $p107^{D/D};p130^{-/-}$  (**Figure 2.3B**). Furthermore, p107<sup>D</sup> is undetectable on this probe in either genotype of extract, consistent with its inability to be assembled into DREAM<sup>36,37</sup> (**Figure 2.3B**). Collectively, these data demonstrate that p130 protein expression is missing in  $p107^{D/D};p130^{-/-}$  mice leading to compromised DREAM assembly and its replacement with MYB-MuvB. This suggests that phenotypes from  $p107^{D/D};p130^{-/-}$  mice will reveal the role of DREAM in adult mammals.

### 2.3.2 $p107^{D/D};p130^{-/-}$ mice exhibit compromised renal function and disrupted tissue structure in multiple organs

Cohorts of eight week old *UBC-CreERT2;p107<sup>D/D</sup>;p130<sup>ff</sup>* mice were injected with a course of tamoxifen ( $p107^{D/D};p130^{-/-}$ ) and aged alongside tamoxifen injected

A



B

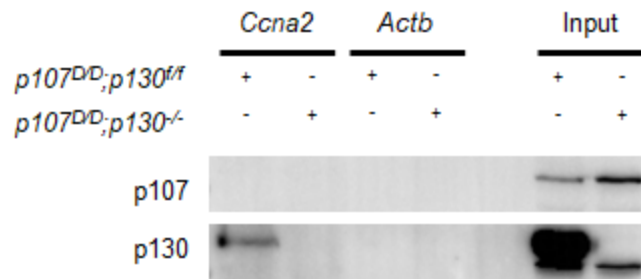


**Figure 2.3. *In vitro* DREAM assembly defect in *p107<sup>D/D</sup>;p130<sup>-/-</sup>* mice.** (A) Schematic to illustrate biotinylated DNA probes used for affinity capture of protein complexes. In these *in vitro* assays, stable binding by DREAM requires simultaneous contact with CDE and CHR elements to capture components. Failure to assemble the complex will prevent detection of any components on the *Ccna2* probe. The *Actb* probe is used as a negative control. (B) Control *p107<sup>D/D</sup>;p130<sup>f/f</sup>* and *p107<sup>D/D</sup>;p130<sup>-/-</sup>* mice were used to produce liver extracts and proteins were bound to the indicated probes and associated protein complexes were isolated. Probe-bound proteins were separated by SDS-PAGE and western blotted to detect p107<sup>D</sup> or p130 to ascertain if DREAM is assembled in these extracts.

*p107<sup>D/D</sup>;p130<sup>ff</sup>* control mice. There was a 16% reduction in lifespan for *p107<sup>D/D</sup>;p130<sup>-/-</sup>* compared to controls that is significantly different (Log-rank test,  $P = 0.0236$ ) (**Figure 2.4A**). Lifespan was similar for both male and female mice and their demise was often without prior symptoms. Some *p107<sup>D/D</sup>;p130<sup>-/-</sup>* displayed distress characterized by shallow breathing and a disheveled coat at this age and these ‘endpoint’ mice were euthanized for further investigation. In contrast, *p107<sup>D/D</sup>;p130<sup>ff</sup>* controls experienced classical aging, characterized by kyphosis and predictable endpoints. To explore the underlying causes of premature mortality in *p107<sup>D/D</sup>;p130<sup>-/-</sup>* mice, we examined tissues from *p107<sup>D/D</sup>;p130<sup>-/-</sup>* mice at their endpoint and compared them histologically with control mice at the end of their full lifespan. There was little evidence to support ectopic cell proliferation in these mice. While some *p107<sup>D/D</sup>;p130<sup>-/-</sup>* mice displayed enlarged organs there was no significant differences in average mass of livers, spleens, or kidneys (**Figure 2.5**). Examination of hematoxylin and eosin (H&E) stained tissues failed to reveal hyperplasia, and Ki67 staining levels and patterns were not altered between genotypes (**Figure 2.6**). However, H&E staining revealed abnormalities in the heart, kidney, liver, and spleen of *p107<sup>D/D</sup>;p130<sup>-/-</sup>* mice (**Figure 2.4B**). Distinctive extracellular, amorphous, hypocellular, and eosinophilic material in these tissues suggested the presence of amyloid fibril deposits. These were found markedly and diffusely in the interstitium of the heart and kidneys, expanding vessel walls in the liver, and on the periphery of the white pulp extending to the red pulp of the spleen (**Figure 2.4B**, indicated by arrows).

The kidneys of *p107<sup>D/D</sup>;p130<sup>-/-</sup>* mice displayed the most visually dramatic deposits with diffusely expanded interstitium, from the cortex to the medulla with variable glomerular involvement (**Figure 2.4B**). Importantly, renal tubular epithelium were swollen

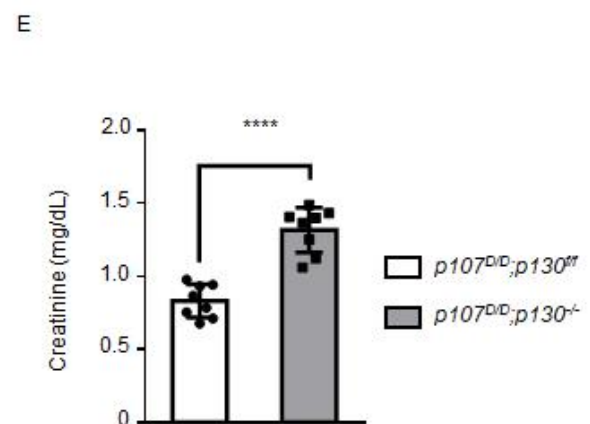
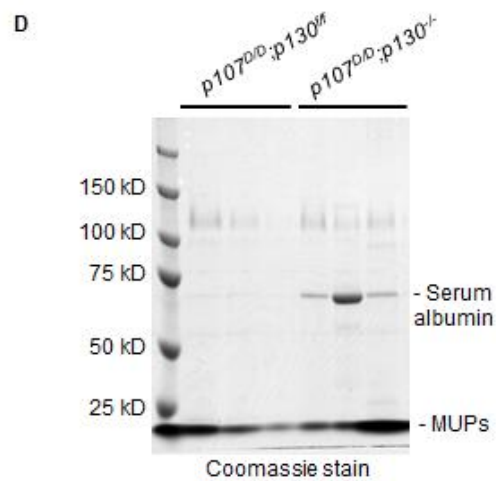
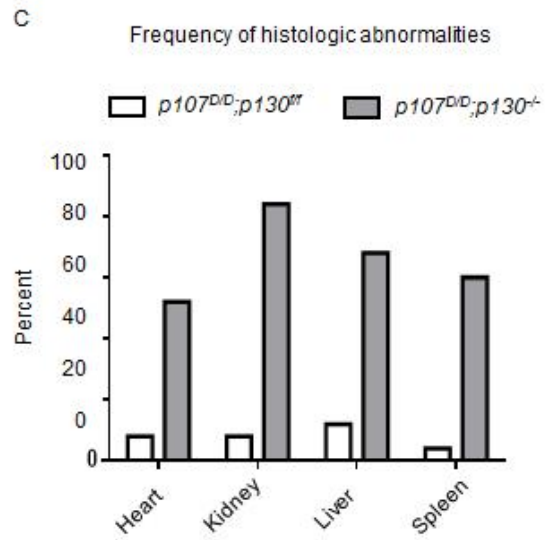
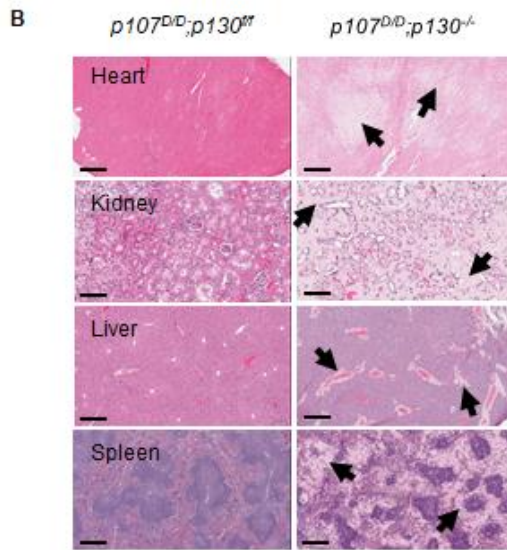
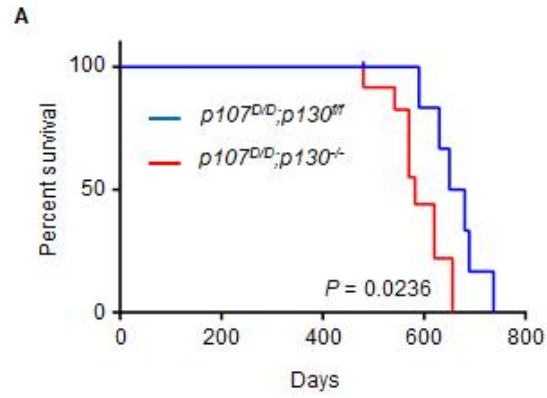


**Figure 2.4.  $p107^{D/D};p130^{-/-}$  mice have shortened lifespan and compromised organ function.** (A) Cohorts of  $p107^{D/D};p130^{-/-}$  (n=30) and  $p107^{D/D};p130^{ff}$  control mice (n=37) were aged to humane endpoints. Kaplan-Meier survival plots reveal survival proportions and a log-rank test was used to compare outcomes ( $P = 0.0236$ ). (B) H&E staining of tissues obtained from  $p107^{D/D};p130^{ff}$  and  $p107^{D/D};p130^{-/-}$  mice at endpoint. Examples of poorly staining homogeneous, acellular, eosinophilic areas found in  $p107^{D/D};p130^{-/-}$  mice are indicated by arrows. Data is representative of 21  $p107^{D/D};p130^{ff}$  and 25  $p107^{D/D};p130^{-/-}$  mice. Scale bars represent 400  $\mu\text{m}$  for heart, liver, and spleen. Scale bars represent 100  $\mu\text{m}$  for kidney. (C) Frequency of histologic abnormalities in  $p107^{D/D};p130^{ff}$  (n=21) and  $p107^{D/D};p130^{-/-}$  mice (n=25) for each of the indicated organs. (D) Urine samples were collected from endpoint  $p107^{D/D};p130^{ff}$  and  $p107^{D/D};p130^{-/-}$  mice and proteins were resolved on SDS-PAGE gel and stained with Coomassie Blue. MUPs = major urinary proteins. (E) Serum samples were collected from endpoint mice and were analyzed for levels of creatinine. Bar graph represents mean quantities for the indicated genotypes and error bars indicate one standard deviation (n=8). A student's t-test was performed and \*\*\*\* denotes  $P < 0.0001$ .

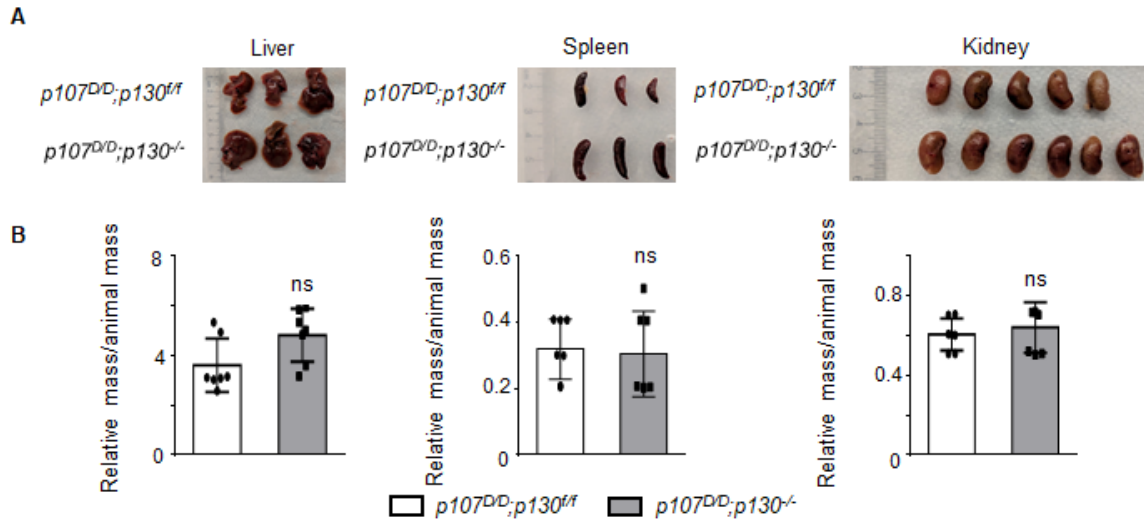


**Figure 2.5. Normal liver, spleen, and kidney mass in  $p107^{D/D};p130^{-/-}$  mice.** (A) Whole mount images of the indicated organs are shown, along with their genotypes. (B) Comparison of organ mass relative to the animal's body mass is shown for  $p107^{D/D};p130^{ff}$  controls and  $p107^{D/D};p130^{-/-}$  mice.

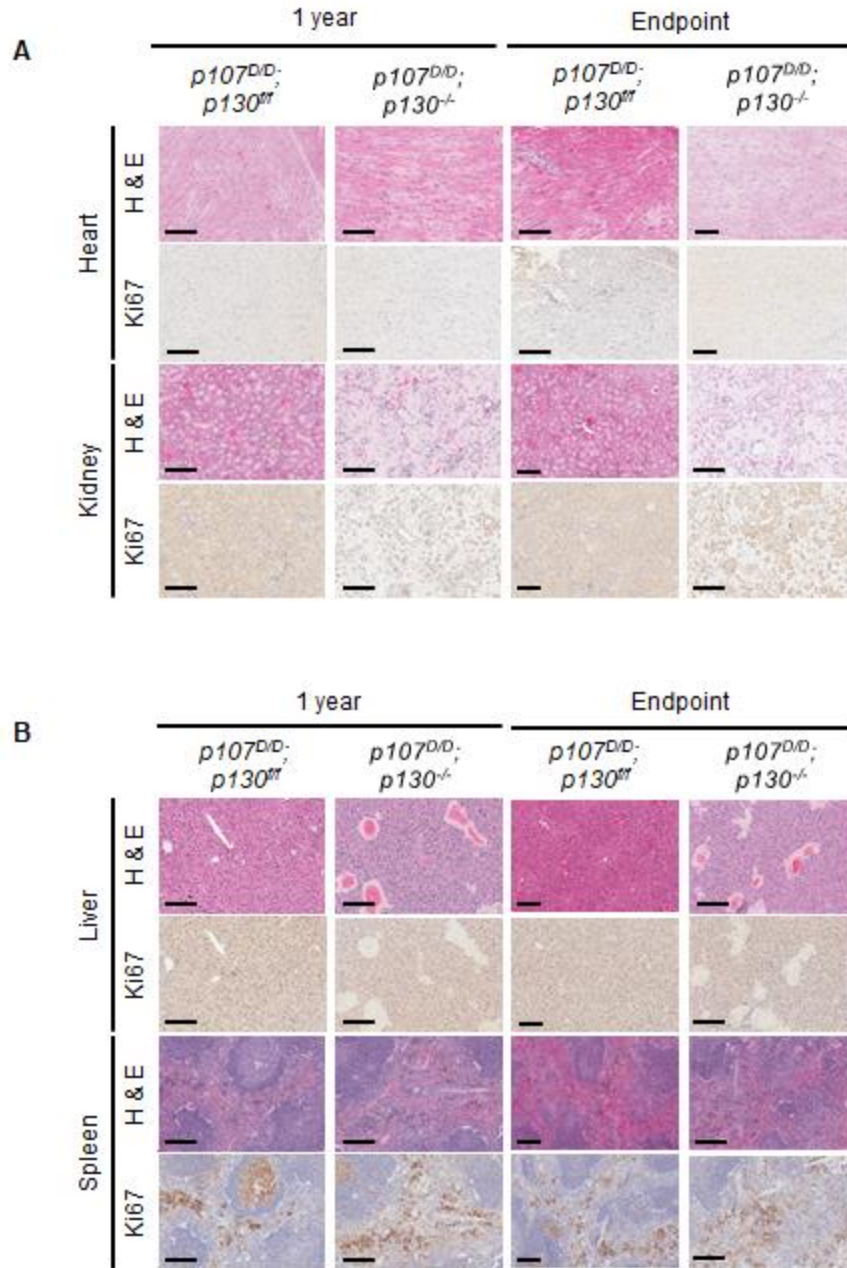


**Figure 2.6. Similar Ki67 staining in control and *p107<sup>D/D</sup>;**p130<sup>-/-</sup>* tissues. (A) Tissue sections were prepared from FFPE kidneys and hearts from mice of the indicated genotypes at the indicated ages. Serial sections were stained with H&E and Ki67. Scale bars represent 200  $\mu$ m. (B) A similar analysis was performed on spleens and livers. Scale bars represent 200  $\mu$ m.**



due to cytoplasmic vacuolation, consistent with deposition leading to progressive decline in renal function<sup>41-43</sup>. Indeed, almost 90% of endpoint  $p107^{D/D};p130^{-/-}$  mice possessed this type of organ damage, while the other affected organs were observed much less frequently (**Figure 2.4C**). To investigate kidney function, we collected urine from endpoint  $p107^{D/D};p130^{ff}$  and  $p107^{D/D};p130^{-/-}$  mice and resolved equal volumes of urine by SDS-PAGE to search for evidence of proteinuria<sup>44</sup>. All samples showed evidence of murine major urinary proteins (MUPs), however the urine of  $p107^{D/D};p130^{-/-}$  mice included a prominent ~60 kD band that we confirmed by mass spectrometry to be serum albumin (**Figure 2.4D**), indicating albuminuria in these mice<sup>45</sup>. Lastly, we tested serum creatinine levels in endpoint mice and determined that it is significantly elevated in  $p107^{D/D};p130^{-/-}$  mice (**Figure 2.4E**). These data suggest that at their endpoint,  $p107^{D/D};p130^{-/-}$  mice exhibit defective kidney function. This is consistent with histological findings in the kidney, and together they indicate kidney failure is the most common ailment in  $p107^{D/D};p130^{-/-}$  mice. Because sudden mortality in a portion of  $p107^{D/D};p130^{-/-}$  mice prevented physiological and histological investigation, it is possible some  $p107^{D/D};p130^{-/-}$  mice succumb to a more rapid cause of death such as cardiac arrest. Overall, multiple organs are damaged in  $p107^{D/D};p130^{-/-}$  mice leading to premature mortality.

### 2.3.3 Systemic amyloidosis is evident in $p107^{D/D};p130^{-/-}$ mice

We investigated the affected organs for potential amyloid deposition through histological stains and transmission electron microscopy (TEM). Heart, kidney, liver, and spleen tissue sections from  $p107^{D/D};p130^{-/-}$  mice were stained with Congo Red and examined under bright field optics and polarized light<sup>46-48</sup>. This demonstrated that weakly

stained eosinophilic material corresponded with regions of apple-green birefringence, a hallmark of amyloid fibril deposition (**Figure 2.7A-D**). The presence of amyloid fibril structures in the medullar regions of kidney tissue was confirmed by TEM from formalin-fixed paraffin-embedded (FFPE) tissue sections (**Figure 2.7E**). Measurement of these medullar amyloid fibrils revealed a mean diameter of 12 nm that is consistent with amyloidosis<sup>49</sup> (**Figure 2.7F**). We similarly detected fibrils using TEM in heart and liver tissues of *p107<sup>D/D</sup>;p130<sup>-/-</sup>* mice (**Figure 2.7G-H**). These experiments confirm that the disrupted tissue structures observed in the heart, kidney, liver, and spleen of *p107<sup>D/D</sup>;p130<sup>-/-</sup>* mice are amyloid in nature.

We next determined the prevalence and impact of amyloids in *p107<sup>D/D</sup>;p130<sup>-/-</sup>* mice compared to *p107<sup>D/D</sup>;p130<sup>ff</sup>* controls. Heart, kidney, liver, spleen, and brain tissue sections from *p107<sup>D/D</sup>;p130<sup>-/-</sup>* and control mice were stained with Congo Red and scored to quantitate amyloid deposition based on the quantity of affected area on a scale from 0 to 3 (**Figure 2.8**). Amyloid deposition scores were plotted for *p107<sup>D/D</sup>;p130<sup>-/-</sup>* and control mice for each age cohort (1-year old and endpoint) (**Figure 2.9A**). We also enumerated these amyloid deposition scores with other abnormal histological features, including relative degree of cellular degeneration and inflammatory cell infiltrates, and plotted the aggregate score for each mouse on an ordinal scale from 0 to 3 that is representative of the observed diagnostic severity (**Figure 2.8**)<sup>50,51</sup>. In heart, kidney, liver, and spleen, *p107<sup>D/D</sup>;p130<sup>-/-</sup>* mice consistently had increased amyloid deposition, cellular degeneration, and inflammation at their endpoint compared to *p107<sup>D/D</sup>;p130<sup>ff</sup>* control mice (**Figure 2.9B**), and a similar trend was also apparent in comparisons of 1-year old *p107<sup>D/D</sup>; p130<sup>-/-</sup>* mice and their age-matched controls. Notably, the striking amyloid deposition and other

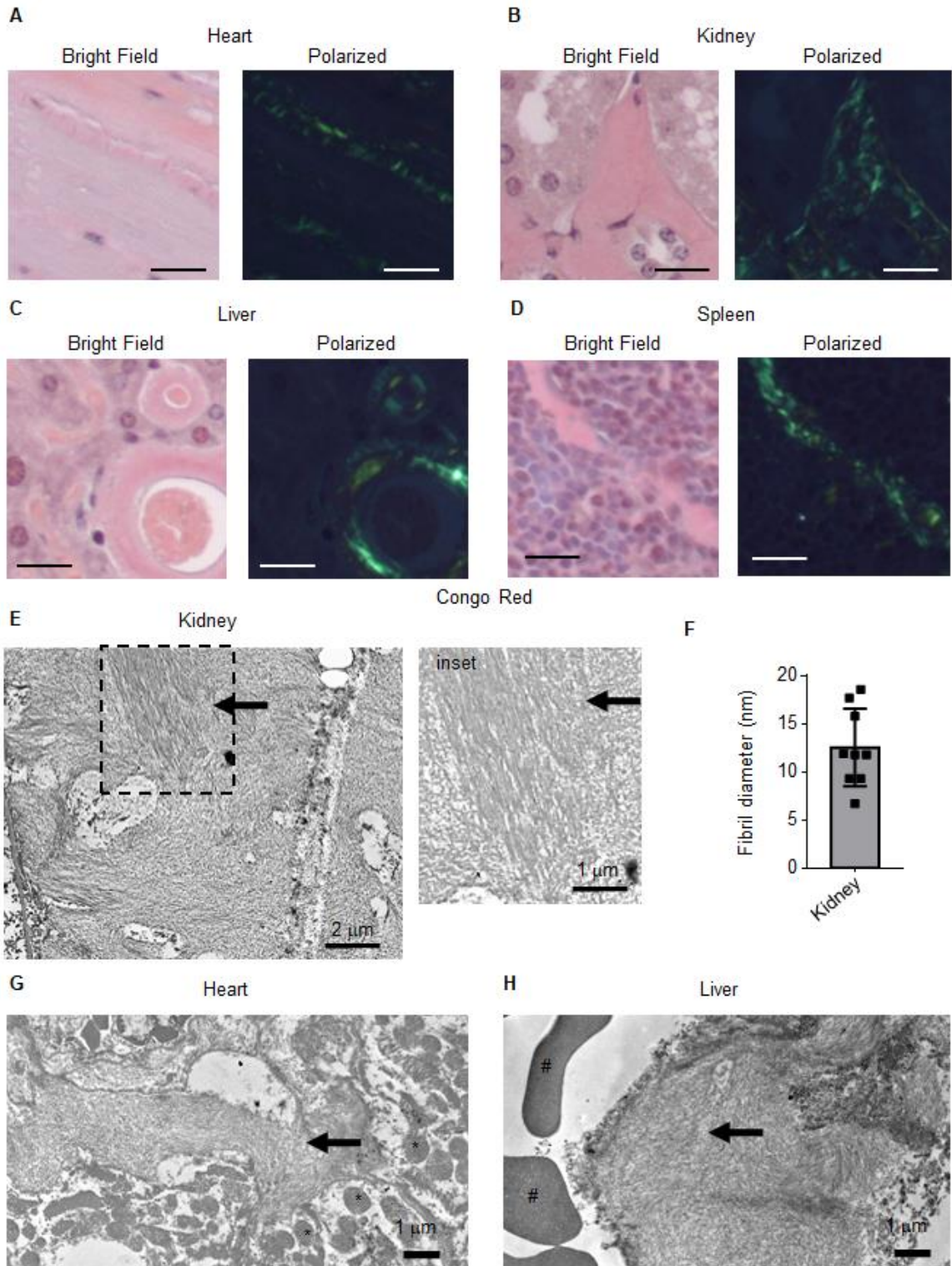


**Figure 2.7. Systemic amyloidosis in  $p107^{D/D};p130^{-/-}$  mice.** (A)-(D) Tissue sections of heart (A), kidney (B), liver (C), and spleen (D) from endpoint  $p107^{D/D};p130^{-/-}$  mice were stained with Congo Red. Bright field images were captured along with corresponding apple green birefringence under polarized light. Scale bars represent 20  $\mu\text{m}$ . (E) FFPE tissues were processed for transmission electron microscopy (TEM). Ultrastructure of acellular material in the kidney is shown. Black arrows indicate fibril structure in this organ. (F) Fibril diameters in kidney TEM images were measured. Bar graph represents mean diameter obtained from individual fibril measurements and error bars indicate one standard deviation (n=9). (G)-(H) TEM of FFPE heart (G) and liver (H) tissue. Black arrows indicate areas of fibril deposition. For orientation, \* indicates mitochondria in cardiomyocytes and # denotes red blood cells in a hepatic capillary.

Amyloid deposition score	
0	No amyloid
1	Multifocal minimal deposits
2	Mild to moderate amyloid
3	Extensive amyloid expanding stroma
Cellular degeneration score	
0	No necrosis
1	Irregular cellular morphology
1.5	Scattered single cell necrosis/degeneration
2	Multifocal areas of necrosis
3	Multifocal to coalescing areas of necrosis
Inflammation score	
0	No inflammation
1	Scattered inflammatory cells
2	Nodular aggregates of inflammatory cells
3	Sheets of inflammatory cells
Aggregated score = Amyloid deposition score + cellular degeneration score + inflammation score	

**Figure 2.8. Aggregate pathology scores for phenotypes observed in tissue sections.** Tissues from 1-year and 2-year old endpoint mice from both cohorts were scored for three criteria (amyloid deposition, cellular degeneration, inflammation) on a scale of 0-3 (n=6). Scores were aggregated for each mouse as described.

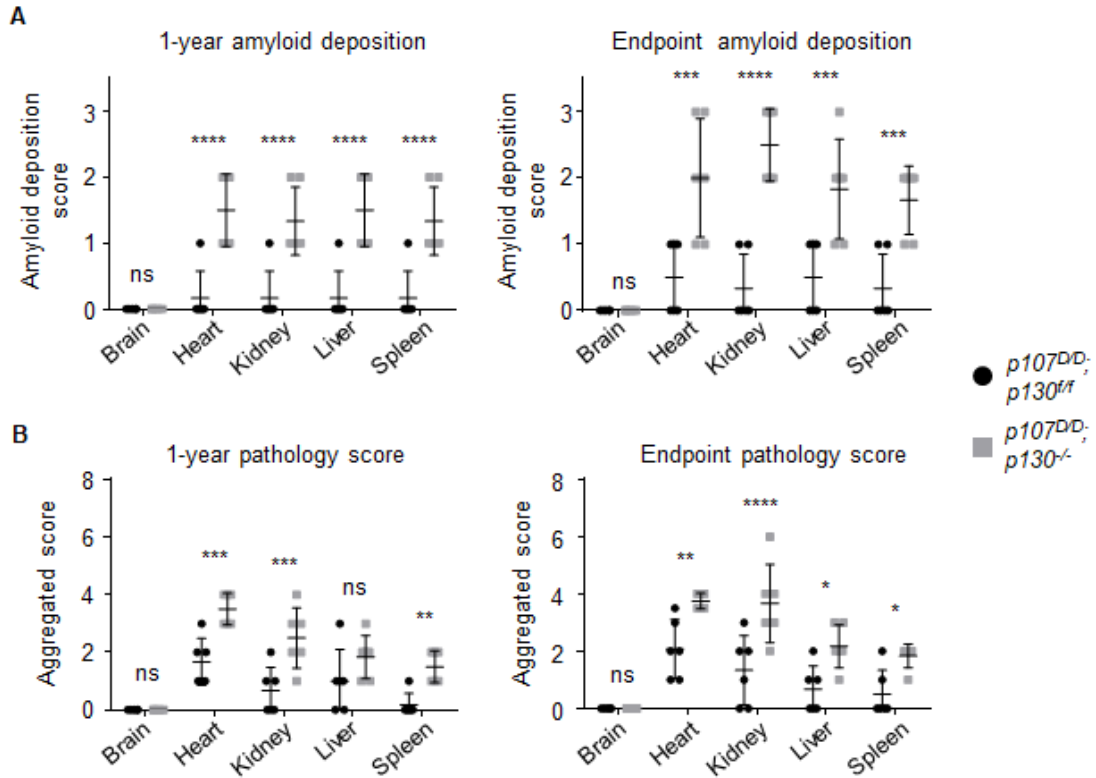


**Figure 2.9. Tissue distribution and disease severity of amyloidosis in  $p107^{D/D};p130^{-/-}$  mice.** (A) Tissues from 1-year and endpoint mice from  $p107^{D/D};p130^{ff}$  and  $p107^{D/D};p130^{-/-}$  cohorts were scored for amyloid deposition on a scale of 0-3 (n=6). Average scores were plotted for 1-year old and endpoint mice and error bars represent one standard deviation. Means were compared by two-way ANOVA and significance levels are indicated (\*\*\*) denotes  $P < 0.001$ ; \*\*\*\* denotes  $P < 0.0001$ ; and ns denotes not significant,  $P > 0.05$ ). (B) Tissues from 1-year old and endpoint mice from  $p107^{D/D};p130^{ff}$  and  $p107^{D/D};p130^{-/-}$  cohorts were scored for three criteria (amyloid deposition, cellular degeneration, inflammation) on a scale of 0-3 (n=6). Scores were aggregated for each mouse and plotted. Mean scores are indicated along with one standard deviation. Means were compared by two-way ANOVA and significance levels are indicated (\* denotes  $P < 0.05$ ; \*\*  $P < 0.01$ ; \*\*\* denotes  $P < 0.001$ ; \*\*\*\* denotes  $P < 0.0001$ ; and ns denotes not significant,  $P > 0.05$ ).

histologic abnormalities found in these tissues was absent from the brain (**Figure 2.9A-B**, and **Figure 2.10**). Collectively, these results indicate  $p107^{D/D};p130^{-/-}$  mice accumulate extensive amyloid fibril deposition in the heart, liver, kidney, and spleen leading to defects in normal organ structure and function. These characteristics are indicative of systemic amyloidosis in  $p107^{D/D};p130^{-/-}$  mice.

#### 2.3.4 Apolipoproteins predominate in amyloid fibrils and are overexpressed in $p107^{D/D};p130^{-/-}$ mice

There are more than 35 amyloid subtypes that have been identified in humans<sup>1,2</sup>. To relate the amyloidosis phenotype in  $p107^{D/D};p130^{-/-}$  mice with human clinical subtypes, we utilized fluorescent optics of Congo Red stained tissue to identify amyloid deposits (**Figure 2.11A-B**). We then performed laser capture microdissection from FFPE tissue sections and used tandem mass spectrometry to determine its protein composition (LMD/MS)<sup>52-54</sup> (**Figure 2.11C**). In LMD/MS analysis, mutations in amyloid causing genes correlate with abundance of their encoded proteins in amyloid deposits<sup>52</sup>. Combined with the increased specificity enabled by focusing only on the Congo Red-stained areas, highly abundant proteins in our analysis may be amyloidogenic in  $p107^{D/D};p130^{-/-}$  mice. Within this proteome, “amyloid signature proteins” are present, which serve as an internal control to denote that amyloid deposition is present. These include apolipoprotein E (apoE), serum amyloid P-component, and possibly clusterin and vitronectin<sup>52,55,56</sup>. Therefore, by examining this enriched Congo Red-stained proteome for the most abundant proteins present, we can identify causative protein candidates from the amyloid plaques in  $p107^{D/D};p130^{-/-}$  mice.

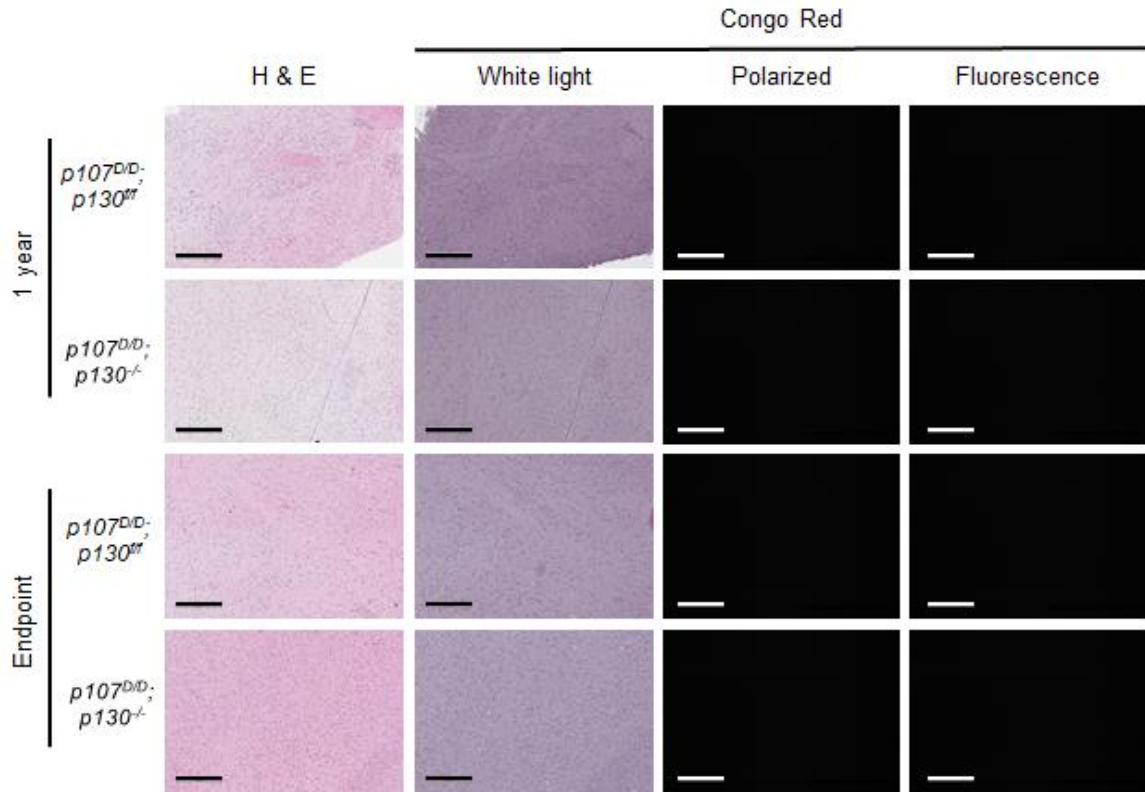


**Figure 2.10. H&E histology of control and  $p107^{D/D};p130^{-/-}$  brains.** Tissue sections were prepared from FFPE brains and stained with H&E or Congo Red. Representative sections used for amyloid scoring, cellular degeneration, and inflammation are shown and ages and genotypes are indicated. Scale bars represent 400  $\mu\text{m}$ .



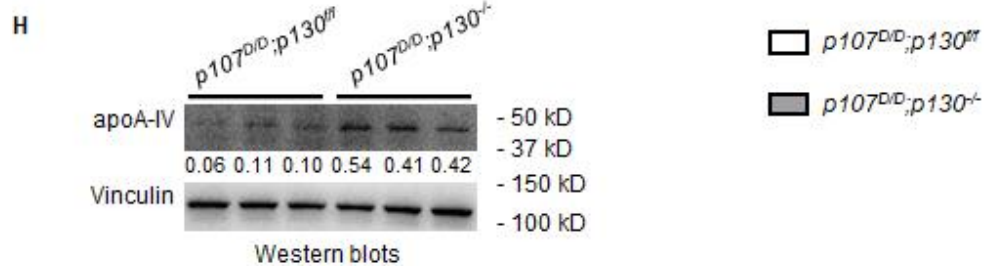
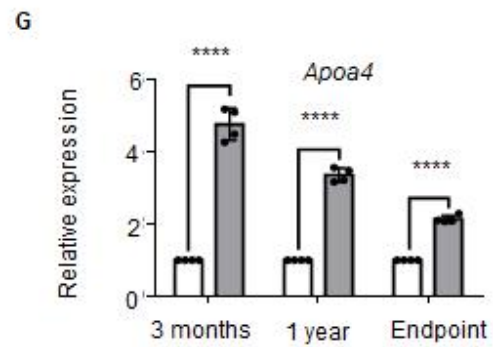
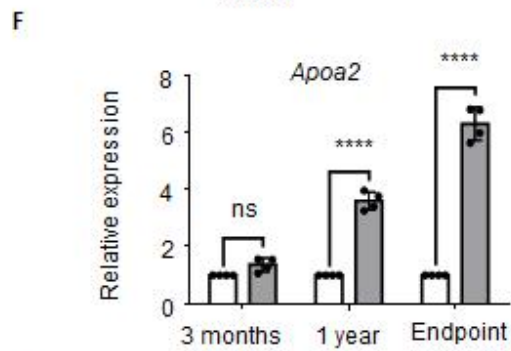
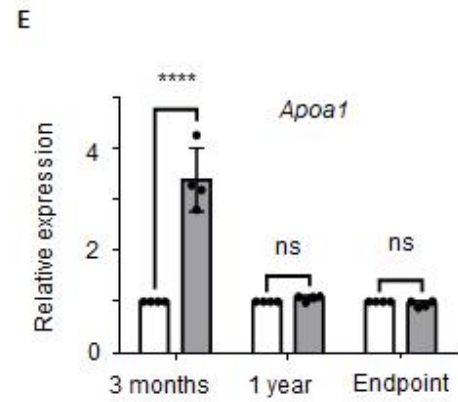
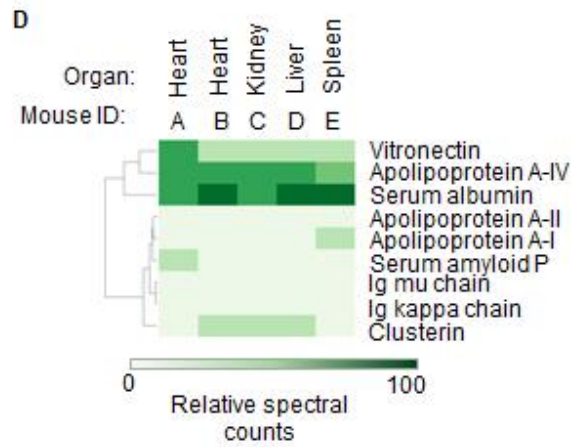
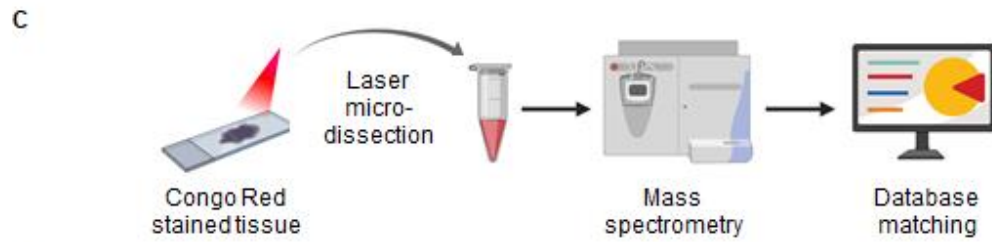
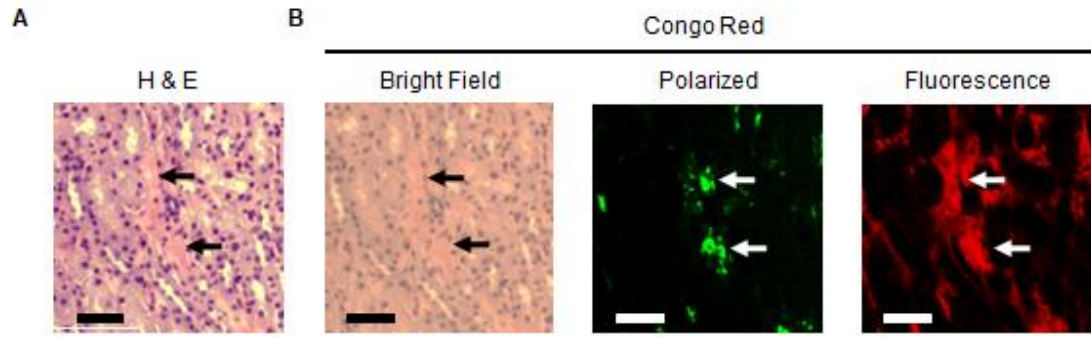


**Figure 2.11. ApoA-IV is the most abundant amyloidogenic protein in  $p107^{D/D};p130^{-/-}$  amyloid deposits.** (A) H&E staining of kidney from an endpoint  $p107^{D/D};p130^{-/-}$  mouse. Arrows indicate acellular eosinophilic material. Scale bar is 50  $\mu\text{m}$ . (B) Congo Red staining of a serial section of the same kidney as in (A). Black arrows indicate the same acellular material under bright field optics as in (A). White arrows mark the same locations under polarized and fluorescent optics. Scale bars are 50  $\mu\text{m}$ . (C) Schematic illustration of LMD/MS procedure: Congo red-positive regions are laser-captured and processed for mass spectrometry to identify peptides present in amyloids. (D) Per spectral match quantities were scaled relative to the most abundant protein in each sample, apoE. Rows (proteins) were clustered and values are represented as indicated by the scale at the bottom. Each column represents an organ from an endpoint  $p107^{D/D};p130^{-/-}$  mouse. (E)-(G) Total RNA used to synthesize cDNA. Gene expression was determined by qPCR in 3-month, 1-year, and endpoint  $p107^{D/D};p130^{ff}$  and  $p107^{D/D};p130^{-/-}$  mice and normalized to *Gapdh* for each age group (n=4). Bar graphs show mean expression values for *Apoa1* (E), *Apoa2* (F), *Apoa4* (G) and error bars represent one standard deviation. Values are normalized to that of  $p107^{D/D};p130^{ff}$  at each age for each gene. Two-way ANOVA was performed for each gene and significance levels are indicated (\*\*\*\* denotes  $P < 0.0001$ ; and ns denotes not significant,  $P > 0.05$ ). (H) Protein extracts from the livers of 3-month old  $p107^{D/D};p130^{ff}$  and  $p107^{D/D};p130^{-/-}$  mice were western blotted for the indicated proteins. Numerical values represent band intensity ratio of apoA-IV relative to vinculin.

LMD/MS analysis was performed on hearts, kidneys, livers, and spleens from endpoint  $p107^{D/D};p130^{-/-}$  mice. This identified a number of known amyloidogenic proteins, as well as common amyloid-accompanying peptides. A representative list of proteins that are known to be causative or associated with amyloidosis in humans, and present in an endpoint  $p107^{D/D};p130^{-/-}$  liver, is shown (**Table 2.1**). Consistent with human clinical cases, the most abundant protein identified in all samples was apoE. Therefore, we normalized spectral counts from each sample to its own apoE and compared the abundance of the remaining amyloidogenic and amyloid-accompanying proteins. Figure 5D shows a heatmap depicting relative spectral counts for each protein across five identically microdissected samples. Among the known amyloidogenic proteins, apolipoprotein A-IV (apoA-IV) consistently had the highest normalized spectral counts (**Figure 2.11D**), followed by apoA-II and apoA-I (**Figure 2.11D**). Immunoglobulin light and heavy chains were also detected in most of these samples at relatively low spectral counts (**Figure 2.11D**). This data suggests that apolipoproteins are the most likely cause of amyloidosis in  $p107^{D/D};p130^{-/-}$  mice.

Amyloid tissue deposition patterns identified by histological analyses and amyloidogenic proteins identified by LMD/MS in  $p107^{D/D};p130^{-/-}$  mice suggests apoA-IV, apoA-II, or apoA-I, or a combination of these as the cause of amyloidosis in these mice. Since DREAM is a transcriptional repressor and its loss promotes assembly of the activating MYB-MuvB complex, we investigated expression levels of these apolipoproteins. We performed qPCR analysis of RNA isolated from livers of 3-month, 1-year, and endpoint  $p107^{D/D};p130^{ff}$  and  $p107^{D/D};p130^{-/-}$  mice (**Figure 2.11E-G**). Each of *Apoa1*, *Apoa2*, and *Apoa4* were found to be over expressed in at least one of the time points

**Table 2.1 LMD/MS analysis of an endpoint *p107<sup>D/D</sup>;p130<sup>-/-</sup>* liver**

Per spectral match quantities for each protein in the amyloid samples are shown in descending order. Presumptive amyloidogenic proteins are indicated with \*, while known amyloid-associated proteins are

Identified peptides	Per spectral match
Apolipoprotein E <sup>#</sup>	34
Serum albumin <sup>#</sup>	33
Apolipoprotein A-IV <sup>*</sup>	21
Apolipoprotein A-II <sup>*</sup>	9
Vitronectin <sup>#</sup>	9
Clusterin <sup>#</sup>	7
Serum amyloid P-component <sup>#</sup>	6
Apolipoprotein A-I <sup>*</sup>	3
Ig kappa chain	3
Ig mu	3

investigated. Only *Apoa4* was significantly increased in  $p107^{D/D};p130^{-/-}$  mice at all ages of investigation (**Figure 2.11G**), and its protein levels were approximately 4-fold increased in liver extracts from 3-month old  $p107^{D/D};p130^{-/-}$  mice (**Figure 2.11H**), further suggesting that it is the best candidate to be a causative protein in the amyloidosis observed. In addition, we investigated the expression of amyloid associated components albumin, serum amyloid P-component, and apolipoprotein E. Consistent with an associated role, *Alb*, *Apcs*, and *ApoE* expression in the livers of  $p107^{D/D};p130^{-/-}$  mice was unaltered (**Figure 2.12**).

An alternative interpretation of the LMD/MS data is that, although the spectral counts for immunoglobulin chains were low, they may play a causative role too. Since DREAM is known to function in proliferative control, and immunoglobulin amyloidosis is common in myeloma patients, we investigated this possibility further. We found the expression of *Ighm* to be significantly increased in the bones and spleens of 1-year and endpoint  $p107^{D/D};p130^{-/-}$  mice compared with controls (**Figure 2.13**). However, a key difference between apolipoprotein- and immunoglobulin-based amyloidoses in human patients is the presence of amyloid deposits in bone marrow and the gastrointestinal track<sup>57</sup>. Neither H&E or Congo Red staining in endpoint  $p107^{D/D};p130^{-/-}$  mice identified amyloid deposits in bone marrow, nor did it reveal the presence of abnormally proliferating plasma cells (**Figure 2.14A**). Examination of the small intestines of endpoint  $p107^{D/D};p130^{-/-}$  mice stained with Congo Red showed scattered amyloid deposits, but nothing distinct by H&E staining as in the previously described organs above (**Figure 2.14B**). Overall, the lack of bone marrow amyloids and only minor intestinal amyloids, but prominent cardiac, renal, hepatic, and splenic involvement is most consistent with an apolipoprotein-derived amyloid condition. In addition, apolipoprotein misexpression and greater detection levels

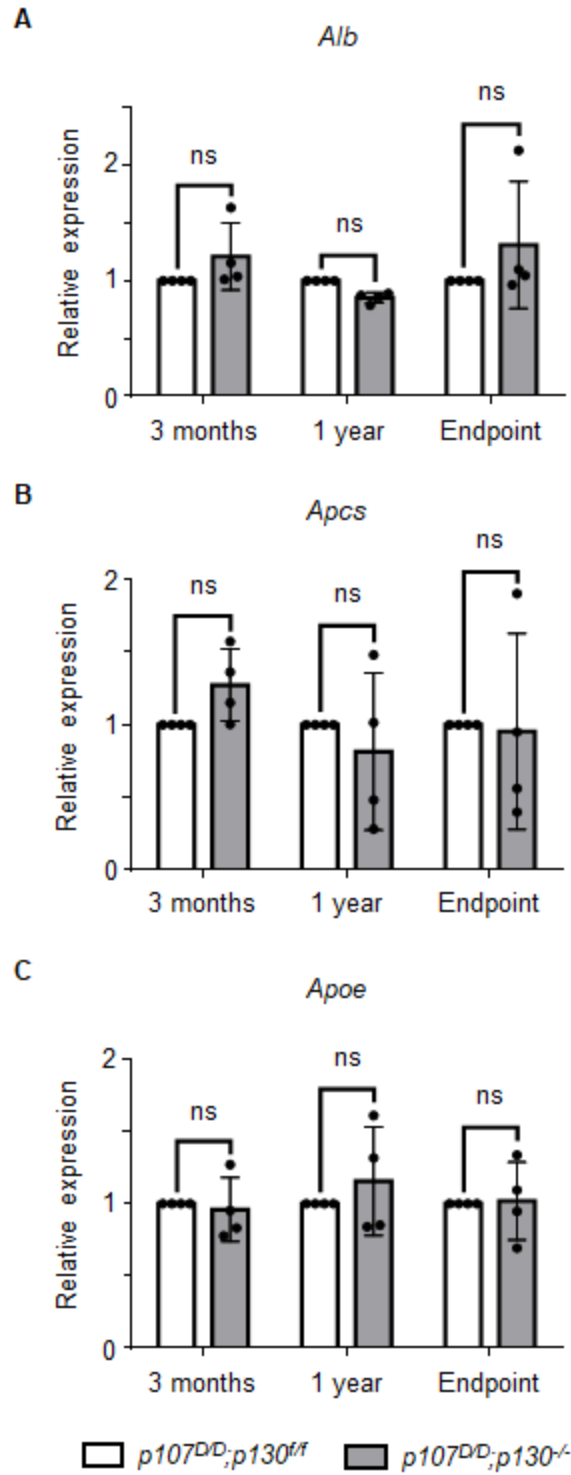


**Figure 2.12. Normal expression of amyloid associated protein coding genes in  $p107^{D/D};p130^{-/-}$  mice.** (A)-(C): Gene expression in 3-month, 1-year, and 2-year old endpoint  $p107^{D/D};p130^{ff}$  and  $p107^{D/D};p130^{-/-}$  livers was assayed by real time qPCR for *Alb* (serum albumin) (A), *Apcs* (serum amyloid P-component) (B), and *ApoE* (apolipoprotein E) (C) (n=4). Expression values are normalized using *Gapdh* to that of  $p107^{D/D};p130^{ff}$  at each age for each gene. Two-way ANOVA was performed for each gene; ns=not significant.

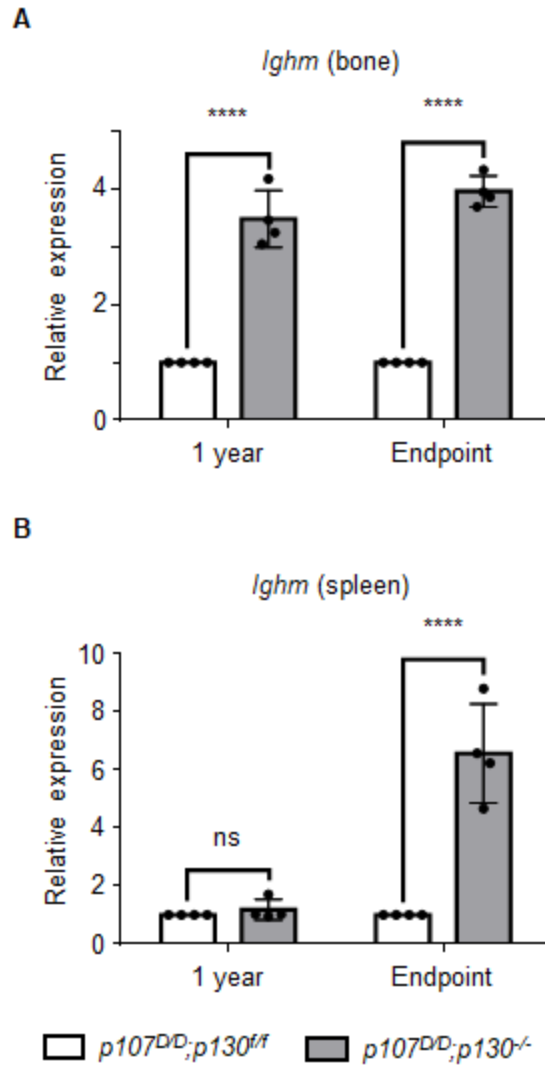


**Figure 2.13. *Ighm* is overexpressed in  $p107^{D/D};p130^{-/-}$  bone and spleen. (A)-(B):** Expression of *Ighm* in 1-year and 2-year old endpoint  $p107^{D/D};p130^{ff}$  and  $p107^{D/D};p130^{-/-}$  mice was assayed by real time qPCR in bone (A) and spleen (B) tissue (n=4). Expression values are normalized to *Gapdh* in  $p107^{D/D};p130^{ff}$  samples at each age. Two-way ANOVA was performed and significance levels are indicated (\*\*\*\* denotes  $P < 0.0001$ ; and ns denotes not significant,  $P > 0.05$ ).



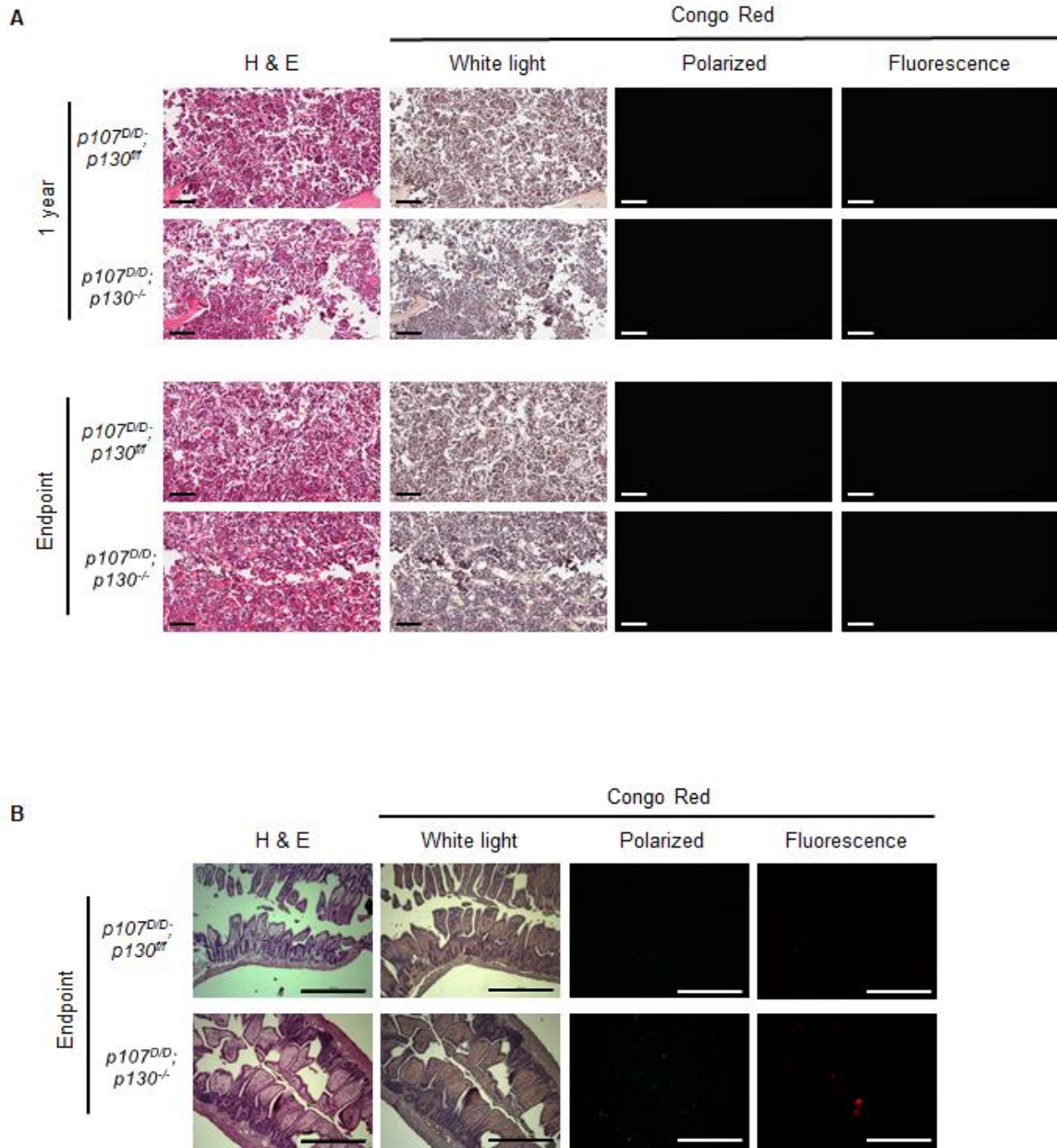


**Figure 2.14. Absence of myeloma like amyloid deposits in *p107<sup>D/D</sup>;**p130<sup>-/-</sup>* mice. (A) Bone tissues were harvested from 1-year and 2-year old endpoint *p107<sup>D/D</sup>;**p130<sup>ff</sup>* and *p107<sup>D/D</sup>;**p130<sup>-/-</sup>* mice. Bones were formalin fixed, demineralized, and stained with H&E or Congo Red. Amyloid deposition was investigated by apple green birefringence and red fluorescence. Scale bars represent 100  $\mu$ m. (B) Intestines were harvested from endpoint *p107<sup>D/D</sup>;**p130<sup>ff</sup>* and *p107<sup>D/D</sup>;**p130<sup>-/-</sup>* mice, fixed, and stained with H&E or Congo Red and analyzed microscopically as before. Scale bars represent 500  $\mu$ m.**

in LMD/MS experiments suggest that they are the more likely cause of amyloidosis in *p107<sup>D/D</sup>;p130<sup>-/-</sup>* mice. Lastly, the most consistent and highly overexpressed apolipoprotein in the liver was apoA-IV and its prominent detection in amyloids indicates that it is the most likely source of misexpressed protein to seed amyloid formation.

### 2.3.5 DREAM disruption leads to H2AZ loss at apolipoprotein genes.

Based on MYB-MuvB binding to the *Mybl2* promoter upon *p130* deletion in our initial characterization of this genetic model, we sought to determine if DREAM loss misregulated apolipoprotein genes. A genome-wide analysis of predicted CHR and CDE motifs has identified candidates for DREAM/ MYB-MuvB regulation<sup>20</sup>. From this dataset, *Apoa1* and *Apoa4* were found to possess both elements and others such as *Alb* and *Apoa2* possess CHR motifs. We performed quantitative chromatin immunoprecipitation (ChIP-qPCR) assays on chromatin from livers of 3-month old mice to determine if DREAM/MYB-MuvB bind any of these promoters (**Figure 2.15A-D**). We detected p107<sup>D</sup> binding to the transcriptional start site (TSS) region of each of these genes in *p107<sup>D/D</sup>;p130<sup>ff</sup>* mice. However, the recruitment of p107<sup>D</sup> was significantly reduced in *p107<sup>D/D</sup>;p130<sup>-/-</sup>* livers at *Apoa1* and *Apoa4* promoters (**Figure 2.15A&C**). The decrease in p107<sup>D</sup> occupancy was accompanied by an increase in B-MYB at the same locations, comparable to what was observed at the *Mybl2* promoter (**Figure 2.1C**) that is indicative of MYB-MuvB binding (**Figure 2.15A&C**). H2AZ – the histone H2A variant that accompanies DREAM-mediated repression in lower organisms<sup>17</sup> – was similarly analyzed. We performed ChIP-qPCR for H2AZ at *Apoa1* and *Apoa4* gene bodies and saw a marked

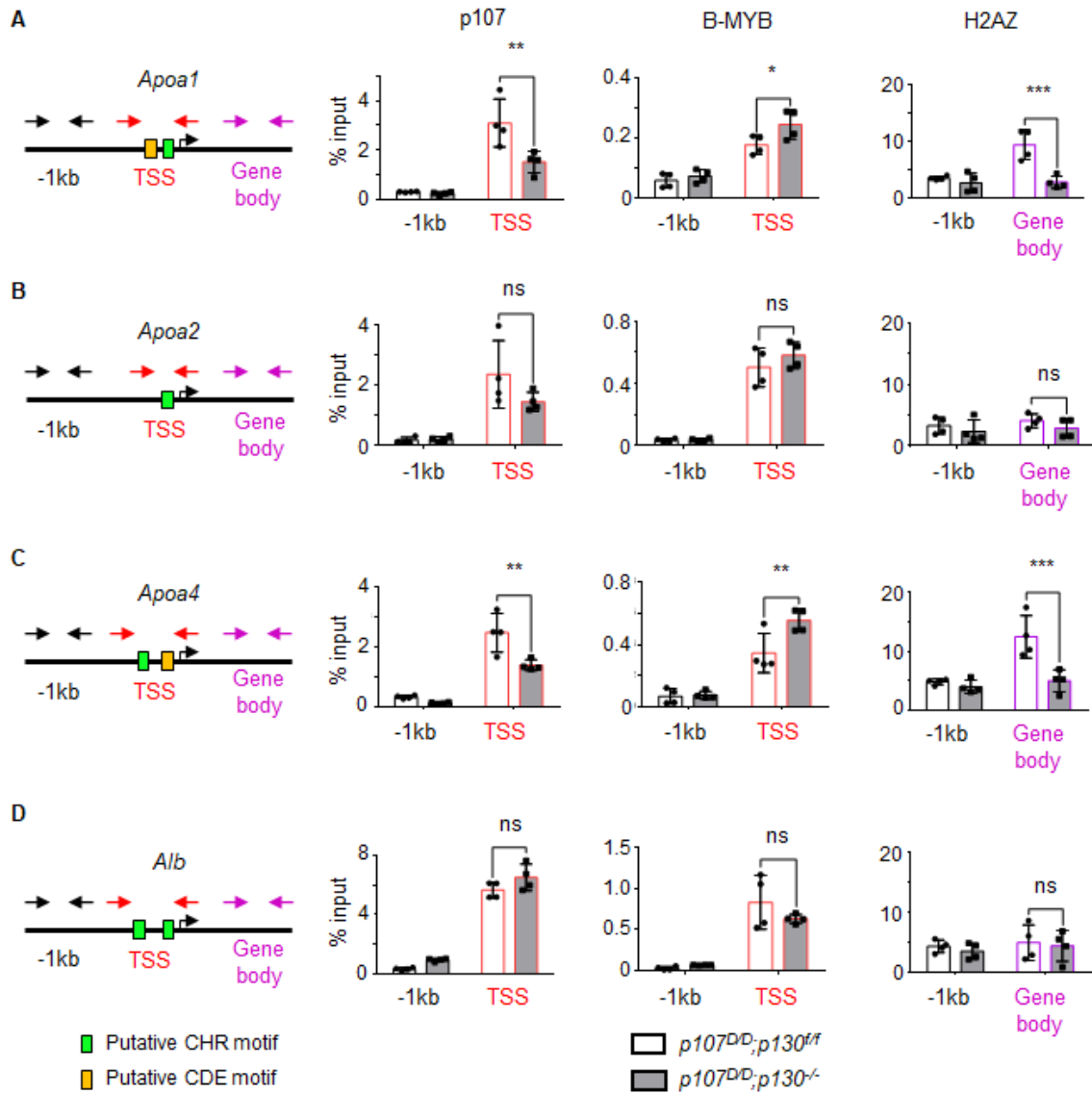


**Figure 2.15. B-MYB is recruited to *Apoa1* and *Apoa4* promoters in DREAM assembly-deficient *p107<sup>D/D</sup>;p130<sup>-/-</sup>* mice.** (A)-(D) Chromatin was prepared from livers of 3-month old *p107<sup>D/D</sup>;p130<sup>fl/fl</sup>* and *p107<sup>D/D</sup>;p130<sup>-/-</sup>* mice and utilized in ChIP assays to detect p107<sup>D</sup>, B-MYB, and H2AZ occupancy at promoters (n=4). For each of *Apoa1* (A), *Apoa2* (B), *Apoa4* (C), and *Alb* (D) genes, a schematic is shown to illustrate primer annealing sites. Arrows depicting primers are color coded: black represents a neutral location 1 kb upstream of the transcriptional start site (TSS); red is an approximately 100 bp region encompassing the CHR and/or CDE motifs near the TSS; purple is within the gene body. ChIP protein targets p107, B-MYB, and H2AZ are organized in columns across the top. Bar graphs depict the mean quantity of chromatin associated with each protein target as detected by qPCR and error bars represent one standard deviation. Two-way ANOVA was performed for each and significance levels are indicated (\* denotes P < 0.05; \*\* P < 0.01; \*\*\* denotes P < 0.001; and ns denotes not significant, P > 0.05).

decrease in  $p107^{D/D};p130^{-/-}$  livers (**Figure 2.15A&C**). Importantly, *Apoa2* and *Alb* exhibited only background levels of H2AZ that were not altered between genotypes, suggesting that these genes are not *bona fide* DREAM targets (**Figure 2.15B&D**). Overall, these data provide evidence of direct transcriptional regulation of *Apoa1* and *Apoa4* by DREAM/MYB-MuvB through the CHR and CDE motifs found in their proximal promoters. Furthermore, *Apoa1* and *Apoa4* lose H2AZ from their gene bodies when DREAM loss is replaced by MYB-MuvB. This data connects DREAM assembly defects to loss of transcriptional control of apolipoprotein genes that leads to protein overexpression and systemic amyloidosis in  $p107^{D/D};p130^{-/-}$  mice.

## 2.4 Discussion

In the present study, we demonstrated loss of DREAM assembly leads to the development of systemic amyloidosis in adult  $p107^{D/D};p130^{-/-}$  mice. The absence of DREAM increased MYB-MuvB recruitment to *Apoa1* and *Apoa4* promoters and is correlated with reduced H2AZ levels and overexpression of *Apoa1* and *Apoa4* genes (**Figure 2.16A**). These mice develop extensive amyloid deposition in the heart, kidney, liver, and spleen but not in the brain or bone. Using mass spectrometry, we discovered similar amyloidogenic and amyloid signature proteins in affected organs that implicated apoA-IV as the most likely causative amyloidogenic protein in  $p107^{D/D};p130^{-/-}$  mice (**Figure 2.16B**). This condition lead to compromised renal function, and likely other organ defects, and a shorter lifespan for  $p107^{D/D};p130^{-/-}$  mice (**Figure 2.16C**). Overall, this mouse model represents an important milestone in understanding idiopathic amyloidosis cases.

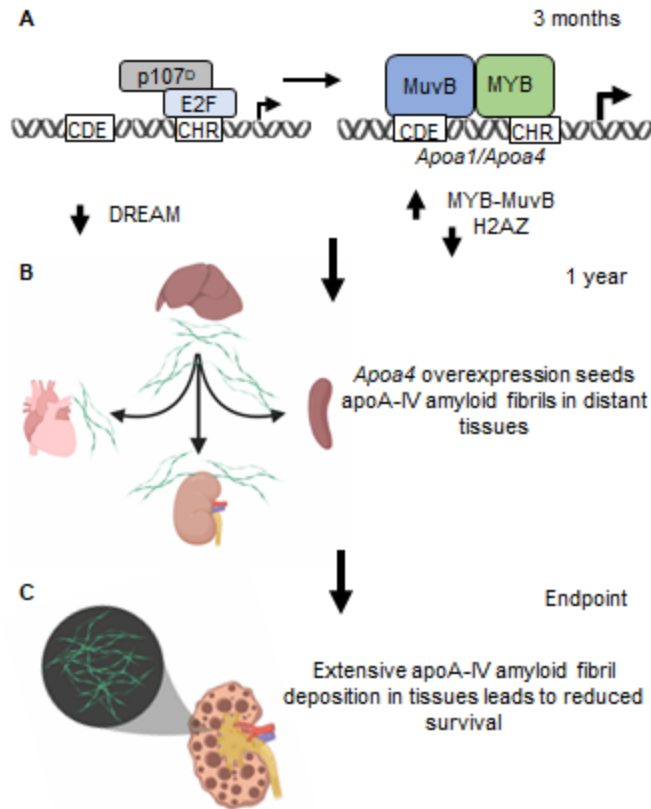


**Figure 2.16. Loss of DREAM assembly in  $p107^{D/D};p130^{-/-}$  mice promotes MYB-MuvB assembly that drives systemic AApoAIV amyloidosis due to constitutive overexpression of *Apoa4*.** A schematic model illustrating the development of systemic AApoAIV amyloidosis in  $p107^{D/D};p130^{-/-}$  mice. At 3-months of age, ablation of p130 by Cre activation combined with mutant p107<sup>D</sup> prevents DREAM assembly and promotes MYB-MuvB activation of transcription. In the liver, MYB-MuvB occupies CHR and CDE motifs at the transcriptional start sites of apolipoprotein genes, particularly *Apoa4*, leading to reduced H2AZ occupancy within its gene body and constitutive overexpression (A). In 1-year old  $p107^{D/D};p130^{-/-}$  mice, small amyloid deposits are evident in the heart, liver, kidney, and spleen (B). By 2-years of age, apoA-IV deposition is more pronounced in the heart, liver, and spleen. Deposition in the kidney of most  $p107^{D/D};p130^{-/-}$  mice leads to organ failure and reduced survival (C).

The phenotype of *p107<sup>D/D</sup>;p130<sup>-/-</sup>* mice, characterized by AApoA-IV amyloidosis, includes other provocative similarities with clinical reports of this condition. Amyloid deposition in *p107<sup>D/D</sup>;p130<sup>-/-</sup>* mice was most apparent in kidneys and found throughout the renal interstitium between the cortex and medulla. Similarly, the first reported case for AApoAIV and subsequent analysis of additional AApoAIV patients revealed extensive amyloid deposition in the interstitial space of the medulla<sup>16,58</sup>. LMD/MS analysis of these patients identified apoA-IV as the major constituent of amyloid fibrils in the kidney along with apoE, serum amyloid P-component, and serum albumin<sup>16,58</sup>, thus matching our findings here. ApoA-I and immunoglobulin light chain peptides were also present in AApoAIV, but at lower levels<sup>16,58</sup>. The involvement of apoE, serum amyloid P-component, and serum albumin in forms of amyloidosis outside of the affected organs observed here further suggests apoA-IV is most likely the causative component of the amyloid. Therefore, our analysis of systemic amyloidosis in *p107<sup>D/D</sup>;p130<sup>-/-</sup>* adult mice is consistent with clinically observed characteristics of AApoAIV. AApoAIV is a newly described form of amyloidosis that has only begun to be appreciated when revealed by LMD/MS analysis. The lack of an underlying mutation in the apoA-IV encoding gene in these patients has created challenges in identifying the source of this disease and its classification. Our data from *p107<sup>D/D</sup>;p130<sup>-/-</sup>* mice indicates that apolipoprotein misexpression and amyloid deposition may result from a host of different sources that converge on H2AZ regulation and underscores our discovery of this epigenetic source of amyloidosis.

Unlike hereditary amyloidosis caused by apoA-I or apoA-II whereby genetic mutations in *Apoa1* or *Apoa2* lead to  $\alpha$ -helix to  $\beta$ -sheet conformational changes in protein structure that ultimately manifest as amyloid fibrils<sup>5</sup>, no such genetic variants have been

implicated in AApoAIV<sup>15</sup>. Binding with HDL or protein-protein interactions are thought to protect apoA-IV's amyloidogenic hotspot regions within its core  $\alpha$ -helices<sup>5</sup>. It can therefore be surmised that overexpression of *Apoa4* may create an imbalance in the concentration of apoA-IV compared to its partner lipids or proteins, thereby increasing the propensity to form amyloid fibrils. Herein, we showed loss of DREAM assembly in *p107<sup>D/D</sup>;p130<sup>-/-</sup>* mice leads to consistent overexpression of *Apoa4* at every age we investigated whereas *Apoa1* overexpression only occurred in 3-month old mice. We observed a direct interaction of p107 and B-MYB with the *Apoa1* and *Apoa4* transcription start sites which contain putative CHR and CDE sites<sup>20</sup>. It is known that loss of DREAM causes a dynamic shift in which the transcriptional activator MYB-MuvB occupies the start site and activates expression<sup>23,36</sup>. Our data demonstrates this switch occurs with a concomitant reduction of the H2AZ repressive mark within *Apoa1* and *Apoa4* gene bodies. This suggests that these are specific and important DREAM target genes and that a combination of H2AZ reduction and MYB-MuvB activation increase their expression. Prior work on worms and flies established DREAM as a regulator of gonadal and sex specific gene expression in addition to cell cycle control<sup>59</sup>; our study indicates that apolipoprotein gene expression is a critical category of DREAM target genes required in mammalian physiology.

In this study we have shown that DREAM loss and gain of MYB-MuvB activates expression of *Apoa4* to drive AApoAIV-mediated amyloidosis. This suggests that enhancement of DREAM or attenuation of B-MYB may offer therapeutic benefit in treating AApoAIV. Additionally, understanding other epigenetic regulators that may help



to control H2AZ deposition levels at these genes are also potential targets to ameliorate expression of amyloidosis causing apolipoprotein genes in the future.

## 2.5 Materials and Methods

### 2.5.1 Mouse genetics

We utilized our mice that are homozygous for *Rbl1*<sup>tm1.1Fad</sup> (referred to as *p107*<sup>D/D</sup>)<sup>36</sup> and *Rbl2*<sup>tm2.1Tyj</sup> (referred to as *p130*<sup>ff</sup>, stock# 008177 Jackson Labs)<sup>35</sup>, in which exon 2 of *p130* is flanked by *loxP* sites. Experimental mice possessed the *Ndor1*<sup>Tg(UBC-cre/ERT2)1Ejb</sup> transgene<sup>38</sup> that was also obtained from Jackson Labs (stock# 007001), while control animals were *p107*<sup>D/D</sup>;*p130*<sup>ff</sup>. All mice received tamoxifen administration intraperitoneally at 8 weeks of age (75 mg/kg body weight administered in corn oil every 24 hours for 3 consecutive days). This experimental design with a Cre deficient cohort allowed us to control for potential tamoxifen induced liver injury in this study<sup>60,61</sup>.

### 2.5.2 Genotyping p130 exon 2 deletion in mice

DNA was isolated from the tail, muscle, liver, heart, brain, testis, and bone from mice 1-week and approximately 2 years after tamoxifen administration. PCR was performed to amplify the region surrounding exon 2 and the products were resolved on agarose gels using standard protocols. Primer sequences are listed in **Table 2.2**.

**Table 2.2 Primers used for PCR experiments in Chapter 2**

Primer	Sequence
p130 ( <i>Rbl2</i> ) PCR forward	GTGTTGTAACATTCTCGTGGG
p130 ( <i>Rbl2</i> ) PCR reverse	GTGTTGTAACATTCTCGTGGG
<i>Apoa1</i> qPCR forward	GTGGCTCTGGTCTTCCTGAC
<i>Apoa1</i> qPCR reverse	ACGGTTGAACCCAGAGTGTC
<i>Apoa2</i> qPCR forward	GCCTGTTCACTCAGTACTTTCAG
<i>Apoa2</i> qPCR reverse	CAGACTAGTTCCTGCTGACC
<i>Apoa4</i> qPCR forward	ATGCCAAGGAGGCTGTAGAA
<i>Apoa4</i> qPCR reverse	CAGTTTCCTGGGCTAGATGC
<i>Alb</i> qPCR forward	CATGTTGCAAGGCTGCTGACAAG
<i>Alb</i> qPCR reverse	AGTGACAAGGTTTGGACCCTCAG
<i>Apcs</i> qPCR forward	TGGACCAAGCATGGACAAGCTAC
<i>Apcs</i> qPCR reverse	GGCTTCTGAAAGAAGGCTGGTG
<i>ApoE</i> qPCR forward	GGACTTGTTTCGGAAGGAGCTGAC
<i>ApoE</i> qPCR reverse	TTGCCACTCGAGCTGATCTGTCAC
<i>Ighm</i> qPCR forward	CACCCATCCACCTGGCTGCTCA
<i>Ighm</i> qPCR reverse	AATGGTGCTGGGCAGGAAGT
<i>Gapdh</i> qPCR forward	TGCACCACCAACTGCTTAG
<i>Gapdh</i> qPCR reverse	GGATGCAGGGATGATGTTC
<i>Ccna2</i> probe forward	TGTCGCCTTGAATGACGTCA
<i>Ccna2</i> probe reverse (biotinylated)	ACCCACCCTCCTGCAGATAT
<i>Actb</i> probe forward	AGAGCTACGAGCTGCCTGAC
<i>Actb</i> probe reverse (biotinylated)	AGCACTGTGTTGGCGTACAG
<i>Mybl2</i> -1kb body ChIP-qPCR forward	GCCTGAGCCTAAAGGGCATT
<i>Mybl2</i> -1kb body ChIP-qPCR reverse	TCTGATGGCAAGGGTTGTCTC
<i>Mybl2</i> TSS ChIP-qPCR forward	ACGCACTTGGCGGGAGATAG
<i>Mybl2</i> TSS ChIP-qPCR reverse	CTCAGGCGTCAGCGTGTCT
<i>Apoa1</i> -1kb ChIP-qPCR forward	CCAAGTGCAAAAACCTGGCCA
<i>Apoa1</i> -1kb ChIP-qPCR reverse	GTCTTCCCAGAGTGGTGAGG
<i>Apoa1</i> TSS ChIP-qPCR forward	GGCCAGGCTGAGCTTATCAG
<i>Apoa1</i> TSS ChIP-qPCR reverse	TCCGACAGTCTGGGTGTCCA
<i>Apoa1</i> gene body ChIP-qPCR forward	CAGAAGCTGCAGGAGCTGCAAG
<i>Apoa1</i> gene body ChIP-qPCR reverse	CTAGCTGTGTGCGCAGAGAGTCTA
<i>Apoa2</i> -1kb ChIP-qPCR forward	AGGAATTTTCATTCATGAGACCTATCA
<i>Apoa2</i> -1kb ChIP-qPCR reverse	CACACACACACACACACC

**Table 2.2** continued from previous page

<b>Primer</b>	<b>Sequence</b>
<i>Apoa2</i> TSS ChIP-qPCR forward	GCCATTCTCCGTATCACCTGACGG
<i>Apoa2</i> TSS ChIP-qPCR reverse	CTGCAGTCCTTCCCGTCTACTCT
<i>Apoa2</i> gene body ChIP-qPCR forward	GAGCTTTGGTTAAGAGACAGGCAGAC
<i>Apoa2</i> gene body ChIP-qPCR reverse	CAGAGACTTACTTGGCCTGGC
<i>Apoa4</i> -1kb ChIP-qPCR forward	AGCAAATCAGACTGGGCACA
<i>Apoa4</i> -1kb ChIP-qPCR reverse	GGGCATCCATCATACTGTCCC
<i>Apoa4</i> TSS ChIP-qPCR forward	GCTGTCAGCTTCCACGTTGTCTTAG
<i>Apoa4</i> TSS ChIP-qPCR reverse	TCCCCAGTGTGACTCCACGTTG
<i>Apoa4</i> gene body ChIP-qPCR forward	CGACGCACTGTGGAGCCCATG
<i>Apoa4</i> gene body ChIP-qPCR reverse	GCTCAAGTGGCTTTCCACCTCC
<i>Alb</i> -1kb ChIP-qPCR forward	TGAGGACACAAGATGAGGTCA
<i>Alb</i> -1kb ChIP-qPCR reverse	AGAGAGGAGGAGGAGGAAGAG
<i>Alb</i> TSS ChIP-qPCR forward	CTGAGCCAGACATTCCCCAA
<i>Alb</i> TSS ChIP-qPCR reverse	ATTCCAGCAGGTCACCATGG
<i>Alb</i> gene body ChIP-qPCR forward	AGTGAGGTGGAGCATGACAC
<i>Alb</i> gene body ChIP-qPCR reverse	AAGACATCCTTGGCCTCAGC

### 2.5.3 Western blotting

Tissues were collected from mice and homogenized using an automatic homogenizer in complete RIPA buffer with protease inhibitors (Sigma #S8820) and incubated for 1 hour on ice. Samples were centrifuged at 12 000 g in a 4°C centrifuge. The supernatant was collected, and protein concentration was determined by Bradford assay. Lysates were mixed with 6x SDS loading dye buffer and resolved using standard SDS-PAGE protocols in 8% acrylamide gels. Antibodies used for blotting were p107 (MyBioSource anti-p107 rabbit antibody #MBS440044), p130 (Santa Cruz anti-p130 rabbit antibody #SC-317), apoA-IV (Cell Signaling Technology anti-ApoA4 mouse antibody #5700), tubulin (Cell Signaling Technology anti-Tubulin rabbit antibody #2125), and vinculin (Cell Signaling Technology anti-Vinculin rabbit antibody #4650). Band intensities were measured and analyzed in ImageJ version 1.53c.

### 2.5.4 Chromatin immunoprecipitation (ChIP)

ChIP assay was performed as described previously<sup>62,63</sup>. Livers were harvested from 3-month old *p107<sup>D/D</sup>;p130<sup>ff</sup>* and *p107<sup>D/D</sup>;p130<sup>-/-</sup>* mice mid-morning. Livers were weighed and cut into 60 mg pieces that were then homogenized in ice cold PBS using an automatic homogenizer. Samples were incubated with 1% formaldehyde for 10 minutes on a rotator at room temperature. Samples were then sonicated. 50 µL protein A/G Dynabeads (Invitrogen) were premixed with ChIP antibodies (p107: 10 µg, MyBioSource anti-p107 rabbit antibody #MBS440044; B-MYB: 10 µg, Millipore Sigma anti-B-MYB mouse antibody #MABE886; H2AZ: 5 µg, Abcam anti-Histone H2A.Z rabbit antibody #ab4174) and then combined with lysed and sonicated samples and incubated overnight at 4°C with

rotation. Dynabeads were then washed and chromatin was eluted using elution buffer (1% SDS, 0.1 M NaHCO<sub>3</sub>) following de-crosslinking DNA was isolated. The resulting ChIP DNA was analyzed by qPCR (as described above) with primers pairs designed to amplify -1 kilobases (kb) upstream of the transcriptional start site (neutral location), primers to amplify the proximal promoter regions, and primers to amplify within the gene bodies of *Apoa1*, *Apoa2*, *Apoa4*, *Alb*, and *Mybl2* (**Table 2.2**).

### 2.5.5 Ccna2 promoter pulldown

Primer pairs (**Table 2.2**) were used to amplify the promoter region of *Ccna2* containing a cell cycle-dependent element (CDE) and a cell cycle genes homology region (CHR) and *Actb*, such that only one primer was biotinylated resulting in the amplicon being biotinylated at one end. These were purified using a PCR cleanup kit (Invitrogen). Dynabeads were washed and prepared in 2x binding & washing buffer (10 mM Tris-HCl pH 7.5, 1 mM EDTA, 2 M NaCl). An equal volume of purified PCR fragments in nuclease free water were added and incubated for 15 minutes at room temperature on a rotator. Dynabeads were then washed 3x with 1x binding and washing buffer and after the final wash, all buffers were removed from the tube. Lysates obtained from livers of 3-month old *p107<sup>D/D</sup>;p130<sup>ff</sup>* and *p107<sup>D/D</sup>;p130<sup>-/-</sup>* mice as described above. one mg of protein in RIPA lysis buffer was added to the Dynabeads as well as 0.1 μL of 10% NP-40 and mixed overnight at 4°C. Dynabeads were then washed twice in lysis buffer and 50 μL release buffer (10 mM EDTA pH 8.2 with 95% formamide) was added and incubated for 2 minutes at 90°C. Supernatant containing bound proteins was collected, 5x SDS loading dye was added, and proteins were resolved by SDS-PAGE and identified by western blotting.

### 2.5.6 Tissue preparation and staining

Mice were either aged until their endpoints or sacrificed at an earlier time point. The following organs were collected and fixed in formalin: brain, heart, lungs, liver, kidney, spleen, ovaries, testes, and lymph nodes. Tissues were processed and sectioned in the Molecular Pathology core facility at Robarts Research Institute (London, Canada). Stained with H&E or Congo Red was carried out by the core facility using standard methods.

### 2.5.7 Scoring amyloid damage to tissues

Tissues stained with H&E or Congo Red were scored for amyloid deposition, cellular degeneration, and inflammation each on a scale of 0-3 as per the criteria shown in **Figure 2.8**. Cumulative scores from all three categories were used to determine an aggregated, semiquantitative pathology score for each tissue and timepoint.

### 2.5.8 Proteinuria assay

Urine from mice was collected and assayed for protein as previously described<sup>44</sup>. Briefly, urine was directly collected into 1.5 mL tubes. 9-parts urine was mixed with 1-part 10x SDS loading dye buffer. 10  $\mu$ L urine per mouse was resolved by SDS-PAGE gels and proteins were stained with Coomassie Blue to visualize proteins.

### 2.5.9 Creatinine assay

Whole blood was collected through cardiac puncture from approximately 2-year old endpoint mice. Blood was allowed to clot undisturbed at room temperature for 15 minutes and the clot was removed by centrifugation at 2,000 g for 15 minutes to separate serum. Serum was diluted 1:1000 and assayed in triplicates using Abcam Creatinine Assay Kit (#ab65340). Samples were measured fluorometrically using a Wallac 1420 Victor2 microplate reader (Perkin Elmer Informatics, Waltham, MA) at Ex/Em 538/587 nm.

### 2.5.10 Protein identification

MALDI-MS was performed at the London Regional Proteomics Centre (London, Canada). Briefly, Coomassie Blue stained bands were excised and in gel digested using a MassPREP automated digester (PerkinElmer, Downers Grove, IL). Peptides were ionized with an AB Sciex 5800 TOF/TOF using a TOF/TOF Series Explorer data acquisition system. Protein identification was made using the Mascot search engine.

### 2.5.11 Transmission Electron Microscopy (TEM)

TEM was performed at the Biotron (London, Canada) on paraffin-embedded tissue blocks. Fragments of paraffin embedded tissue were cut into 1 mm<sup>3</sup> pieces using a biopsy punch. Using the methods of Lighezan et al.<sup>64</sup>, tissues were deparaffinized in xylene three times for 30 minutes at room temperature. Specimens were then rehydrated in a descending series of ethanol solutions followed by rinsing in 0.1 M cacodylate buffer for 10 minutes. Tissues were then post-fixed in a 3% glutaraldehyde in 0.1 M cacodylate buffer (pH 7.4) overnight (~12 hours) at 4°C and then were rinsed in 0.1 M cacodylate buffer. Post-fixation

was carried out for 1 hour with 1.0% osmium tetroxide in 0.1 M cacodylate buffer. Specimens were dehydrated in an ascending series of ethanol solutions and embedded in Spurr's resin at 60°C for 2 days. Ultra-thin (70 nm) sections were cut using an ultramicrotome (Ultramicrotome Reichert-Jung Ultracut E; Leica Microsystems, Wetzlar, Denmark). Imaging was carried out using a Philips CM10 transmission electron microscope (Philips Electron Optics, Eindhoven, The Netherlands) and amyloid fiber diameters was measured using CM10 image analysis software.

#### 2.5.12 Amyloid subtyping by laser microdissection mass spectrometry (LMD/MS)

Sample preparation and proteomics analysis were performed at University Health Network's Laboratory Medicine Program (Toronto, Canada). A modified method previously published by Dogan's group<sup>65</sup>, was used for protein extraction from mouse tissue. Briefly, a 10 µm thick section of formalin-fixed paraffin-embedded (FFPE) tissue was mounted on a Director slide (NantOmics, Rockville, MD) and stained with Congo red. Amyloid-positive regions were then extracted with the LMD7000 laser capture microdissection (LMD) system (Leica Microsystems, Wetzler, Germany) and collected via gravity in caps of 0.5 mL microtubes containing 35 µL of protein extraction buffer (mix of 10 mM Tris, 1 mM EDTA, and 0.002% Zwittergent 3-16 (Calbiochem, San Diego, CA)). After tissue collection, microtubes were centrifuged for 2 min at 9,295g (Eppendorf microcentrifuge, 5417C). To extract proteins from FFPE matrix we heated the samples at 98 °C for 90 min with occasional vortexing. Samples were then sonicated in a water bath for 1 h (VWR Scientific Aquasonic, P250D) and then digested with 0.5 µg of trypsin



(Promega, Madison, WI) overnight at 37°C. Digested samples were reduced with 2 µL of 0.1 M dithiothreitol at 95°C for 5 min and diluted with 7 µL of 0.5% trifluoroacetic acid and 0.15% formic acid solution made in LC-MS grade water. 18 µL of sample was analyzed using nanoflow liquid chromatography-tandem mass spectrometry (nLC-MS/MS).

All samples were analyzed using a hybrid Thermo LTQ Orbitrap XL mass spectrometer coupled to a Thermo Easy nLC 1000 liquid chromatography system. Peptides were applied to a trap C8 column (150 µm ID x 20 mm, New Objective, Woburn, MA; 5 µm Magic C8 packing, Michrom Bioresources, Auburn, CA) and separated on a reverse phase C18 column (75 µm ID x 150 mm, New Objective, Woburn, MA; 3 µm Agilent Pursuit C18 packing, Agilent Technologies, Santa Clara, CA) using a linear gradient from 1% to 65% acetonitrile containing 0.1% formic acid over 112 min at a flow rate of 300 nl/min. Eluting peptides were ionized using Nanospray Flex Ion source (Thermo Electron, Bremen, Germany) and the corresponding spectra in the positive ion mode were obtained under data-dependent acquisition mode. Full MS scans were collected in the orbitrap (400 – 1500 *m/z* range, 60,000 resolution) while the top 7 most intense precursor ions that underwent collisionally induced dissociation at 35 V were detected by the linear ion trap.

The resulting raw data files were processed using the Proteome Discoverer 1.4 (Thermo Scientific) and the Sequest HT algorithm. The fragmentation spectra were searched against the UniProt *Mus musculus* database (last modified January 15, 2020). The search parameters were as follows: the precursor mass tolerance was 7 ppm and the fragment mass tolerance was set to ±0.05 Da. The peptide false discovery rate (FDR) was

less than 1%. Peptides associated with a high confidence level identification (probability of identification >90%) were filtered and selected for protein identification.

### 2.5.13 RT-qPCR

Tissues were collected from mice at different time points (3 months, 1-year, and endpoint mice) and processed using the Monarch Total RNA Miniprep Kit (NEB #T2010S). RNA was reverse transcribed using iScript (Bio-Rad #1708891) and cDNA was diluted 5x with nuclease-free water. Real-time qPCR was performed for *Apoa1*, *Apoa2*, *Apoa4*, *Alb*, *ApoE*, *Apcs*, *Ighm*, using PowerUP SYBR (Applied Biosystems #A25742). *Gapdh* was used as the internal control. Primer sequences are available in **Table 2.2**.

### 2.5.14 Statistics

Specific statistical tests used are indicated in the figure legends for each experiment. Analysis was done using GraphPad Prism version 7. A *P*-value of less than 0.05 was considered significant.

### 2.5.15 Study Approval

All animal experiments were approved by Western Universities animal use committee in accordance with regulations from the Canadian Council on Animal Care.

## 2.6 Acknowledgements

The authors wish to thank Drs. G. DiMattia, M. Huff, and M. Cecchini for experimental and analytical advice throughout the course of this work. We are also greatly indebted to colleagues in the Biotron, Molecular Pathology Core, and London Regional Proteomics Centre at Western University for services. Illustrations were created in BioRender.com. PP was supported by the Strategic Training program in Cancer Research. GEL was a recipient of a Dean's Undergraduate Research opportunity fellowship. FAD is the Wolfe Senior Fellow in Tumor Suppressor Genes at Western University. This work was supported by grants from CCSRI and CIHR.

## 2.7 References

- 1 Wechalekar, A. D., Gillmore, J. D. & Hawkins, P. N. Systemic amyloidosis. *The Lancet* 387, 2641-2654, doi:10.1016/s0140-6736(15)01274-x (2016).
- 2 Benson, M. D. *et al.* Amyloid nomenclature 2018: recommendations by the International Society of Amyloidosis (ISA) nomenclature committee. *Amyloid* 25, 215-219, doi:10.1080/13506129.2018.1549825 (2018).
- 3 Luo, H. *et al.* Extracellular deposition of mouse senile AApoAII amyloid fibrils induced different unfolded protein responses in the liver, kidney, and heart. *Lab Invest* 95, 320-333, doi:10.1038/labinvest.2014.158 (2015).
- 4 Nuvolone, M. & Merlini, G. Systemic amyloidosis: novel therapies and role of biomarkers. *Nephrol Dial Transplant* 32, 770-780, doi:10.1093/ndt/gfw305 (2017).
- 5 Das, M. & Gursky, O. Amyloid-Forming Properties of Human Apolipoproteins: Sequence Analyses and Structural Insights. *Adv Exp Med Biol* 855, 175-211, doi:10.1007/978-3-319-17344-3\_8 (2015).
- 6 Lamou-Fava, S. & Micherone, D. Regulation of apoA-I gene expression: mechanism of action of estrogen and genistein. *Journal of lipid research* 45, 106-112, doi:10.1194/jlr.M300179-JLR200 (2004).
- 7 Wang, Y. *et al.* ApoA-I deficiency in mice is associated with redistribution of apoA-II and aggravated AApoAII amyloidosis. *J Lipid Res* 52, 1461-1470, doi:10.1194/jlr.M013235 (2011).
- 8 Lu, C. *et al.* Apolipoprotein A-1-related amyloidosis 2 case reports and review of the literature. *Medicine (Baltimore)* 96, e8148, doi:10.1097/MD.00000000000008148 (2017).
- 9 Ge, F. *et al.* Amyloidosis in transgenic mice expressing murine amyloidogenic apolipoprotein A-II (Apoa2c). *Lab Invest* 87, 633-643, doi:10.1038/labinvest.3700559 (2007).
- 10 Nakamura, T. *et al.* Transcription factors and age-related decline in apolipoprotein A-I expression. *Journal of lipid research* 40, 1709-1718 (1999).
- 11 Wang, Z. *et al.* Apolipoprotein A-IV involves in glucose and lipid metabolism of rat. *Nutr Metab (Lond)* 16, 41, doi:10.1186/s12986-019-0367-2 (2019).
- 12 Tubb, M. R., Silva, R. A. G. D., Fang, J., Tso, P. & Davidson, W. S. A three-dimensional homology model of lipid-free apolipoprotein A-IV using cross-linking and mass spectrometry. *The Journal of biological chemistry* 283, 17314-17323, doi:10.1074/jbc.M800036200 (2008).
- 13 Walker, R. G. *et al.* The structure of human apolipoprotein A-IV as revealed by stable isotope-assisted cross-linking, molecular dynamics, and small angle x-ray scattering. *The Journal of biological chemistry* 289, 5596-5608, doi:10.1074/jbc.M113.541037 (2014).
- 14 Mollee, P. *et al.* Implementation and evaluation of amyloidosis subtyping by laser-capture microdissection and tandem mass spectrometry. *Clin Proteomics* 13, 30, doi:10.1186/s12014-016-9133-x (2016).
- 15 Obici, L., Nuvolone, M. & Merlini, G. Expanding the spectrum of systemic amyloid diseases: a new hint from the kidney. *Kidney Int* 90, 479-481, doi:10.1016/j.kint.2016.05.029 (2016).
- 16 Sethi, S. *et al.* Medullary amyloidosis associated with apolipoprotein A-IV deposition. *Kidney Int* 81, 201-206, doi:10.1038/ki.2011.316 (2012).

- 17 Latorre, I. *et al.* The DREAM complex promotes gene body H2A.Z for target repression. *Genes Dev* 29, 495-500, doi:10.1101/gad.255810.114 (2015).
- 18 Creighton, M. P. *et al.* H2AZ is enriched at polycomb complex target genes in ES cells and is necessary for lineage commitment. *Cell* 135, 649-661, doi:10.1016/j.cell.2008.09.056 (2008).
- 19 Sevilla, A. & Binda, O. Post-translational modifications of the histone variant H2AZ. *Stem Cell Res* 12, 289-295, doi:10.1016/j.scr.2013.11.004 (2014).
- 20 Muller, G. A. *et al.* The CHR site: definition and genome-wide identification of a cell cycle transcriptional element. *Nucleic Acids Res* 42, 10331-10350, doi:10.1093/nar/gku696 (2014).
- 21 Sadasivam, S. & DeCaprio, J. A. The DREAM complex: master coordinator of cell cycle-dependent gene expression. *Nature reviews. Cancer* 13, 585-595, doi:10.1038/nrc3556 (2013).
- 22 Mages, C. F., Wintsche, A., Bernhart, S. H. & Muller, G. A. The DREAM complex through its subunit Lin37 cooperates with Rb to initiate quiescence. *Elife* 6, doi:10.7554/eLife.26876 (2017).
- 23 Litovchick, L. *et al.* Evolutionarily conserved multisubunit RBL2/p130 and E2F4 protein complex represses human cell cycle-dependent genes in quiescence. *Mol Cell* 26, 539-551 (2007).
- 24 Ceol, C. J. & Horvitz, H. R. dpl-1 DP and efl-1 E2F act with lin-35 Rb to antagonize Ras signaling in *C. elegans* vulval development. *Mol Cell* 7, 461-473 (2001).
- 25 Fay, D. S. & Han, M. The synthetic multivulval genes of *C. elegans*: functional redundancy, Ras-antagonism, and cell fate determination. *Genesis* 26, 279-284 (2000).
- 26 Korenjak, M. *et al.* Native E2F/RBF complexes contain Myb-interacting proteins and repress transcription of developmentally controlled E2F target genes. *Cell* 119, 181-193, doi:10.1016/j.cell.2004.09.034 (2004).
- 27 Lewis, P. W. *et al.* Identification of a *Drosophila* Myb-E2F2/RBF transcriptional repressor complex. *Genes Dev* 18, 2929-2940 (2004).
- 28 Schmit, F. *et al.* LINC, a human complex that is related to pRB-containing complexes in invertebrates regulates the expression of G2/M genes. *Cell Cycle* 6, 1903-1913 (2007).
- 29 Sadasivam, S., Duan, S. & DeCaprio, J. A. The MuvB complex sequentially recruits B-Myb and FoxM1 to promote mitotic gene expression. *Genes & development* 26, 474-489, doi:10.1101/gad.181933.111 (2012).
- 30 Pilkinton, M., Sandoval, R. & Colamonici, O. R. Mammalian Mip/LIN-9 interacts with either the p107, p130/E2F4 repressor complex or B-Myb in a cell cycle-phase-dependent context distinct from the *Drosophila* dREAM complex. *Oncogene* 26, 7535-7543, doi:10.1038/sj.onc.1210562 (2007).
- 31 Cobrinik, D. *et al.* Shared role of the pRB-related p130 and p107 proteins in limb development. *Genes Dev* 10, 1633-1644 (1996).
- 32 Reichert, N. *et al.* Lin9, a subunit of the mammalian DREAM complex, is essential for embryonic development, for survival of adult mice, and for tumor suppression. *Molecular and cellular biology* 30, 2896-2908, doi:10.1128/MCB.00028-10 (2010).

- 33 Gaubatz, S. *et al.* E2F4 and E2F5 play an essential role in pocket protein-mediated G1 control. *Mol Cell* 6, 729-735 (2000).
- 34 Kohn, M. J., Bronson, R. T., Harlow, E., Dyson, N. J. & Yamasaki, L. Dp1 is required for extra-embryonic development. *Development* 130, 1295-1305 (2003).
- 35 MacPherson, D. *et al.* Murine bilateral retinoblastoma exhibiting rapid-onset, metastatic progression and N-myc gene amplification. *EMBO J* 26, 784-794, doi:10.1038/sj.emboj.7601515 (2007).
- 36 Forristal, C. *et al.* Loss of the mammalian DREAM complex deregulates chondrocyte proliferation. *Mol Cell Biol* 34, 2221-2234 (2014).
- 37 Guiley, K. Z. *et al.* Structural mechanisms of DREAM complex assembly and regulation. *Genes Dev* 29, 961-974, doi:10.1101/gad.257568.114 (2015).
- 38 Ruzankina, Y. *et al.* Deletion of the developmentally essential gene ATR in adult mice leads to age-related phenotypes and stem cell loss. *Cell Stem Cell* 1, 113-126, doi:10.1016/j.stem.2007.03.002 (2007).
- 39 MacDonald, J. *et al.* A Systematic Analysis of Negative Growth Control Implicates the DREAM Complex in Cancer Cell Dormancy. *Mol Cancer Res* 15, 371-381, doi:10.1158/1541-7786.MCR-16-0323-T (2017).
- 40 Fischer, M., Quaas, M., Steiner, L. & Engeland, K. The p53-p21-DREAM-CDE/CHR pathway regulates G2/M cell cycle genes. *Nucleic Acids Res* 44, 164-174, doi:10.1093/nar/gkv927 (2016).
- 41 Kuroda, T. *et al.* Significant association between renal function and area of amyloid deposition evident in kidney biopsy specimens in both AA and AL amyloidosis. *Amyloid : the international journal of experimental and clinical investigation : the official journal of the International Society of Amyloidosis* 24, 151-152, doi:10.1080/13506129.2017.1291421 (2017).
- 42 Erdogmus, S. *et al.* Profile of renal AA amyloidosis in older and younger individuals: a single-centre experience. *Amyloid : the international journal of experimental and clinical investigation : the official journal of the International Society of Amyloidosis* 25, 115-119, doi:10.1080/13506129.2018.1474733 (2018).
- 43 Sethi, S. & Theis, J. D. Pathology and diagnosis of renal non-AL amyloidosis. *J Nephrol* 31, 343-350, doi:10.1007/s40620-017-0426-6 (2018).
- 44 Guo, X., Guo, H., Zhao, L., Zhang, Y.-H. & Zhang, J.-X. Two predominant MUPs, OBP3 and MUP13, are male pheromones in rats. *Front Zool* 15, 6-6, doi:10.1186/s12983-018-0254-0 (2018).
- 45 Tougaard, B. G. *et al.* A case report of hereditary apolipoprotein A-I amyloidosis associated with a novel APOA1 mutation and variable phenotype. *Eur J Med Genet* 59, 474-477, doi:10.1016/j.ejmg.2016.05.015 (2016).
- 46 Sipe, J. D. *et al.* Amyloid fibril proteins and amyloidosis: chemical identification and clinical classification International Society of Amyloidosis 2016 Nomenclature Guidelines. *Amyloid : the international journal of experimental and clinical investigation : the official journal of the International Society of Amyloidosis* 23, 209-213, doi:10.1080/13506129.2016.1257986 (2016).
- 47 Clement, C. G. & Truong, L. D. An evaluation of Congo red fluorescence for the diagnosis of amyloidosis. *Human pathology* 45, 1766-1772, doi:10.1016/j.humpath.2014.04.016 (2014).

- 48 Menter, T., Bachmann, M., Grieshaber, S. & Tzankov, A. A More Accurate Approach to Amyloid Detection and Subtyping: Combining in situ Congo Red Staining and Immunohistochemistry. *Pathobiology* 84, 49-55, doi:10.1159/000447304 (2017).
- 49 Sunde, M. *et al.* Common core structure of amyloid fibrils by synchrotron X-ray diffraction<sup>11</sup> Edited by F. E. Cohen. *Journal of Molecular Biology* 273, 729-739, doi:<https://doi.org/10.1006/jmbi.1997.1348> (1997).
- 50 Lundmark, K., Vahdat Shariatpanahi, A. & Westermark, G. T. Depletion of spleen macrophages delays AA amyloid development: a study performed in the rapid mouse model of AA amyloidosis. *PLoS One* 8, e79104, doi:10.1371/journal.pone.0079104 (2013).
- 51 Sen, S. & Sarsik, B. A proposed histopathologic classification, scoring, and grading system for renal amyloidosis: standardization of renal amyloid biopsy report. *Arch Pathol Lab Med* 134, 532-544, doi:10.1043/1543-2165-134.4.532 (2010).
- 52 Vrana, J. A. *et al.* Classification of amyloidosis by laser microdissection and mass spectrometry-based proteomic analysis in clinical biopsy specimens. *Blood* 114, 4957-4959, doi:10.1182/blood-2009-07-230722 (2009).
- 53 Abildgaard, N. *et al.* Immunoelectron microscopy and mass spectrometry for classification of amyloid deposits. *Amyloid : the international journal of experimental and clinical investigation : the official journal of the International Society of Amyloidosis* 27, 59-66, doi:10.1080/13506129.2019.1688289 (2020).
- 54 Vrana, J. A. *et al.* Clinical diagnosis and typing of systemic amyloidosis in subcutaneous fat aspirates by mass spectrometry-based proteomics. *Haematologica* 99, 1239-1247, doi:10.3324/haematol.2013.102764 (2014).
- 55 Miyahara, H. *et al.* Comprehensive proteomic profiles of mouse AApoAII amyloid fibrils provide insights into the involvement of lipoproteins in the pathology of amyloidosis. *J Proteomics* 172, 111-121, doi:10.1016/j.jprot.2017.10.003 (2018).
- 56 Brambilla, F. *et al.* Shotgun protein profile of human adipose tissue and its changes in relation to systemic amyloidosis. *J Proteome Res* 12, 5642-5655, doi:10.1021/pr400583h (2013).
- 57 Blanc, P. *et al.* Mature IgM-expressing plasma cells sense antigen and develop competence for cytokine production upon antigenic challenge. *Nat Commun* 7, 13600, doi:10.1038/ncomms13600 (2016).
- 58 Dasari, S. *et al.* Clinical, biopsy, and mass spectrometry characteristics of renal apolipoprotein A-IV amyloidosis. *Kidney Int* 90, 658-664, doi:10.1016/j.kint.2016.04.003 (2016).
- 59 Dimova, D. K., Stevaux, O., Frolov, M. V. & Dyson, N. J. Cell cycle-dependent and cell cycle-independent control of transcription by the Drosophila E2F/RB pathway. *Genes Dev.* 17, 2308-2320. (2003).
- 60 Blackburn, A. M., Amiel, S. A., Millis, R. R. & Rubens, R. D. Tamoxifen and liver damage. *Br Med J (Clin Res Ed)* 289, 288-288, doi:10.1136/bmj.289.6440.288 (1984).
- 61 Gao, F.-F. *et al.* Tamoxifen induces hepatotoxicity and changes to hepatocyte morphology at the early stage of endocrinotherapy in mice. *Biomed Rep* 4, 102-106, doi:10.3892/br.2015.536 (2016).

- 62 Hassan, H. M. *et al.* Regulation of Active DNA Demethylation through RAR-Mediated Recruitment of a TET/TDG Complex. *Cell Rep* 19, 1685-1697, doi:10.1016/j.celrep.2017.05.007 (2017).
- 63 Thillainadesan, G. *et al.* TGF-beta-dependent active demethylation and expression of the p15ink4b tumor suppressor are impaired by the ZNF217/CoREST complex. *Molecular cell* 46, 636-649, doi:10.1016/j.molcel.2012.03.027 (2012).
- 64 Lighezan, R. *et al.* The value of the reprocessing method of paraffin-embedded biopsies for transmission electron microscopy.
- 65 Rodriguez, F. J. *et al.* Immunoglobulin derived depositions in the nervous system: novel mass spectrometry application for protein characterization in formalin-fixed tissues. *Lab Invest* 88, 1024-1037, doi:10.1038/labinvest.2008.72 (2008).



## Chapter 3

### 3 BEAVR: A Browser-based tool for the Exploration and Visualization of RNA-seq data

#### 3.1 Abstract

**Background:** The use of RNA-sequencing (RNA-seq) in molecular biology research and clinical settings has increased significantly over the past decade. Despite its widespread adoption, there is a lack of simple and interactive tools to analyze and explore RNA-seq data. Many established tools require programming or Unix/Bash knowledge to analyze and visualize results. This requirement presents a significant barrier for many researchers to efficiently analyze and present RNA-seq data.

**Results:** Here we present BEAVR, a **B**rowser-based tool for the **E**xploration **A**nd **V**isualization of **R**N<sub>A</sub>-seq data. BEAVR is an easy-to-use tool that facilitates interactive analysis and exploration of RNA-seq data. BEAVR is developed in R and uses DESeq2 as its engine for differential gene expression (DGE) analysis, but assumes users have no prior knowledge of R or DESeq2. BEAVR allows researchers to easily obtain a table of differentially-expressed genes with statistical testing and then visualize the results in a series of graphs, plots and heatmaps. Users are able to customize many parameters for statistical testing, dealing with variance, clustering methods and pathway analysis to generate high quality figures.

**Conclusion:** BEAVR simplifies analysis for novice users but also streamlines the RNA-seq analysis process for experts by automating several steps. BEAVR and its documentation can

be found on GitHub at <https://github.com/developerpiru/BEAVR>. BEAVR is available as a Docker container at <https://hub.docker.com/r/pirunthan/beavr>.

## 3.2 Background

RNA-sequencing (RNA-seq) has revolutionized molecular biology research in the last decade [1]. RNA-seq is a high-throughput sequencing method that allows for the quantification of gene expression patterns between experimental groups using differential gene expression (DGE) methods [2]. Analysis of DGE may guide the early phases of studies by highlighting transcripts and/or pathways with altered expression in a given experimental system or may be used to assess the downstream impacts of a treatment or other experimental condition. RNA-seq experiments may follow almost any variation of *in vitro* or *in vivo* study in which RNA is collected [3]. Most recently, RNA-seq has been employed clinically, including in numerous cancer-related clinical trials [4-6].

Once the wet lab components of an RNA-seq experiment are completed, the data must be analyzed computationally. To date, a multitude of tools are available to researchers depending on the experimental question (*e.g.* the discovery of novel transcripts or determining gene expression changes) [3, 7]. Regardless of the analysis tool selected, the vast majority of currently available tools require knowledge of programming (C/C++, Perl, Python, R) or shell scripting (Unix/Bash shell). DESeq2, one of the most popular analytical software packages for DGE, is written in R and requires an understanding of this language to manipulate data and visualize results [8]. The requirement for users to navigate one or more computational languages in order to analyze RNA-seq data presents a

substantial barrier for many researchers who are adept with respect to the wet lab components of RNA-seq but unfamiliar with the computational aspects.

Here, we present BEAVR, a **B**rowser-based tool for the **E**xploration **A**nd **V**isualization of **R**N<sub>A</sub>-seq data. BEAVR is an operating system (OS)-independent software package written in R that can run locally on a user's computer or on a remote server. BEAVR provides an easy-to-use graphical frontend to allow both novices and experts to perform DGE analyses on RNA-seq datasets. Specifically, BEAVR simplifies the process of visualization and exploration of results and allows users to generate visually-appealing graphs, tables, plots, heatmaps and pathways maps. At its core, BEAVR uses the heavily-cited DESeq2 as the engine for its analysis. While there is no single superior method for RNA-seq analyses, DESeq2 is an ideal choice because it requires only raw, unnormalized read counts and provides functions to perform DGE and statistical analyses. Our implementation allows for the visualization of PCA plots, read count plots, volcano plots, heatmaps and enriched pathways and facilitates the exploration of DGE results to aid researchers in their study of known gene interactions as well as providing tools for the discovery of novel gene interactions.

### 3.3 Implementation

#### 3.3.1 Interface & typical workflow

BEAVR's graphical user interface (GUI) is developed in R using the shiny framework. The layout is divided into a main panel and a sidebar panel (**Figure 3.1A**). The main panel presents the user with a tabbed environment that breaks the workflow of DGE

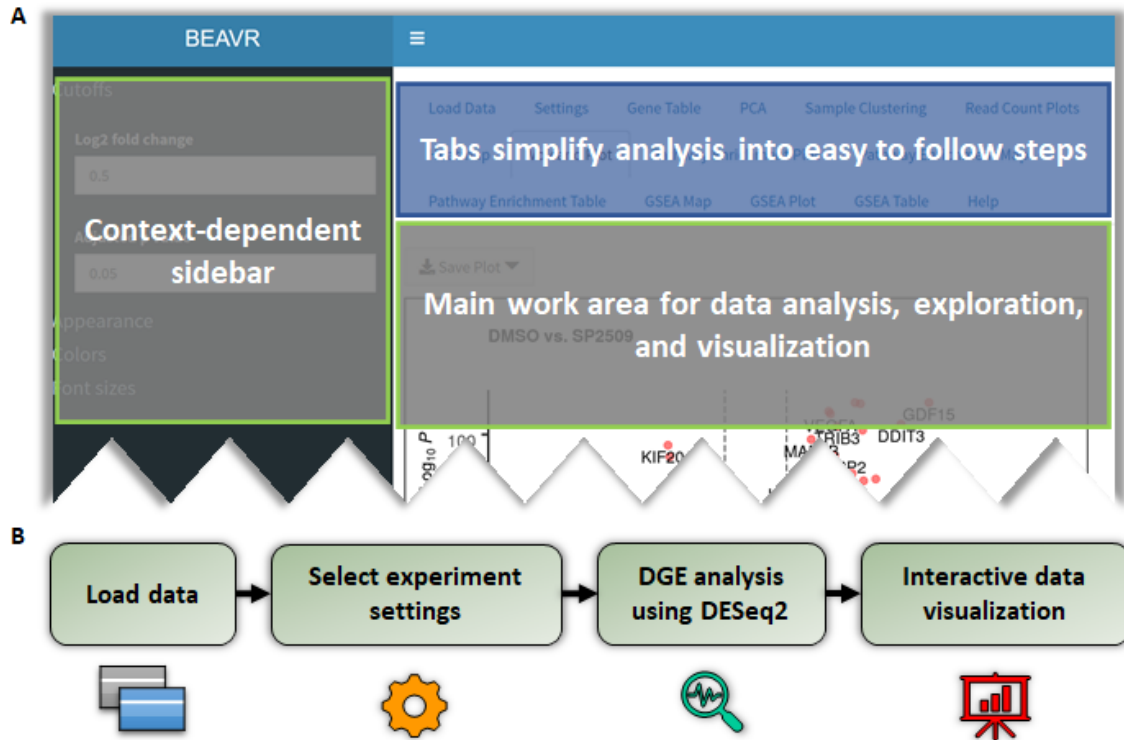


**Figure 3.1. Overview of BEAVR's graphical user interface and typical workflow.** (A) BEAVR's easy-to-use graphical user interface (GUI) is divided into two areas; a main work area and a sidebar. The main work area has a tabbed-interface to select data output and figure displays. Depending on the tab selected in the main working area, the context-dependent sidebar will show appropriate options and parameters that allow the user to customize analysis, data output and figures. (B) BEAVR breaks down the RNA-seq analysis workflow into logical steps. Users begin by loading their data (raw read counts and sample information) and select experimental settings for analysis and statistical tests. Then differential gene expression (DGE) analysis is performed automatically using DESeq2, lastly the data is displayed in interactive tables, graphs and plots that users can explore, manipulate and customize.

analysis into easy-to-follow logical steps. Depending on which tab is open, the sidebar will display context-dependent parameters that control the output and display of data in the work area of the main panel. The user can manipulate these parameters at any time and the results will be recalculated and updated in real-time, drastically reducing the amount of time required compared to command-line based approaches.

A typical workflow for RNA-seq analysis using BEAVR is shown in **Figure 3.1B**. Briefly, data is loaded into BEAVR, DGE analysis is performed using DESeq2 and the results are visualized in interactive tables, in graphs and other displays. In the Load Data tab, the user must provide a DESeq2 compatible read count table file containing raw, unnormalized read counts (obtained using alignment tools such as STAR or HTSeq) as well as a sample treatment matrix file (created in a text editor or spreadsheet program). The read count table file (either TXT or CSV) should contain the read quantities for all of the samples in the experiment (**Figure 3.2A**). The first column must contain ENSEMBL identifiers for each gene. The heading for this column must be `gene_id`. The next  $n$  columns must contain raw read counts for each of the  $n$  samples. The headings for these  $n$  columns must be unique sample identifiers (*e.g.* `wildtype-1`, `wildtype-2`, `wildtype-3`, `mutant-1`, `mutant-2`, `mutant-3`). The sample treatment matrix file (either TXT or CSV) informs BEAVR which columns (samples) in the read count table file belong to which treatment groups (**Figure 3.2B**). This allows multiple replicates to be grouped together across different experimental conditions. The first column must list in each row the sample identifiers for all  $n$  columns in the read count table file (*e.g.* `wildtype-1`, `wildtype-2`,

**A**

Samples →

gene_id	Sample-1	Sample-2	...	Sample-n
ENSG...	2063	2583	...	529
ENSG...	2946	3942	...	665
ENSG...	3708	2809	...	593
ENSG...	2459	2041	...	556

Genes (ENSEMBL)

**B**

	condition	replicate
Sample-1	Wildtype	Replicate-1
Sample-2	Wildtype	Replicate-2
Sample-3	Mutant	Replicate-1
...	...	...
Sample-n	Drug-Treated	Replicate-n

Samples

↓

**Treatment groups**

↓

**Replicates or any other user-defined grouping**

**Figure 3.2. BEAVR requires two inputs: a read count table file and a sample treatment matrix file.** (A) BEAVR requires raw, unnormalized read counts as input. This can be obtained using tools such as STAR or HTSeq. The first column of the read count table file must have the heading `gene_id` and contain unique ENSEMBL IDs. Every column after must contain read counts for one sample, each with a unique identifier in the heading (e.g. `Sample-1`, `Sample-2`, ..., `Sample-n`). The read count table file must be either a TXT or CSV format. (B) BEAVR requires an additional file, called a sample treatment matrix file, that contains important characteristics about each sample, such as which treatment group the samples belong to. The first column of this file must contain in each row all the samples found in the read count table file (e.g. `Sample-1`, `Sample-2`, ..., `Sample-n`) in the same order. The second column must have the heading `condition`. The third column must have the heading `replicate`. In the `condition` column, users must specify which experimental group each sample belongs to (e.g. `Wildtype`, `Mutant`, or `Drug-Treated`). In the `replicate` column, users can provide any other additional grouping information or replicate information (e.g. `Replicate-1`, `Replicate-2`, ..., `Replicate-n`). The sample treatment matrix file must be either a TXT or CSV format.

wildtype-3, mutant-1, mutant-2, mutant-3). The second column of the `sample treatment matrix` file specifies which experimental condition each sample belongs to (e.g. wildtype and mutant, or untreated and drug-treated). The heading for this column must be `condition`. In the third column, the user may specify any additional characteristics for each sample, such as replicate numbers/letters or genotype groups (e.g. replicate-A, replicate-B, replicate-C). The heading for this column must be `replicate`. Both the `read count table` file and the `sample treatment matrix` file must contain at least two experimental conditions with a minimum of 2 samples each. Treatment groups do not need to contain the same number of samples in each group.

In the `Settings` tab, the user must select a control condition and a treatment condition (condition choices are loaded from those available in the `sample treatment matrix` file). For DGE analyses, DESeq2 is used to compare the selected treatment condition against the selected control condition. The user may specify a minimum cutoff for reads if desired (reads below this cutoff value are dropped before analysis), specify a false discovery rate (FDR) to determine adjusted  $p$  values ( $p_{adj}$ ) and also specify an effect size shrinkage method using DESeq2 [8] or `apeglm` (approximate posterior estimation) [9].

### 3.3.2 Representation of results & data exploration

Clicking on the `Gene Table` tab will initiate automated DGE analysis using the parameters specified by the user. A progress bar will be shown in the bottom right of the



main work area. Upon completion, an interactive table displays the results including gene IDs as HUGO Gene Nomenclature Committee (HGNC) symbols,  $\log_2$  fold changes (LFC),  $p$  values and  $p_{adj}$  values for each gene. Controls in the sidebar may be used to filter the table as desired and a copy may be saved using the `Download Table` button.

Visualization of all plots is implemented using `ggplot2`. The `PCA` tab will generate a principal component analysis (PCA) plot and display all the samples found in the `read count table` file. In the `Sample Clustering` tab, the user can select a distance measurement method to use (Pearson correlation, Euclidean, Maximum, Manhattan, Canberra, Binary, or Minkowski) which will compute a distance matrix using the `ComplexHeatmap` and `dist` packages and display the sample variation as a heatmap. The `Read Count Plots` tab will generate normalized read count plots, either as boxplots or jitter plots, for desired genes. The user can enter gene names separated by a comma and change the grid layout as desired (use a `1x1` grid for a single plot or increase the grid size as necessary to fit multiple plots). The `Heatmap` tab will allow the user to generate a heatmap with gene clustering for the top  $n$  significantly variable genes (where  $n$  is a user-defined number), or for any list of genes entered by the user. Dependence of the variance on the mean is removed using either variance stabilization (`vst`) or regularized logarithm (`rlog`) transformations [8] as specified by the user. The user can also specify a hierarchical clustering method (Ward.D/D2, Single, Complete, Average, McQuitty, Median, or Centroid) to be used by the `hclust` package (for row and/or column clustering) and a distance measurement method as described above. The `Volcano Plot` tab will generate a volcano plot using the `EnhancedVolcano` package to illustrate differentially-expressed genes that meet the user-defined LFC and  $p_{adj}$  cutoffs for the

control and treatment conditions specified on the `Settings` tab. Pathway over-representation analysis and gene set enrichment analysis (GSEA) are performed using the `ReatomePA` and `enrichplot` packages [10] and figures are shown in the `Pathway Enrichment Plot`, `Pathway Enrichment Map`, `GSEA Plot` and `GSEA Map` tabs with the tabular results being displayed in the `Pathway Enrichment Table` and `GSEA Table` tabs. All customization options are presented in the sidebar and allow users to control many parameters when plotting figures, including the ability to customize colors, font sizes and legend positions and directions (horizontal or vertical) for all figures. The size and aspect ratio of all figures can be adjusted by clicking and dragging the outside edges of the plot area. The `Save Plot` button located above every plot allows figures to be saved in multiple formats (JPEG, PDF, PNG, SVG, TIFF) while the `Download Table` button in the sidebar allows data from any table to be saved (CSV).

### 3.3.3 Installation

Since BEAVR is developed in R (+3.5), it is OS-independent and runs on Linux, Mac OS and Windows. We provide several methods to install and use BEAVR depending on user preference: 1) the easiest method for those unfamiliar with R is to install Docker (<https://docker.com>) and use our Docker container (<https://hub.docker.com/r/pirunthan/beavr>) which comes pre-installed with all of the required components; or 2) users can use our OS-specific scripts to install and configure R with all of the required packages for BEAVR; or 3) users who already have R installed can download BEAVR from GitHub. Additionally, system administrators may install BEAVR in a multi-user server environment which is useful for research groups that want to have a

centralized server for BEAVR. This is implemented using ShinyProxy (<https://shinyproxy.io>) and Docker which provide a secure, sandboxed environment for every connected user. We provide automated install scripts on GitHub to easily accomplish this and system administrators can customize the installation to their specific network requirements. Each of these methods simplify and streamline setup for novice and expert users alike and are well-documented on the GitHub page for BEAVR located at <https://github.com/developerpiru/BEAVR>.

### 3.3.4 Run time consideration

Computation time is dependent on the user's device specifications since all DGE analyses, statistical tests and visualization steps are performed locally (or the server specifications when running BEAVR on a shared server). For a typical mammalian RNA-seq experiment containing two experimental groups with three replicates each using the human genome as a reference (88 million reads total), automated calculations will take approximately 1 minute with a dual-core Intel Core i5 CPU and 4 GB RAM or approximately 30 seconds with a 6-core Core i7 and 16 GB RAM. Generation of each figure, as well as subsequent modifications thereto, will take a few additional seconds. These short processing times will allow users to repeatedly manipulate experimental settings to recalculate DGE as desired with different parameters. Users may then explore the results, generating figures and filtering and downloading the data for downstream applications.

## 3.4 Results & Discussion

### 3.4.1 A typical use case

To demonstrate a typical use case for BEAVR, we utilized a previously published RNA-seq dataset by Sehwat *et al.* [11]. In this study, LNCaP cell cultures were treated with either DMSO or SP2509 (a small molecule lysine-specific demethylase 1 [LSD1] inhibitor) for 24 hours [11]. RNA-seq was performed on RNA harvested from triplicate cell cultures corresponding to each treatment condition. We downloaded raw, unnormalized read counts from GEO (GSE59009) and merged the read counts from all samples to make a single read count table file (TXT). We created a sample treatment matrix file (CSV) using Microsoft Excel to specify the treatment condition group (either DMSO or SP2509) and replicate number for each sample. Once these two files were prepared, they were loaded into BEAVR from the Load data tab. In the Settings tab, we selected ‘DMSO’ as the control condition and ‘SP2509’ as the treatment condition. The FDR was set to 10% and the minimum threshold to drop reads was set to 10.

**Figure 3.3A** shows the DGE results from the Gene table tab, which has been sorted by ascending  $p_{adj}$  values. This table can be saved as-is or it can be filtered. For example, it is often desirable to have a list of only those genes that exceed a specific LFC threshold (*e.g.*  $\pm 1.0$ ) and fall below a  $p_{adj}$  threshold (*e.g.*  $< 0.05$ ). These values can be set using the sidebar (**Figure 3.3B**) and the results table will be updated automatically to display genes meeting the selected criteria. These parameters also instruct the thresholds used in generating the volcano plot and pathway analyses.

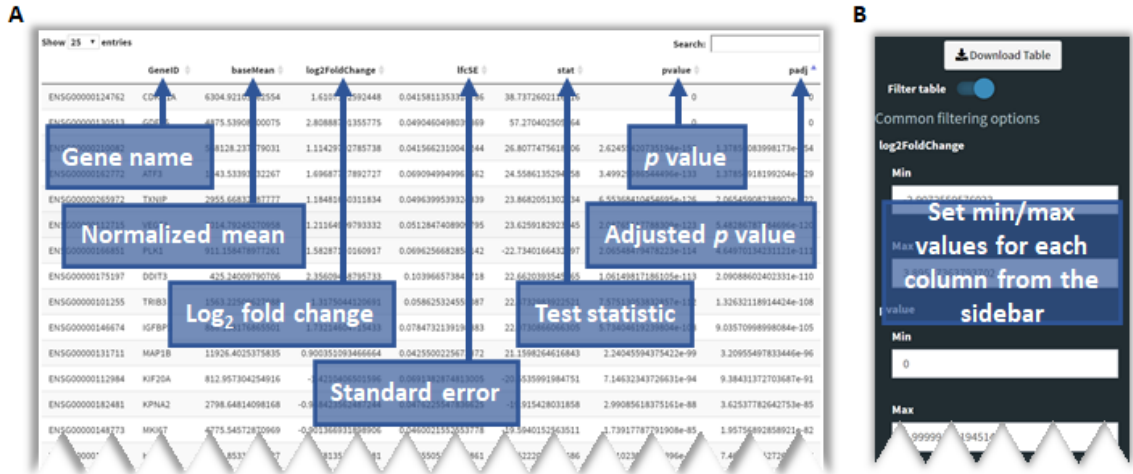


**Figure 3.3. DGE table output from a typical use case for BEAVR.** (A) Once DGE analysis completes in BEAVR, an interactive table is shown in the Gene Table tab. This table provides users with  $\log_2$  fold change (LFC) values for each gene as well as  $p$  values and adjusted  $p$  values ( $p_{adj}$ ). Users can search for a particular gene of interest by its gene name or sort the table based on the contents of any column. A copy of the table can be saved using the download button in the sidebar. The data shown here is the output of DGE analysis performed on the Sehrawat *et al.* dataset. ‘DMSO’ was selected as the control condition and ‘SP2509’ was selected as the treatment condition in the Settings tab. The false discovery rate (FDR) was set to 10% and genes with less than 10 reads were dropped from analysis. (B) The DGE results table in the Gene Table tab can be filtered by any metric using the controls provided in the sidebar. The available filtering options are min/max LFC, min/max  $p$  value, min/max  $p_{adj}$ , min/max baseMean (normalized mean), min/max lfcSE (LFC standard error) and min/max stat (test statistic). The filtered table can be downloaded using the download button in the sidebar. If filtering is enabled, the filtered table will be used to generate the volcano plot in the Volcano Plot tab.

PCA is an important consideration in RNA-seq analysis for small and large studies. Depending on the experimental design, PCA plots can be used for quality control or as a discovery tool [12]. In studies with only two control groups and just two or three biological replicates, it can inform researchers of replicates that are not congruent and have high variance which can skew results and reduce statistical power. In larger studies, it can provide insight into the heterogeneity within experimental conditions. The `PCA Plot` tab displays a PCA plot from our example dataset. The plot shows that there is a very small amount of variance (1%) between replicates within each experimental group (DMSO- or SP2509-treated), while there is very large variance, as expected, between the two experimental groups (98%) (**Figure 3.4A**). Further quality control and insight into sample and replicate variation can be interrogated through a distance matrix and subsequent sample clustering. We defined the parameters in the `Sample Clustering` tab to compute Pearson correlation distances and the result is shown in **Figure 3.4B**. Replicates in the same experimental group cluster together and are very similar to each other, indicating very low variance. Together, these two graphs provide researchers with useful information about experimental groups and consistency of biological replicates.

Sehrawat *et al.* found inhibition of LSD1 in LNCaP cells caused downregulation of previously characterized embryonic stem cell-like genes [11, 13]. Using the `Read Count Plots` tab, we explored the normalized read counts of these genes and generated plots that showed reduced normalized reads in the SP2509-treated cells compared to DMSO-treated cells (**Figure 3.5A**). In situations where genes or pathways of interest are already known, read count plots can be used as a tool to investigate changes in gene expression across samples. However, RNA-seq is also used in experimental systems to inform

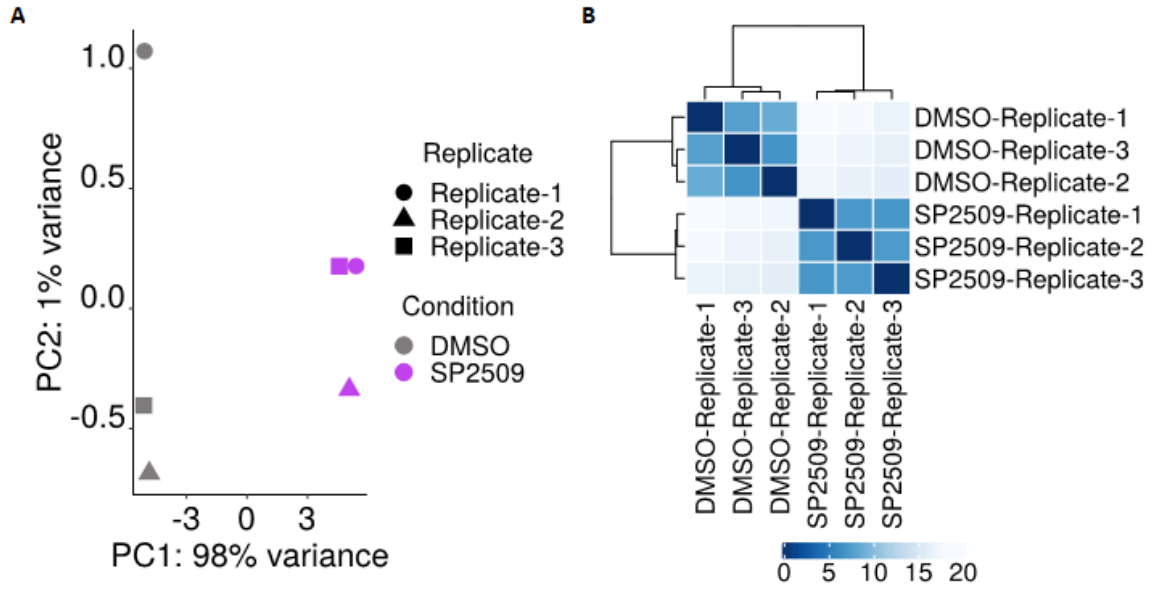


**Figure 3.4. Illustrating variance across samples using principal component analysis (PCA) and sample clustering.** (A) PCA is a useful tool to determine the variance within and across different experimental groups and replicates. The PCA output from the PCA tab is shown for the Sehrawat *et al.* dataset. High variance (98%), as expected, is observed between the two experimental groups (DMSO- vs SP2509-treated) whereas low variance (1%) is observed between replicates within each group. (B) Hierarchical sample clustering is also a useful tool to determine variances. The output from the Sample Clustering tab is shown for the Sehrawat *et al.* dataset. Pearson correlation was selected as the distance measurement method in the sidebar. Similar to the PCA plot, the clustered heatmap shows that replicates in each experimental group (DMSO- or SP2509-treated) cluster strongly together, indicating low variance between biological replicates.

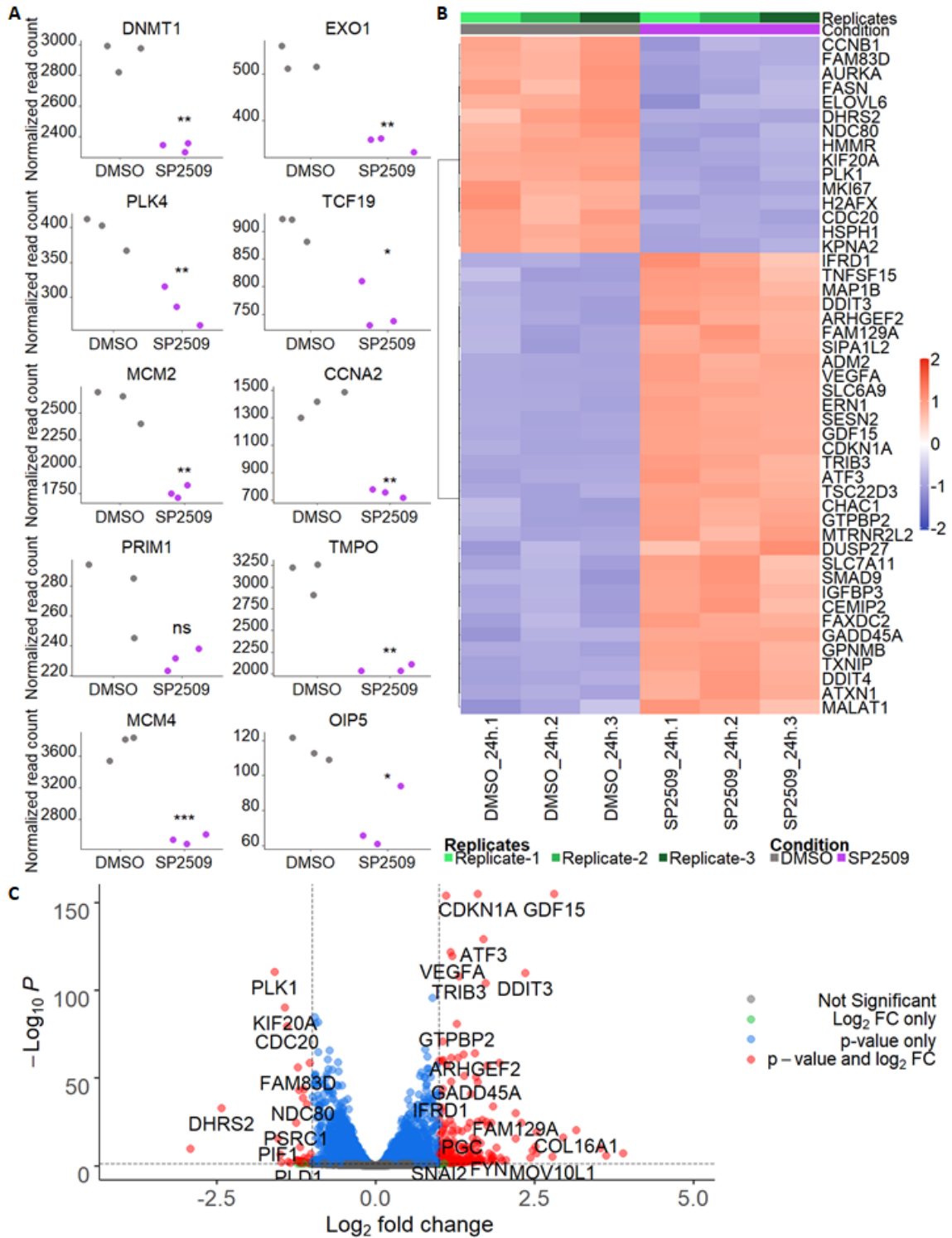




**Figure 3.5. Visualizing normalized read counts and differential gene expression between experimental groups.** (A) Normalized read count plots are shown for ten embryonic stem cell-like genes of interest from the Sehwat *et al.* dataset to illustrate changes between the DMSO- and SP2509-treated groups. BEAVR allows users to enter a list of genes to illustrate expression behavior as jitter plots (shown) or boxplots (not shown). A 5x2 (rows x columns) grid was selected to display these 10 genes. (B) The top 50 most differentially-expressed genes between DMSO- and SP2509-treated groups are shown in the clustered heatmap for the Sehwat *et al.* dataset. This heatmap was generated in the Heatmap tab using the Ward.D hierarchical clustering method and Euclidean distance measurements. Row (gene) clustering clustering was enabled. Clustered heatmaps are useful for displaying expression changes across treatment groups. (C) A volcano plot highlighting genes that meet both LFC and  $p_{adj}$  cutoffs are shown for the Sehwat *et al.* dataset. This volcano plot was generated in the Volcano Plot tab with the LFC cutoff set to  $\pm 1$  and the  $p_{adj}$  cutoff set to  $< 0.05$ . The volcano plot is another way to visualize the data shown in the heatmap in (B), however the volcano plot also illustrates the statistical significance of genes (the y-axis).

researchers of genes and pathways that may be of interest. For such purposes, a heatmap with gene clustering or a volcano plot are useful tools. The `Heatmap` tab generates heatmaps for the top  $n$  genes (where  $n$  is a user-defined number) or for specific genes entered by the user. **Figure 3.5B** shows the top 50 most differentially-expressed genes after variance stabilization with hierarchical clustering performed across rows (Ward.D2 method). This provides information on the most strongly upregulated and downregulated genes. Although the data for a heatmap is transformed and variance is stabilized, it does not provide information on significance ( $p$  values or  $p_{adj}$ ) [8]. The volcano plot from the `Volcano Plot` tab illustrates genes that meet a specified LFC threshold as well as a  $p_{adj}$  threshold (**Figure 3.5C**). We set the LFC threshold to  $\pm 1.0$  and the  $p_{adj}$  cutoff to  $< 0.05$ . Genes highlighted in red (meeting both the LFC and  $p_{adj}$  cutoffs) were also found in the heatmap, demonstrating the usefulness of heatmaps and volcano plots and how the two can be used together for discovery of novel gene expression patterns.

Following identification of upregulated and downregulated genes, it is useful to perform pathway enrichment or gene set enrichment analysis (GSEA) [14, 15] to identify important pathways of interest that will inform investigators of downstream experiments. The `Pathway Enrichment Plot` tab performs over-representation analysis and produces either a dot plot or bar graph of the top  $n$  pathways (where  $n$  is a user-defined number) (**Figure 3.6A**). The `Pathway Enrichment Map` tab provides a broader look at all enriched pathways using an interconnected network map (**Figure 3.6B**) that shows the results of over-representation analysis, however users may also wish to perform GSEA on the `GSEA Map` tab. The `GSEA Plot` tab displays a plot of the running enrichment score for a specific enriched pathway as defined by the user (**Figure 3.6C**). The input data

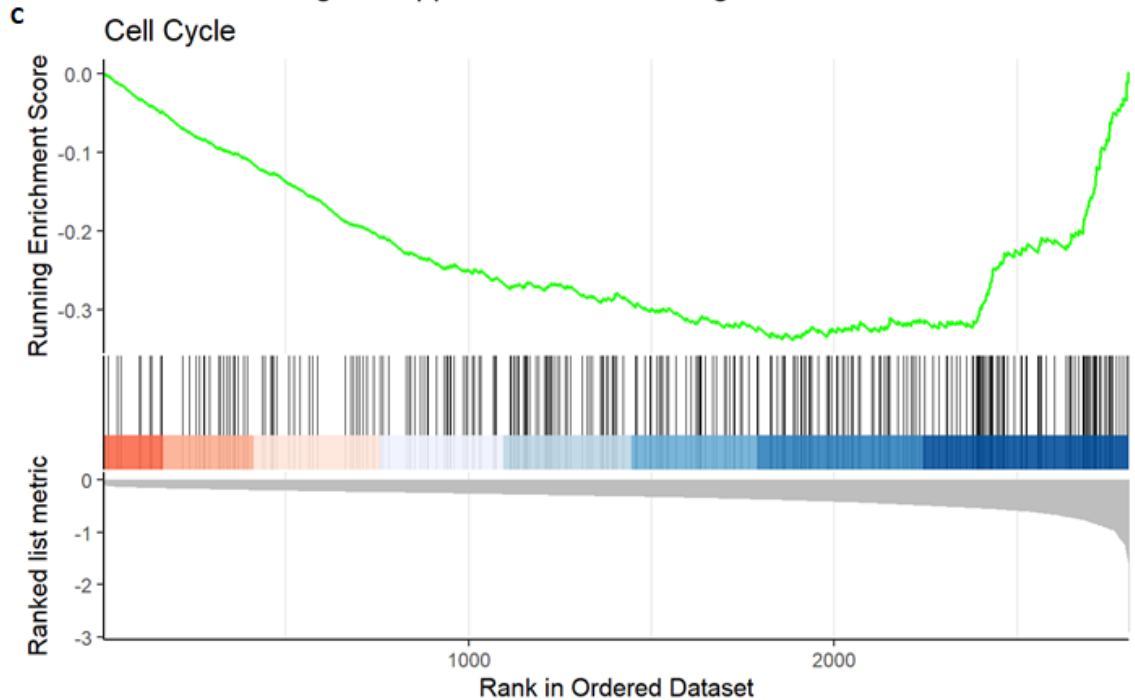
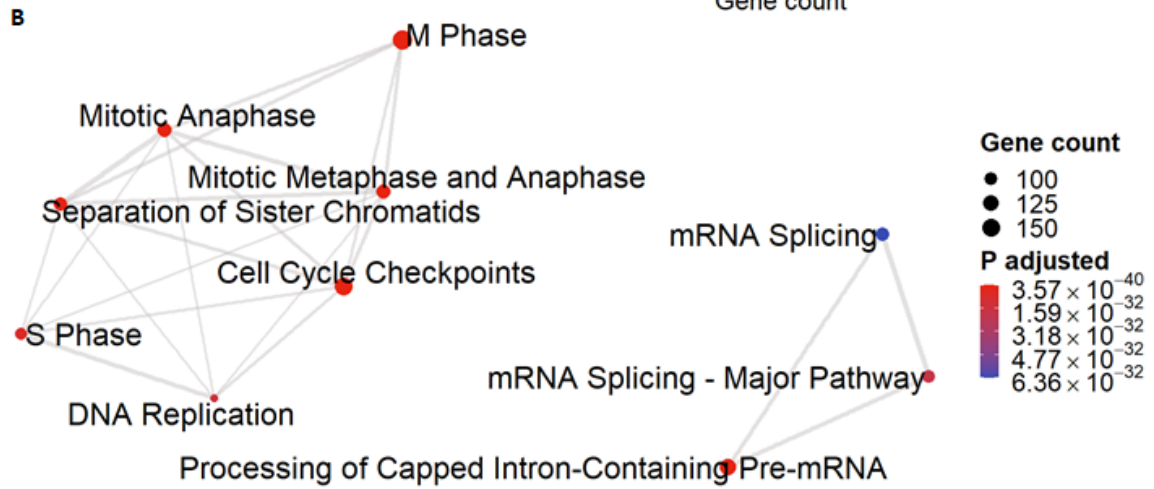
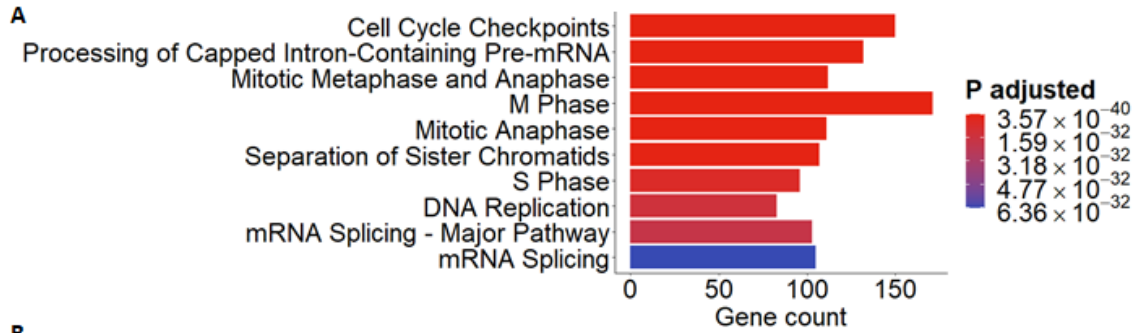


**Figure 3.6. Identification of enriched pathways among differentially expressed genes.** (A) Bar graph showing the results of over-representation analysis using the Pathway Enrichment Plot tab. The maximum number of pathways/categories to show was set to 10 and the enrichment  $p_{adj}$  value cutoff was set to  $< 1 \times 10^{-30}$ . The gene count ( $x$ -axis) indicates the number of genes enriched in each pathway and colors indicate level of significant ( $p_{adj}$ ). The pathways are plotted on the  $y$ -axis in order of increasing significance. (B) While the Pathway Enrichment Plot tab shows a bar graph or dot plot for only a subset of enriched pathways, the Pathway Enrichment Map tab shows all of the enriched pathways in an interconnected network map. The size of each node indicates the gene count (number of genes enriched in each category) and the color represents the  $p_{adj}$  (the cutoff was set to  $< 1 \times 10^{-30}$ ). (C) The GSEA Plot tab generates a plot of the running enrichment score for a specified pathway/category. The plot for the category “cell cycle” is illustrated here. Currently only Reactome pathways/categories are supported for each of these figures. The input data for A-C is the filtered or unfiltered data from the Gene Table tab (we set the LFC to  $< 0$  and the  $p_{adj}$  cutoff to  $< 0.05$ ).

used to generate these figures is the filtered or unfiltered data from the Gene Table tab (we filtered the data using  $LFC < 0$  and  $p_{adj} < 0.05$ ). The pathways identified in **Figures 3.6A-C** are consistent with the most downregulated genes shown in the heatmap (**Figure 3.5B**) and volcano plot (**Figure 3.5C**) (such as *H2AX*, *CDC20*, *CCNBI*, *AURKA*) and indicate the most significantly enriched pathways among downregulated genes are related to cell cycle and DNA replication processes. Together, the read count plots, heatmap, volcano plot and pathway plots inform researchers of gene expression changes and provide insight into which genes and pathways may play an important role in their experimental system.

### 3.4.2 Future work

DGE analyses computes differences between two groups at a time, such as Wildtype and Single-knockout, even though users can load data files containing >2 groups (e.g. Wildtype, Single-knockout and Double-knockout). Currently, users must perform one comparison first (e.g. Wildtype vs Single-knockout), download the results and then perform another comparison (e.g. Wildtype vs Double-knockout) and download the new results. Users must then manually perform comparisons outside of BEAVR to identify overlapping or non-overlapping genes. Future updates to BEAVR will allow users to perform multiple DGE analyses and allow them to interact with both results at once to perform direct comparisons within BEAVR. Implementation of additional plotting tools, such as Euler or Venn diagrams, will allow for the visualization of overlapping or non-overlapping dysregulated genes across different comparisons such as Wildtype vs Single-knockout and Wildtype vs Double-

knockout. These overlapping or non-overlapping datasets can then be used to perform pathway analysis or GSEA within BEAVR.

Presently, BEAVR only supports Reactome categories for pathway analysis and GSEA. Future updates will enable support for Gene Ontology (GO) [16], Disease Ontology (DO) [17], KEGG [18], WikiPathways [19] and Molecular Signature Database (MSigDb) [14, 20] to provide users with more options.

### 3.5 Conclusions

RNA-seq analyses has largely relied on command-line-driven tools, such as DESeq2 [8], EdgeR [21] or ALDEx [22], thereby creating a barrier to entry for scientists wishing to conduct RNA-seq analyses. Here we presented BEAVR, a graphically-driven tool that greatly simplifies DGE analyses through a logical workflow that makes use of DESeq2 as the core DGE engine. BEAVR is easy-to-use and allows researchers to not only quickly and easily change experimental parameters in real-time to visualize results, but also provides an intuitive interface for researchers to explore their results in-depth and generate highly customizable figures. Various other tools have been developed to provide users with graphical interfaces for RNA-seq analyses, most notably GENAVi [23], START [24], iDEP [25], DEBrowser [26], DEIVA [27] and DEApp [28]. While these tools have undoubtedly provided a significant evolution in RNA-seq analysis tools, we found that BEAVR offers meaningful advantages in comparison. Specifically, the ease of installation and usage, combined with more flexibility in data output features are important advancements. None of these programs offers each of our key features in one complete

package, such as filtering capabilities of gene lists, all of the different data displays that BEAVR provides (heat-map, PCA plots, etc.), the ability to customize and export figures in as many formats, or the ability to integrate pathway analysis. Based on these differences we expect BEAVR will be widely utilized.

BEAVR was developed to be simple enough for novices, yet fast and powerful enough for experts to streamline and automate DGE analyses. Even with modest computing power by today's standards, BEAVR is capable of completing analyses within minutes, allowing researchers to quickly automate analyses of large datasets. With uses for RNA-seq continuing to expand — both experimentally and clinically — BEAVR is well-positioned to allow analysis of these datasets to be quick and efficient, while providing the latitude for customization as per the user's requirements.

## 3.6 Availability and Requirements

**Project name:** BEAVR

**Project home page:** <https://github.com/developerpiru/BEAVR> and <https://hub.docker.com/r/pirunthan/beavr>

**Project documentation:**

<https://github.com/developerpiru/BEAVR/blob/master/README.md>

**Operating system:** Linux, Mac OS, Windows

**Programming language:** R

**Other requirements:** R 3.5 or higher, web browser

**License:** GNU General Public License v3.0

**Any restrictions to use by non-academics:** None

### 3.7 Availability of data and materials

The dataset used in this article is available in the GEO repository ([GSE59009](#)).

### 3.8 Funding

PP was supported by CaRTT. FAD is the Wolfe Senior Fellow in Tumor Suppressor Genes at Western University. This study was funded by the Canadian Institutes of Health Research and funds provided by the London ‘Run for Ovarian Cancer’. No funding sources participated in the design, data collection, analysis, interpretation of data, or preparation of the manuscript.

### 3.9 Acknowledgements

We wish to thank Dr. John W. Barrett, Dr. Haider M. Hassan and Mike Roes (London Regional Cancer Program, London Health Sciences Centre) for beta testing BEAVR and providing key feedback.



### 3.10 References

1. Hrdlickova R, Toloue M, Tian B: RNA-Seq methods for transcriptome analysis. *Wiley Interdiscip Rev RNA* 2017, 8(1).
2. Stark R, Grzelak M, Hadfield J: RNA sequencing: the teenage years. *Nat Rev Genet* 2019, 20(11):631-656.
3. Conesa A, Madrigal P, Tarazona S, Gomez-Cabrero D, Cervera A, McPherson A, Szczesniak MW, Gaffney DJ, Elo LL, Zhang X *et al*: A survey of best practices for RNA-seq data analysis. *Genome Biol* 2016, 17:13.
4. Kamps R, Brandao RD, Bosch BJ, Paulussen AD, Xanthouleas S, Blok MJ, Romano A: Next-Generation Sequencing in Oncology: Genetic Diagnosis, Risk Prediction and Cancer Classification. *Int J Mol Sci* 2017, 18(2).
5. Buzdin A, Sorokin M, Garazha A, Glusker A, Aleshin A, Poddubskaya E, Sekacheva M, Kim E, Gaifullin N, Giese A *et al*: RNA sequencing for research and diagnostics in clinical oncology. *Semin Cancer Biol* 2019, 60:311-323.
6. Marco-Puche G, Lois S, Benitez J, Trivino JC: RNA-Seq Perspectives to Improve Clinical Diagnosis. *Front Genet* 2019, 10:1152.
7. Costa-Silva J, Domingues D, Lopes FM: RNA-Seq differential expression analysis: An extended review and a software tool. *PLoS One* 2017, 12(12):e0190152.
8. Love MI, Huber W, Anders S: Moderated estimation of fold change and dispersion for RNA-seq data with DESeq2. *Genome Biol* 2014, 15(12):550.
9. Zhu A, Ibrahim JG, Love MI: Heavy-tailed prior distributions for sequence count data: removing the noise and preserving large differences. *Bioinformatics* 2019, 35(12):2084-2092.
10. Yu G, He Q-Y: ReactomePA: an R/Bioconductor package for reactome pathway analysis and visualization. *Molecular BioSystems* 2016, 12(2):477-479.
11. Sehrawat A, Gao L, Wang Y, Bankhead A, 3rd, McWeeney SK, King CJ, Schwartzman J, Urrutia J, Bisson WH, Coleman DJ *et al*: LSD1 activates a lethal prostate cancer gene network independently of its demethylase function. *Proc Natl Acad Sci U S A* 2018, 115(18):E4179-E4188.
12. Ma S, Dai Y: Principal component analysis based methods in bioinformatics studies. *Brief Bioinform* 2011, 12(6):714-722.
13. Wong DJ, Liu H, Ridky TW, Cassarino D, Segal E, Chang HY: Module map of stem cell genes guides creation of epithelial cancer stem cells. *Cell Stem Cell* 2008, 2(4):333-344.
14. Subramanian A, Tamayo P, Mootha VK, Mukherjee S, Ebert BL, Gillette MA, Paulovich A, Pomeroy SL, Golub TR, Lander ES *et al*: Gene set enrichment analysis: A knowledge-based approach for interpreting genome-wide expression profiles. *Proceedings of the National Academy of Sciences* 2005, 102(43):15545.
15. Mootha VK, Lindgren CM, Eriksson K-F, Subramanian A, Sihag S, Lehar J, Puigserver P, Carlsson E, Ridderstråle M, Laurila E *et al*: PGC-1 $\alpha$ -responsive genes involved in oxidative phosphorylation are coordinately downregulated in human diabetes. *Nature Genetics* 2003, 34(3):267-273.
16. The Gene Ontology Consortium: The Gene Ontology Resource: 20 years and still GOing strong. *Nucleic Acids Research* 2018, 47(D1):D330-D338.

17. Schriml LM, Arze C, Nadendla S, Chang Y-WW, Mazaitis M, Felix V, Feng G, Kibbe WA: Disease Ontology: a backbone for disease semantic integration. *Nucleic acids research* 2012, 40(Database issue):D940-D946.
18. Kanehisa M, Sato Y, Furumichi M, Morishima K, Tanabe M: New approach for understanding genome variations in KEGG. *Nucleic acids research* 2019, 47(D1):D590-D595.
19. Slenter DN, Kutmon M, Hanspers K, Riutta A, Windsor J, Nunes N, Mélius J, Cirillo E, Coort SL, Digles D *et al*: WikiPathways: a multifaceted pathway database bridging metabolomics to other omics research. *Nucleic acids research* 2018, 46(D1):D661-D667.
20. Liberzon A, Birger C, Thorvaldsdóttir H, Ghandi M, Mesirov JP, Tamayo P: The Molecular Signatures Database (MSigDB) hallmark gene set collection. *Cell Syst* 2015, 1(6):417-425.
21. Robinson MD, McCarthy DJ, Smyth GK: edgeR: a Bioconductor package for differential expression analysis of digital gene expression data. *Bioinformatics (Oxford, England)* 2010, 26(1):139-140.
22. Fernandes AD, Macklaim JM, Linn TG, Reid G, Gloor GB: ANOVA-like differential expression (ALDEx) analysis for mixed population RNA-Seq. *PloS one* 2013, 8(7):e67019-e67019.
23. Reyes ALP, Silva TC, Coetzee SG, Plummer JT, Davis BD, Chen S, Hazelett DJ, Lawrenson K, Berman BP, Gayther SA *et al*: GENAVi: a shiny web application for gene expression normalization, analysis and visualization. *BMC Genomics* 2019, 20(1):745.
24. Nelson JW, Sklenar J, Barnes AP, Minnier J: The START App: a web-based RNAseq analysis and visualization resource. *Bioinformatics (Oxford, England)* 2017, 33(3):447-449.
25. Ge SX, Son EW, Yao R: iDEP: an integrated web application for differential expression and pathway analysis of RNA-Seq data. *BMC Bioinformatics* 2018, 19(1):534.
26. Kucukural A, Yukselen O, Ozata DM, Moore MJ, Garber M: DEBrowser: interactive differential expression analysis and visualization tool for count data. *BMC Genomics* 2019, 20(1):6.
27. Harshbarger J, Kratz A, Carninci P: DEIVA: a web application for interactive visual analysis of differential gene expression profiles. *BMC Genomics* 2017, 18(1):47.
28. Li Y, Andrade J: DEApp: an interactive web interface for differential expression analysis of next generation sequence data. *Source Code for Biology and Medicine* 2017, 12(1):2.

## Chapter 4

### 4 GO-CRISPR: a highly controlled workflow to improve discovery of gene essentiality in loss-of-function screens

#### 4.1 Abstract

Genome-wide CRISPR screens are an effective discovery tool for genes that underlie diverse cellular mechanisms that can be scored through cell fitness. Loss-of-function screens are particularly challenging compared to gain-of-function because of the limited dynamic range of decreased sgRNA sequence detection. Here we describe **Guide-Only control CRISPR (GO-CRISPR)**, an improved loss-of-function screening workflow, and its companion software package, **Toolset for the Ranked Analysis of GO-CRISPR Screens (TRACS)**. We demonstrate a typical GO-CRISPR workflow in a non-proliferative 3D spheroid model of dormant high grade serous ovarian cancer and demonstrate superior performance to standard screening methods. The unique integration of the pooled sgRNA library quality and guide-only controls allows TRACS to identify novel molecular pathways that were previously unidentified in tumor dormancy. Together, GO-CRISPR and TRACS can robustly improve the discovery of essential genes in challenging biological scenarios.

#### 4.2 Introduction

Gene editing using CRISPR/Cas9 technology has seen widespread adoption across most biomedical disciplines, including cancer research <sup>1,2</sup>. In particular, the ability to

multiplex CRISPR gene knockouts on a genome-wide scale has stimulated systematic interrogation of cell biology <sup>3</sup>. Pooled single guide RNA (sgRNA) libraries are used to create single-gene knockouts in individual cells and selective pressure is applied through culture conditions or drug treatment. Genetic deficiencies that produce resistance or susceptibility are quantitated using sgRNA coding sequences as barcodes to compare gene knockout abundance between the start and end of the experiment <sup>4</sup>. CRISPR screens can therefore discover functional roles for genes and pathways not suggested by more traditional hypothesis-driven research.

Gain-of-function genome-wide CRISPR screens can lead to several orders of magnitude change in sgRNA sequence abundance because of resistant cell proliferation, unequivocally identifying resistance genes <sup>5-7</sup>. Conversely, loss-of-function is more challenging to quantitate because complete disappearance of sgRNA sequences for a gene may represent technical failure of the screen design, or its execution <sup>8</sup>. In addition, knockout of an individual gene in the chosen culture condition may not cause lethality with complete penetrance <sup>9</sup>. Ultimately, identification of essential genes in loss-of-function screens has relied on prolonged periods of cell proliferation to separate the abundance of bystander sgRNA abundance from true deleterious changes <sup>4</sup>. For this reason, CRISPR screens have generally utilized rapidly proliferating 2D cell culture conditions. Scenarios such as the tumor microenvironment, metastasis and tumor dormancy, are better assessed in 3D culture models such as multicellular tumor spheroids or organoids <sup>10-13</sup>. However, the inability of organoids to quantitatively regenerate from individual cells upon subculture has prevented robust library representation <sup>14</sup>, and in some cases this has been compensated by screening more compact, partial genome libraries <sup>15</sup>. Furthermore, most 3D spheroids

exhibit slower growth kinetics due to hypoxia and necrosis which can further hamper detection of gene loss events <sup>16</sup>. All of these factors likely contribute to stochastic loss of guides which can confound loss-of-function studies since current methods cannot distinguish these Cas9-independent events from bona fide loss-of-function due to gene editing. For these reasons, the classification of gene ‘essentiality’ is highly challenging in 3D culture conditions.

Therefore, there is a need for a screening method that can be adapted for a broad range of complex culture conditions that include low proliferation rates to identify essential genes. This motivated us to develop **Guide-Only control CRISPR (GO-CRISPR)**. GO-CRISPR is a scalable loss-of-function screening method that can be used to discover essential genes in standard monolayer (2D) or complex 3D culture conditions such as dormant tumor spheroids that exhibit arrested cell proliferation. To support broad usability, we also developed TRACS (**T**oolset for the **R**anked **A**nalysis of **GO-CRISPR S**creens) to automate the analysis of GO-CRISPR screens in an easy-to-use software package. Together, GO-CRISPR and TRACS allowed us to discover novel survival pathways in dormant ovarian cancer spheroids, whereas established CRISPR screening and analysis approaches were unable to find essential genes. We expect that this approach can be broadly applied to genome-wide loss-of-function CRISPR screens in low proliferation biological contexts.

## 4.3 Results

### 4.3.1 The GO-CRISPR Workflow

The challenges presented by genome wide CRISPR screening in growth arrested populations of cells motivated us to develop a new workflow that could reveal critical insights into mechanisms of survival in cancer cell dormancy. We developed GO-CRISPR to overcome these challenges and its typical experimental workflow is illustrated in **Figure 4.1A**. CRISPR screens depend on high-level Cas9 expression to ensure maximum efficiency of gene disruption in Cas9-positive cells transduced with a pooled sgRNA library ( $L_0$ )<sup>4,17</sup>. GO-CRISPR uniquely incorporates sequencing data from a parallel screen in which Cas9-negative cells are also transduced with the same pooled sgRNA library ( $L_0$ ). Both the Cas9-positive and Cas9-negative cells are treated in an identical manner. Following antibiotic selection for sgRNA transduction and expansion into triplicate cultures, cells are harvested from the initial culture condition ( $T_0$ ). Next, both Cas9-positive and Cas9-negative populations are exposed to the desired selective pressure or culture conditions ( $P_s$ ) and cells are harvested from the final culture condition ( $T_f$ ). Next-generation sequencing (NGS) is then used to quantitate the abundance of PCR-amplified sgRNA sequences from these 12 samples, as well the initial library preparation ( $L_0$ ).

To evaluate GO-CRISPR screens, we developed the TRACS algorithm that integrates data from Cas9-positive and Cas9-negative populations to make gene essentiality predictions (**Figure 4.2**). It is based on assigning genes enrichment scores similar to the single gene score previously described by Wang *et. al.*<sup>18</sup>. However, TRACS differs by calculating three different enrichment scores for each gene (**Figure 4.1A** in red). These include a Library Enrichment Score (Library ES) that compares sgRNA read counts

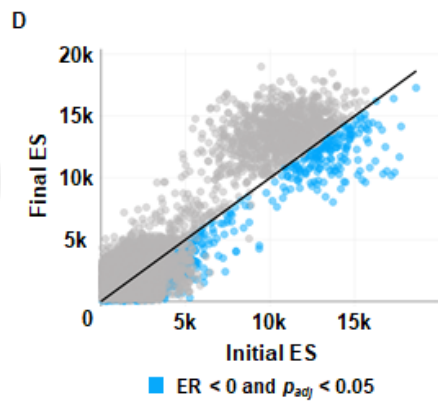
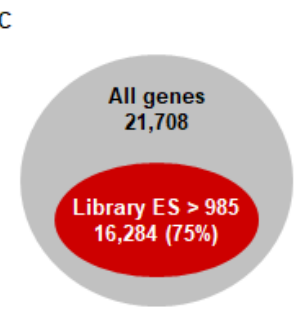
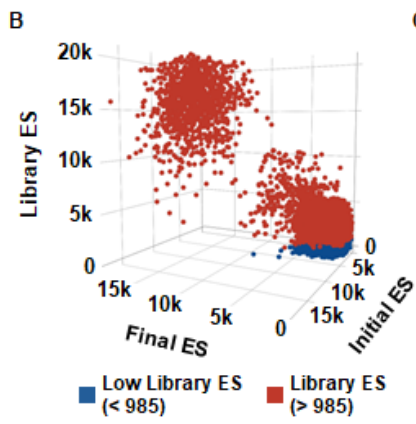
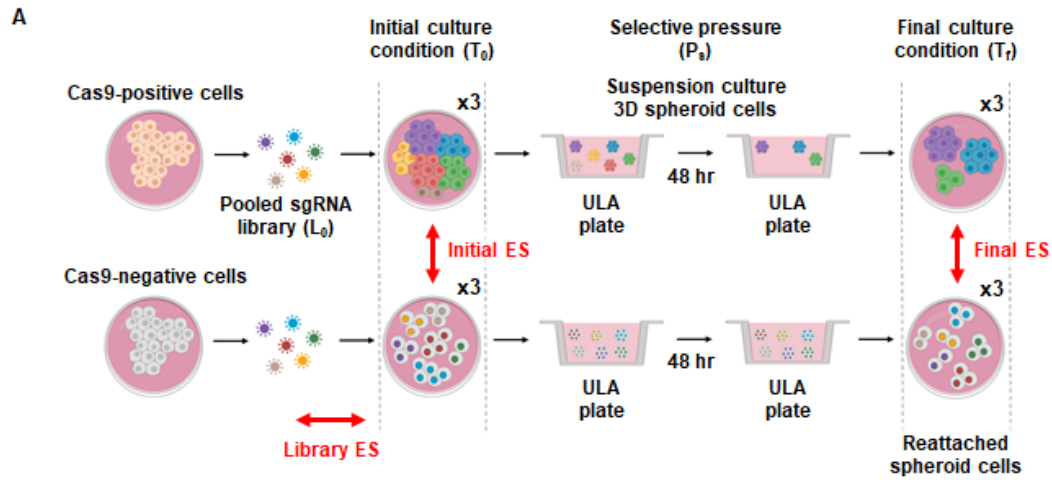


**Figure 4.1. Typical experimental workflow for GO-CRISPR screening and analysis using TRACS.** (A) iOvCa147 High-grade serous ovarian cancer (HGSOC) cells were transduced with lentivirus expressing Cas9. High efficiency Cas9-positive cells (top row) and Cas9-negative cells (bottom row) were transduced with the GeCKO v2 pooled sgRNA library ( $L_0$ ). After antibiotic selection, both Cas9 positive and negative cells were split into triplicates (x3) and maintained in initial culture conditions ( $T_0$ ) before being transferred to suspension culture conditions in ULA plasticware (selective pressure,  $P_s$ ) to induce spheroid formation and select for cell survival. Viable spheroid cells were then transferred to standard plasticware to facilitate reattachment in the final culture condition ( $T_f$ ). The initial pooled sgRNA library ( $L_0$ ) and Cas9-positive and Cas9-negative cells were collected at  $T_0$  and  $T_f$  for sgRNA quantitation by NGS. TRACS was used to calculate Library, Initial and Final Enrichment Scores (ES) using read quantities from  $L_0$  and Cas9-positive and Cas9-negative samples. (B) 3D plot output from TRACS illustrating the Library ES, Initial ES and Final ES for each gene. Genes highlighted in dark blue have low Library ES (determined by calculating the first quartile value across all Library ES;  $< 985$  in this experiment). (C) Euler diagram showing the distribution of retained (in red) and discarded genes based on the Library ES (16,284 genes had Library ES  $> 985$ ). (D) 2D scatter plot output from TRACS showing the distribution of Initial ES and Final ES for all genes. Genes highlighted in light blue (6,717 genes) met the low Library ES cutoff and had a negative Enrichment Ratio (ER) and  $p_{adj} < 0.05$ , indicating their sgRNA abundance decreases in  $T_f$  compared to  $T_0$ .



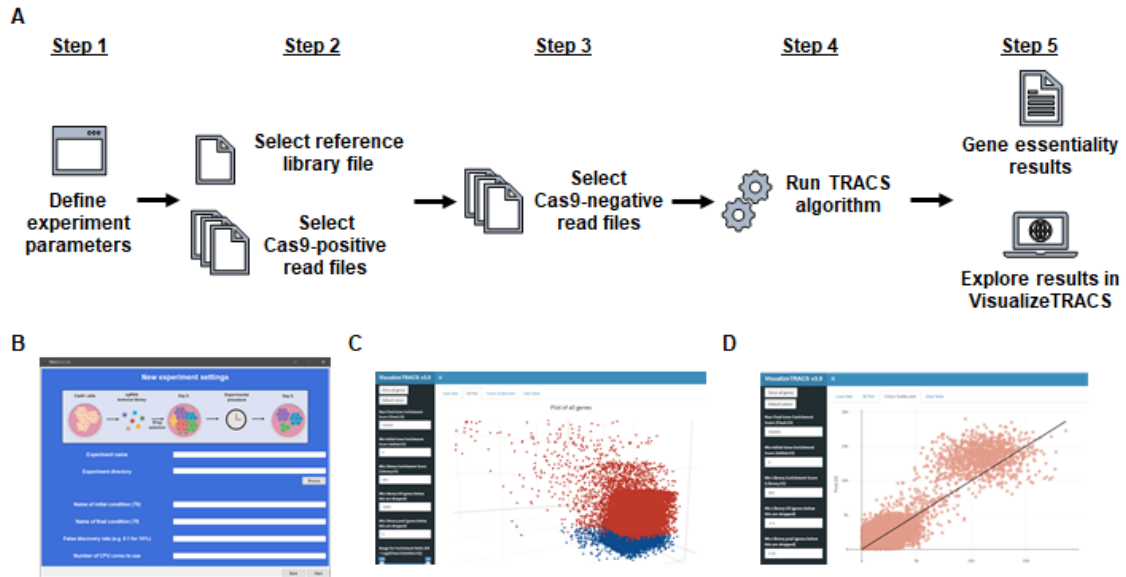


**Figure 4.2. Typical analysis workflow using TRACS to identify essential genes. (A)** The TRACS workflow is separated into five steps. *Step 1*: Experiment parameters are entered in the graphical user interface (GUI). *Step 2*: Library reference file (.csv format) and raw read files (.fastq format) for all Cas9-positive replicates are selected in the GUI. *Step 3*: Raw read files (.fastq format) for all Cas9-negative replicates are selected in the GUI. *Step 4*: Raw reads are trimmed and aligned to generate read counts, then the TRACS algorithm runs to calculate Library ES, Initial ES, Final ES and the ER for each gene. *Step 5*: TRACS saves the results with all scores in an output file which can then be explored using the accompanying VisualizeTRACS data explorer. **(B)** Screenshot of the easy-to-use TRACS GUI asking user to enter experimental parameters (*Step 1*). Subsequent displays provide a similar interface for selecting input data files for *Steps 2-4*. **(C-D)** Screenshot of the accompanying VisualizeTRACS data explorer that researchers can use to visualize and inspect their TRACS output files and generate publication-ready figures. Researchers can control all aspects of filtering and data manipulation (Library ES, Initial ES, Final ES, ER,  $p_{adj}$ ) to fine-tune selection of genes.

for each gene between Cas9-negative cells and the library ( $L_0$ ) to determine Cas9-independent non-gene-editing-related changes in abundance. This is an important consideration since pooled sgRNA library preparations do not uniformly represent all genes<sup>19</sup>. An Initial Enrichment Score (Initial ES) is calculated by comparing sgRNA abundances for each gene in Cas9-positive cells relative to their abundances in Cas9-negative cells where they cannot direct gene editing. Lastly, a Final Enrichment Score (Final ES) determines sgRNA abundance between Cas9-positive and Cas9-negative cells following the exposure of both populations to the desired selective pressure or culture conditions ( $P_s$ ). For each gene, the Library ES, Initial ES and Final ES are weighted according to the number of sgRNAs that are detected for that gene. Thus, a relatively low Initial ES or Final ES indicate reduced sgRNA abundance in the Cas9-positive population and these scores incorporate a penalty for undetected sgRNAs to emphasize the most reliable sgRNA measurements. Finally, TRACS calculates an Enrichment Ratio (ER) that is the  $\log_2$ -fold-change (LFC) value between the Final ES and Initial ES to reveal changes in relative abundance between  $T_0$  and  $T_f$  culture conditions to detect sgRNAs that depleted under the selective pressure ( $P_s$ ), thereby identifying gene essentiality. The ER informs researchers if a gene shows essentiality for fitness (negative ER) or is non-essential (positive ER) in the experimental conditions.

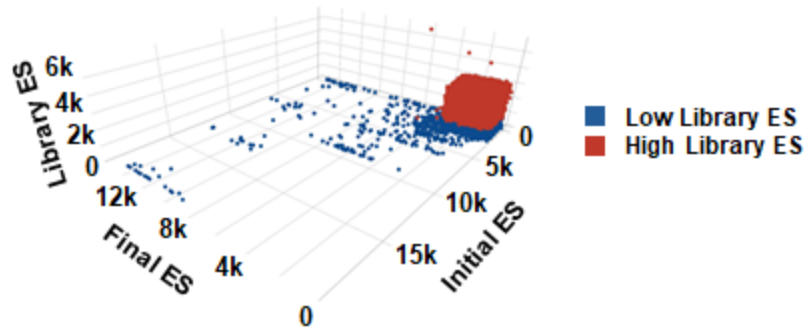
#### 4.3.2 Discovering Ovarian Cancer Spheroid Vulnerabilities

To demonstrate the value of the GO-CRISPR and TRACS workflow, we performed a genome-wide screen in iOvCa147 high-grade serous ovarian cancer (HGSOC) cells. HGSOC is a highly metastatic disease in which cells detach from primary tumors and

aggregate to form 3D spheroids in the abdomen<sup>20</sup>. These spheroid cells are growth arrested and highly resistant to chemotherapy, emphasizing the need to discover their vulnerabilities to improve treatment<sup>21</sup>. We designed a GO-CRISPR screen experiment (**Figure 4.1A**) to elucidate the genes and pathways that are critical to spheroid cell survival using ultra-low attachment (ULA) plasticware to induce spheroid formation *in vitro*<sup>22</sup>. Ovarian cancer cells undergo significant cell death in suspension culture while spheroids form, therefore after 48-hours we transferred cells back to standard plasticware to allow reattachment and purification of viable cells.

Following analysis with TRACS, we sought to discover genes that were most selectively required for survival in suspension conditions; these represent potential therapeutic targets for dormant ovarian cancer cell spheroids. **Figure 4.1B** displays each ES in a 3D plot that reveals the distribution of scores in each dimension and highlights genes with low Library ES in dark blue. A low Library ES means that a gene's sgRNA sequences were poorly represented at T<sub>0</sub> due to non-gene-editing events that occurred between viral transduction of the pooled sgRNA library and antibiotic selection. This is an important consideration because when a gene's Library ES is low, its initial sgRNA abundance is also low, and relatively small changes in sgRNA abundance can lead to extreme enrichment scores at T<sub>0</sub> (Initial ES) or T<sub>f</sub> (Final ES) (**Figure 4.3A**). To avoid these false positives, we excluded the first quartile of Library ES from further analysis (Library ES < 985 in this experiment) (**Figure 4.1C and Figure 4.3B**). To discover genes essential for spheroid cell survival, we focused our attention on those that had a negative ER. In **Figure 4.1D**, genes highlighted in light blue met the Library ES cutoff (> 985) and had ER < 0 and  $p_{adj} < 0.05$  at a false discovery rate (FDR) of 10%. We found 6,717 genes that met

A



B

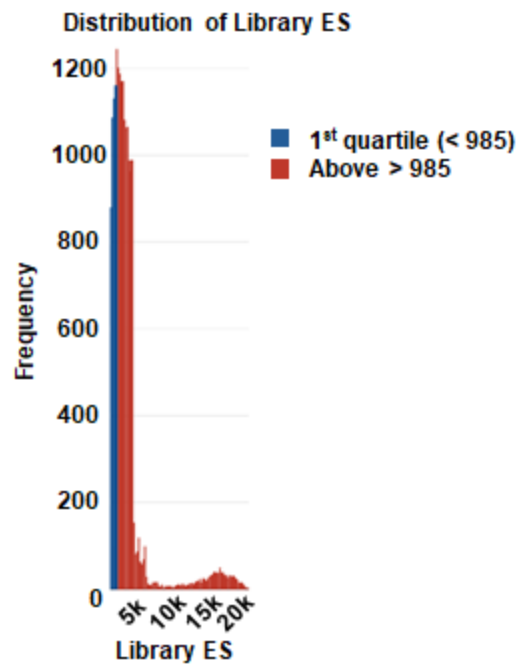


**Figure 4.3. Genes with low Library ES tend to have extreme Initial ES and/or Final ES.** (A) TRACS 3D plot illustrating the distribution of Library ES, Initial ES, Final ES in an extreme case example screen that had very poor representation of sgRNAs at  $T_0$  in Cas9-negative cells. Genes that have low Library ES (genes that fall into the first quartile of all Library ES across all genes) are shown in dark blue. These genes also tend to have extreme values for Initial ES and/or Final ES which can lead to potential false positives. This extreme example demonstrates how initial sgRNA abundances can be low due to non-gene-editing events and skew gene scores at  $T_0$  (Initial ES) and  $T_f$  (Final ES). (B) Histogram illustrating the distribution of Library ES across all genes in our GO-CRISPR experiment. To diminish the effects of poorly represented sgRNAs, TRACS determines the distribution of the Library ES across all genes and computes the cutoff value for the first quartile (the bottom 25% of all Library ES; highlighted in dark blue). TRACS then discards genes that have Library ES below this threshold ( $< 985$  for our iOvCa147 screen), however researchers can increase or decrease the threshold within the TRACS software suite for further fine-tuning.

these criteria and the top 10 genes with the most negative ER are shown in **Table 4.1**. This data suggests these are the ten most essential genes required for spheroid cell viability in iOvCa147 cells.

### 4.3.3 Validation of TRACS Gene Essentiality Predictions

To determine the validity of gene essentiality predictions made by TRACS, we measured its ability to categorize the 1,000 non-targeting control (NTC) sgRNAs from the GeCKO v2 pooled library. These NTC sgRNAs target non-coding intergenic sequences and should rank as non-essential<sup>19</sup>. We computed a receiver operating characteristic curve (ROC) and determined the area under the curve (AUC) was 98.5%, demonstrating that TRACS correctly identified NTC sgRNAs as non-essential (**Figure 4.4A**). This is a critical control because amplified genome regions produce false essential calls among non-coding controls<sup>23,24</sup>. HGSOc is characterized by extensive amplifications and deletions<sup>25</sup> and this data demonstrates TRACS eliminates this potentially confounding interpretation. For added validation, we used CRISPR/Cas9 to disrupt the top five genes with the most negative ER (**Table 4.1**) in iOvCa147 cells. Independent knockout of each gene showed significant loss of viability under suspension culture conditions (**Figure 4.4B**). Conversely, knockout of the top five genes with the most positive ER did not compromise viability, suggesting our GO-CRISPR screen approach reliably discovers loss-of-function events (**Figure 4.4C**).

**Table 4.1 Top 10 genes with the most negative Enrichment Ratio (ER) in TRACS**

<b>Gene</b>	<b>Library ES</b>	<b>Initial ES</b>	<b>Final ES</b>	<b>ER</b>	<b><i>p</i><sub>adj</sub></b>
<i>AGPS</i>	2648.39	1384.00	16.61	-6.38	1.01 x 10 <sup>-2</sup>
<i>SLC2A11</i>	2421.17	2216.28	37.33	-5.89	1.06 x 10 <sup>-2</sup>
<i>ZC3H7A</i>	2397.67	2592.22	62.67	-5.37	5.19 x 10 <sup>-3</sup>
<i>PDCD2L</i>	1449.39	3018.56	82.67	-5.19	1.86 x 10 <sup>-3</sup>
<i>NPM1</i>	2966.72	2070.89	68.06	-4.93	9.78 x 10 <sup>-3</sup>
<i>KIAA1731</i>	3063.72	2050.61	83.78	-4.61	4.92 x 10 <sup>-3</sup>
<i>MAP3K6</i>	1741.61	2206.22	93.39	-4.56	2.76 x 10 <sup>-4</sup>
<i>SSH1</i>	1281.61	1347.67	57.50	-4.55	1.64 x 10 <sup>-2</sup>
<i>MFN2</i>	2779.67	2080.00	89.83	-4.53	1.16 x 10 <sup>-2</sup>
<i>CREBL2</i>	1449.78	2211.22	96.67	-4.52	6.69 x 10 <sup>-3</sup>

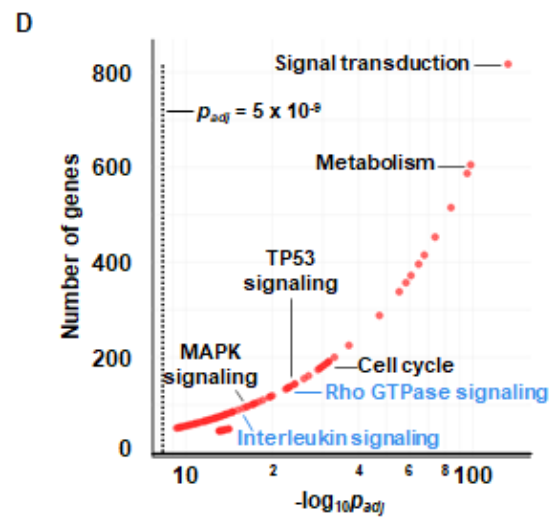
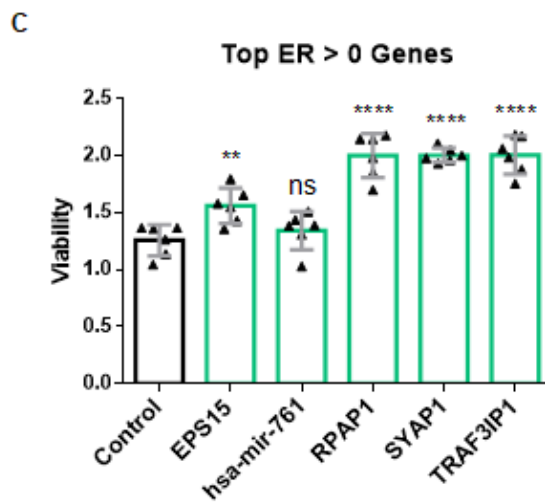
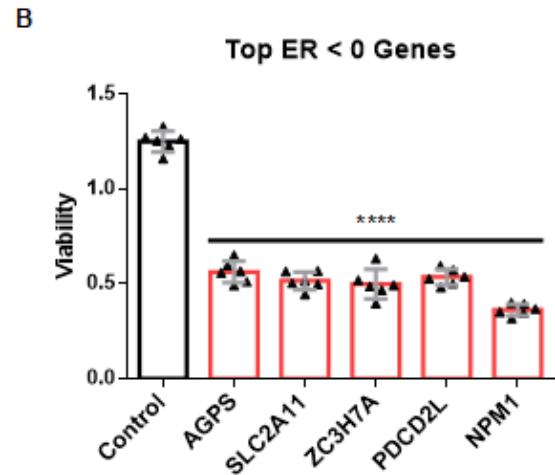
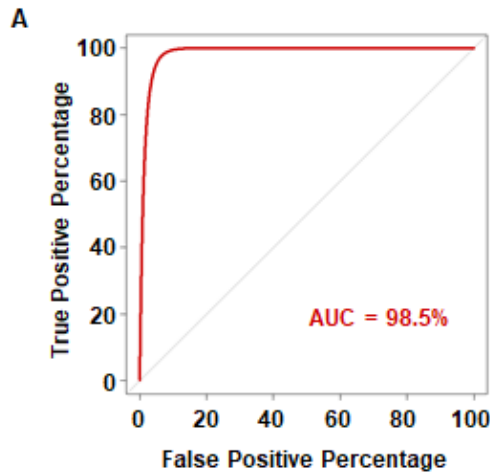




**Figure 4.4. Validation of TRACS gene essentiality predictions.** (A) The GeCKO v2 pooled library contains 1,000 non-targeting control (NTC) sgRNAs that should not elicit a change in cell fitness. We evaluated the ability of TRACS to classify these sgRNAs by computing a receiver operating characteristic curve (ROC). The area under the curve (AUC) was determined to be 98.5%, indicating TRACS accurately classifies these NTC sgRNAs as non-essential. (B) We evaluated the essentiality of the top five genes with the most negative ER: *AGPS*, *SLC2A11*, *ZC3H7A*, *PDCD2L*, *NPM1* (see **Table 4.1**). CRISPR/Cas9 was used to disrupt each gene in iOvCa147 cells and pure single-gene knockout populations were assayed for spheroid cell viability in suspension culture conditions. Disruption of these genes resulted in significantly reduced cell viability. Genes in bar graph are arranged from most negative ER to least negative ER. (C) We similarly knocked out the top five genes with the most positive ER (*EPS15*, *hsa-mir-761*, *RPAP1*, *SYAP1*, *TRAF3IP1*) and assayed for viability in suspension culture conditions. Disruption of these genes did not adversely affect viability. Genes in bar graph are arranged from smallest to largest ER. (D) We performed gene ontology and pathway enrichment analysis with the 6,717 genes identified by TRACS to have negative ER and plotted the results. The minimum genes required for enrichment per category was set to 45 to ensure stringent selection of pathways. The dashed vertical line represents a  $p_{adj}$  value of  $5 \times 10^{-9}$ . Pathways to the right of this line have  $p_{adj} < 5 \times 10^{-9}$  after controlling for FDR at 10%. Pathways labelled in blue are previously undescribed in HGSOc. For (B) and (C), each point represents a biological replicate (n = 6). Bars represent means and error bars represent standard deviation. Statistics was performed using one-way ANOVA; \*\* denotes  $p < 0.01$ ; \*\*\* denotes  $p < 0.001$ ; \*\*\*\* denotes  $p < 0.0001$ ; ns denotes not significant ( $p > 0.05$ ).

#### 4.3.4 GO-CRISPR and TRACS Identify Novel Pathways in HGSOC

To further explore the genes identified, we performed gene ontology and pathway enrichment analysis with genes that had a negative ER and  $p_{adj} < 0.05$  and found 109 significantly enriched pathways (**Figure 4.4D**). Among these are cell cycle regulation <sup>22</sup>, MAPK signaling <sup>26</sup> and TP53 signaling <sup>25</sup> which are known to be involved in HGSOC progression and metastasis. Remarkably, our analysis also found novel pathways that have not yet been implicated in HGSOC including Rho GTPase signaling and interleukin signaling. Together, these data demonstrate that GO-CRISPR and TRACS can robustly identify functionally connected genes to enable novel pathway discoveries.

#### 4.3.5 Comparison of GO-CRISPR with conventional CRISPR screen workflows

Formation of growth arrested HGSOC spheroids in suspension culture is a stressful process in which many cells die without being incorporated into a spheroid. Moreover, the communal nature of spheroids further suggests that individual gene loss events in single cells may be masked in loss-of-function CRISPR screens through non-cell autonomous mechanisms. Thus GO-CRISPR and TRACS were born out of the desire to screen a significantly challenging biological scenario. To fully illustrate the advantages of GO-CRISPR and TRACS, we have analyzed the triplicate replicates of  $T_0$  and  $T_f$  solely in Cas9-expressing cells using MAGeCK-RRA, MAGeCK-MLE <sup>27</sup> and BAGEL <sup>28</sup> as this represents a commonly used CRISPR screen workflow that lacks guide only controls (**Figure 4.5**). A basic premise for genome-wide CRISPR screens using only Cas9-expressing cells is that poorly represented sgRNAs, or stochastic changes unrelated to the

experiment in question, will be removed through statistical cutoffs. Analysis of this data using MAGeCK-RRA/MLE did not detect any essential genes using standard statistical cutoffs (**Figure 4.5A-D**), including the genes with the most negative ER that were found to be essential by TRACS (**Figure 4.5I**). BAGEL did not discover essential genes either (**Figure 4.5G-H**). We then removed statistical cutoffs in MAGeCK-RRA/MLE and found approximately 30% of top-ranked genes had low Library ES according to TRACS, reinforcing the previously described phenomenon of identifying false positives due to low initial sgRNA abundances (**Figure 4.5E-F and Figure 4.6**). Additionally, our computed ER discriminates essentiality of NTCs effectively (**Figure 4.4A**), whereas MAGeCK (without statistical cutoffs) frequently misclassifies NTCs as essential (**Figure 4.7A**). TRACS was also noticeably more reliable at identifying universally essential and non-essential gene sets <sup>28</sup> (**Figure 4.7B-C**). TRACS penalizes genes that have low sgRNA numbers and favors those with higher sgRNA values to further mitigate the effects of stochastic sgRNA loss and ensure that gene essentiality predictions are made using the largest possible sample size (**Figure 4.8A**). Without statistical cutoffs, many MAGeCK-MLE top-ranked gene decisions are based on single gRNAs (**Figure 4.8B**). Overall, integrating data from the pooled sgRNA library and Cas9-negative populations allows TRACS to outperform other methods to accurately predict gene essentiality in a challenging low proliferation, suspension culture scenario.

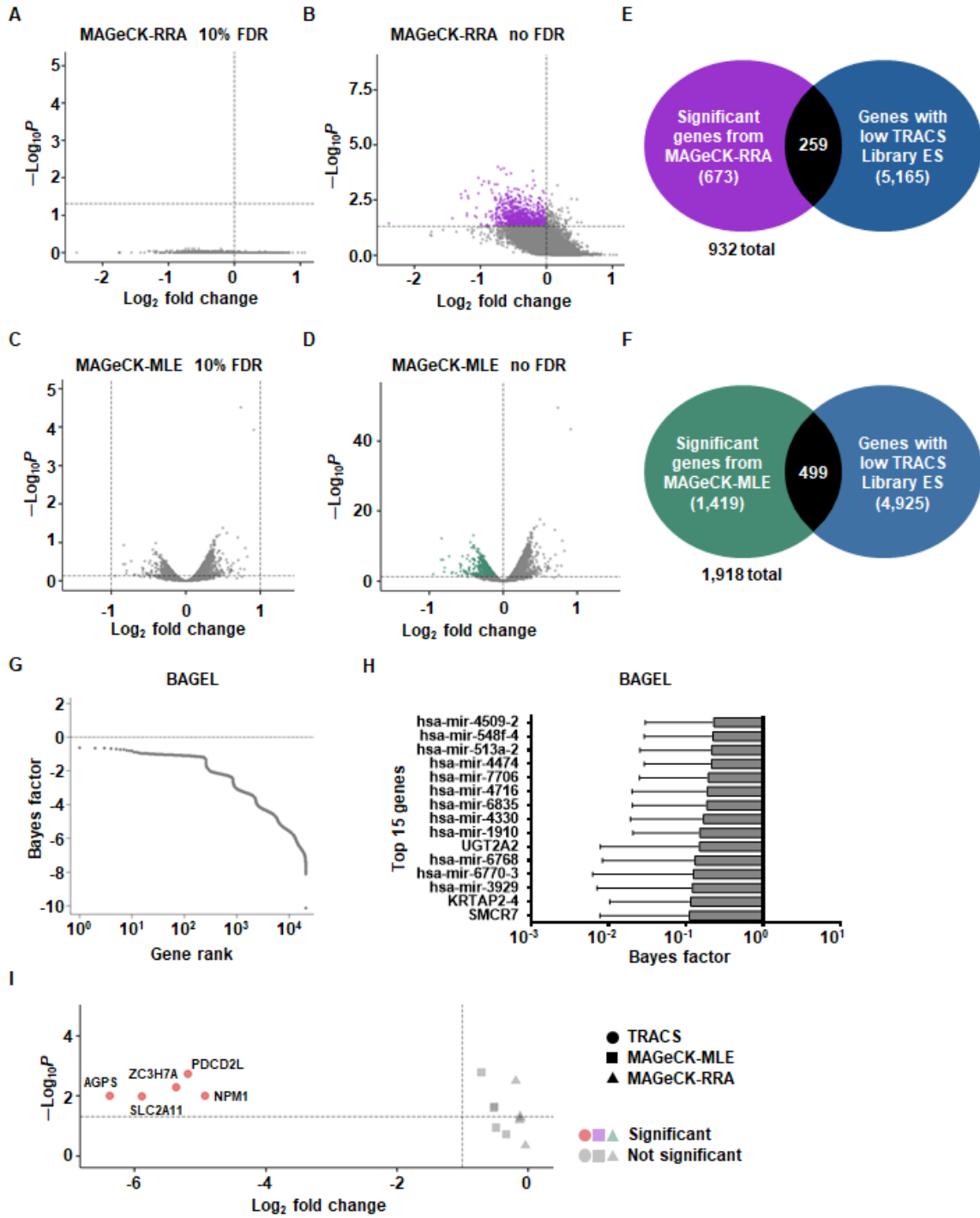


**Figure 4.5. MAGeCK and BAGEL are unable to identify essential genes in our screen using Cas9 positive read data.** (A) We analyzed our screen data using Cas9-positive replicates from  $T_0$  and  $T_f$  using the MAGeCK-RRA (robust rank aggregation) method with a controlled FDR of 10%. The dashed horizontal line represents  $p < 0.05$ ; any genes above this line are significant. Genes to left of the dashed vertical line have  $\log_2$ -fold-change (LFC)  $< 0$  indicating their sgRNA abundances decrease from  $T_0$  to  $T_f$ . We did not find any genes to be significant using these typical parameters for MAGeCK-RRA. (B) Removal of FDR control with MAGeCK-RRA revealed 932 genes (highlighted in purple) that had LFC  $< 0$  and unadjusted  $p$  value  $< 0.05$ . Genes shown in grey did not meet these criteria. (C) We analyzed our screen data using Cas9-positive replicates from  $T_0$  and  $T_f$  using the MAGeCK-MLE (maximum likelihood estimation) method with a controlled FDR of 10%. Genes above the dashed horizontal line have  $p < 0.05$  and are significant. Genes to the left of the dashed vertical line have LFC  $< -1$ , the typically used cutoff for gene essentiality using this method. We did not find any genes that met both of these criteria. (D) Removal of FDR control with MAGeCK-MLE and increasing the LFC cutoff to  $< 0$  revealed 1,918 genes (highlighted in green) that had LFC  $< 0$  and  $p$  value  $< 0.05$ . Genes shown in grey did not meet these criteria. (E) Venn diagram showing overlap of the 932 genes (in purple) identified by MAGeCK-RRA with the genes identified by TRACS as having low Library ES (5,424 genes total). 259 genes overlap between the two sets (27.8%). (F) Venn diagram showing overlap of the 1,918 genes (in green) identified by MAGeCK-MLE with the genes identified by TRACS as having low Library ES. 499 genes overlap between the two sets (26%). (G) We analyzed our screen data using Cas9-positive replicates from  $T_0$  and  $T_f$  using BAGEL and plotted the Bayes factor output for each gene in relation to the gene ranking. The Bayes factors for all genes were negative, indicating BAGEL did not discover any perturbations in sgRNA abundances between  $T_0$  and  $T_f$ . (H) A graphical representation of Bayes factors calculated by BAGEL for the top 15 genes with the highest integer value Bayes factors. All Bayes factors are  $< 0$  indicating gene essentiality was not detected. Error bars show standard deviation for each gene as calculated by BAGEL. (I) We explored the output from MAGeCK-RRA and MAGeCK-MLE to determine how each method ranked the top five most essential genes we identified using TRACS. TRACS found these genes to have an ER of at least -4.93 (see **Table 4.1**). MAGeCK-RRA and MAGeCK-MLE found these genes to have LFC near 0 and were not significant. The dashed vertical line represents a typical LFC or ER cutoff of -1 and the dashed horizontal line represents a  $p$  value of 0.05. Genes above and to the left of these lines are significant.

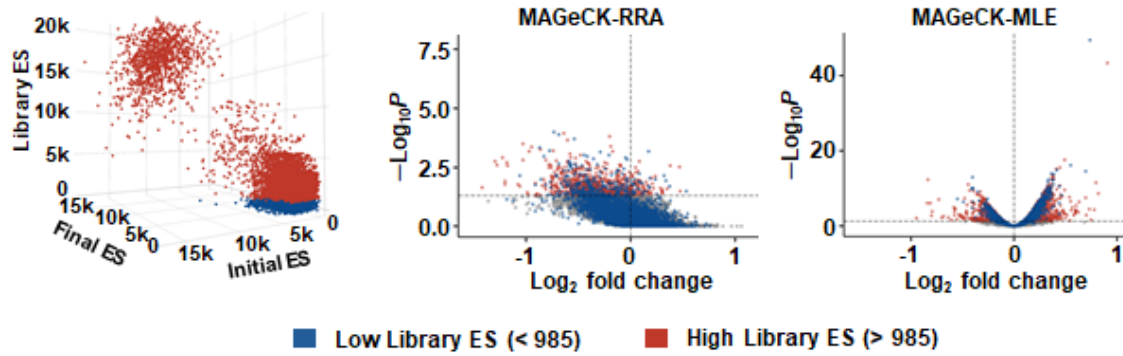


**Figure 4.6. Top-ranked genes by MAGeCK have low representation in the  $T_0$  pool of cells.** The 3D plot highlights in dark blue the genes that TRACS determined to have low Library ES. The vertical axis represents Library ES. The volcano plots illustrate genes that were found to be essential by MAGeCK-RRA or MAGeCK-MLE (LFC < 0 and unadjusted  $p$  value < 0.05; no FDR cutoffs). Dark blue data points in volcano plots indicate genes that TRACS found to have low Library ES, demonstrating that removing the FDR cutoff selects for genes with poor sgRNA representation. In all three plots, genes in red have Library ES > 985 and genes in dark blue have Library ES < 985.

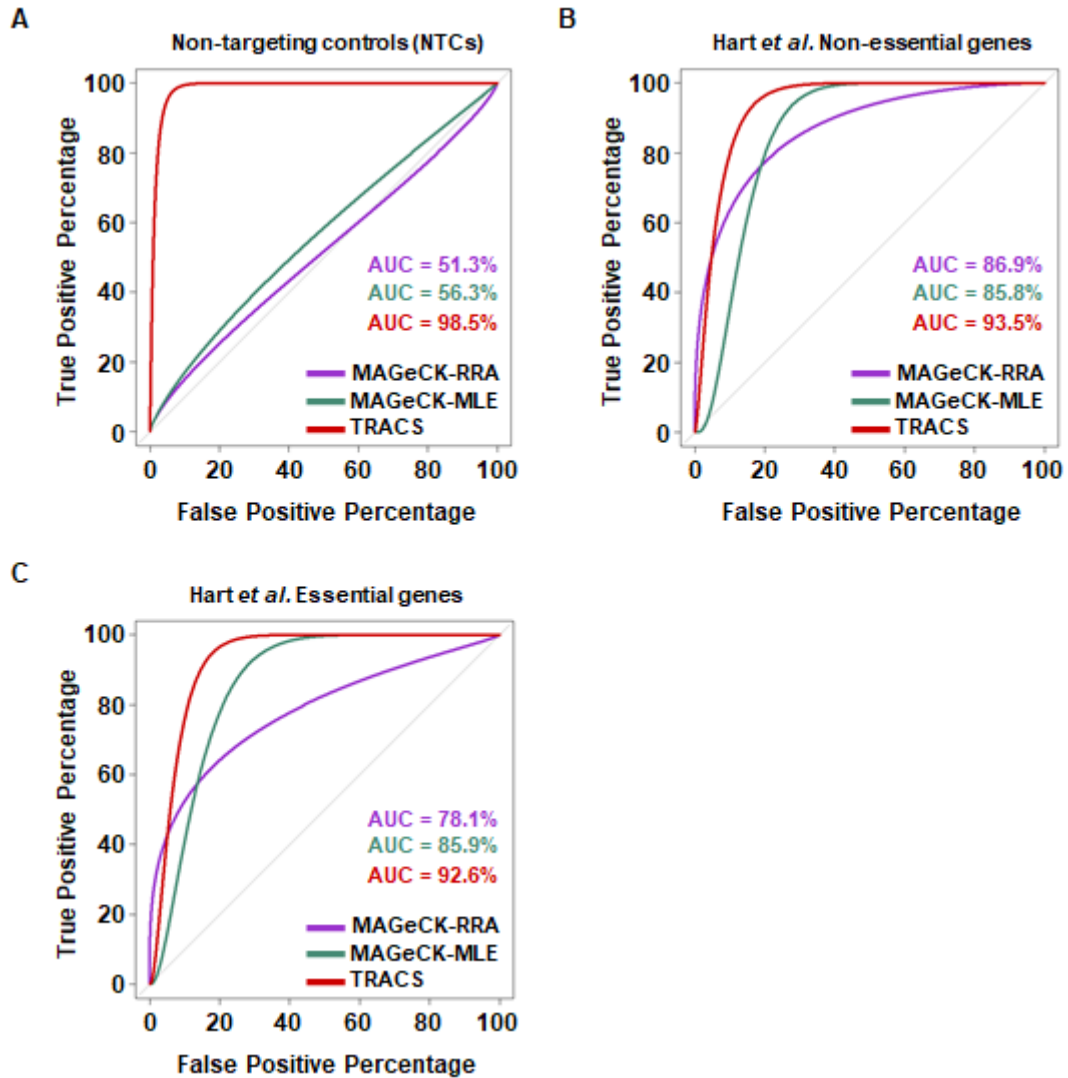


**Figure 4.7. TRACS accurately classifies non-targeting controls and robustly classifies known essential and non-essential gene sets.** (A) We evaluated the ability of MAGeCK to classify the 1,000 NTC sgRNAs in the GeCKO v2 pooled library as non-essential and compared it to TRACS as shown in **Figure 4.4A**. The AUC for MAGeCK-RRA (51.3%) and MAGeCK-MLE (56.3%) were considerably lower than TRACS (98.5%). (B) We evaluated the ability of TRACS and MAGeCK to classify the previously described Hart *et al.* gene set of universally non-essential genes. TRACS (AUC: 93.5%) outperformed MAGeCK-RRA (AUC: 86.9%) and MAGeCK-MLE (AUC: 85.8%) suggesting it can reliably identify these non-essential genes. (C) We also evaluated the ability of TRACS and MAGeCK to classify a known set of universally essential genes. TRACS (AUC: 92.6%) consistently outperformed MAGeCK-RRA (AUC:78.1%) and MAGeCK-MLE (AUC: 85.9%) indicating it can robustly identify essential genes.

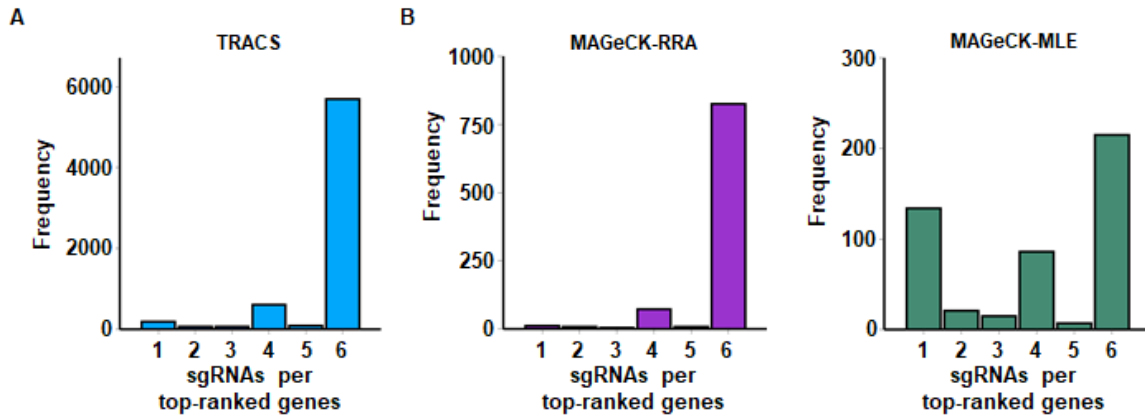


**Figure 4.8. TRACS selects for essential genes based on the most sgRNAs.** (A) Bar plot showing the distribution of the number of sgRNAs per gene for the 6,717 genes that had  $ER < 0$  and  $p_{adj} < 0.05$  in TRACS. Light blue color corresponds to light blue data points shown in **Figure 4.1D**. (B) Bar plots showing the distribution of sgRNAs per gene discovered by MAGeCK-RRA and MAGeCK-MLE with  $LFC < 0$  and unadjusted  $p$  value  $< 0.05$ . Purple and green colors correspond to the colored data points in the volcano plots in **Figure 4.5**. Most top-ranked genes identified by MAGeCK-RRA had 6 sgRNAs per gene although at reduced frequency which is attributed to fewer genes discovered by MAGeCK. MAGeCK-MLE had wider disparity across genes as it made essentiality calls using as low as 1 sgRNA per gene. The peaks at 4 sgRNAs per gene in each of the three histograms represent miRNAs which have a maximum of 4 sgRNAs instead of 6.



## 4.4 Discussion

The GO-CRISPR and TRACS workflow offers an important alternative to conventional genome-wide loss-of-function CRISPR screens. It rigorously identifies genes that contribute to survival and facilitates novel mechanistic discoveries in low proliferation culture conditions by controlling for the stochastic effects of Cas9-independent sgRNA loss. Most notably, we demonstrated the use of this screening workflow in a 3D ovarian cancer spheroid model to identify novel pathways that have not yet been described in HGSOC. This would not have been possible using conventional screening methods that lack guide-only controls.

To accommodate guide-only controls, we needed a new analysis pipeline. CRISPR screen analysis pipelines generally require an understanding of programming or advanced Unix/Linux knowledge to setup and manipulate raw NGS read files. In contrast, the TRACS software suite (<https://github.com/developerpiru/TRACS>) presents researchers with an easy-to-use graphical environment for analysis and data exploration. TRACS fully automates the analysis process – from raw NGS files to output – which will significantly reduce the barrier for many researchers to use GO-CRISPR. Furthermore, TRACS is fully scalable and can be deployed on a local workstation or a multi-CPU platform such as Amazon Web Services, Google Cloud Platform, or Microsoft Azure. We also provide example workflows and documentation to use TRACS on these platforms, including Docker containers for Linux, Mac OS and Windows that will automate setup.

We used the GeCKO v2 pooled sgRNA library<sup>19</sup> in our screen. However, the modularity of GO-CRISPR and TRACS will allow for the use of any pooled sgRNA library as long as Cas9 expression is separate from sgRNA viral delivery. In addition, the

flexibility of TRACS in terms of unrestricted replicates and sgRNA library size will support the use of validated libraries, such as GeCKO v2, or custom libraries to answer novel questions across biological systems of interest. Taken together, we anticipate GO-CRISPR and TRACS will open new opportunities for loss-of-function screens across diverse model systems and biological questions.

## 4.5 Materials and methods

### 4.5.1 Generation of Cas9-positive cells

High-grade serous ovarian cancer (HGSOC) iOvCa147 cells have previously been reported <sup>22</sup>. They were transduced with viral particles encoding a Cas9 expression cassette (lentiCas9-Blast, Addgene #52962) to generate cells constitutively expressing Cas9 (Cas9-positive cells). Cells were selected with blasticidin (20 µg/mL). Single-cell clones were isolated by limiting dilution. Lysates were collected from clones and western blots were performed to determine Cas9 expression (Cell Signaling #14697). Cas9 editing efficiency was determined by viability studies using sgRNAs targeting selected fitness genes (*PSMD1*, *PSMD2*, *EIF3D*) and a non-targeting control (*LacZ*) as previously reported <sup>28</sup>. A single clone showing the most effective Cas9 activity was selected for all further studies.

### 4.5.2 GeCKO v2 library preparation

HEK293T cells were transfected with the combined A and B components of the GeCKO v2 (Addgene #1000000048, #1000000049) whole genome library (123,411 sgRNAs in total) along with plasmids encoding lentiviral packaging proteins. Media was

collected 2-3 days later and any cells or debris were pelleted by centrifugation at 500 x g. Supernatant containing viral particles was filtered through a 0.45  $\mu$ M filter and stored at -80°C with 1.1 g/100 mL BSA.

#### 4.5.3 GO-CRISPR screen in iOvCa147 cells

iOvCa147 Cas9-positive or Cas9-negative cells were transduced with virus collected as described above at a multiplicity of infection of 0.3 and with a predicted library coverage of >1000-fold. Cells were grown in media containing 2  $\mu$ g/mL puromycin (Sigma #P8833) to eliminate non-transduced cells. Cells were maintained in complete media containing puromycin in all following steps. A total of  $1.1 \times 10^9$  cells were collected and split into three groups consisting of approximately  $3.0 \times 10^8$  cells each and were cultured for an additional 2-3 days in complete media, then collected and counted. Triplicate samples of  $6.2 \times 10^7$  cells were saved for sgRNA sequence quantitation at  $T_0$ . The remaining cells (approximately  $1.4 \times 10^9$ /set) were plated at a density of  $2.0 \times 10^6$  cells/mL in each of twenty 10 cm ULA plates (total of 60 ULA plates). Following 2 days of culture, media containing spheroids was transferred to ten, 15 cm adherent tissue culture plates (total of 30 plates). The next day unattached spheroid cells were collected and re-plated onto additional 15 cm plates. This process was repeated for a total of 5 days at which point very few spheroids remained unattached. The attached cells were collected for DNA extraction and this population represents  $T_f$ . Complete media refers to DMEM/F12 media (Gibco #11320033) supplemented with 10% FBS (Wisent FBS Performance lot #185705), 1% penicillin-streptomycin glutamine (Wisent #450-202-EL) and 2  $\mu$ g/mL puromycin (Sigma #P8833).

#### 4.5.4 High-throughput next generation sequencing (NGS)

Cells were harvested and DNA was extracted using QIAmp Blood Maxi Kits (QIAGEN #51194). Genomic encoded sgRNA sequences were PCR amplified as previously described <sup>29</sup>. Two rounds of PCR were performed. The initial round serves to increase the abundance of the initial sgRNA population, while the second round inserts barcodes necessary for identification of group and replicate number (sample barcode). PCR products were gel purified, quantitated by Qubit (Invitrogen), pooled and sequenced using an Illumina NextSeq 550 75-cycle high output kit (#20024906). FASTQ files were obtained containing raw reads and were demultiplexed to obtain individual FASTQ files for each sample. FASTQ files were processed accordingly for downstream analysis with TRACS, MAGeCK, or BAGEL.

#### 4.5.5 Analysis with MAGeCK

FASTQ files were trimmed with Cutadapt (1.15) to remove adapter sequences and sample barcode identifiers. The library reference file (CSV) for the GeCKOv2 library was used in Bowtie2 (2.3.4.1) to align the initial library read FASTQ file and generate a BAM file (Samtools 1.7) in order to increase the read depth of the initial library. This library BAM file and trimmed FASTQ files for all samples were then inputted into the MAGeCK (0.5.6) count function to generate read counts. Differences in sgRNA abundance were computed using the MAGeCK-RRA (robust ranking aggregation) or MAGeCK-MLE (maximum likelihood estimation) methods. All plots and comparisons to TRACS were performed in R (3.6.2).

#### 4.5.6 Analysis with BAGEL

BAGEL (0.91) was run using read counts generated by the MAGeCK (0.5.6) count function as described above. Standard non-essential and essential training gene sets were used as previously described<sup>28</sup>. Bayes factors (BFs) obtained by BAGEL were plotted in R (3.6.2).

#### 4.5.7 Analysis with TRACS

The library reference file containing a list of all sgRNAs and their sequences (CSV file), raw reads for the pooled sgRNA library (FASTQ files ( $L_0$ ) and raw reads (FASTQ files) for all Initial ( $T_0$ ) and Final ( $T_f$ ) replicates for Cas9-positive and Cas9-negative cells (12 replicates) were loaded into TRACS (<https://github.com/developerpiru/TRACS>). TRACS then automatically trimmed the reads using Cutadapt (1.15). TRACS builds a Bowtie2 (2.3.4.1) index and aligns the trimmed initial sgRNA library read file to generate a BAM file using Samtools 1.7. MAGeCK (0.5.6) is then used to generate read counts from this library BAM file and all the trimmed sample FASTQ files. Instead of dropping all reads below a certain threshold (*e.g.* <30 counts), all reads were incremented by 1 to prevent zero counts and division by zero errors. The TRACS algorithm was then run using this read count file to determine the Library Enrichment Score (ES), Initial ES, Final ES and the Enrichment Ratio (ER) for each gene (see *The TRACS algorithm* section).

#### 4.5.8 Data exploration using VisualizeTRACS

The VisualizeTRACS feature, part of the TRACS software suite, was then used to visualize and explore the data output from TRACS. Gene filtering (Library ES > 985, ER

$< 0$ ,  $p_{adj} < 0.05$  for our example ovarian cancer workflow) was performed, figures were generated and the final table of essential genes that met these criteria were downloaded for further analysis.

#### 4.5.9 The TRACS algorithm

After read count preprocessing, TRACS first determines a Gene Score,  $GS$ , for every gene in the supplied library reference file by calculating the  $\log_2$ -fold-change (LFC) from all sgRNAs for that gene for  $n$  replicates (minimum of 2 replicates required) of Cas9-positive and Cas9-negative samples:

$$GS_j = \sum_{i=1}^s \left( \log_2 \frac{[normalized\ sgRNA\ abundance]_{Cas9+}}{[avg\ normalized\ sgRNA\ abundance]_{Cas9-}} \right)$$

Where  $s$  is the number of unique sgRNAs for a gene  $j$ . This is done for each replicate such that for  $n$  replicates, there are  $n$  gene scores,  $GS$ , for a gene  $j$ . For each  $n$  replicates, the  $GS$  for all genes are then ranked in ascending order from 1 to  $x$ , where  $x$  is the rank of the gene with the highest  $GS$  in each respective replicate. TRACS then determines the Enrichment Score,  $ES_j$ , which is the average rank across all  $n$  replicates of a gene  $j$ , divided by the total number of sgRNAs,  $s$ , identified for that gene.

$$ES_j = \frac{\frac{1}{n} \sum_{i=1}^n GS\ rank}{s}$$

TRACS then determines the Enrichment Ratio,  $ER$ , for gene  $j$  by determining the LFC of the  $ES_{jTf}$  compared to  $ES_{jT0}$ .

$$ER_j = \log_2 \frac{ES_{jTf}}{ES_{jT0}}$$

TRACS calculates the  $p$  value for each gene using a paired t-test by pairing each of the  $n$  replicates together per gene per the initial ( $T_0$ ) condition and final ( $T_f$ ) condition. The Benjamini–Hochberg procedure is used to control the false discovery rate (FDR) at the user-defined level (10% in our example workflow).

After the ER is calculated, TRACS determines the distribution of Library ES values across all genes. The cutoff value for the Library ES was set to the first quartile for our example screen.

#### 4.5.10 Pathway analysis

Using the final list of essential genes from TRACS, we performed gene ontology and pathway enrichment analysis using the ConsensusPathDB enrichment analysis test (Release 34 (15.01.2019)) for top-ranked genes of interest.  $p_{adj}$  values and ER values for each gene were used as inputs. The minimum required genes for enrichment was set to 45 and the FDR-corrected  $p_{adj}$  value cutoff was set to  $< 0.01$ . The Reactome pathway dataset was used as the reference. For each identified pathway, ConsensusPathDB provides the number of enriched genes and a  $q$  value ( $p_{adj}$ ) for the enrichment. Scatter plots were generated in R (3.6.2) using these values to depict the significant pathways identified.

#### 4.5.11 Generation of single-gene knockouts

Gibson Assembly (NEB #E2611) was used to clone a pool of four sgRNAs per gene (*AGPS*, *SLC2A11*, *ZC3H7A*, *PDCD2L*, *NPM1*, *EPS15*, *hsa-mir-761*, *RPAP1*, *SYAP1*, *TRAF3IP1*, and *EGFP*) into lentiCRISPR v2 (Addgene #52961). iOvCa147 cells were transduced with viral particles encoding a Cas9 and sgRNA expression cassettes. Cells were selected for 2-3 days in media containing 2 µg/mL puromycin. Knockout cells were cultured for 72 hours in suspension conditions using ULA plasticware (2 x 10<sup>6</sup> cells per well) to induce spheroid formation. Spheroid cells were then collected and transferred to standard plasticware to facilitate reattachment for 24 hours. Reattached cells were fixed with fixing solution (25% methanol in 1x PBS) for 3 minutes. Fixed cells were incubated for 30 minutes with shaking in crystal violet staining solution (0.5% crystal violet, 25% methanol in 1x PBS). Plates were carefully immersed in ddH<sub>2</sub>O to remove residual crystal violet. Plates were incubated with detaining solution (10% acetic acid in 1x PBS) for 1 hour with shaking to extract crystal violet from cells. Absorbance of crystal violet at 590 nm was measured using a microplate reader (Perkin Elmer Wallac 1420) for each knockout and normalized to the EGFP control. Percent survival is inferred from relative absorbance.

#### 4.5.12 Statistics

All error bars in the bar graphs represent standard deviation. Statistical significances were determined using two-way ANOVA. \* denotes P < 0.05, \*\*\* denotes P < 0.001, \*\*\*\* denotes P < 0.0001 and ns denotes not significant (P > 0.05).



## 4.6 Data and Code Availability

High throughput sequencing data from the GO-CRISPR screen is available from the GEO repository (accession number GSE150246). TRACS is available for download from the GitHub repository at <https://github.com/developerpiru/TRACS> or on Docker Hub at <https://hub.docker.com/r/pirunthan/tracs>. Complete documentation, reference sgRNA library file and TRACS output files are also available on the GitHub repository.

## 4.7 References

- 1 Shalem, O., Sanjana, N. E. & Zhang, F. High-throughput functional genomics using CRISPR-Cas9. *Nat Rev Genet* **16**, 299-311, doi:10.1038/nrg3899 (2015).
- 2 Lytle, N. K. *et al.* A Multiscale Map of the Stem Cell State in Pancreatic Adenocarcinoma. *Cell* **177**, 572-586 e522, doi:10.1016/j.cell.2019.03.010 (2019).
- 3 Wang, T., Wei, J. J., Sabatini, D. M. & Lander, E. S. Genetic screens in human cells using the CRISPR-Cas9 system. *Science* **343**, 80-84, doi:10.1126/science.1246981 (2014).
- 4 Shalem, O. *et al.* Genome-scale CRISPR-Cas9 knockout screening in human cells. *Science* **343**, 84-87, doi:10.1126/science.1247005 (2014).
- 5 Parnas, O. *et al.* A Genome-wide CRISPR Screen in Primary Immune Cells to Dissect Regulatory Networks. *Cell* **162**, 675-686, doi:10.1016/j.cell.2015.06.059 (2015).
- 6 Sanson, K. R. *et al.* Optimized libraries for CRISPR-Cas9 genetic screens with multiple modalities. *Nat Commun* **9**, 5416, doi:10.1038/s41467-018-07901-8 (2018).
- 7 Cai, M. Y. *et al.* Cooperation of the ATM and Fanconi Anemia/BRCA Pathways in Double-Strand Break End Resection. *Cell Rep* **30**, 2402-2415 e2405, doi:10.1016/j.celrep.2020.01.052 (2020).
- 8 Koike-Yusa, H., Li, Y., Tan, E. P., Velasco-Herrera Mdel, C. & Yusa, K. Genome-wide recessive genetic screening in mammalian cells with a lentiviral CRISPR-guide RNA library. *Nat Biotechnol* **32**, 267-273, doi:10.1038/nbt.2800 (2014).
- 9 Thyme, S. B., Akhmetova, L., Montague, T. G., Valen, E. & Schier, A. F. Internal guide RNA interactions interfere with Cas9-mediated cleavage. *Nat Commun* **7**, 11750, doi:10.1038/ncomms11750 (2016).
- 10 Kenny, H. A. *et al.* Quantitative high throughput screening using a primary human three-dimensional organotypic culture predicts in vivo efficacy. *Nat Commun* **6**, 6220, doi:10.1038/ncomms7220 (2015).
- 11 Jacob, F. *et al.* A Patient-Derived Glioblastoma Organoid Model and Biobank Recapitulates Inter- and Intra-tumoral Heterogeneity. *Cell* **180**, 188-204 e122, doi:10.1016/j.cell.2019.11.036 (2020).
- 12 Fujii, M. *et al.* A Colorectal Tumor Organoid Library Demonstrates Progressive Loss of Niche Factor Requirements during Tumorigenesis. *Cell Stem Cell* **18**, 827-838, doi:10.1016/j.stem.2016.04.003 (2016).
- 13 Vlachogiannis, G. *et al.* Patient-derived organoids model treatment response of metastatic gastrointestinal cancers. *Science* **359**, 920-926, doi:10.1126/science.aao2774 (2018).
- 14 Ringel, T. *et al.* Genome-Scale CRISPR Screening in Human Intestinal Organoids Identifies Drivers of TGF-beta Resistance. *Cell Stem Cell* **26**, 431-440 e438, doi:10.1016/j.stem.2020.02.007 (2020).
- 15 Planas-Paz, L. *et al.* YAP, but Not RSPO-LGR4/5, Signaling in Biliary Epithelial Cells Promotes a Ductular Reaction in Response to Liver Injury. *Cell Stem Cell* **25**, 39-53 e10, doi:10.1016/j.stem.2019.04.005 (2019).
- 16 Zanoni, M. *et al.* 3D tumor spheroid models for in vitro therapeutic screening: a systematic approach to enhance the biological relevance of data obtained. *Sci Rep* **6**, 19103, doi:10.1038/srep19103 (2016).

- 17 Zhou, Y. *et al.* High-throughput screening of a CRISPR/Cas9 library for functional genomics in human cells. *Nature* **509**, 487-491, doi:10.1038/nature13166 (2014).
- 18 Wang, T. *et al.* Gene Essentiality Profiling Reveals Gene Networks and Synthetic Lethal Interactions with Oncogenic Ras. *Cell* **168**, 890-903 e815, doi:10.1016/j.cell.2017.01.013 (2017).
- 19 Sanjana, N. E., Shalem, O. & Zhang, F. Improved vectors and genome-wide libraries for CRISPR screening. *Nat Methods* **11**, 783-784, doi:10.1038/nmeth.3047 (2014).
- 20 Matulonis, U. A. *et al.* Ovarian cancer. *Nat Rev Dis Primers* **2**, 16061, doi:10.1038/nrdp.2016.61 (2016).
- 21 Bowtell, D. D. *et al.* Rethinking ovarian cancer II: reducing mortality from high-grade serous ovarian cancer. *Nat Rev Cancer* **15**, 668-679, doi:10.1038/nrc4019 (2015).
- 22 MacDonald, J. *et al.* A Systematic Analysis of Negative Growth Control Implicates the DREAM Complex in Cancer Cell Dormancy. *Mol Cancer Res* **15**, 371-381, doi:10.1158/1541-7786.MCR-16-0323-T (2017).
- 23 Aguirre, A. J. *et al.* Genomic Copy Number Dictates a Gene-Independent Cell Response to CRISPR/Cas9 Targeting. *Cancer Discov* **6**, 914-929, doi:10.1158/2159-8290.CD-16-0154 (2016).
- 24 Wang, T. *et al.* Identification and characterization of essential genes in the human genome. *Science* **350**, 1096-1101, doi:10.1126/science.aac7041 (2015).
- 25 Patch, A. M. *et al.* Whole-genome characterization of chemoresistant ovarian cancer. *Nature* **521**, 489-494, doi:10.1038/nature14410 (2015).
- 26 Sun, C. *et al.* Rational combination therapy with PARP and MEK inhibitors capitalizes on therapeutic liabilities in RAS mutant cancers. *Sci Transl Med* **9**, doi:10.1126/scitranslmed.aal5148 (2017).
- 27 Wang, B. *et al.* Integrative analysis of pooled CRISPR genetic screens using MAGeCKFlute. *Nat Protoc* **14**, 756-780, doi:10.1038/s41596-018-0113-7 (2019).
- 28 Hart, T. *et al.* High-Resolution CRISPR Screens Reveal Fitness Genes and Genotype-Specific Cancer Liabilities. *Cell* **163**, 1515-1526, doi:10.1016/j.cell.2015.11.015 (2015).
- 29 Joung, J. *et al.* Genome-scale CRISPR-Cas9 knockout and transcriptional activation screening. *Nat Protoc* **12**, 828-863, doi:10.1038/nprot.2017.016 (2017).

## Chapter 5

### 5 Netrin and its dependence receptors are mediators of high-grade serous ovarian cancer cell survival

#### 5.1 Abstract

We previously showed that DYRK1A is essential for ovarian cancer spheroid cell survival. DYRK1A regulates transcription by assembling the DREAM repressor complex and also regulates RNA polymerase II. However, the present understanding of how DYRK1A regulates transcription in high-grade serous ovarian cancer (HGSOC) spheroid cells to promote quiescence and survival is lacking. Here we performed GO-CRISPR screens in a panel of HGSOC spheroid cells in combination with transcriptional analyses of DYRK1A deficient spheroid cells. We identified netrin signaling components as essential factors of HGSOC spheroid cell survival. Netrin is well-characterized in axon development but has recently been implicated in other cancer types. We found that knockout of netrin ligands or receptors affects viability of spheroid cells. Netrin ligands and receptors are upregulated in HGSOC cells in suspension conditions. Together, this work suggests that the netrin signaling pathway may be a potential therapeutic target to specifically eliminate spheroid cells in HGSOC and highlights it as an important area requiring further investigation in the context of ovarian cancer.

#### 5.2 Introduction

Ovarian cancer is the leading cause of death among gynecologic malignancies. Although awareness of ovarian cancer has increased over the last decade, patient survival

trends have failed to increase significantly<sup>1,2</sup>. Poor prognosis of ovarian cancer patients is attributed to late diagnosis; over 70% of women are not diagnosed until the disease has progressed to stage III or IV primarily due to non-specific symptoms which are common to non-malignant diseases<sup>2-4</sup>. By late-stage disease, tumours spread beyond the site of origin and form numerous distant metastatic nodules that are difficult to remove by surgical debulking<sup>5</sup>. This metastatic spread is facilitated by multicellular spheroids that are clusters of tumour cells that shed from primary tumours and disseminate into the peritoneal cavity through malignant ascites to colonize new sites<sup>5</sup>. The non-proliferative state of spheroid cells renders them chemoresistant and contributes to recurrence<sup>6-8</sup>; more than 80% of patients with late-stage disease will experience recurrence<sup>9</sup>, further complicating treatment and resulting in poor survival<sup>5</sup>. A comparison of the five-year survival rate of women with stage I disease (90%) to those with late-stage metastatic disease (< 25%) reveals a critical need to improve diagnostics and therapeutics for advanced stage ovarian cancer<sup>2,3,10</sup>.

Malignant ascites and spheroids are observed in almost all patients with late-stage high-grade serous ovarian cancer (HGSOC), the most common form of ovarian cancer<sup>1,11</sup>, yet the processes controlling ovarian cancer spheroid formation and survival are not well understood. Unlike other cancers which metastasize hematogenously or lymphatically, ovarian cancer cells shed directly from primary tumours to the peritoneal cavity that immediately requires adaptability to non-adherent or suspension conditions<sup>12,13</sup>. It has been suggested that shedding ovarian tumour cells undergo epithelial-to-mesenchymal transition (EMT), but spheroid cells within ascites maintain epithelial features and cell-cell interactions with neighboring spheroid cells<sup>14</sup> which affords them the ability to escape anoikis and decreases responsiveness to chemotherapy<sup>15-17</sup>. It can therefore be surmised

that spheroid cells are influenced by pro-survival signals which allow entry into quiescence while retaining epithelial features, and withdrawal of these factors would reduce chemoresistance and survival. Recent studies have revealed that HGSOC spheroid cells require AMPK-LKB1 signaling<sup>18,19</sup> and STAT3-DKK signaling<sup>20</sup> for survival and chemoresistance. We have also previously shown that HGSOC spheroids are dependent on dual-specificity tyrosine phosphorylation regulated kinase 1A (DYRK1A) and DREAM<sup>6</sup>. Loss of DYRK1A or DREAM components inhibited entry into dormancy and reduced spheroid cell viability<sup>6</sup>. These studies have demonstrated that HGSOC spheroids harbor vulnerabilities which can be exploited to increase drug sensitivity, however, as in the case of DYRK1A/DREAM, such vulnerabilities may only be present during non-adherent conditions to offer spheroid cells protection in suspension<sup>6</sup>. In the present study, we performed a genome-wide CRISPR screen in parallel with transcriptomic analyses to identify a novel role for netrin signaling in HGSOC spheroid survival.

The netrin family is a highly conserved family of proteins that participate in neuronal guidance cues. Netrins, together with their receptors, have been implicated in cancer progression and metastases. Netrin-1, netrin-3, netrin-4, and netrin-5 are secreted netrin ligands whereas netrin-G1 and netrin G2 are membrane bound<sup>21</sup>. Netrin-1 (NTN1) is the most studied due to its importance in nervous system development. It has been characterized as an oncogene in several cancers<sup>22-26</sup> and has been used as a reliable diagnostic biomarker in breast cancer, colorectal cancer, and gastric cancer<sup>27-30</sup>. NTN1 over expression in both cancer cell lines and animal models lead to pro-survival signals<sup>21,23-25,31-34</sup>. In glioblastoma, melanoma, and pancreatic cancer, NTN1 stimulates metastases<sup>25,26</sup>. The functions of other netrin family members in cancer are not yet fully understood. Netrin-

4 (NTN4) has been shown to have either a positive or negative effect on tumour survival depending on the cancer type<sup>21</sup>. NTN4 over expression in breast cancer has been correlated with improved patient outcomes<sup>35-37</sup>, but its expression in gastric cancer, neuroblastoma, and melanoma are associated with more aggressive disease<sup>38-41</sup>. Both netrin-3 (NTN3) and netrin-5 (NTN5) – the most recently discovered netrins – have not been characterized outside of the nervous system<sup>21</sup>.

A growing number of studies are focusing on netrins in cancer. They present an attractive therapeutic target not only because they act on accessible extracellular receptors, but also because netrin receptors belong to a family of receptors called dependence receptors (DRs)<sup>42-44</sup>. DRs are grouped not for their similar homology – of which they have none – but for their dual function<sup>21,42</sup>. DRs offer cells a protective function by propagating anti-apoptotic signals only in the presence of a ligand. In the absence of a ligand, DRs induce programmed cell death<sup>42</sup>. DCC, the prototypical netrin DR, and the UNC5 homology (UNC5H) DRs have been found to be mutated in various cancers<sup>45,46</sup>. Here we show that netrins and its family of receptors act as DRs in HGSOC spheroid cells. Our novel genome-wide GO-CRISPR screen identified netrin signaling components, including NTN1 and UNC5H (UNC5 homology) DRs as vulnerabilities for HGSOC spheroid cell survival. Parallel transcriptomic analyses of HGSOC spheroids revealed netrin signaling components were enriched in HGSOC spheroids compared to adherent cells. We show that individual knockdown of netrin signaling components decreases viability of spheroid cells in suspension and that different patient-derived HGSOC cell lines have differing sensitivities towards specific receptors. Our study highlights netrin signaling as a

requirement for HGSOC spheroid survival and suggests it may be a potential therapeutic target for HGSOC therapies.

## 5.3 Results

### 5.3.1 Components of netrin signaling are essential factors for HGSOC spheroid cell survival

We performed a genome-wide CRISPR screen on three HGSOC cell lines (iOvCa147, OVCAR8 and TOV1946) to identify genes and pathways that are important for spheroid cell survival. We utilized the GO-CRISPR (Guide Only CRISPR) workflow in our three-dimensional spheroid cell culture model to recapitulate metastatic dissemination of spheroids *in vitro* (**Figure 5.1A**). GO-CRISPR uniquely incorporates sgRNA abundances from non-Cas9-expressing cells to control for stochastic death in challenging three-dimensional culture conditions and the data was analyzed using the accompanying software, TRACS (Toolset for the Ranked Analysis of GO-CRISPR Screens)<sup>47</sup>. To identify genes that contributed to spheroid cell survival and reattachment after 48 hours in suspension, we filtered the results for genes that had an Enrichment Ratio (ER) less than 0 which is indicative of sgRNAs that were relatively depleted in suspension conditions. We found 6,717 genes with an ER < 1.0 and  $p_{adj} < 0.05$  in iOvCa147 cells; 7,637 genes in TOV1946 cells; and 7,640 genes in OVCAR8 cells (**Figure 5.1B**). Among these genes, 1,382 were commonly depleted in all three cell lines and had an ER below 1.0 and  $p_{adj} < 0.05$  (**Figure 5.1C**). To discover common molecular pathways that may be broadly important for HGSOC spheroid survival and metastasis, we performed gene ontology and pathway enrichment analysis on the 1,382 genes that were common across



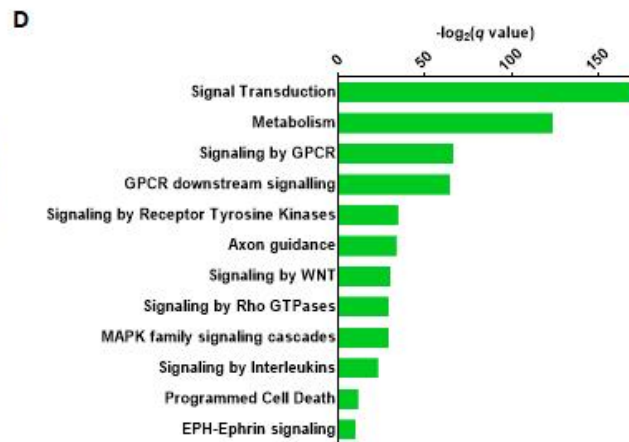
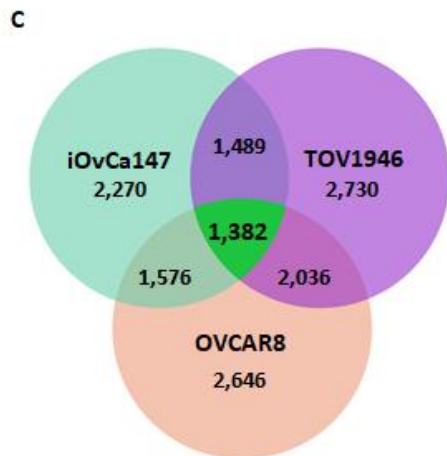
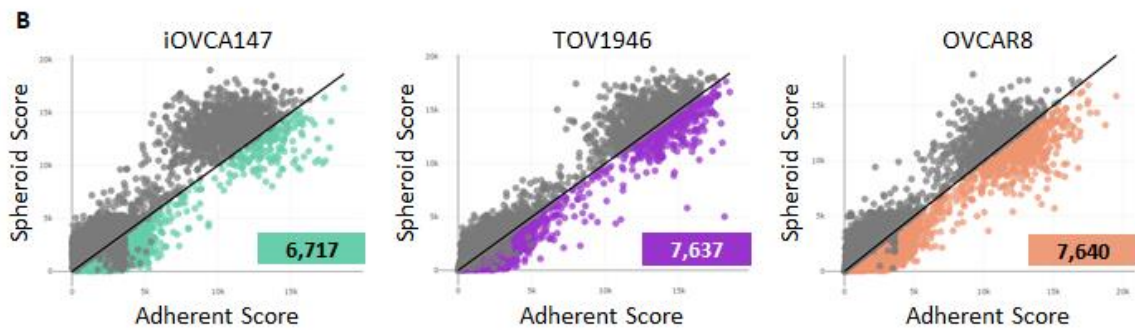
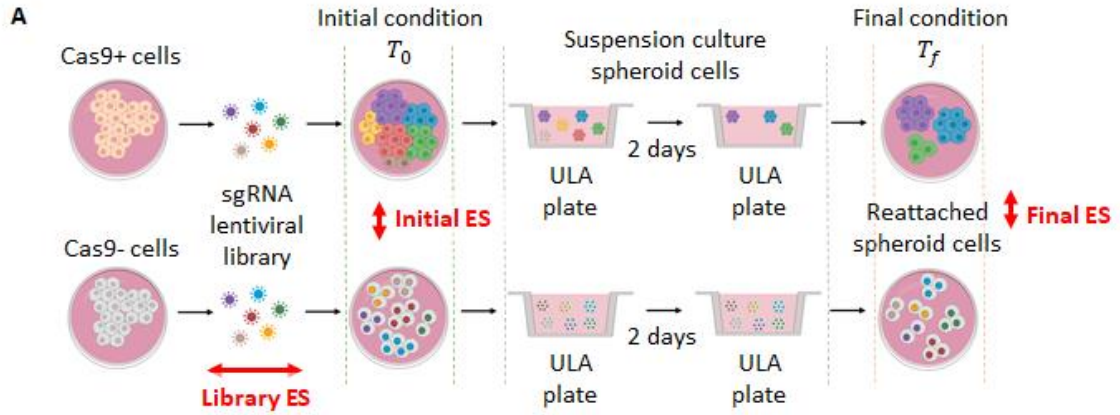


**Figure 5.1. Components of netrin signaling are essential factors for HGSOC spheroid viability.** (A) iOvCa147, TOV1946, or OVCAR8 HGSOC cells were transduced with lentivirus expressing Cas9. High efficiency Cas9-positive cells (top row) and Cas9-negative cells (bottom row) were transduced with the GeCKO v2 pooled sgRNA library ( $L_0$ ). After antibiotic selection, both Cas9 positive and negative cells were split into triplicates (x3) and maintained in initial culture conditions ( $T_0$ ) before being transferred to suspension culture conditions in ULA plasticware (selective pressure,  $P_s$ ) to induce spheroid formation and select for cell survival. Viable spheroid cells were then transferred to standard plasticware to facilitate reattachment in the final culture condition ( $T_f$ ). The initial pooled sgRNA library ( $L_0$ ) and Cas9-positive and Cas9-negative cells were collected at  $T_0$  and  $T_f$  for sgRNA quantitation by NGS. TRACS was used to calculate Library, Initial and Final Enrichment Scores (ES) using read quantities from  $L_0$  and Cas9-positive and Cas9-negative samples. (B) Scatter plots representing spheroid score ( $T_f$ ) on y-axis and adherent ( $T_0$ ) score on x-axis calculated in TRACS for each gene in each cell line (iOvCa147, TOV1946, OVCAR8). Diagonal black line represents  $y = x$ ; genes on this line did not have altered sgRNA levels in spheroid conditions ( $T_f$ ) compared to adherent conditions ( $T_0$ ); genes below this line had reduced sgRNA levels in spheroid conditions ( $T_f$ ), indicating loss of that gene decreased survival in spheroid conditions, suggesting the gene was essential; genes above this line had increased sgRNA levels in spheroid conditions ( $T_f$ ), indicating loss of that gene increased survival in spheroid conditions. Colored data points represent genes with  $ER < 0$  and  $p_{adj} < 0.05$  (5% FDR). 6,717 essential genes were identified in iOvCa147 spheroid cells (highlighted in light green); 7,637 essential genes were identified in TOV1946 spheroid cells (highlighted in purple); 7,640 essential genes were identified in OVCAR8 spheroid cells (highlighted in warm pink). (C) Venn diagram illustrating overlap of genes with  $ER < 0$ ,  $p_{adj} < 0.05$  in iOvCa147, TOV1946, and OVCAR8 spheroid cells. 1,382 genes (shown in bright green) were found to be commonly essential across all three cell lines. Colors are coordinated with those in (B). (D) Venn diagram depicting overlapping enriched pathways identified in GO-CRISPR screen from the commonly essential genes found in all three cell lines (iOvCa147, TOV1946, OVCAR8) shown in bright green in (C). Genes with  $ER < 0$  and  $p_{adj} < 0.05$  were evaluated for enriched pathways. 433 pathways were found to be both significantly enriched ( $p_{adj} < 0.05$ ) and common between all three cell lines (shown in bright green).

all three cell lines. We identified several significantly enriched pathways including those related to metabolism, GPCR signaling, receptor tyrosine kinase signaling, WNT signaling, MAPK signaling, and axon guidance, which includes components of the netrin signaling pathway (**Figure 5.1D**).

### 5.3.2 Netrin signaling components are enriched in HGSOC spheroid cells

We previously discovered *DYRK1A* as supporting survival of ovarian cancer cells<sup>6</sup>. Since *DYRK1A* is a direct regulator of RNA polymerase II transcriptional initiation<sup>48,49</sup>, we sought to determine if it facilitates spheroid cell dormancy and survival in suspension conditions through the regulation of gene expression. To this end, we used CRISPR/Cas9 to delete *DYRK1A* in iOvCa147 cells (*DYRK1A*<sup>-/-</sup>). We excised exon 2 (**Figure 5.2A-C**) to disrupt *DYRK1A* protein expression (**Figure 5.2D**) and inhibit its kinase activity (**Figure 5.2E**). As expected, *DYRK1A*<sup>-/-</sup> spheroid cells failed to repress known target genes, *MYBL2* and *CDK1* (**Figure 5.2F-G**), and had reduced viability (**Figure 5.3A**) and increased sensitivity to carboplatin (**Figure 5.3B**). We next sought to identify transcriptional programming changes that occur in HGSOC spheroid cells during the transition from adherent to suspension conditions. Using the parental iOvCa147 cells and *DYRK1A*<sup>-/-</sup> cell lines, we performed RNA-seq in adherent and spheroid cells (**Figure 5.4A**). We collected spheroids following a 6-hour incubation period in suspension conditions since over expression of known DREAM targets due to *DYRK1A* loss were first evident at this time point (**Figure 5.2F-G**).

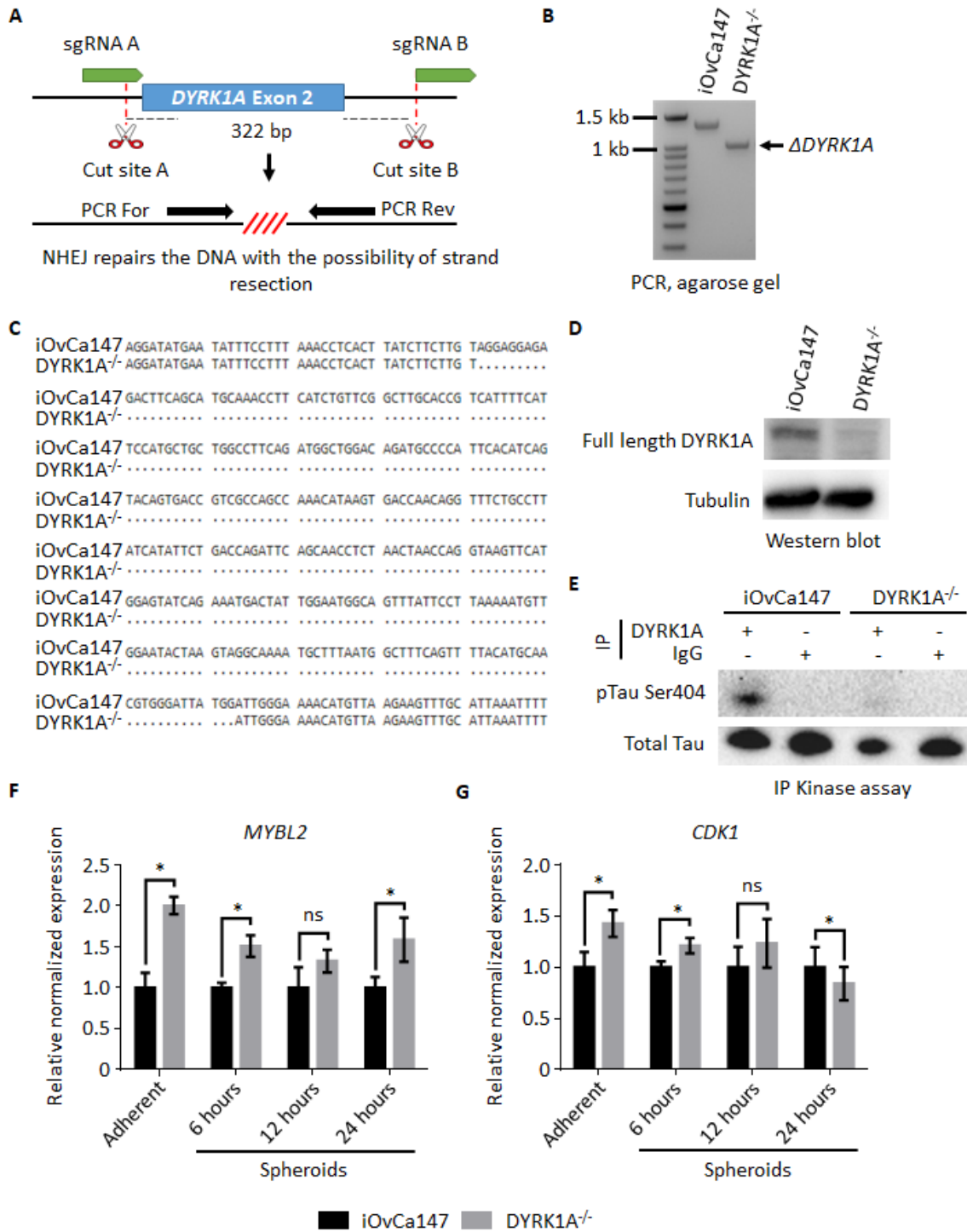


**Figure 5.2. Generation of *DYRK1A*<sup>-/-</sup> iOvCa147 cells and validation of abrogated *DYRK1A* activity.** (A) Strategy to knockout *DYRK1A* in iOvCa147 cells to generate *DYRK1A*<sup>-/-</sup> cells. A pair of sgRNAs (sgRNA A and sgRNA B) that flank exon 2 of *DYRK1A* were designed for use with wild type Cas9 to completely excise a 322 bp region containing exon 2. Dotted red lines show where cuts were made relative to exon 2. After non-homologous end joining (NHEJ), the cut DNA is repaired without the excised fragment containing exon 2. PCR “For” and PCR “Rev” primers flank exon 2 as indicated and were used to detect deletion events. (B) Agarose gel showing PCR products for parental iOvCa147 cells and *DYRK1A*<sup>-/-</sup> cells. DNA was extracted from parental iOvCa147 cells or iOvCa147 cells treated with sgRNAs and Cas9 to delete exon 2 of *DYRK1A* (indicated as *DYRK1A*<sup>-/-</sup>). Full length amplicon containing exon 2 was detected in parental iOvCa147 cells (1,348 bp). A smaller amplicon (1,026 bp) was detected in *DYRK1A*<sup>-/-</sup> cells, indicating successful excision of the 322 bp region encompassing exon 2. (C) Sequence alignments of PCR fragments identified from parental iOvCa147 cells and *DYRK1A*<sup>-/-</sup> cells. The dashed lines in *DYRK1A*<sup>-/-</sup> indicate where the deletion occurred leading to mismatch with exon 2 of *DYRK1A* in parental iOvCa147 cells. (D) Western blot depicting *DYRK1A* protein expression in parental iOvCa147 cells and *DYRK1A*<sup>-/-</sup> cells. *DYRK1A* is present in parental iOvCa147 cells but not in *DYRK1A*<sup>-/-</sup> cells. (E) Immunoprecipitation (IP) kinase assay to evaluate kinase activity in *DYRK1A*<sup>-/-</sup> cells. *DYRK1A* or IgG was immunoprecipitated from either iOvCa147 or *DYRK1A*<sup>-/-</sup> cells and incubated with ATP and Tau protein (a *DYRK1A* substrate). Samples were resolved by SDS-PAGE and probed with phosphospecific Tau antibody. *DYRK1A* that was immunoprecipitated from *DYRK1A*<sup>-/-</sup> cells was not able to phosphorylate Tau. (F)-(G) Gene expression of known DREAM targets (*MYBL2* (F) and *CDK1* (G)) in parental iOvCa147 cells and *DYRK1A*<sup>-/-</sup> cells. Cells were incubated in adherent conditions for 24 hours, or in suspension conditions for 6 hours, 12 hours, or 24 hours to induce spheroid formation prior to RNA extraction. Transcript levels of *MYBL2* and *CDK1* were increased in *DYRK1A*<sup>-/-</sup> cells indicating a failure to repress genes by DREAM as a result of *DYRK1A* deficiency. Bar graphs show mean expression values and error bars represent one standard deviation. Values are normalized to parental iOvCa147 cells for each gene. Two-way ANOVA was performed for each gene and significance levels are indicated (\* denotes P < 0.05; and ns denotes not significant, P > 0.05).

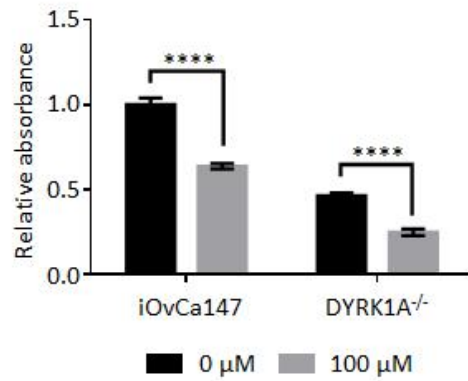
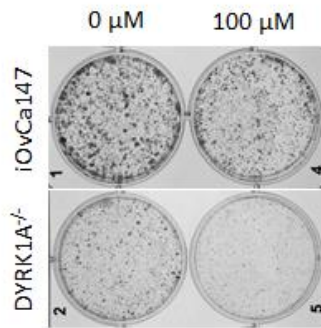
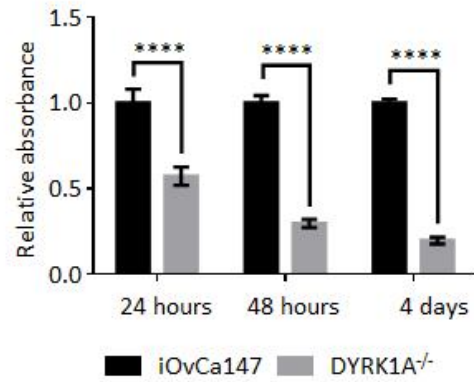
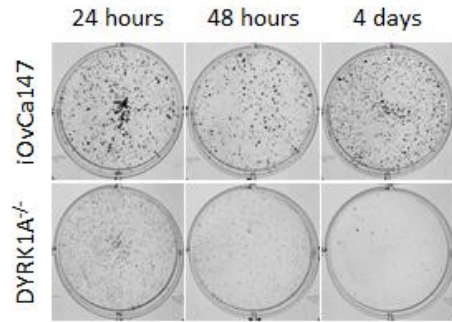


**Figure 5.3. *DYRK1A*<sup>-/-</sup> spheroid cells have impaired reattachment ability and increased chemosensitivity.** (A) Parental iOvCa147 or *DYRK1A*<sup>-/-</sup> cells were incubated in suspension conditions for 24 hours, 72 hours, or 4 days to induce spheroid formation, and then re-plated in adherent conditions for 24 hours to allow reattachment. Reattached spheroid cells were stained with crystal violet and absorbance was quantified. *DYRK1A*<sup>-/-</sup> spheroid cells had impaired reattachment compared to parental iOvCa147 spheroid cells at each time point. Bar graphs indicate mean relative absorbance (n=6). Two-way ANOVA was performed and significance levels are indicated (\*\*\*\* denotes P < 0.0001). (B) Parental iOvCa147 or *DYRK1A*<sup>-/-</sup> cells were incubated in suspension conditions for 24 hours to induce spheroid formation with or without carboplatin (0  $\mu$ m or 100  $\mu$ m), and then re-plated in adherent conditions for 24 hours to allow reattachment. Reattached spheroid cells were stained with crystal violet and absorbance was quantified. *DYRK1A*<sup>-/-</sup> spheroid cells had increased sensitivity to carboplatin compared to parental iOvCa147 spheroid cells. Bar graphs indicate mean relative absorbance (n=6). Two-way ANOVA was performed and significance levels are indicated (\*\*\*\* denotes P < 0.0001).

We first compared parental iOvCa147 adherent cells to 6-hour parental iOvCa147 spheroid cells to identify transcriptional changes that occur as these cells transitioned from adherent conditions to suspension conditions (**Figure 5.4B**). We identified 1,937 genes that were downregulated and 1,834 genes that were upregulated. We then compared parental spheroid cells to *DYRK1A*<sup>-/-</sup> spheroid cells to identify transcriptional changes caused by DYRK1A deficiency during the transition to spheroids (**Figure 5.4C**). We identified 744 genes that were downregulated and 96 genes that were upregulated in spheroid cells in the absence of *DYRK1A*.

We used the 1,834 upregulated genes identified in parental iOvCa147 spheroid cells (**Figure 5.4B**) to perform pathway enrichment analysis to elucidate signaling processes that may be important for the normal transition from adherent to suspension conditions (**Figure 5.4D**). Many of these pathways – including metabolism, GPCR signaling, and axon guidance – resembled the pathways that were enriched among the 1,382 genes we found to be commonly essential across iOvCa147, TOV1946, and OVCAR8 spheroid cells in our GO-CRISPR screen (**Figure 5.1D**). Pathway enrichment analysis using the 744 downregulated genes identified in *DYRK1A*<sup>-/-</sup> spheroid cells (**Figure 5.4C**) also revealed pathways similar to those found in the GO-CRISPR screen (**Figure 5.4E**). 78 pathways were commonly enriched across the GO-CRISPR screen and transcriptomic analyses, including 78 of the 83 pathways identified in *DYRK1A*<sup>-/-</sup> spheroid cells (**Figure 5.4F**). The axon guidance pathway was consistently and significantly one of the most enriched among these common pathways (**Figure 5.4G**). These data show our GO-CRISPR screen and transcriptomic analyses converge on this axon guidance category, which includes netrin



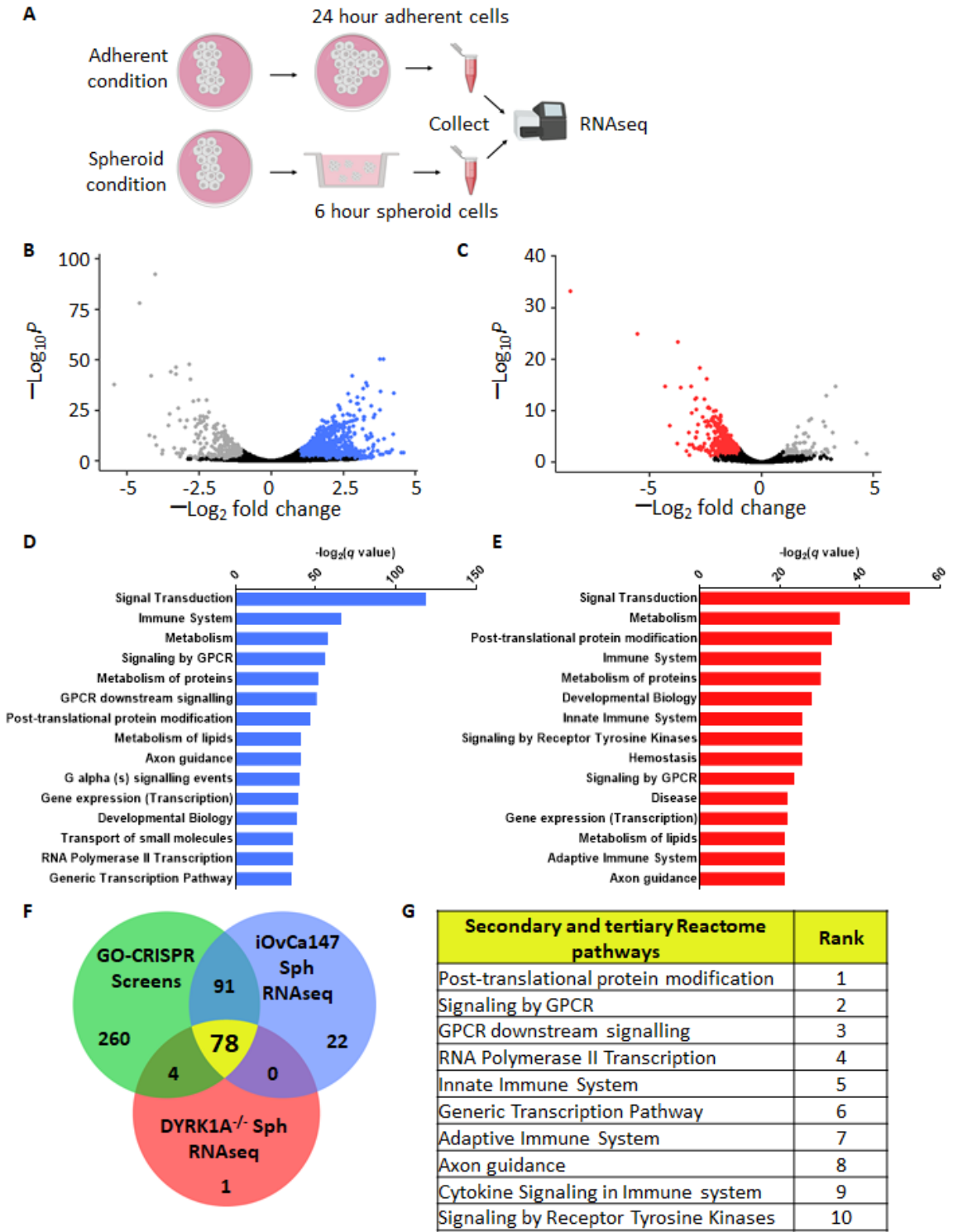


**Figure 5.4. Netrin signaling pathway components are upregulated in iOvCa147 spheroid cells but downregulated in *DYRK1A*<sup>-/-</sup> spheroid cells.** (A) Experimental design for RNA-seq in parental iOvCa147 or *DYRK1A*<sup>-/-</sup> cells. Cells were incubated in either adherent conditions for 24 hours or suspension conditions to induce spheroid formation for 6 hours. Cells were collected in triplicates and then processed for bulk RNA-seq. (B) Volcano plot showing differentially expressed genes in parental iOvCa147 spheroid cells compared to parental iOvCa147 adherent cells. 1,937 genes were found to be downregulated in iOvCa147 spheroid cells ( $\log_2$  fold change  $< 1$ ,  $p_{\text{adj}} < 0.05$ , FDR 10%, highlighted in grey) and 1,834 genes were upregulated ( $\log_2$  fold change  $> 1$ ,  $p_{\text{adj}} < 0.05$ , FDR 10%, highlighted in blue). Genes highlighted in black did not meet  $\log_2$  fold change cutoff or  $p_{\text{adj}}$  cutoffs. (C) Volcano plot showing differentially expressed genes in *DYRK1A*<sup>-/-</sup> spheroid cells compared to iOvCa147 spheroid cells. 744 genes were found to be downregulated in *DYRK1A*<sup>-/-</sup> spheroid cells ( $\log_2$  fold change  $< 1$ ,  $p_{\text{adj}} < 0.05$ , FDR 10%, highlighted in red) and 96 genes were upregulated ( $\log_2$  fold change  $> 1$ ,  $p_{\text{adj}} < 0.05$ , FDR 10%, highlighted in grey). Genes highlighted in black did not meet  $\log_2$  fold change cutoff or  $p_{\text{adj}}$  cutoffs. (D) Top 15 most significantly enriched pathways ( $p_{\text{adj}} < 0.05$ ) that were represented by the significant upregulated genes highlighted in blue in (B). The axon guidance pathway, containing netrin signaling components, was 9<sup>th</sup> overall. (E) Top 15 most significantly enriched pathways ( $p_{\text{adj}} < 0.05$ ) that were represented by the significant downregulated genes highlighted in red in (C). The axon guidance pathway, containing netrin signaling components, was 15<sup>th</sup> overall. (F) Venn diagram depicting overlapping enriched pathways identified in GO-CRISPR screen in three cell lines (iOvCa147, TOV1946, OVCAR8) in green; enriched pathways identified in upregulated genes in parental iOvCa147 spheroid cells in blue; and enriched pathways identified in downregulated genes in *DYRK1A*<sup>-/-</sup> spheroid cells in red. 78 pathways were commonly enriched in all three datasets (shown in yellow). (G) Top 10 most significant pathways ( $p_{\text{adj}} < 0.05$ ) commonly enriched pathways from all three datasets identified in and highlighted in yellow in (F). The axon guidance pathway, which was 8<sup>th</sup> overall, was enriched with netrin signaling components.

signaling components, suggesting it may play an important role in HGSOC spheroid formation and viability.

### 5.3.3 Netrin signaling components are commonly essential in HGSOC spheroid cells

The axon guidance gene ontology category encompasses a network of ligands and receptors that make up the axon pathfinding processes<sup>50</sup>. Key among these processes are guidance cues regulated by the netrin family of ligands and their receptors which have been shown to provide pro-survival cues in various other cancer types<sup>50</sup>. To better understand the role of netrin signaling in HGSOC and how it contributes to spheroid cell survival, we compiled the results from our GO-CRISPR screen in a pathway map using colors to indicate how often a particular component was identified across the three cell lines (**Figure 5.5**). This pathway map illustrates that extracellular components, such as the NTN1 ligand and receptors (UNC5 homologs and DCC), as well as intracellular components such as FAK, Fyn, Cdc42, DIP13 $\alpha$ , MAPK, AKT, and NF $\kappa$ B were identified by the GO-CRISPR screen across the three cell lines. This data suggests that netrin signaling is a potential mediator of HGSOC spheroid cell viability.

Netrin's role in other cancers have positioned the UNC5H and DCC receptors as DRs that regulate apoptosis and provide tumour cells with pro-survival signals<sup>42,45,51</sup>. Additionally, the extracellular nature of netrin ligands and their DRs present an opportunity to use therapeutic modalities that disable their interactions. Netrin signaling is therefore a compelling target for cancer therapy. To confirm its requirement in HGSOC spheroid cell survival, we independently knocked out *NTN1*, *DCC*, *DSCAM*, the UNC5 receptor

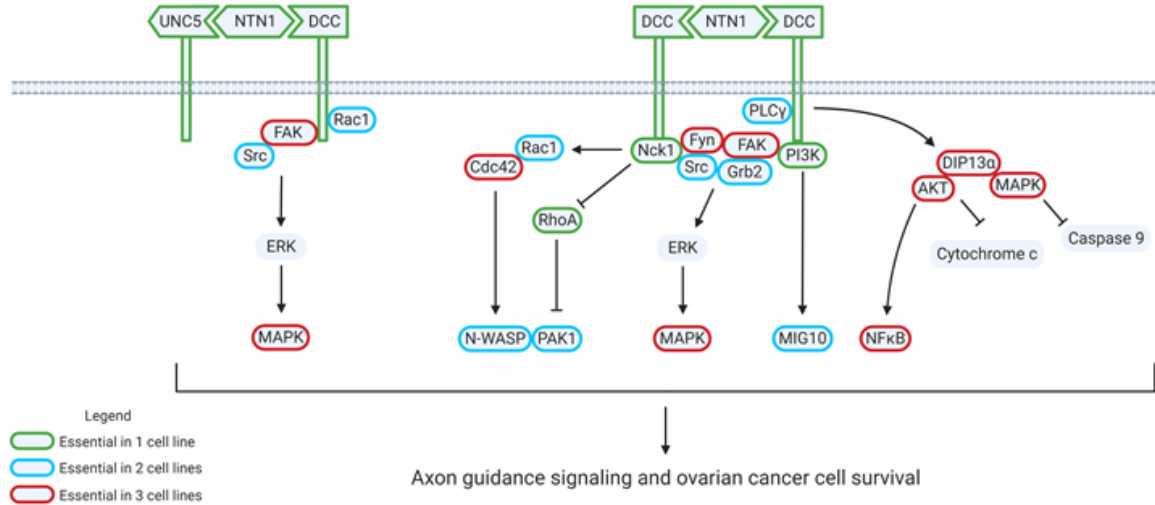


**Figure 5.5. Netrin signaling components are commonly essential in HGSOc spheroid cells.** Pathway map highlighting essential factors of netrin signaling in HGSOc cell survival. Netrin signaling components are highlighted in either green, blue, or red to indicate the frequency of observations across the three cell lines (iOvCa147, TOV1946, OVCAR8) investigated in the GO-CRISPR screen. Green indicates the encoding gene was found to be essential in only one cell line; blue indicates it was found to be essential in two cell lines; red indicates it was found to be essential across all three cell lines.

homologs (*UNC5A*, *UNC5B*, *UNC5C*, and *UNC5D*), and *FAK* in a panel of HGSOC cell lines (iOvCa147, TOV1946, OVCAR3, OVCAR4, OVCAR8, and COV318). We induced spheroid formation for 5 days in suspension conditions and then quantified their ability to reattach after reintroduction to adherent conditions as a proxy for spheroid viability as previously described<sup>6</sup> (**Figure 5.6A**). Loss of netrin signaling components resulted in reduced spheroid cell survival across all cell lines however it varied depending on which component of netrin signaling was knocked out. Loss of the ligand NTN1 reduced spheroid survival by approximately 23-48% in iOvCa147, OVCAR3, OVCAR4, and COV318 spheroid cells. Loss of the DCC DR reduced survival by approximately 62% in OVCAR3 and OVCAR4 spheroid cells while only a 9-20% reduction was observed in iOvCa147 and TOV1946 spheroid cells, respectively. Variable sensitivity to loss of UNC5 homologs (*UNC5A*, *UNC5B*, *UNC5C*, *UNC5D*) was observed in iOvCa147, TOV1946, OVCAR3, OVCAR4, and COV318 spheroid cells. Independent loss of these DRs reduced survival by approximately 13-71% in these cells (**Figure 5.6A**). As the hierarchical clustering indicates, iOvCa147, OVCAR3, and OVCAR4 spheroid cells were more sensitive to loss of these netrin components than TOV1946, OVCAR8, or COV318 spheroid cells (**Figure 5.6A**). Knockout of *UNC5A* reduced the viability of TOV1946 spheroid cells by approximately 54% whereas knockout of DCC reduced viability by approximately 20%. Only loss of NTN1, *UNC5C*, or *FAK* reduced survival of COV318 spheroid cells. The viability of OVCAR8 spheroid cells was only reduced upon loss of *FAK*. (**Figure 5.6A**). This data shows that these HGSOC spheroid cells are differentially affected by loss of netrin signaling components.

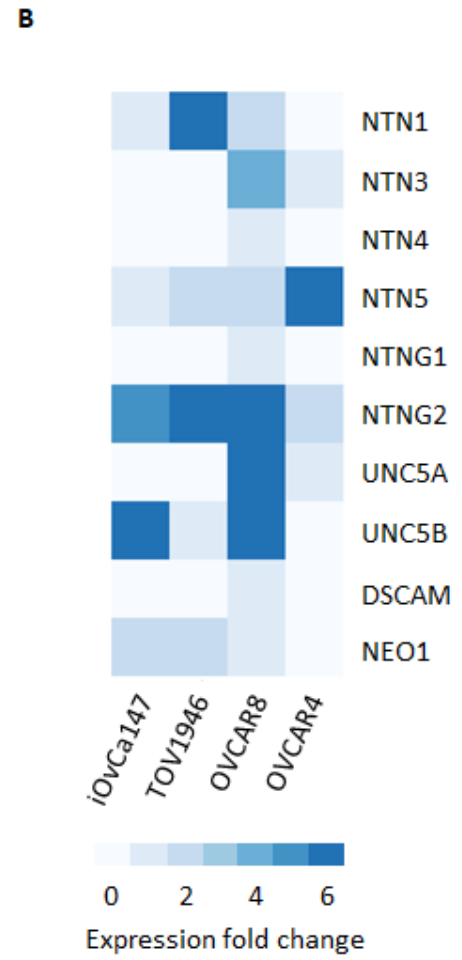
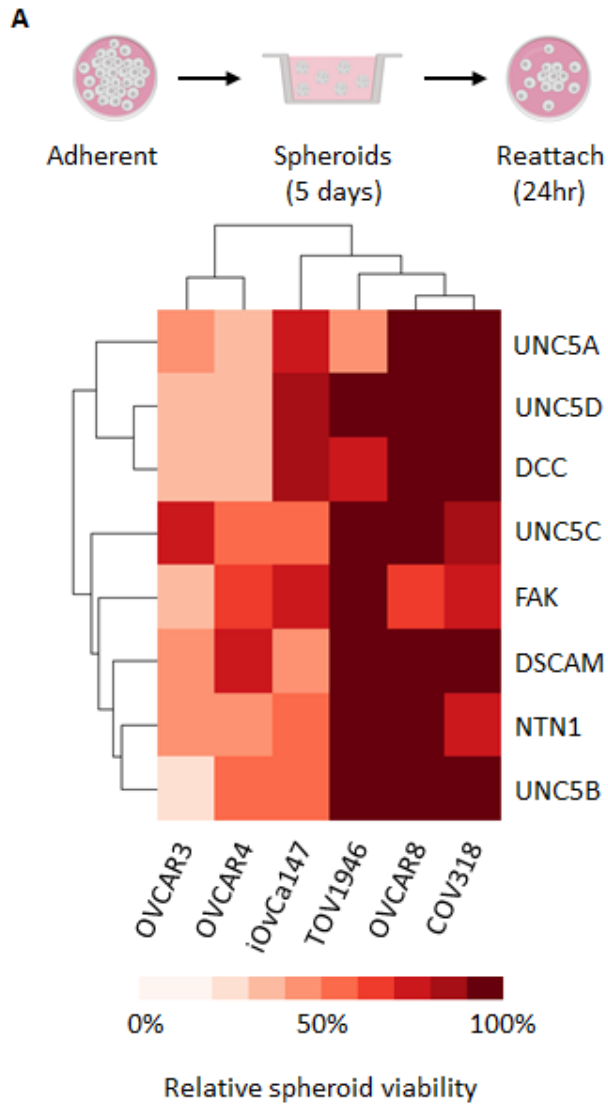


**Figure 5.6. Netrin signaling components are upregulated in HGSOc spheroid cells and mediate viability.** (A) We deleted genes encoding netrin signaling components (*NTN1*, *DCC*, *DSCAM*, *UNC5A*, *UNC5B*, *UNC5C*, *UNC5D*, *FAK*, or *EGFP*) in a panel of HGSOc cell lines (iOvCa147, TOV1946, OVCAR3, OVCAR4, OVCAR8, or COV318). A pooled Lentiviral CRISPR/Cas9 strategy (4 sgRNAs per gene) was used to disrupt each gene to generate pure single-gene knockout populations. Spheroid formation was induced for 5 days in suspension conditions and then spheroids were transferred to adherent conditions for 24 hours to facilitate reattachment. Cells were stained with crystal violet and absorbance was measured as a proxy for spheroid viability. Heatmap shows spheroid cell viability relative to control spheroid cells (*EGFP*). Disruption of these genes involved in netrin signaling reduced viability of spheroid cells. (B) Expression of genes encoding netrin ligands (*NTN1*, *NTN3*, *NTN4*, *NTN5*, *NTNG1*, and *NTNG2*) and receptors (*UNC5A*, *UNC5B*, *DSCAM*, and *NEO1*) was detected by RT-qPCR in a panel of HGSOc cell lines (iOvCa147, TOV1946, OVCAR4, or OVCAR8). Heatmap represents gene expression in 24 hour spheroid cells relative to 24 hour adherent cells. HGSOc cells variably over express netrin signaling components in suspension conditions.

We next hypothesized that some cell lines may upregulate different ligands or receptors that may compensate for loss of individual components. To investigate this, we interrogated the expression of a panel of genes that encoded netrin ligands (*NTN1*, *NTN3*, *NTN4*, *NTN5*, *NTNG1*, and *NTNG2*) and receptors (*UNC5A*, *UNC5B*, *DSCAM*, and *NEO1*) in iOvCa147, TOV1946, OVCAR4, and OVCAR8 cells (**Figure 5.6B**). We found that OVCAR8 spheroid cells had increased expression of each of these genes compared to adherent cells. Compared to adherent cells, both iOvCa147 and TOV1946 spheroid cells had increased expression of *NTN1*, *NTN5*, *NTNG2*, *UNC5B*, and *NEO1*. OVCAR4 spheroid cells had increased expression of *NTN3*, *NTN5*, *NTNG2*, and *UNC5A* relative to adherent cells (**Figure 5.6B**). This data shows that these HGSOc cell lines increase expression of various netrin ligands and receptors upon spheroid formation in suspension conditions.

## 5.4 Discussion

HGSOc spheroid cell biology has presented a unique challenge to cancer chemotherapies. Spheroids present in patients with late-stage disease – which constitute the vast majority of ovarian cancer patients – and their dormancy and metastatic potential complicate chemotherapies or surgical debulking that may otherwise be effective in early-stage patients<sup>5,10,17</sup>. Hence there is a strong need to understand HGSOc spheroid cell biology in order to develop effective therapies. In this study, we highlighted an important role for netrin signaling in ovarian cancer spheroid cell survival. Our novel GO-CRISPR screen paired with our transcriptomic analyses identified netrin signaling components as



essential mediators of HGSOc spheroid cell viability and potentially as a regulator of metastases and disease progression.

While netrin's functions outside of the central nervous system are not well understood, several studies have highlighted its contributions to cancer progression and metastases in breast cancer, colorectal cancer, glioblastoma, melanoma, neuroblastoma, non-small cell lung cancer, and pancreatic cancer<sup>21</sup>. Comparatively, very few studies have focused on netrin in ovarian cancer<sup>52-54</sup>. A 2011 study showed *NTN1* was over expressed in malignant but not benign ovarian cancer tumours and suggested it may have value as a biomarker for ovarian cancer<sup>53</sup>. More recently, NTN1 was shown to counteract the tumour suppressor function of SOX6 in an ovarian teratocarcinoma cell line and a grade III ovarian adenocarcinoma cell line<sup>52</sup>.

We found that individual knockout of netrin components across a panel of HGSOc cell lines adversely affected spheroid cell viability (**Figure 5.6A**). Quantification of spheroid cell viability showed that it was reduced at varying amounts across all cell lines. However, we only observed a reduction in viability in OVCAR8 spheroids upon loss of FAK but not any of the other components. This is in contrast to the results from our GO-CRISPR screen which found netrin signaling components were essential across all three cell lines (iOvCa147, TOV1946, and OVCAR8). Interrogation of gene expression showed that OVCAR8 spheroid cells upregulate every netrin ligand and receptor we investigated (**Figure 5.6B**). Over expression of these various ligands and receptors in the spheroid state may explain our inability to detect loss of viability in OVCAR8 spheroids. The divergent homology of netrin ligands may allow binding to different receptors to elicit complementary or compensatory effects within cells<sup>21,55</sup>. This suggests the need to

simultaneously disrupt multiple components of netrin signaling to study the effects within spheroid cells. For example, our pooled lentiviral CRISPR/Cas9 approach to disrupt each component individually could easily be adapted to knockout combinations of secreted netrins or UNC5 DR homologs in the same cell. This also beseeches the need to perform a broader investigation of gene expression in ascites-derived HGSOC cell lines to determine the expression patterns of netrin signaling components. A broader panel of cells could inform reliance on different netrin family members or different DRs. Moreover, we only deleted *NTN1*, *DCC*, *DSCAM* and the UNC5H DRs; we did not target other netrin ligands (*NTN3*, *NTN4*, *NTN5*, *NTNG1*, or *NTNG2*) or the neogenin (*NEO1*) receptor (**Figure 5.6A**). Indeed, our data shows that iOvCa147, TOV1946, OVCAR4, and OVCAR8 spheroid cells increase expression of these components in suspension conditions (**Figure 5.6B**). Different ligand-DR combinations may provide survival advantages to HGSOC spheroid cells. For example, netrin ligands may bind to neogenin to stimulate HGSOC spheroid cells with survival signals even in the absence of NTN1, DCC, or UNC5H. Both NTN1 and NTN4 are known to bind to the NEO1 receptor to promote survival and metastases in neuroblastoma<sup>39</sup>.

The multitude of ligands and receptors that comprise the netrin signaling network may present difficulty in developing a universal drug candidate that can block netrins ligands from binding to DRs. This is especially true if multiple ligand-DR signals converge on the same downstream effectors due to complementary or compensatory effects. Our GO-CRISPR screen implicated all three HGSOC cell lines (iOvCa147, TOV1946, OVCAR8) with dependence on FAK (**Figure 5.5**). Further work is required to characterize the mechanisms by which netrin regulates survival in HGSOC spheroid cells. Netrin has

also been shown to stimulate angiogenesis and invasiveness in xenograft tumour models and may act as factors for spheroid cell survival<sup>44,56-59</sup>. Future xenograft models will demonstrate if loss of netrin components in spheroid cells confers reduced spheroid viability or metastases *in vivo*. Additionally, several downstream mediators of netrin signaling converge on actin polymerization and cytoskeletal restructuring<sup>60,61</sup>, which may play an important role during HGSOc spheroid formation. Our GO-CRISPR screen also identified FAK as an essential component for spheroid cell survival in all three HGSOc cell lines (iOvCa147, TOV1946, OVCAR8) (**Figure 5.5**). Consistent with our findings, FAK have been shown to promote chemoresistance in HGSOc patients<sup>62,63</sup>. FAK inhibition may therefore present another opportunity to inhibit netrin signaling downstream of DRs to block pro-survival cues. Further studies are required to elucidate the mechanism of action for netrin in HGSOc which may be a combination of these possibilities. The netrin signaling pathway provides an attractive therapeutic target since its ligands or receptors are extracellularly accessible and could potentially be inhibited. A clinical trial (NCT02977195) is already underway for a humanized monoclonal netrin-1 antibody (NP137) that prevents binding of NTN1 to its DRs in patients with advanced solid tumours. This trial marks the first time a drug candidate targeting DRs is evaluated in humans and presents a promising new therapeutic opportunity for several cancers.

This study revealed multiple signaling pathways that are differentially expressed in spheroid cells including those that are disrupted upon loss of DYRK1A. Specifically, our study highlighted netrin signaling components as appealing factors that mediate spheroid cell viability. Further work is required to fully elucidate how netrins and their receptors

cooperate to provide spheroid cells with pro-survival cues and these findings may potentially inform new therapeutic strategies to treat dormant ovarian cancer.

## 5.5 Materials and methods

### 5.5.1 Engineering Cas9+ cells

High-grade serous ovarian cancer (HGSOC) iOvCa147 cells have previously been reported (MacDonald et al., 2017). Cas9-positive and Cas9-negative TOV1946 cells were provided by Rob Rottapel. iOvCa147 and OVCAR8 cells were engineered to express Cas9 as follows: cells were transduced with viral particles encoding a Cas9 expression cassette (lentiCas9-Blast, Addgene #52962) to generate cells constitutively expressing Cas9 (Cas9-positive cells). Cells were selected with Blasticidin (20 µg/mL) and single-cell clones were isolated by limiting dilution. Lysates were collected from clones and western blots were performed to determine Cas9 expression (Cell Signaling #14697). Cas9 editing efficiency was determined by viability studies using sgRNAs targeting selected fitness genes (*PSMD1*, *PSMD2*, *EIF3D*) and a non-targeting control (*LacZ*) as previously reported (Hart et al., 2015). A single clone showing the most effective Cas9 activity was selected for all further studies.

### 5.5.2 GeCKO v2 library preparation

HEK293T cells were transfected with the combined A and B components of the GeCKO v2 (Addgene #1000000048, #1000000049) pooled whole-genome library (123,411 sgRNAs in total) along with plasmids encoding lentiviral packaging proteins.

Media was collected 2-3 days later and any cells or debris were pelleted by centrifugation at 500 x g. Supernatant containing viral particles was filtered through a 0.45  $\mu$ M filter and stored at  $-80^{\circ}\text{C}$  with 1.1 g/100 mL BSA.

### 5.5.3 GO-CRISPR screen in iOvCa147, OVCAR8, and TOV1946 cells

GO-CRISPR screening was carried out separately in each of iOvCA147, OVCAR8, and TOV1946 as follows: Cas9-positive or Cas9-negative cells were transduced with virus collected as described above at a multiplicity of infection of 0.3 and with a predicted library coverage of  $>1000$ -fold. Cells were grown in media containing 2  $\mu\text{g/mL}$  puromycin (Sigma #P8833) to eliminate non-transduced cells. Cells were maintained in complete media containing puromycin in all following steps. A total of  $1.1 \times 10^9$  cells were collected and split into three groups consisting of approximately  $3.0 \times 10^8$  cells each and were cultured for an additional 2-3 days in complete media, then collected and counted. Triplicate samples of  $6.2 \times 10^7$  cells were saved for sgRNA sequence quantitation at  $T_0$ . The remaining cells (approximately  $1.4 \times 10^9$ /set) were plated at a density of  $2.0 \times 10^6$  cells/mL in each of twenty 10 cm ULA plates (total of 60 ULA plates). Following 2 days of culture, media containing spheroids was transferred to ten, 15 cm adherent tissue culture plates (total of 30 plates). The next day unattached spheroid cells were collected and re-plated onto additional 15 cm plates. This process was repeated for a total of 5 days at which point very few spheroids remained unattached. The attached cells were collected for DNA extraction and this population represents  $T_f$ . Complete media refers to DMEM/F12 media (Gibco #11320033) supplemented with 10% FBS (Wisent FBS Performance lot #185705),

1% penicillin-streptomycin glutamine (Wisent #450-202-EL) and 2 µg/mL puromycin (Sigma #P8833).

#### 5.5.4 GO-CRISPR screen analysis with TRACS

GO-CRISPR screening from each of the three cell lines (iOvCa147, OVCAR8, TOV1946) was analyzed as follows: The library reference file containing a list of all sgRNAs and their sequences (CSV file), raw reads for the pooled sgRNA library (FASTQ files (L0) and raw reads (FASTQ files) for all Initial ( $T_0$ ) and Final ( $T_f$ ) replicates for Cas9-positive and Cas9-negative cells (12 replicates) were loaded into TRACS<sup>47</sup> (<https://github.com/developperpiru/TRACS>). TRACS then automatically trimmed the reads using Cutadapt (1.15). TRACS automatically built a Bowtie2 (2.3.4.1) index and aligned the trimmed initial sgRNA library read file to generate a BAM file using Samtools 1.7. TRACS then invoked the MAGeCK read count function (0.5.6) to generate read counts from this library BAM file and all the trimmed sample FASTQ files. TRACS incremented all reads by 1 to prevent zero counts and division-by-zero errors. The TRACS algorithm (as previously described<sup>47</sup>) was then run using this read count file to determine the Library Enrichment Score (ES), Initial ES, Final ES and the Enrichment Ratio (ER) for each gene (see The TRACS algorithm section). The VisualizeTRACS feature was then used to visualize the results and generate figures.

#### 5.5.5 Generating DYRK1A knockout cells

A double cutting CRISPR/Cas9 approach with a pair of sgRNAs (sgRNA A and B) was used to completely excise exon 2 (322 bp region) of *DYRK1A* using a px458 vector

(Addgene #48138) that was modified to express the full CMV promoter. PCR primers that flank the targeted region of *DYRK1A* were used to verify deletion. Single-cell clones were generated by limiting dilutions and evaluated for *DYRK1A* status by PCR, western blot, and sequencing. See **Table 5.1** for sgRNA and primer sequences.

### 5.5.6 *DYRK1A* immunoprecipitation kinase assay

Whole-cell lysates from adherent parental iOvCa147 cells and *DYRK1A*<sup>-/-</sup> cells were extracted using complete RIPA buffer and incubated overnight with *DYRK1A* antibody (Cell Signaling Technology anti-*DYRK1A* rabbit antibody #8765). Samples were then washed with buffer and Dynabeads (Thermo Fisher Scientific Dynabeads Protein G #10003D) were added for 2 hours. Samples were then washed with buffer and recombinant Tau protein (Sigma recombinant Tau protein #T0576) and ATP (Sigma #A1852) were added and samples were incubated for 30 minutes at 37°C. 5x SDS was then added and samples were resolved SDS-PAGE. Antibodies used for western blotting were phosphospecific Tau antibody (Cell Signaling Technology phospho-Tau Ser-404 rabbit antibody #20194) and Tau protein (Cell Signaling Technology anti-Tau rabbit antibody #46687)

### 5.5.7 Real-time qPCR (RT-qPCR)

Parental iOvCa147 cells and *DYRK1A*<sup>-/-</sup> cells were cultured in regular 6-well plasticware for adherent conditions or in 6-well ultra-low attachment (ULA) plates to induce spheroid formation in suspension conditions for 6, 12, or 24 hours. Spheroids were then collected from wells (2 x 10<sup>5</sup> cells per well; 3 wells pooled together per replicate in

**Table 5.1 Primers used for experiments in Chapter 5**

<b>sgRNAs for DYRK1A deletion</b>	<b>Sequence</b>
sgRNA A Top	CACCGCTCACTTATCTTCTTGTAGG
sgRNA A Bottom	AAACCCTACAAGAAGATAAGTGAGC
sgRNA B Top	CACCGCAACGTGGGATTATGGATT
sgRNA B Bottom	AAACAATCCATAATCCCACGTTGC
<b>PCR primers</b>	<b>Sequence</b>
<i>DYRK1A</i> Exon2 Forward	GGTTTCACCTGGTTTGGGGA
<i>DYRK1A</i> Exon2 Reverse	TCCGTGGGGCAAGAACTTT
<b>RT-qPCR primers</b>	<b>Sequence</b>
<i>β-Actin</i> Forward	AGAGCTACGAGCTGCCTGAC
<i>β-Actin</i> Reverse	AGCACTGTGTTGGCGTACAG
<i>CDK1</i> Forward	TAAGCCGGGATCTACCATACCC
<i>CDK1</i> Reverse	TCATGGCTACCACTTGACCTGTAG
<i>DCC</i> Forward	AGCCAATGGGAAAATTACTGCTTAC
<i>DCC</i> Reverse	AGGTTGAGATCCATGATTTGATGAG
<i>DSCAM</i> Forward	GATGGTCCACCTCAGGAAGTTC
<i>DSCAM</i> Reverse	CCAGTGCTGTACTCTCGGTAAC
<i>GAPDH</i> Forward	CGGAGTCAACGGATTTGGTCGTAT
<i>GAPDH</i> Reverse	AGCCTTCTCCATGGTGGTGAAGAC
<i>MYBL2</i> Forward	TGCCCAAGTCTCTATCCTTGCC
<i>MYBL2</i> Reverse	CCTGGTTGAGCAAGCTGTTGTC
<i>NEO1</i> Forward	GTCACTGAGACCTTGGAAGCG
<i>NEO1</i> Reverse	TCAGCAGACAGCCAGTCAGTTG
<i>NTN1</i> Forward	TGCAAGAAGGACTATGCCGTC
<i>NTN1</i> Reverse	GCTCGTGCCCTGCTTATACAC
<i>NTN3</i> Forward	TGCAAGCCCTTCTACTGCGACA
<i>NTN3</i> Reverse	CAGTCGGTACAGCTCCATGTTG
<i>NTN4</i> Forward	CAGAAGGACAGTATTGCCAGAGG
<i>NTN4</i> Reverse	GCAGAAGGTCACTGAGTTGGCA
<i>NTN5</i> Forward	CTTGCCACTACTCCTGGTGCTT
<i>NTN5</i> Reverse	AGTACCTCCGAAGGCTCATGTG
<i>NTNG1</i> Forward	GCACGCTACTTTTACGCGATCTC
<i>NTNG1</i> Reverse	CTGGACCTGTAGTGTTGTGCTC
<i>NTNG2</i> Forward	ATGCGCCTGAAGGACTACGTCA
<i>NTNG2</i> Reverse	TTGGAGGCGTCACACTCGTTGC
<i>UNC5A</i> Forward	ATCACCAAGGACACAAGGTTTGC
<i>UNC5B</i> Reverse	GGCTGGAAATTATCTTCTGCCGAA
<i>UNC5C</i> Forward	GCAAATTGCTGGCTAAATATCAGGAA
<i>UNC5C</i> Reverse	GCTCCACTGTGTTTCAGGCTAAATCTT



triplicates), pelleted, and washed twice with 1x PBS. For adherent cells grown in 6-well plates ( $1 \times 10^5$  cells per well; 3 wells pooled together per replicate in triplicates), media was aspirated, wells were washed twice in 1x PBS, then cells were scraped off in 1x PBS. All cell pellets were then processed for total RNA extraction using the Monarch Total RNA Miniprep Kit (NEB #T2010S). RNA was reverse transcribed using iScript (Bio-Rad #1708891). cDNA was diluted 5x with nuclease-free water. Real-time qPCR was performed for *MYBL2* and *CDK1* using PowerUP SYBR (Applied Biosystems #A25742). Human  $\beta$ -actin or *GAPDH* was used as the internal control. See **Table 5.1** for primer sequences.

### 5.5.8 RNA preparation and RNA-sequencing

Total RNA was collected from parental iOvCa147 cells and *DYRK1A*<sup>-/-</sup> cells from 24-hour adherent or 6-hour spheroid conditions using the Monarch Total RNA Miniprep Kit (NEB #T2010S) as described above. RNA was collected in three replicates for each condition (adherent and spheroids). Samples were submitted to the London Regional Genomics Centre (Robarts Research Institute, London, Ontario, Canada) for quantification using Qubit 2.0 Fluorometer (Thermo Fisher Scientific) and quality control analysis using Agilent 2100 Bioanalyzer (Agilent Technologies #G2939BA) and RNA 6000 Nano Kit (Agilent Technologies #5067-1511). Ribosomal RNA removal and library preparation was performed using ScriptSeq Complete Gold Kit (Illumina #BEP1206). High-throughput sequencing was performed on an Illumina NextSeq 500 platform (mid-output, 150-cyclekit).

### 5.5.9 RNA-sequencing analyses

Raw FASTQ data was downloaded from Illumina BaseSpace. Reads were aligned using STAR 2.6.1a<sup>64</sup> to the human genome (Homo\_sapiens.GRCh38.dna.primary\_assembly.fa; sjdbGTFfile: Homo\_sapiens.GRCh38.92.gtf) to generate read counts. BEAVR<sup>65</sup> was then used to analyze read counts (settings: False discovery rate (FDR): 10%; drop genes with less than 1 reads) to identify differentially expressed genes ( $\log_2$  fold change  $> 1$  for upregulated genes; or  $\log_2$  fold change  $< -1$  for downregulated genes;  $p_{\text{adj}} < 0.05$ ) for the following comparisons: parental iOvCa147 adherent cells vs. parental iOvCa147 spheroid cells; or parental iOvCa147 spheroid cells vs. *DYRK1A*<sup>-/-</sup> spheroid cells.

### 5.5.10 Pathway enrichment analyses

For GO-CRISPR screen, we used the filtered list of genes obtained using TRACS<sup>47</sup> and performed gene ontology and pathway enrichment analysis using the ConsensusPathDB enrichment analysis test (Release 34 (15.01.2019), <http://cpdb.molgen.mpg.de/>) for top-ranked genes of interest.  $p_{\text{adj}}$  values and ER values for each gene were used as inputs. The minimum required genes for enrichment was set to 45 and the FDR-corrected  $p_{\text{adj}}$  value cutoff was set to  $< 0.01$ . The Reactome pathway dataset was used as the reference. For each identified pathway, ConsensusPathDB provides the number of enriched genes and a q value ( $p_{\text{adj}}$ ) for the enrichment. Bar plots were generated in R 3.6.2 using these values to depict the significant pathways identified. For RNA-seq pathway analyses, we formed pathway analyses in BEAVR<sup>65</sup> and downloaded the pathway enrichment table to construct bar plots and determine overlapping pathways using R 3.6.2.

### 5.5.11 Western blots

Cells were washed in 1x PBS and lysed in complete RIPA buffer with protease inhibitors (Sigma #S8820) and incubated for 1 hour on ice. Samples were then centrifuged at 14,000 RPM at 4°C for 10 minutes. The supernatant was collected and protein concentration was determined by Bradford assay. Lysates were mixed with 6x SDS loading dye buffer and resolved using standard SDS-PAGE protocols. Antibodies used for blotting were DYRK1A (Cell Signaling Technology anti-DYRK1A rabbit antibody #8765), p130 (Santa Cruz anti-p130 rabbit antibody #SC-317), and tubulin (Cell Signaling Technology anti-Tubulin rabbit antibody #2125).

### 5.5.12 Generation of single-gene knockouts

Gibson Assembly (NEB #E2611) was used to clone a pool of four sgRNAs per gene (*NTN1*, *DCC*, *DSCAM*, *UNC5A*, *UNC5B*, *UNC5C*, *UNC5D*, *FAK*, and *EGFP* control) into lentiCRISPR v2 (Addgene #52961). Sequences for sgRNAs were obtained from the GeCKO v2 library. For each gene, HEK293T cells were transfected with the assembled plasmid along with plasmids encoding lentiviral packaging proteins. Media was collected 2-3 days later and any cells or debris were pelleted by centrifugation at 500 x g. Supernatant containing viral particles was filtered through a 0.45 µM filter. For each targeted gene, iOvCa147, OVCAR3, OVCAR4, OVCAR8, COV318, or TOV1946 cells were transduced with viral particles encoding Cas9 and sgRNA expression cassettes. Cells were selected for 2-3 days in media containing 2 µg/mL puromycin.

### 5.5.13 Spheroid viability assays

For each targeted gene in iOvCa147, TOV1946, OVCAR3, OVCAR4, OVCAR8, or COV318 cells, spheroid viability was assayed as follows: Knockout cells were cultured for 5 days in suspension conditions using ULA plasticware ( $2 \times 10^6$  cells per well) to allow spheroid formation. Spheroid cells were then collected and transferred to standard plasticware to facilitate reattachment for 24 hours. Reattached cells were fixed with fixing solution (25% methanol in 1x PBS) for 3 minutes. Fixed cells were incubated for 30 minutes with shaking in crystal violet staining solution (0.5% crystal violet, 25% methanol in 1x PBS). Plates were carefully immersed in ddH<sub>2</sub>O to remove residual crystal violet. Plates were incubated with destaining solution (10% acetic acid in 1x PBS) for 1 hour with shaking to extract crystal violet from cells. Absorbance of crystal violet was measured at 590 nm using a microplate reader (Perkin Elmer Wallac 1420). Each knockout and normalized to the EGFP control. Percent of spheroid cells surviving suspension and reattachment is inferred from relative absorbance.

### 5.5.14 Statistical analyses

Statistical tests for GO-CRISPR screens were performed in TRACS<sup>47</sup>. Statistical tests for RNA-seq were performed in BEAVR<sup>65</sup>. Specific statistical tests used for RT-qPCR and spheroid viability assays are indicated in the figure legends for each experiment. These were performed in GraphPad Prism 6.

## 5.6 References

- 1 Al Habyan, S., Kalos, C., Szymborski, J. & McCaffrey, L. Multicellular detachment generates metastatic spheroids during intra-abdominal dissemination in epithelial ovarian cancer. *Oncogene* **37**, 5127-5135, doi:10.1038/s41388-018-0317-x (2018).
- 2 Menon, U., Karpinskyj, C. & Gentry-Maharaj, A. Ovarian Cancer Prevention and Screening. *Obstetrics & Gynecology* **131** (2018).
- 3 Stewart, C., Ralyea, C. & Lockwood, S. Ovarian Cancer: An Integrated Review. *Semin Oncol Nurs* **35**, 151-156, doi:10.1016/j.soncn.2019.02.001 (2019).
- 4 Lheureux, S., Gourley, C., Vergote, I. & Oza, A. M. Epithelial ovarian cancer. *The Lancet* **393**, 1240-1253, doi:10.1016/s0140-6736(18)32552-2 (2019).
- 5 Ahmed, N. & Stenvers, K. L. Getting to know ovarian cancer ascites: opportunities for targeted therapy-based translational research. *Front Oncol* **3**, 256, doi:10.3389/fonc.2013.00256 (2013).
- 6 MacDonald, J. *et al.* A Systematic Analysis of Negative Growth Control Implicates the DREAM Complex in Cancer Cell Dormancy. *Mol Cancer Res* **15**, 371-381, doi:10.1158/1541-7786.MCR-16-0323-T (2017).
- 7 Correa, R. J. *et al.* Combination of AKT inhibition with autophagy blockade effectively reduces ascites-derived ovarian cancer cell viability. *Carcinogenesis* **35**, 1951-1961, doi:10.1093/carcin/bgu049 (2014).
- 8 Correa, R. J., Peart, T., Valdes, Y. R., DiMattia, G. E. & Shepherd, T. G. Modulation of AKT activity is associated with reversible dormancy in ascites-derived epithelial ovarian cancer spheroids. *Carcinogenesis* **33**, 49-58, doi:10.1093/carcin/bgr241 (2012).
- 9 Matulonis, U. A. *et al.* Ovarian cancer. *Nature Reviews Disease Primers* **2**, 16061, doi:10.1038/nrdp.2016.61 (2016).
- 10 Narod, S. Can advanced-stage ovarian cancer be cured? *Nature Reviews Clinical Oncology* **13**, 255-261, doi:10.1038/nrclinonc.2015.224 (2016).
- 11 Vargas, A. N. Natural history of ovarian cancer. *Ecancermedicalscience* **8**, 465-465, doi:10.3332/ecancer.2014.465 (2014).
- 12 Ahmed, N., Thompson Ew Fau - Quinn, M. A. & Quinn, M. A. Epithelial-mesenchymal interconversions in normal ovarian surface epithelium and ovarian carcinomas: an exception to the norm.
- 13 Shield, K., Ackland, M. L., Ahmed, N. & Rice, G. E. Multicellular spheroids in ovarian cancer metastases: Biology and pathology. *Gynecol Oncol* **113**, 143-148, doi:10.1016/j.ygyno.2008.11.032 (2009).
- 14 Latifi, A. *et al.* Isolation and characterization of tumor cells from the ascites of ovarian cancer patients: molecular phenotype of chemoresistant ovarian tumors.
- 15 Shield, K. *et al.* Alpha2beta1 integrin affects metastatic potential of ovarian carcinoma spheroids by supporting disaggregation and proteolysis. *J Carcinog* **6**, 11, doi:10.1186/1477-3163-6-11 (2007).
- 16 Achilli, T. M., Meyer J Fau - Morgan, J. R. & Morgan, J. R. Advances in the formation, use and understanding of multi-cellular spheroids.
- 17 Keyvani, V. *et al.* Ovarian cancer stem cells and targeted therapy. *Journal of Ovarian Research* **12**, 120, doi:10.1186/s13048-019-0588-z (2019).

- 18 Peart, T. *et al.* Intact LKB1 activity is required for survival of dormant ovarian cancer spheroids.
- 19 Buensuceso, A., Ramos-Valdes, Y., DiMattia, G. E. & Shepherd, T. G. AMPK-Independent LKB1 Activity Is Required for Efficient Epithelial Ovarian Cancer Metastasis.
- 20 Chen, M. W. *et al.* The STAT3-miRNA-92-Wnt Signaling Pathway Regulates Spheroid Formation and Malignant Progression in Ovarian Cancer.
- 21 Bruikman, C. S., Zhang, H., Kemper, A. M. & van Gils, J. M. Netrin Family: Role for Protein Isoforms in Cancer. *J Nucleic Acids* **2019**, 3947123, doi:10.1155/2019/3947123 (2019).
- 22 Delloye-Bourgeois, C. *et al.* Nucleolar localization of a netrin-1 isoform enhances tumor cell proliferation.
- 23 Fitamant, J. *et al.* Netrin-1 expression confers a selective advantage for tumor cell survival in metastatic breast cancer.
- 24 Delloye-Bourgeois, C. *et al.* Netrin-1 acts as a survival factor for aggressive neuroblastoma.
- 25 Dumartin, L. *et al.* Netrin-1 mediates early events in pancreatic adenocarcinoma progression, acting on tumor and endothelial cells.
- 26 Kaufmann, S., Kuphal S Fau - Schubert, T., Schubert T Fau - Bosserhoff, A. K. & Bosserhoff, A. K. Functional implication of Netrin expression in malignant melanoma.
- 27 Ramesh, G., Berg A Fau - Jayakumar, C. & Jayakumar, C. Plasma netrin-1 is a diagnostic biomarker of human cancers.
- 28 Li, B. *et al.* Serum netrin-1 as a biomarker for colorectal cancer detection.
- 29 Yin, K. *et al.* Netrin-1 induces the proliferation of gastric cancer cells via the ERK/MAPK signaling pathway and FAK activation.
- 30 Zhang, J. *et al.* IGF2BP1 silencing inhibits proliferation and induces apoptosis of high glucose-induced non-small cell lung cancer cells by regulating Netrin-1.
- 31 Mehlen, P. *et al.* The DCC gene product induces apoptosis by a mechanism requiring receptor proteolysis.
- 32 Mehlen, P. & Furne, C. Netrin-1: when a neuronal guidance cue turns out to be a regulator of tumorigenesis.
- 33 Llambi, F., Causeret F Fau - Bloch-Gallego, E., Bloch-Gallego E Fau - Mehlen, P. & Mehlen, P. Netrin-1 acts as a survival factor via its receptors UNC5H and DCC.
- 34 Mazelin, L. *et al.* Netrin-1 controls colorectal tumorigenesis by regulating apoptosis.
- 35 Esseghir, S. *et al.* Identification of NTN4, TRA1, and STC2 as prognostic markers in breast cancer in a screen for signal sequence encoding proteins.
- 36 Srivastava, S. *et al.* Expression of proteins associated with hypoxia and Wnt pathway activation is of prognostic significance in hepatocellular carcinoma.
- 37 Thakkar, A. D. *et al.* Identification of gene expression signature in estrogen receptor positive breast carcinoma.
- 38 Lv, B. *et al.* Netrin-4 as a biomarker promotes cell proliferation and invasion in gastric cancer.
- 39 Villanueva, A. A. *et al.* The Netrin-4/ Neogenin-1 axis promotes neuroblastoma cell survival and migration.

- 40 Jayachandran, A. *et al.* Identifying and targeting determinants of melanoma cellular invasion.
- 41 Larrieu-Lahargue, F., Welm Al Fau - Thomas, K. R., Thomas Kr Fau - Li, D. Y. & Li, D. Y. Netrin-4 induces lymphangiogenesis in vivo.
- 42 Goldschneider, D. & Mehlen, P. Dependence receptors: a new paradigm in cell signaling and cancer therapy. *Oncogene* **29**, 1865-1882, doi:10.1038/onc.2010.13 (2010).
- 43 Mehlen, P. & Guenebeaud, C. Netrin-1 and its dependence receptors as original targets for cancer therapy.
- 44 Kefeli, U. *et al.* Netrin-1 in cancer: Potential biomarker and therapeutic target?
- 45 Gibert, B. & Mehlen, P. Dependence Receptors and Cancer: Addiction to Trophic Ligands. *Cancer Res* **75**, 5171-5175, doi:10.1158/0008-5472.CAN-14-3652 (2015).
- 46 Toda, K. *et al.* Genetic and epigenetic alterations of netrin-1 receptors in gastric cancer with chromosomal instability. *Clinical Epigenetics* **7**, 73, doi:10.1186/s13148-015-0096-y (2015).
- 47 Perampalam, P., McDonald, J. I. & Dick, F. A. GO-CRISPR: a highly controlled workflow to discover gene essentiality in loss-of-function screens. *bioRxiv*, 2020.2006.2004.134841, doi:10.1101/2020.06.04.134841 (2020).
- 48 Yu, D., Cattoglio, C., Xue, Y. & Zhou, Q. A complex between DYRK1A and DCAF7 phosphorylates the C-terminal domain of RNA polymerase II to promote myogenesis. *Nucleic Acids Res* **47**, 4462-4475, doi:10.1093/nar/gkz162 (2019).
- 49 Di Vona, C. *et al.* Chromatin-wide profiling of DYRK1A reveals a role as a gene-specific RNA polymerase II CTD kinase. *Mol Cell* **57**, 506-520, doi:10.1016/j.molcel.2014.12.026 (2015).
- 50 Ziel, J. W. & Sherwood, D. R. Roles for netrin signaling outside of axon guidance: a view from the worm. *Dev Dyn* **239**, 1296-1305, doi:10.1002/dvdy.22225 (2010).
- 51 Grandin, M. *et al.* Structural Decoding of the Netrin-1/UNC5 Interaction and its Therapeutical Implications in Cancers. *Cancer Cell* **29**, 173-185, doi:10.1016/j.ccell.2016.01.001 (2016).
- 52 Li, Y., Xiao, M. & Guo, F. The role of Sox6 and Netrin-1 in ovarian cancer cell growth, invasiveness, and angiogenesis. *Tumour Biol* **39**, 1010428317705508, doi:10.1177/1010428317705508 (2017).
- 53 Papanastasiou, A. D., Pampalakis G Fau - Katsaros, D., Katsaros D Fau - Sotiropoulou, G. & Sotiropoulou, G. Netrin-1 overexpression is predictive of ovarian malignancies.
- 54 Yuan, Y. *et al.* Netrin-4 is upregulated in breast carcinoma effusions compared to corresponding solid tumors.
- 55 Meijers, R., Smock, R. G., Zhang, Y. & Wang, J. H. Netrin Synergizes Signaling and Adhesion through DCC. *Trends Biochem Sci*, doi:10.1016/j.tibs.2019.10.005 (2019).
- 56 Wu, W., Lei, H., Shen, J. & Tang, L. The role of netrin-1 in angiogenesis and diabetic retinopathy: a promising therapeutic strategy.
- 57 Jiao, X. *et al.* Netrin-1 works with UNC5B to regulate angiogenesis in diabetic kidney disease.

- 58 Zhang, X. *et al.* Netrin-1 elicits metastatic potential of non-small cell lung carcinoma cell by enhancing cell invasion, migration and vasculogenic mimicry via EMT induction.
- 59 Yin, K. *et al.* Netrin-1 promotes cell neural invasion in gastric cancer via its receptor neogenin.
- 60 Drummond, M. L. *et al.* Actin polymerization controls cilia-mediated signaling.
- 61 Sundararajan, L. A.-O. *et al.* Actin assembly and non-muscle myosin activity drive dendrite retraction in an UNC-6/Netrin dependent self-avoidance response.
- 62 Diaz Osterman, C. J. *et al.* FAK activity sustains intrinsic and acquired ovarian cancer resistance to platinum chemotherapy. LID - 10.7554/eLife.47327 [doi] LID - e47327.
- 63 Byeon, Y. *et al.* CD44-Targeting PLGA Nanoparticles Incorporating Paclitaxel and FAK siRNA Overcome Chemoresistance in Epithelial Ovarian Cancer.
- 64 Dobin, A. *et al.* STAR: ultrafast universal RNA-seq aligner. *Bioinformatics* **29**, 15-21, doi:10.1093/bioinformatics/bts635 (2013).
- 65 Perampalam, P. & Dick, F. A. BEAVR: a browser-based tool for the exploration and visualization of RNA-seq data. *BMC Bioinformatics* **21**, 221, doi:10.1186/s12859-020-03549-8 (2020).



## Chapter 6

### 6 Discussion

#### 6.1 Summary of findings

Chemoresistance and dormancy are a major challenge in the treatment of HGSOc leading to treatment failure and disease recurrence in up to 90% of patients<sup>1,2</sup>. This is facilitated by spheroids, which are multicellular aggregates of tumour cells that have exfoliated from primary tumours and are carried throughout the peritoneal cavity by ascites fluid to invade distant tissues<sup>3,4</sup>. Spheroid cells reversibly exit the cell cycle to become quiescent, allowing them to evade chemotherapy<sup>5-10</sup>. This process is mediated by the DREAM complex and its initiating kinase, DYRK1A<sup>5,11-13</sup>. Depletion of DYRK1A significantly reduces spheroid cell survival while also increasing sensitivity to chemotherapy<sup>5</sup>. Additionally, pharmacologic inhibition of DYRK1A is sufficient to enhance sensitivity to chemotherapy in ovarian cancer as well as other dormant cancers *in vitro*<sup>5,14-17</sup>. Thus, DREAM and DYRK1A are attractive targets to specifically inhibit dormancy in disseminated spheroid cells. However, pharmacological DYRK1A inhibitors used in *in vitro* studies have not been approved for clinical use<sup>18,19</sup>. Additionally, while *in vivo* studies have indicated a requirement for DREAM in normal growth arrest during early development, a role for DREAM in adults has not been identified. Furthermore, while we have previously shown that DYRK1A is required for HGSOc spheroid cell survival, the mechanisms of how it affects survival in terms of the genes and pathways it regulates is still not understood<sup>5</sup>.

## 6.2 Prolonged loss of DREAM causes systemic amyloidosis in mice

To characterize the role of DREAM in adults, we developed a conditional mouse model to disrupt DREAM assembly. We did not observe any defects in proliferation or the development of neoplasms in DREAM deficient mice. Our previous mouse model that constitutively disrupted DREAM assembly had endochondral bone defects due to loss of growth arrest in chondrocytes<sup>20</sup>. This was not observed in the conditional knockout model presented in Chapter 2 and this was consistent with our expectations. Endochondral ossification is finished by adulthood and growth plates of bones are closed<sup>21</sup>. The absence of these early developmental defects allowed us to characterize the role of long-term DREAM loss in adult mice.

We identified a significant difference in survival of DREAM deficient mice relative to wild type mice. The cause of this early mortality was due to amyloidosis. Specifically, loss of DREAM assembly led to an overexpression of *Apoa1* and *Apoa4* in liver tissue. These genes specifically encode for the apolipoproteins apoA-I and apoA-IV, respectively<sup>22</sup>. Our work showed that these genes have putative CDE/CHR motifs in their promoters that can bind DREAM leading to transcriptional repression which is mediated by H2AZ deposition within their gene bodies. Upon loss of DREAM, MMB is found at the *Apoa1* and *Apoa4* promoters and this is concomitant with decreased H2AZ in their gene bodies. Transcriptional activation of these promoters led to increased apolipoprotein levels which circulated to other tissues, including kidney, spleen, and heart and deposited as amyloid fibrils. Kidneys in DREAM-deficient mice were most affected as they had widespread amyloid deposition in the cortex and medulla likely leading to kidney

disfunction which was detected by albuminuria and increased serum creatinine. Together, this model uncovered a previously unknown role for DREAM and MMB in adults and showed an important connection between transcriptional de-repression and amyloidosis.

Our conditional mouse model demonstrated that the consequence of DREAM deficiency in adults is systemic amyloidosis (Chapter 2). This is an important finding in the context of cancer. Several *in vitro* studies in cancer cell lines, including those in quiescent colon, pancreatic, and ovarian cancer cells, have shown that DYRK1A/B inhibition enhances sensitivity to chemotherapy and reduces viability of cancer cells<sup>5,14-17</sup>. DYRK1A/B is therefore an appealing target for treating dormant cancer in patients. The three clinical trials (NCT03904862, NCT03897036, and NCT01199718) presently underway for the DYRK1A inhibitor, CX-4945, have not reported any results to date hence no conclusions can be made about its toxicity<sup>18,23</sup>. However, our study suggests that constitutive, long-term disruption of DREAM could result in systemic amyloidosis in patients. The extent of potential amyloid development may depend on the dose of CX-4945. As our data shows, *Apoa1* and *Apoa4* gene expression are dynamically controlled by DREAM and MMB. Upon complete ablation of DREAM, the balance is shifted towards the MMB complex which abundantly occupies its target promoters<sup>24-26</sup>. This suggests that side effects of DREAM loss due to DYRK1A inhibition may be potentiated by the dose of the inhibitor. Furthermore, while DREAM deficient mice were short-lived compared to their wild type counterparts, the amyloid deposition observed in these mice was chronic and occurred between 8 weeks of age (the age of tamoxifen administration) to 1 year (earliest amyloid detected) and beyond. Therefore, appropriately coordinated pharmacological inhibition of DYRK1A that is administrated with adjuvant or neoadjuvant

therapy may mitigate development of amyloidosis in patients. Further preclinical studies will be required to explore these challenges. The completion of the aforementioned clinical trials will also inform safe dosage for CX-4945 administration.

### 6.3 Components of netrin signaling are essential factors for spheroid cell viability

The role of DREAM in cancer has become increasingly apparent over the last decade. Several studies – including our own in ovarian cancer – have identified a role for DREAM in quiescence and dormant cancer<sup>5,16,27-29</sup>. DREAM and DYRK1A cooperate to facilitate cell cycle exit and re-entry in HGSOc spheroid cells<sup>5</sup>. However, the transcriptional programming and cellular pathways under the control of DREAM and DYRK1A in the context of ovarian cancer is not known. Elucidating these processes will improve our understanding of HGSOc spheroid cell biology and highlight the selective advantages that spheroid cells acquire to remain viable in suspension conditions. To this end, we devised an integrated strategy that consisted of transcriptional analyses of spheroid cells and a loss-of-function genome-wide CRISPR screen. This required the development of new tools: BEAVR, a bioinformatics tool to allow rapid analysis of RNAseq data (Chapter 3); and GO-CRISPR and TRACS (Chapter 4), a new method and software that reduces confounding biases caused by non-gene editing events in CRISPR screens. We later used these tools in Chapter 5 to identify the netrin signaling pathway as a critical mediator of HGSOc spheroid cell viability. Transcriptional analysis of parental iOvCa147 and *DYRK1A*<sup>-/-</sup> spheroid cells with BEAVR uncovered differential gene expression patterns. Components of netrin signaling were found to be upregulated in iOvCa147 cells

upon spheroid formation. In contrast, netrin signaling components were downregulated in *DYRK1A*<sup>-/-</sup> spheroid cells compared to parental spheroid cells. Additionally, we used TRACS to analyze GO-CRISPR screen data from three cell lines and found that netrin signaling sgRNAs were depleted in the loss-of-function screens. Together, this data indicated that netrin signaling was required for spheroid cell survival.

The significance of the data presented in Chapter 5 is twofold. First, validation experiments in which knockout of netrin components led to loss of cell viability in ovarian cancer spheroids demonstrates that GO-CRISPR and TRACS can robustly identify essential genes in loss-of-function screens. This is of particular importance to CRISPR screen studies involving three-dimensional *in vitro* models, such as spheroids or organoids. Such models more accurately represent the tumour microenvironment (TME) compared to two-dimensional monolayer cell culture systems<sup>30-33</sup>. However, the challenges imposed by these models, such as dormancy, slow cycling, or hypoxia, can contribute to poor representation of sgRNA libraries and may also lead to stochastic loss of sgRNAs<sup>34,35</sup>. For example, as described in Chapter 4, established CRISPR screening methods and tools were unable to find essential genes in our experimental system. In comparison, GO-CRISPR and TRACS not only correctly identified genes that are universally known to be essential across all cell lines, including *AGPS*, *SLC2A11*, *ZC3H7A*, *PDCD2L*, and *NPM1* (Chapter 4), it also identified several pathways that are known to promote survival of quiescent cancer cells such as p38 MAPK and cell cycle genes (Chapter 4)<sup>36-42</sup>. Furthermore, the identification of netrin signaling as a critical mediator of survival in the GO-CRISPR screens was consistent with upregulation of these components in unperturbed iOvCa147

spheroid cells. Therefore, we have validated the usefulness and reliability of GO-CRISPR and TRACS in a three-dimensional cell culture system using independent assays.

Secondly, the identification of netrin signaling as a mediator of HGSOc spheroid cell survival advances our understanding of spheroid cell biology. Our study indicates netrin signaling is downstream of DYRK1A and DREAM. Netrin was originally discovered for its role in axon guidance and it is well-characterized in this process<sup>43</sup>. Recently it has been implicated in cancer and has been characterized as an oncogene, but its role in cancer is still poorly understood<sup>44,45</sup>. Netrin ligand binding to receptor homo- or heterodimers appear to protect cells from apoptosis<sup>46,47</sup>. The DCC and UNC5H receptors are therefore known as dependence receptors (DRs)<sup>48,49</sup>. However, there are several receptor and ligand homologs that may impart a positive or negative growth signal on tumour cells as evidenced by the overexpression of the NTN4 ligand in other cancer types<sup>44,50-53</sup>. Additionally, multiple ligands and receptors may play complementary or divergent roles in ovarian cancer<sup>44</sup>. Therefore, while the netrin signaling data presented herein is encouraging as a therapeutic target for HGSOc, it requires further investigation. Specifically, downstream effectors must be identified to better understand how netrin signaling affects viability. Knowledge from axon guidance pathways indicate netrin is positioned upstream of PI3K/AKT/mTOR, p38 MAPK, and NFκB signaling pathways<sup>54-57</sup>. Activation or de-activation of these effectors can be detected upon depletion or overexpression of netrin ligands or receptors in HGSOc spheroid cells. The *in vitro* data presented in Chapter 5 must also be followed by *in vivo* xenograft studies. Specifically, HGSOc spheroid cells with netrin receptor knockouts (either individually or in combination) need to be transplanted into mice intraperitoneally to characterize

tumorigenesis, metastases, and ascites development relative to unperturbed HGSOC spheroid cells. Knockout of receptors instead of ligands in spheroid cells is important since murine netrin ligands secreted into the peritoneum may activate receptors on transplanted cells<sup>58</sup>. Finally, netrin ligands are secreted into the ECM and netrin receptors are extracellular<sup>43</sup>. This presents opportunities to antagonize the pathway using targeted antibodies. Indeed, a monoclonal antibody targeting the NTN1 ligand has been developed and is currently undergoing clinical trials (NCT02977195). It will be interesting to determine if this antibody is sufficient to inhibit spheroid viability and potentially suppress metastases *in vivo* in xenograft models. These investigations are currently underway.

## 6.4 Transcriptional control by DREAM and DYRK1A

In chapter 2 we identified *Apoa1* and *Apoa4* gene expression are regulated by DREAM and MMB. These genes were not described in the 2007 study which established DREAM as a regulator of several hundred cell cycle genes<sup>11</sup>. The authors of that study employed a liquid chromatography-based approach to identify promoters which bound DREAM subunits<sup>11,59</sup>. Our findings illustrate that this list is not exhaustive. More advanced technologies such as CHIP-seq can be used in subsequent studies to identify novel DREAM targets. Additionally, in Chapter 5 we found that genes involved in netrin signaling were differentially expressed in *DYRK1A*<sup>-/-</sup> spheroid cells compared to parental iOvCa147 spheroid cells. We have also performed transcriptional analysis of p130<sup>-/-</sup> spheroid cells and did not find extensive overlap of differentially expressed genes. This suggests that DYRK1A can regulate transcription independently of DREAM in spheroid cells. Indeed,

DYRK1A has been shown to be a transcriptional regulator that phosphorylates the C-terminal domain of RNA polymerase II to promote transcription<sup>60,61</sup>.

In chapter 2 we also demonstrated that loss of DREAM leads to a decrease in H2AZ deposition within gene bodies of target genes (*Apoa1*, *Apoa4*, and *Mybl2*). This provides a mechanistic link to studies performed in *C. elegans* and *Drosophila* which have shown that DREAM repression is marked by gene body deposition of H2AZ<sup>13,62</sup>. A recent study in MEFs suggests the SIN3B/HDAC complex is among the chromatin remodeling factors recruited by DREAM<sup>63</sup>. The epigenetic mechanisms behind DREAM mediated repression of target genes is an evolving story and there are important differences between mammals and lower organisms<sup>13</sup>. Our DREAM deficient mouse model is an important advancement because it will allow for these mechanisms to be investigated in a mammalian system.

## 6.5 Significance of bioinformatic tools

A focus of this thesis has been on the development and importance of bioinformatic tools. Studies have demonstrated the use of novel computational methods to aid in high-throughput genomic and transcriptional studies, particularly in ovarian cancer. For example, in the 2011 study that characterized the genomic landscape of HGSOE, only about 6-8% of cases were found with PTEN alterations<sup>64</sup>. However, it was later suggested that the stromal signature of tumours can confound analysis and a new computational approach that corrected for stromal signatures identified PTEN alterations in 50-70% of cases<sup>65</sup>. Similarly, there have been studies which have identified transcriptomic signatures across ovarian cancer that allows patient samples to be stratified into subtypes<sup>66,67</sup>. Subsequent studies have built on these findings, and as computational approaches improve,



researchers have found that subtypes can be further divided into more distinct clusters<sup>66,68</sup>. This shows how our current understanding of ovarian cancer is continuously evolving, in part due to the advancement of bioinformatic tools and computational methods.

Likewise, the tools presented here have allowed for the identification of new genes and pathways that are important for HGSOc spheroid cell survival. We have developed these tools to have broad usability. Both BEAVR and TRACS have a graphical user interface that is more user-friendly compared to typical command-line driven tools. This reduces a substantial barrier to entry that many researchers face during computation analysis. Both tools support collaboration and allow data to be analyzed and visualized by multiple users. Additionally, both tools can be scaled on high-compute clusters which are becoming more common in research settings<sup>69-71</sup>. We anticipate BEAVR and TRACS will provide researchers the ability to efficiently analyze transcriptional studies and GO-CRISPR screens in-house.

## 6.6 Conclusion

The data presented in this thesis highlight the role of the mammalian DREAM complex and DYRK1A in ovarian cancer spheroid cell survival. The data presented in chapter 2 characterized the effects of long-term DREAM loss in adult mice and uncovered a link between DREAM and amyloidosis. Chapters 3 and 4 described novel tools to rapidly analyze transcriptional studies and perform loss-of-function CRISPR screening, respectively. Chapter 5 utilized these tools to identify a role for netrin signaling in HGSOc spheroid cell survival. The work presented herein advances our knowledge of ovarian cancer and presents DREAM, DYRK1A, and the netrin signaling pathway as critical

mediators of spheroid cell survival. Advancing our understanding of the molecular mechanisms orchestrating dormancy, chemoresistance, and survival in spheroid cells may allow us to exploit these vulnerabilities with novel therapies that can effectively eliminate them in patients.

## 6.7 References

- 1 Bowtell, D. D. *et al.* Rethinking ovarian cancer II: reducing mortality from high-grade serous ovarian cancer. *Nat Rev Cancer* **15**, 668-679, doi:10.1038/nrc4019 (2015).
- 2 Yang, Y. n. *et al.* Reversing platinum resistance in ovarian cancer multicellular spheroids by targeting Bcl-2. *Oncotargets Ther* **12**, 897-906, doi:10.2147/OTT.S187015 (2019).
- 3 Worzfeld, T. *et al.* The Unique Molecular and Cellular Microenvironment of Ovarian Cancer. *Frontiers in oncology* **7**, 24-24, doi:10.3389/fonc.2017.00024 (2017).
- 4 Tan, D. S., Agarwal, R. & Kaye, S. B. Mechanisms of transcoelomic metastasis in ovarian cancer. *Lancet Oncol* **7**, 925-934, doi:10.1016/s1470-2045(06)70939-1 (2006).
- 5 MacDonald, J. *et al.* A Systematic Analysis of Negative Growth Control Implicates the DREAM Complex in Cancer Cell Dormancy. *Mol Cancer Res* **15**, 371-381, doi:10.1158/1541-7786.MCR-16-0323-T (2017).
- 6 Correa, R. J. *et al.* Combination of AKT inhibition with autophagy blockade effectively reduces ascites-derived ovarian cancer cell viability. *Carcinogenesis* **35**, 1951-1961, doi:10.1093/carcin/bgu049 (2014).
- 7 Shield, K. *et al.* Alpha2beta1 integrin affects metastatic potential of ovarian carcinoma spheroids by supporting disaggregation and proteolysis. *J Carcinog* **6**, 11, doi:10.1186/1477-3163-6-11 (2007).
- 8 Shield, K., Ackland, M. L., Ahmed, N. & Rice, G. E. Multicellular spheroids in ovarian cancer metastases: Biology and pathology. *Gynecol Oncol* **113**, 143-148, doi:10.1016/j.ygyno.2008.11.032 (2009).
- 9 Dong, Y. *et al.* Paclitaxel Resistance and Multicellular Spheroid Formation Are Induced by Kallikrein-Related Peptidase 4 in Serous Ovarian Cancer Cells in an Ascites Mimicking Microenvironment. *PLOS ONE* **8**, e57056, doi:10.1371/journal.pone.0057056 (2013).
- 10 Peart, T. *et al.* Intact LKB1 activity is required for survival of dormant ovarian cancer spheroids. *Oncotarget* **6**, 22424-22438, doi:10.18632/oncotarget.4211 (2015).
- 11 Litovchick, L. *et al.* Evolutionarily conserved multisubunit RBL2/p130 and E2F4 protein complex represses human cell cycle-dependent genes in quiescence. *Mol Cell* **26**, 539-551 (2007).
- 12 Litovchick, L., Florens, L. A., Swanson, S. K., Washburn, M. P. & DeCaprio, J. A. DYRK1A Protein Kinase Promotes Quiescence and Senescence Through DREAM Complex Assembly. *Genes Dev* **25**, 801-813 (2011).
- 13 Fischer, M. & Muller, G. A. Cell cycle transcription control: DREAM/MuvB and RB-E2F complexes. *Crit Rev Biochem Mol Biol* **52**, 638-662, doi:10.1080/10409238.2017.1360836 (2017).
- 14 Li, Y.-L. *et al.* DYRK1A inhibition suppresses STAT3/EGFR/Met signalling and sensitizes EGFR wild-type NSCLC cells to AZD9291. *Journal of cellular and molecular medicine* **23**, 7427-7437, doi:10.1111/jcmm.14609 (2019).

- 15 Li, Y. *et al.* DYRK1A suppression restrains Mcl-1 expression and sensitizes NSCLC cells to Bcl-2 inhibitors. *Cancer Biol Med* **17**, 387-400, doi:10.20892/j.issn.2095-3941.2019.0380 (2020).
- 16 DeCaprio, J. A. & Duensing, A. The DREAM complex in antitumor activity of imatinib mesylate in gastrointestinal stromal tumors. *Curr Opin Oncol* **26**, 415-421, doi:10.1097/CCO.000000000000090 (2014).
- 17 Luna, J. *et al.* DYRK1A modulates c-MET in pancreatic ductal adenocarcinoma to drive tumour growth. *Gut* **68**, 1465-1476, doi:10.1136/gutjnl-2018-316128 (2019).
- 18 Kim, H. *et al.* A chemical with proven clinical safety rescues Down-syndrome-related phenotypes in through DYRK1A inhibition. *Disease models & mechanisms* **9**, 839-848, doi:10.1242/dmm.025668 (2016).
- 19 Ionescu, A. *et al.* DYRK1A kinase inhibitors with emphasis on cancer. *Mini Rev Med Chem* **12**, 1315-1329, doi:10.2174/13895575112091315 (2012).
- 20 Forristal, C. *et al.* Loss of the mammalian DREAM complex deregulates chondrocyte proliferation. *Mol Cell Biol* **34**, 2221-2234 (2014).
- 21 Crockett, J. C., Rogers, M. J., Coxon, F. P., Hocking, L. J. & Helfrich, M. H. Bone remodelling at a glance. *J Cell Sci* **124**, 991-998, doi:10.1242/jcs.063032 (2011).
- 22 Das, M. & Gursky, O. Amyloid-Forming Properties of Human Apolipoproteins: Sequence Analyses and Structural Insights. *Adv Exp Med Biol* **855**, 175-211, doi:10.1007/978-3-319-17344-3\_8 (2015).
- 23 Mandato, E. *et al.* CX-4945, a Selective Inhibitor of Casein Kinase 2, Synergizes with B Cell Receptor Signaling Inhibitors in Inducing Diffuse Large B Cell Lymphoma Cell Death. *Curr Cancer Drug Targets* **18**, 608-616, doi:10.2174/1568009617666170427110450 (2018).
- 24 Sadasivam, S. & DeCaprio, J. A. The DREAM complex: master coordinator of cell cycle-dependent gene expression. *Nature reviews. Cancer* **13**, 585-595, doi:10.1038/nrc3556 (2013).
- 25 Iness, A. N. & Litovchick, L. MuvB: A Key to Cell Cycle Control in Ovarian Cancer. *Front Oncol* **8**, 223, doi:10.3389/fonc.2018.00223 (2018).
- 26 Sadasivam, S., Duan, S. & DeCaprio, J. A. The MuvB complex sequentially recruits B-Myb and FoxM1 to promote mitotic gene expression. *Genes & development* **26**, 474-489, doi:10.1101/gad.181933.111 (2012).
- 27 Boichuk, S. *et al.* The DREAM complex mediates GIST cell quiescence and is a novel therapeutic target to enhance imatinib-induced apoptosis. *Cancer Res* **73**, 5120-5129, doi:10.1158/0008-5472.CAN-13-0579 (2013).
- 28 Becker, W. A wake-up call to quiescent cancer cells - potential use of DYRK1B inhibitors in cancer therapy. *FEBS J* **285**, 1203-1211, doi:10.1111/febs.14347 (2018).
- 29 Engeland, K. Cell cycle arrest through indirect transcriptional repression by p53: I have a DREAM. *Cell Death & Differentiation* **25**, 114-132, doi:10.1038/cdd.2017.172 (2017).
- 30 Fujii, M. *et al.* A Colorectal Tumor Organoid Library Demonstrates Progressive Loss of Niche Factor Requirements during Tumorigenesis. *Cell Stem Cell* **18**, 827-838, doi:10.1016/j.stem.2016.04.003 (2016).

- 31 Jacob, F. *et al.* A Patient-Derived Glioblastoma Organoid Model and Biobank Recapitulates Inter- and Intra-tumoral Heterogeneity. *Cell* **180**, 188-204 e122, doi:10.1016/j.cell.2019.11.036 (2020).
- 32 Kenny, H. A. *et al.* Quantitative high throughput screening using a primary human three-dimensional organotypic culture predicts in vivo efficacy. *Nat Commun* **6**, 6220, doi:10.1038/ncomms7220 (2015).
- 33 Vlachogiannis, G. *et al.* Patient-derived organoids model treatment response of metastatic gastrointestinal cancers. *Science* **359**, 920, doi:10.1126/science.aao2774 (2018).
- 34 Ringel, T. *et al.* Genome-Scale CRISPR Screening in Human Intestinal Organoids Identifies Drivers of TGF-beta Resistance. *Cell Stem Cell* **26**, 431-440 e438, doi:10.1016/j.stem.2020.02.007 (2020).
- 35 Zanoni, M. *et al.* 3D tumor spheroid models for in vitro therapeutic screening: a systematic approach to enhance the biological relevance of data obtained. *Sci Rep* **6**, 19103, doi:10.1038/srep19103 (2016).
- 36 Hart, T. *et al.* High-Resolution CRISPR Screens Reveal Fitness Genes and Genotype-Specific Cancer Liabilities. *Cell* **163**, 1515-1526, doi:10.1016/j.cell.2015.11.015 (2015).
- 37 Bragado, P. *et al.* TGF- $\beta$ 2 dictates disseminated tumour cell fate in target organs through TGF- $\beta$ -RIII and p38 $\alpha$ / $\beta$  signalling. *Nature Cell Biology* **15**, 1351-1361, doi:10.1038/ncb2861 (2013).
- 38 Borges, L., Oliveira, V. K. P., Baik, J., Bendall, S. C. & Perlingeiro, R. C. R. Serial transplantation reveals a critical role for endoglin in hematopoietic stem cell quiescence. *Blood* **133**, 688-696, doi:10.1182/blood-2018-09-874677 (2019).
- 39 Park, S.-Y. & Nam, J.-S. The force awakens: metastatic dormant cancer cells. *Experimental & Molecular Medicine* **52**, 569-581, doi:10.1038/s12276-020-0423-z (2020).
- 40 Yu-Lee, L. Y. *et al.* Osteoblast-Secreted Factors Mediate Dormancy of Metastatic Prostate Cancer in the Bone via Activation of the TGF $\beta$ RIII-p38MAPK-pS249/T252RB Pathway. *Cancer Res* **78**, 2911-2924, doi:10.1158/0008-5472.Can-17-1051 (2018).
- 41 Lee, S. H., Reed-Newman, T., Anant, S. & Ramasamy, T. S. Regulatory Role of Quiescence in the Biological Function of Cancer Stem Cells. *Stem Cell Reviews and Reports* **16**, 1185-1207, doi:10.1007/s12015-020-10031-8 (2020).
- 42 Recasens, A. & Munoz, L. Targeting Cancer Cell Dormancy. *Trends Pharmacol Sci* **40**, 128-141, doi:10.1016/j.tips.2018.12.004 (2019).
- 43 Boyer, N. P. & Gupton, S. L. Revisiting Netrin-1: One Who Guides (Axons). *Front Cell Neurosci* **12**, 221, doi:10.3389/fncel.2018.00221 (2018).
- 44 Bruikman, C. S., Zhang, H., Kemper, A. M. & van Gils, J. M. Netrin Family: Role for Protein Isoforms in Cancer. *J Nucleic Acids* **2019**, 3947123, doi:10.1155/2019/3947123 (2019).
- 45 Mehlen, P. & Guenebeaud, C. Netrin-1 and its dependence receptors as original targets for cancer therapy.
- 46 Goldschneider, D. & Mehlen, P. Dependence receptors: a new paradigm in cell signaling and cancer therapy. *Oncogene* **29**, 1865-1882, doi:10.1038/onc.2010.13 (2010).

- 47 Kefeli, U. *et al.* Netrin-1 in cancer: Potential biomarker and therapeutic target?  
48 Gibert, B. & Mehlen, P. Dependence Receptors and Cancer: Addiction to Trophic  
Ligands. *Cancer Res* **75**, 5171-5175, doi:10.1158/0008-5472.CAN-14-3652  
(2015).
- 49 Toda, K. *et al.* Genetic and epigenetic alterations of netrin-1 receptors in gastric  
cancer with chromosomal instability. *Clinical Epigenetics* **7**, 73,  
doi:10.1186/s13148-015-0096-y (2015).
- 50 Esseghir, S. *et al.* Identification of NTN4, TRA1, and STC2 as prognostic markers  
in breast cancer in a screen for signal sequence encoding proteins.
- 51 Srivastava, S. *et al.* Expression of proteins associated with hypoxia and Wnt  
pathway activation is of prognostic significance in hepatocellular carcinoma.
- 52 Thakkar, A. D. *et al.* Identification of gene expression signature in estrogen  
receptor positive breast carcinoma.
- 53 Lv, B. *et al.* Netrin-4 as a biomarker promotes cell proliferation and invasion in  
gastric cancer.
- 54 Lv, J. *et al.* Netrin-1 induces the migration of Schwann cells via p38 MAPK and  
PI3K-Akt signaling pathway mediated by the UNC5B receptor.
- 55 Jin, X. *et al.* Netrin-1 interference potentiates epithelial-to-mesenchymal transition  
through the PI3K/AKT pathway under the hypoxic microenvironment conditions  
of non-small cell lung cancer. *Int J Oncol* **54**, 1457-1465,  
doi:10.3892/ijo.2019.4716 (2019).
- 56 Yin, K. *et al.* Netrin-1 promotes gastric cancer cell proliferation and invasion via  
the receptor neogenin through PI3K/AKT signaling pathway. *Oncotarget* **8**, 51177-  
51189, doi:10.18632/oncotarget.17750 (2017).
- 57 Paradisi, A. *et al.* NF- $\kappa$ B Regulates Netrin-1 Expression and Affects the  
Conditional Tumor Suppressive Activity of the Netrin-1 Receptors.  
*Gastroenterology* **135**, 1248-1257, doi:10.1053/j.gastro.2008.06.080 (2008).
- 58 Sharma, M. *et al.* Netrin-1 Alters Adipose Tissue Macrophage Fate and Function  
in Obesity. *Immunometabolism* **1**, e190010, doi:10.20900/immunometab20190010  
(2019).
- 59 Florens, L. & Washburn, M. P. Proteomic analysis by multidimensional protein  
identification technology. *Methods Mol Biol* **328**, 159-175, doi:10.1385/1-59745-  
026-x:159 (2006).
- 60 Yu, D., Cattoglio, C., Xue, Y. & Zhou, Q. A complex between DYRK1A and  
DCAF7 phosphorylates the C-terminal domain of RNA polymerase II to promote  
myogenesis. *Nucleic Acids Res* **47**, 4462-4475, doi:10.1093/nar/gkz162 (2019).
- 61 Di Vona, C. *et al.* Chromatin-wide profiling of DYRK1A reveals a role as a gene-  
specific RNA polymerase II CTD kinase. *Mol Cell* **57**, 506-520,  
doi:10.1016/j.molcel.2014.12.026 (2015).
- 62 Latorre, I. *et al.* The DREAM complex promotes gene body H2A.Z for target  
repression. *Genes Dev* **29**, 495-500, doi:10.1101/gad.255810.114 (2015).
- 63 Bainor, A. J. *et al.* The HDAC-Associated Sin3B Protein Represses DREAM  
Complex Targets and Cooperates with APC/C to Promote Quiescence. *Cell reports*  
**25**, 2797-2807.e2798, doi:10.1016/j.celrep.2018.11.024 (2018).
- 64 Cancer Genome Atlas Research, N. Integrated genomic analyses of ovarian  
carcinoma. *Nature* **474**, 609-615, doi:10.1038/nature10166 (2011).

- 65 Martins, F. C. *et al.* Combined image and genomic analysis of high-grade serous ovarian cancer reveals PTEN loss as a common driver event and prognostic classifier. *Genome Biol* **15**, 526, doi:10.1186/s13059-014-0526-8 (2014).
- 66 Konecny, G. E. *et al.* Prognostic and therapeutic relevance of molecular subtypes in high-grade serous ovarian cancer. *Journal of the National Cancer Institute* **106**, dju249, doi:10.1093/jnci/dju249 (2014).
- 67 Tohill, R. W. *et al.* Novel molecular subtypes of serous and endometrioid ovarian cancer linked to clinical outcome. *Clin Cancer Res* **14**, 5198-5208, doi:10.1158/1078-0432.Ccr-08-0196 (2008).
- 68 Wang, C. *et al.* Pooled Clustering of High-Grade Serous Ovarian Cancer Gene Expression Leads to Novel Consensus Subtypes Associated with Survival and Surgical Outcomes. *Clinical Cancer Research* **23**, 4077, doi:10.1158/1078-0432.CCR-17-0246 (2017).
- 69 Carrasco-Ramiro, F., Peiró-Pastor, R. & Aguado, B. Human genomics projects and precision medicine. *Gene Therapy* **24**, 551-561, doi:10.1038/gt.2017.77 (2017).
- 70 Sobeslav, V., Maresova, P., Krejcar, O., Franca, T. C. & Kuca, K. Use of cloud computing in biomedicine. *J Biomol Struct Dyn* **34**, 2688-2697, doi:10.1080/07391102.2015.1127182 (2016).
- 71 Agarwal, P. & Owzar, K. Next generation distributed computing for cancer research. *Cancer Inform* **13**, 97-109, doi:10.4137/cin.S16344 (2014).

## Appendices

### **Appendix A Permission for reproduction from the Journal of Clinical Investigation**

The data presented in Chapter 2 is published in the manuscript titled “Disrupting the DREAM transcriptional repressor complex induces apolipoprotein overexpression and systemic amyloidosis in mice”. P. Perampalam, H. M. Hassan, G. E. Lilly, D. T. Passos, J. Torchia, P. K. Kiser, A. Bozovic, V. Kulasingam, F. A. Dick. *Journal of Clinical Investigation*. 2021;131(4):e140903, doi:10.1172/JCI140903.

The manuscript has been modified from its original published format to adhere to the formatting of this thesis.

The original manuscript is available at <https://www.jci.org/articles/view/140903>.



## Appendix B Permission for reproduction from BMC Bioinformatics

The data presented in Chapter 3 is published in the manuscript “BEAVR: a browser-based tool for the exploration and visualization of RNA-seq data”. P. Perampalam & F. A. Dick. *BMC Bioinformatics* **21**, 221, doi:10.1186/s12859-020-03549-8 (2020).

The manuscript has been modified from its original published format to adhere to the formatting of this thesis under the Creative Commons Attribution (CC-BY) license.

The original manuscript is available at

<https://bmcbioinformatics.biomedcentral.com/articles/10.1186/s12859-020-03549-8>.

## Appendix C Pre-print availability of manuscript presented in Chapter 4

The data presented in Chapter 4 is available on bioRxiv as a pre-print manuscript titled “GO-CRISPR: a highly controlled workflow to discover gene essentiality in loss-of-function screens”. P. Perampalam, J. I. MacDonald, F. A. Dick. *bioRxiv*, 2020.2006.2004.134841, doi:10.1101/2020.06.04.134841 (2020).

The manuscript has been modified from its original format to adhere to the formatting of this thesis.

The original manuscript is available at

<https://www.biorxiv.org/content/10.1101/2020.06.04.134841v1.full>

# Curriculum Vitae

## PIRUNTHAN (PIRU) PERAMPALAM

### EDUCATION

<b>PhD – Biochemistry</b> Western University, London, ON	2014-2020
<b>BSc – Specialized Honors Biomedical Science</b> York University, Toronto, ON	2010-2014
<b>BEng – Mechatronics Engineering</b> McMaster University, Hamilton, ON	2004-2009

### RESEARCH EXPERIENCE

<b>Graduate Research Assistant</b> <i>London Health Sciences Centre (LHSC), Western University, London, ON</i> <ul style="list-style-type: none"><li>• Elucidating the cellular mechanisms of ovarian cancer cell dormancy and the contribution of the DREAM/DYRK1A pathway to metastasis and chemoresistance</li><li>• Developed transgenic mouse model and patient-derived xenograft (PDX) models</li><li>• Developed novel methodology for genome-wide CRISPR screens to improve loss-of-function screening in complex 3D culture systems (GO-CRISPR: Guide-Only CRISPR)</li><li>• Developed a novel interactive computational algorithm &amp; software to analyze and visualize GO-CRISPR screens (TRACS: Toolset for the Ranked Analysis of CRISPR Screens) and RNA-seq experiments (BEAVR: Browser-based tool for the Exploration And Visualization of RNAseq data)</li><li>• Extensive experience with high-throughput next-generation sequencing data analyses</li><li>• Qualified to PhD with Distinction</li></ul>	2014-2020
<b>Research Assistant</b> <i>York University, Toronto, ON</i> <ul style="list-style-type: none"><li>• Characterized the asynchronous behaviour of pancreatic ghrelinoma cells following stimulation by norepinephrine and elucidated the interplay of voltage-gated calcium channels and other calcium-binding factors.</li><li>• Investigated the role of intracellular calcium in ghrelin secretion from pancreatic epsilon cells in the islet of Langerhans.</li><li>• Characterized the function of calcium, chloride, potassium, and sodium ion channels in mouse intestinal cells using whole-cell patch clamp electrophysiology.</li><li>• Investigated the role of MEF2 interacting partners in vascular smooth muscle cell gene expression.</li></ul>	2011-2014

**Instructor**

2014-2014

*York University, Toronto, ON*

- Helix Summer Science Institute Instructor for high school (Gr9-12) students
- Designed curriculum to teach students introductory biochemistry, immunology, and virology
- Developed exciting lab activities to engage students in learning fundamental biochemistry techniques.

**EXPERTISE**

- Programming: R, Python, Java, C/C++, HTML, PHP, CSS, ASP .NET, Visual Basic .NET, SQL
- Experience with machine learning using TensorFlow and Keras
- Experience leveraging cloud computing for large data analysis (GCP, Azure, AWS)
- Experience in data mining and visualization including development of custom, task-specific software as needs require
- Big data queries and interpretation

**AWARDS**

<b>Top poster award \$250; London Health Research Day</b>	April 2019
<b>Top poster award \$150; Genes &amp; Cancer, Cambridge, UK</b>	April 2019
<b>Travel award \$1,000; London Regional Cancer Program</b>	Jan 2019
<b>Travel award \$1,000; Department of Oncology, Western University</b>	Dec 2018
<b>Travel award \$2,000; Department of Biochemistry, Western University</b>	June 2018
<b>Top poster award \$50; Oncology Research &amp; Education Day</b>	June 2018
<b>Travel award \$250; Canadian Conference on Ovarian Cancer Research</b>	May 2018
<b>Cancer Research and Technology Transfer Strategic Training Program Award (CaRTT) scholarship \$18,000; Schulich School of Medicine &amp; Dentistry</b>	2017-2018
<b>Travel award \$250; Canadian Conference on Ovarian Cancer Research</b>	May 2016
<b>Cancer Research and Technology Transfer Strategic Training Program Award (CaRTT) scholarship \$18,000; Schulich School of Medicine &amp; Dentistry</b>	2015-2016
<b>Graduate Research Scholarship \$4,500 per annum; Western University</b>	2014-2020
<b>Entrance Scholarship \$2,000; York University</b>	2010-2011
<b>HELIX Instructor Award; York University</b>	2014

**TEACHING AND OTHER EXPERIENCE**

<b>Teaching Assistant</b>	2018-2018
<i>Western University, London, ON</i>	
<b>CaRTT Speaker Selection Committee</b>	2017-2018
<i>London Health Sciences Centre, London, ON</i>	
<b>Doctoral Leadership Forum</b>	2018

Western University, London, ON

**Helix Summer Science Institute Instructor**

2014-2014

York University, Toronto, ON

### STUDENT MENTORSHIP

Komila Zakirova, PhD student

2019-2020

Teodora Marginean, undergrad student

2018-2019

Grace Lily, medical student

2018-2019

Justin Senecal, medical student

2017-2018

Mike Roes, PhD student

2016-2017

Joon Kim, PhD student

2015-2016

### PUBLICATIONS

**Perampalam P**, Hassan HM, Lilly GE, Passos DT, Torchia J, Kiser PK, Bozovic A, Kulasingam V, Dick FA. Disrupting the DREAM transcriptional repressor complex induces apolipoprotein overexpression and systemic amyloidosis in mice. *Journal of Clinical Investigation*. (in press).

**Perampalam P**, Dick, FA. BEAVR: a browser-based tool for the exploration and visualization of RNA-seq data. *BMC Bioinformatics* 21, 221 (2020).

**Perampalam P**, MacDonald JI, Dick FA. GO-CRISPR screening: a highly controlled workflow to discover gene essentiality. *BioRxiv* doi: <https://doi.org/10.1101/2020.06.04.134841> (2020). (pre-print).

MacDonald JI, Ramos-Valdes Y, **Perampalam P**, Litovchick L, DiMattia G, and Dick F. A systematic analysis of negative growth control implicates the DREAM complex in cancer cell dormancy. *Mol. Cancer Res.* 15, 371-81 (2017).

### INVITED TALKS

**Perampalam P**, MacDonald J, DiMattia G, Dick F (2019) A CRISPR screening approach to identify therapeutic targets to treat dormant epithelial ovarian cancer. *London Health Sciences Centre Grand Rounds*. January 15, London, ON.

**Perampalam P**, MacDonald J, Ramos-Valdes Y, Litovchick L, DiMattia G, Dick F (2017) Regulation of dormancy in epithelial ovarian cancer by DREAM/DYRK1A. *Biochemistry Fall Symposium*. October 12, London, ON.

**Perampalam P**, MacDonald J, Ramos-Valdes Y, Litovchick L, DiMattia G, Dick F (2017) DREAM complex contributes to ovarian cancer cell dormancy. *Oncology Research & Education Day*. June 16, London, ON.

**Perampalam P** (2016) Robotics and nanotechnology in healthcare. *Retiring with Strong Minds, Windermere on the Mount*, October 7, London, ON.

**Perampalam P**, MacDonald J, Ramos-Valdes Y, Litovchick L, DiMattia G, Dick F (2016) Regulation of ovarian cancer cell dormancy and gene expression by DREAM. *Biochemistry Symposium, Western University*, May 13, London, ON.

**Perampalam P** (2016) Ovarian Cancer: where we are and where we are headed. *Retiring with Strong Minds, Windermere on the Mount*, April 1, London, ON.

**Perampalam P**, MacDonald J, Ramos-Valdes Y, Litovchick L, DiMattia G, Dick F (2016) The regulation of ovarian cancer cell dormancy and gene expression by the DREAM complex. *LRCPC Cancer Research Trainee Forum*, January 28, London, ON.

**Perampalam P**, MacDonald J, Ramos-Valdes Y, Passos T, Forristal C, Litovchick L, DiMattia G, Dick F (2015) Regulation of gene expression in ovarian cancer by DREAM. *Cancer Research Laboratory Program Seminar Series*, March 5, London, ON.

**Perampalam P**, MacDonald J, Ramos-Valdes Y, Passos T, Forristal C, Litovchick L, DiMattia G, Dick F (2015) Regulation of gene expression in ovarian cancer cells by the mammalian DREAM complex. *Department of Biochemistry Seminar, Western University*, January 16, London, ON.

**Perampalam P**, Tsushima R (2014) Role of intracellular calcium in ghrelin secretion from mouse pancreatic epsilon cells. *Ontario Biology Day 2014*, March 22-23, Mississauga, ON.

### **POSTERS PRESENTATIONS**

**Perampalam P**, MacDonald J, DiMattia G, Dick F (2019) A CRISPR screening approach to identify therapeutic targets to treat dormant epithelial ovarian cancer. *London Health Research Day*. April 30, London, ON.

**Perampalam P**, MacDonald J, DiMattia G, Dick F (2019) A CRISPR screening approach to identify therapeutic targets to treat dormant epithelial ovarian cancer. *Genes & Cancer Annual Meeting*. April 8-11, Cambridge, England, UK.

**Perampalam P**, MacDonald J, Ramos-Valdes Y, Litovchick L, DiMattia G, Dick F (2018) DREAM as a novel regulator of ovarian cancer cell dormancy. *AACR Cancer Dormancy and Residual Disease*. June 19-22, Montreal, QC.

**Perampalam P**, MacDonald J, Ramos-Valdes Y, Litovchick L, DiMattia G, Dick F (2018) DREAM as a novel regulator of ovarian cancer cell dormancy. *Oncology Research & Education Day*. June 8, London, ON.

**Perampalam P**, MacDonald J, Ramos-Valdes Y, Litovchick L, DiMattia G, Dick F (2018) DREAM as a novel regulator of ovarian cancer cell dormancy. *9<sup>th</sup> Canadian Conference on Ovarian Cancer Research*. May 26-29, Edmonton, AB.

**Perampalam P**, MacDonald J, Ramos-Valdes Y, Litovchick L, DiMattia G, Dick F (2018) DREAM as a novel regulator of ovarian cancer cell dormancy. *London Health Research Day*. May 10, London, ON.

**Perampalam P**, MacDonald J, Ramos-Valdes Y, Litovchick L, DiMattia G, Dick F (2017) A systematic analysis of negative growth control implicates the DREAM complex in ovarian cancer cell dormancy. *London Health Research Day*, March 28, London, ON.

**Perampalam P**, MacDonald J, Ramos-Valdes Y, Litovchick L, DiMattia G, Dick F (2016) DREAM complex contributes to epithelial ovarian cancer cell dormancy. *Oncology Research & Education Day*, June 17, London, ON.

**Perampalam P**, MacDonald J, Ramos-Valdes Y, Litovchick L, DiMattia G, Dick F (2016) DREAM complex contributes to epithelial ovarian cancer cell dormancy. *8th Canadian Conference on Ovarian Cancer Research*, May 15-17, Niagara Falls, ON.